ISSN 0915-6348

NATIONAL INSTITUTE FOR FUSION SCIENCE

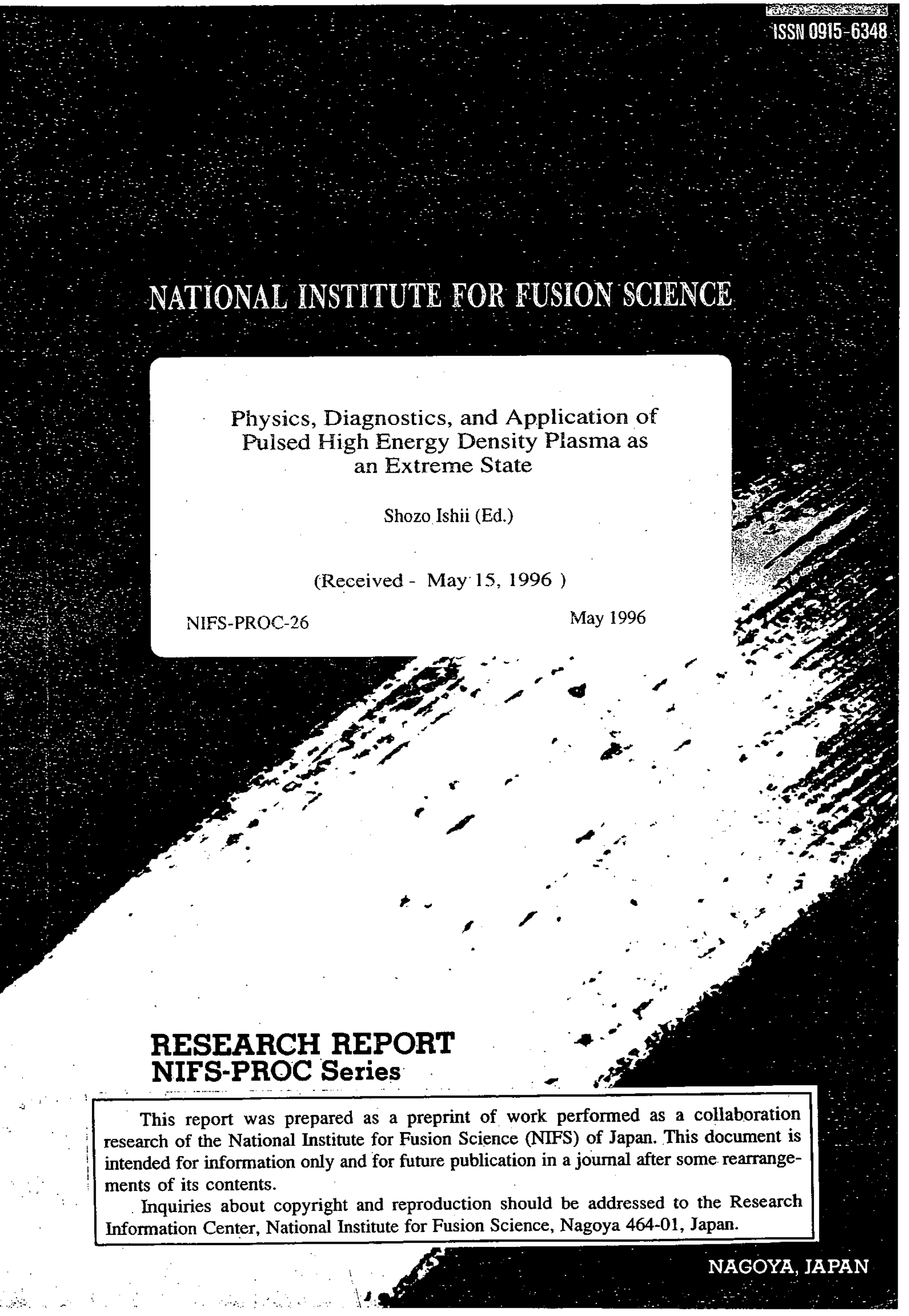

Physics, Diagnostics, and Application of Pulsed High Energy Density Plasma as an Extreme State

Shozo Ishii (Ed.)

(Received - May 15, 1996)

NIFS-PROC-26 May 1996

RESEARCH REPORT
NIFS-PROC Series

NAGOYA, JAPAN

Physics, Diagnostics, and Application of Pulsed High Energy Density Plasma as an Extreme State

Edited by Shozo Ishii

December 11-12, 1995
National Institute for Fusion Science
Nagoya, JAPAN

KEYWORDS: High Energy Density Plasma, Z-Pinch, Plasma Focus, High Power Pulsed Ion Beam, Intense Relativistic Electron Beam, Pulsed Power, Soft X-ray Source, Material Science

PREFACE

The collaborative research symposium entitled "Physics, Diagnostics, and Application of Pulsed High Energy Density Plasma as an Extreme State" was held at National Institute for Fusion Science, Nagoya, from 11 to 12 December 1995. The symposium was attended by 44 people from universities. Papers were presented on Z-Pinches, high power particle beams, and pulsed power. A variety of applications of pulsed high energy density plasmas was also reported. These proceedings contain most of the papers presented at the symposium.

We wish to extend our thanks to the authors, participants, and National Institute for Fusion Science.

Shozo Ishii
Symposium Chairman
Tokyo Institute of Technology

CONTENTS

Characteristics of Magnetically Insulated Diode in a Multi-Shot Operation ············· 1
E. Chishiro, K. Masugata and K. Yatsui (Nagaoka Univ. of Tech.)

Effects of Space Charge Current on Power Flow of Magnetically Insulated Transmission Lines ································· 8
K. Hiraoka, M. Nakajima and K. Horioka (Tokyo Inst. of Tech.)

Time-evolution of IREB Energy and Angular Distribution due to Strong Langmuir Turbulence ··· 15
H. Koguchi, S. Takahata, R. Ando, K. Kamada, M. Masuzaki (Kanazawa Univ.),
M. Yoshikawa (Univ. of Tsukuba)

Preparation of Thin Films and Nanosize Powders by Intense Pulsed Light Ion Beam Evaporation ···························· 25
C. Grigoriu, Y. Nakagawa, E.P.A. Chamdani, T. Sonegawa, K. Nishiura, K.S. Nathan,
K. Masugata and K. Yatsui (Nagaoka Univ. of Tech.)

Effects of Pulsed REB Irradiation on Nitriding in Surface Layers of Irons ············· 35
M. Sato (Gunma Univ.), H. Matsushita, H. Iwasaki, S. Nobuhara (Himeji Inst. of Tech.),
R. Ando, M. Masuzaki (Kanazawa Univ.)

Characterization of $BaTiO_3$ Thin Films prepared by Intense, Pulsed, Ion-Beam Evaporation ························ 45
T. Sonegawa, C. Grigoriu, K. Masugata, K. Yatsui (Nagaoka Univ. of Tech.),
Y. Shimotori, S. Furuuchi (Nippon Seiki), H. Yamamoto (Nichicon)

A Study of Material Processing using an Intense Pulsed Ion Beam ·················· 53
Y. Hashimoto (Kobe City College of Tech.),
M. Yatsuzuka, T. Yamasaki, H. Uchida (Himeji Inst. of Tech.)

Removal of NO_X by Pulsed Power ··· 61
T. Takeshita (Kumamoto Univ.), S. Tsukamoto (Ariake National College of Tech.),
S. Katsuki, H. Akiyama (Kumamoto Univ.)

Fusion Approaches based on Self-Magnetic Field Confinement ····················· 71
T. Miyamoto (Nihon Univ.)

Measurement of Beam Energy of Spherical Plasma Focus Diode and its PIC Code Simulations ································ 81
K. Imanari, K. Sasaki, W. Jiang, K. Masugata and K. Yatsui (Nagaoka Univ. of Tech.)

Effects of Impurities on Operation of Grid-Controlled Vacuum Arc Ion Source ········· 90
J. Hasegawa, H. Nakai, H. Iwasaki, M. Nakajima and K. Horioka (Tokyo Inst. of Tech.)

Air Breakdown induced by a High-Power Short-Pulse Microwave ·················· 95
T. Wakisaka, M. Yatsuzuka and S. Nobuhara (Himeji Inst. of Tech.)

Dielectric Surface Flashover with UV and Plasma Background ··················· 104
F. Hegeler (Kumamoto Univ.) ,
H.Krompholz, L.L.Hatfield, M.Kristiansen (Texas Tech Univ.)

Characteristics of Multichannel Gap ·· 115
S. Takano, Y. Hasegawa, T. Muso and J. Irisawa (Nagaoka Univ. of Tech.)

Unstable Behavior of Parallel Fuses as Opening Switches ························ 123
N. Shimomura, M. Nagata (Univ. of Tokushima) , C.Grabowski (Univ. of New Mexico) ,
K. Murayama, H. Akiyama (Kumamoto Univ.)

Correlation between Plasma Behavior and Hot Spots Generation on Plasma Focus Experiments ··· 132
T. Yanagidaira, H. Kurita, T. Yamamoto, K. Shimoda,
M.Sato and K. Hirano (Gunma Univ.)

Spatial Distribution of the Soft X-ray Emission in 150kJ Plasma Focus with a High Z Gas Puff ··························· 140
H. Kitaoka, A. Sakurai, T. Yamamoto, K. Shimoda,
M.Sato and K. Hirano (Gunma Univ.)

Pinch Characteristics and Soft X-ray Radiation of Z-pinch Plasma produced by Fine Particle Injection ································· 146
D. Itagaki, S. Furuya, D. Kaneko, T. Okuda and S. Ishii (Tokyo Inst. of Tech.)

The Soft X-ray Radiation from Z-pinch Plasma produced by Injecting Metal Vapor; the Vapor is produced by a Wire Explosion ·········· 155
E. Goto, S. Furuya, B. Rahmani, O. Tsuboi and S. Ishii (Tokyo Inst. of Tech.)

Gas-Puff Z-Pinch Plasmas driven by Inductive Energy Storage Pulsed Power Generator ASO-II ······························· 164
K. Murayama, S. Katsuki and H. Akiyama (Kumamoto Univ.)

Soft X-ray Lithography by a Gas-Puff Pinch ································ 174
T. Yamamoto, J. Du, T. Ohata, K.Shimoda, M. Sato and K. Hirano (Gunma Univ.)

Soft X-ray Emission from Capillary Z-discharges driven by Fast Pulse Power Generator ···························· 179
T. Hosokai, M. Nakajima, T. Aoki, K. Horioka and M. Ogawa (Tokyo Inst. of Tech.)

Early Phenomena of Capillary Discharges in Different Ambient Pressures ·········· 187
T. Sueda, S. Katsuki and H. Akiyama (Kumamoto Univ.)

LIST OF PARTICIPANTS

H. Akiyama	Kumamoto University
N. Amakawa	Nihon University
E. Chishiro	Nagaoka University of Technology
J. Du	Gunma University
S. Furuya	Tokyo Institute of Technology
E. Goto	Tokyo Institute of Technology
C. Grigoriu	Nagaoka University of Technology
J. Hasegawa	Tokyo Institute of Technology
Y. Hashimoto	Kobe City College of Technology
F. Hegeler	Kumamoto University
K. Hiraoka	Tokyo Institute of Technology
K. Horioka	Tokyo Institute of Technology
T. Hosokai	Tokyo Institute of Technology
S. Ikegami	Toyokawa Physical Laboratory
K. Imanari	Nagaoka University of Technology
J. Irisawa	Nagaoka University of Technology
S. Ishii	Tokyo Institute of Technology
D. Itagaki	Tokyo Institute of Technology
H. Kitaoka	Gunma University
H. Koguchi	Kanazawa University
K. Masugata	Nagaoka University of Technology
M. Masuzaki	Kanazawa University
T. Miyamoto	Nihon University
K. Murayama	Kumamoto University
J. Nakamura	Nihon University
M. Nakayama	Himeji Institute of Technology
N. Nishino	Hiroshima University
M. Ogawa	Tokyo Institute of Technology
B. Rahmani	Tokyo Institute of Technology

M. Sato	Gunma University
N. Shimomura	The University of Tokushima
T. Sonegawa	Nagaoka University of Technology
T. Sueda	Kumamoto University
T. Tajima	National Institute for Fusion Science
S. Takano	Nagaoka University of Technology
K. Takasugi	Nihon University
T. Takeshita	Kumamoto University
K. Tatsumi	Nihon University
T. Wakisaka	Himeji Institute of Technology
T. Yamamoto	Gunma University
T. Yanagidaira	Gunma University
K. Yasuoka	Tokyo Institute of Technology
K. Yatsui	Nagaoka University of Technology
M. Yatsuzuka	Himeji Institute of Technology

Characteristics of Magnetically Insulated Diode in a Multi-Shot Operation

Etsuji Chishiro, Katsumi Masugata, and Kiyoshi Yatsui

Laboratory of Beam Technology, Nagaoka University of Technology
Nagaoka, Niigata 940-21

Abstract

To clarify the mechanism of the production of anode plasma in magnetically insulated diode (MID), beam characteristics in a multi-shot operation were evaluated experimentally. The MID was successively operated without braking the vacuum. An ion current density (J_i) of 350 A/cm^2 was observed at the first shot when diode gap was 5 mm. The value decreased with increasing the number of shot, and at 7th shot J_i was decreased to be less than 150 A/cm^2. After 7 shots, the surface of anode was observed and found that it was covered with sticked matter of metallic materials such as Zn, Al, Fe, Cu, and it seems to be produced by the ablation of the electrode of MID. By eliminating the sticked matter form the surface, J_i was recovered to the initial value. From the fact, the decrease of J_i is due to that the anode is covered with the sticked matter, which prevents the growth of anode plasma.

1. Introduction

An intense, pulsed, light-ion beam (LIB) is considered as a hopeful candidate for an energy driver of inertial-confinement fusion.1) Furthermore, it has been successfully demonstrated to be applied for materials science.2-4)

A magnetically insulated diode (MID) has been used to generate LIB. In the MID, a magnetic field is applied parallel to the surface of electrodes to inhibit electron flow to the anode. Thereby the anode has rare damage in MID, which enable the multi-shot operate without replacing anode. However, when the MID is successively operated without braking the vacuum, ion current density (J_i) decrease with increasing number of shot.

In this study, the decrease of J_i for several diode gap was measured by biased ion collector (BIC), and effects of deterioration of ion source, backstreaming oil of vacuum pumps and sticked matter covered on ion source were evaluated.

2. Experimental setup

Figure 1 shows the schematic of the experimental setup. The MID utilized in the experiment was a racetrack type diode,$^{5)}$ where flat electrodes of anode and cathode were utilized. In the MID, an insulating magnetic field was produced by an external current through a one-turn coil, which also acted as a cathode. In the beam extraction side of the cathode, a brass vanes were installed. Inside the cathode, aluminum anode was placed, which was connected to an output of pulse-power system "ETIGO-II". As an ion source, the anode had thirteen of polyethylene-filled, 70-mm-long grooves on an active anode area. The grooves had a width and a pitch of 3 and 6 mm, respectively, and they were oriented parallel to magnetic field.

An inductively corrected diode voltage (V_d) was monitored by a capacitive divider. J_i was measured by a BIC what had four apertures. As shown in Fig.1, the measured points were center area on the active ion source. The BIC was made from copper and was located at 34-37 mm downstream from the anode surface. The BIC was biased at a voltage of -1.0 kV to remove accompanying electrons.

Successive operating process is as follows: First shot was operated at 90 minutes after a start of evacuation. After the 1st shot, successive shots were done with a interval of 15 minutes. After those shots, vacuum was broken to replace the anode. The pressure in the experiment was in the range of (1 to 2) × 10^{-2} Pa.

3. Successive operation characteristics

The decrease of J_i in successive operation was evaluated under several diode gap (d) conditions. For all d conditions, a ratio of insulating magnetic field for critical insulating field $^{6)}$ was set in 1.1 ~ 1.2.

Figure 2 shows typical waveforms of V_d and J_i when d is 6.5 mm. As seen in the figure, V_d had a pre-pulse of 150 kV, with duration of 150 ns. J_i rose at about 30 ns after the main voltage pulse. Through all shots, this delay time ranged from 20 to 50 ns and it was independent on d or number of shot. A peak value of J_i was 330 A/cm^2 at 1st shot (Fig.2 (a)), and after 7 shots, the value decreased up to 150 A/cm^2 (Fig.2 (b)). Furthermore, in 1st and 7th shot, delay times from initiation of main voltage pulse to J_i -peak (t_d) were 127 and 150 ns, respectively.

Figure 3 shows dependence of J_i on number of shot. Series of the successive operation was repeated 8 ~ 11 times for each gap length. Dots and error bars indicate averages and deviations of peak value of J_i, respectively. In 1st shot, the shorter gap the larger J_i was measured, and averaged J_i of 350 A/cm^2 was observed in d = 5 mm. These J_i decreased with increasing the number of shot, ant at 7th shot J_i decreased up to ≈150 A/cm^2, although the MID was operated with different d.

Figure 4 shows dependence of t_d on number of shot. As seen in the figure, t_d tend to increase with increasing number of shot.

4. Effect of sticked matter on ion beam generation

When MID is successively operated, sticked matter is stacked on the ion source surface. By eliminating the matter, we examined the effect of the matter.

To analyze the composition of the matter, Si substrate was attached on the center of the active anode and operated for 7 shots. After the shots, mass spectrum of the surface of the sample was analyzed by an X-ray fluorescence analysis, the result of which is shown in Fig. 5. From the figure we see that it consists of Al, Zn, Fe and Cu, which seems to be produced by the ablation of the electrodes of the MID by the irradiation of ion beam or electron beam.

Figure 6 shows the photographs of ion source surface after 7 shots taken by scanning electron microscope. As seen in the figure, the full surface of the ion source (polyethylene) is covered with the sticked matter, and many depression are observed on it (Fig. 6 (b)).

To evaluate the effect of the sticked matter on the generation of ion beam, change of ion current density is observed on the following procedure.

(a) Operate 6 shots.

(b) Break a vacuum in the MID chamber and exhaust again. (non-elimination)

(c) Operate 3 shots.

(d) Break the vacuum, eliminate the matter by wiping the surface and exhaust again. (elimination)

(e) Operate 5 shots.

(f) Switch to rotary pumps from diffusion pumps, keep the MID in low vacuum of 10 Pa for 20 minutes and after that, exhaust again.

(g) Operate 1 shot.

Above procedure was repeated for 5 times, and obtained the statistics of the data. Figure 7 shows the experimental result. On the process (c), high value of J_i was obtained only at the first shot, and after the 2nd shot J_i became low, and t_d kept a long time. On the other hand, on the process (e), J_i of 300 A/cm^2 is obtained at the first shot and it gradually decreased with increasing number of shot. The value of t_d becomes longer with increasing shot, too. This characteristics is almost similar to the process (a). From the experiment, we see that the anode is refreshed by eliminating the sticked matter from the surface.

In oily exhausting system, 0.5% of residual gas in a vacuum chamber are generally backstreaming oil molecules.7) The backstreaming oil is expected to be enhanced in the process (f) and it may affect the production of ion beam. However, on the process (g), clear change of J_i and t_d is not observed, which shows that backstreaming oil in the vacuum dose not strongly affect the characteristics of ion source.

In the process (c) we see the change of the color of the surface of polyethylene from translucent to white, which seems to be due to the deterioration of the surface by the irradiation of the anode plasma. However, we found that the deterioration did not contribute to successive characteristics.

5. Discussion

In this section we try to consider why J_i decreases in the successive operation. The decrease of J_i is caused by a increase of effective gap, a change of beam composition or, by a decrease of ion source. Since the effective gap of MID is decreased by the expansion of anode plasma and by the reduction of expansion velocity, effective gap is elongated as compared to the previous shot. The expansion velocity seems to depend on the density, temperature or the composition of the plasma, however it is not investigate in detail.8),9)

For the diode of which beam consists of multiple ion species, the Child-Langmuir space charge limited current density is lower than for that of pure proton. The Child-Langmuir current density ($J_{s\ell}$) such as the diode 10) is given by

$$J_{s\ell} = \frac{J_1}{\alpha_1 + \sum_{k \neq 1} \alpha_k \sqrt{\frac{m_k}{z_k m_1}}} \tag{1}$$

where

$$\alpha_k = \frac{J_k}{J_{s\ell}} \tag{2}$$

is the current density fraction of the kth ion species and, z_k, m_k and J_k are the charge state, mass and the current density of atomic number=k. J_1 is the Child-Langmuir current density for proton (k=1). From the equation, it is found that $J_{s\ell}$ extremely decreases if heavy ion is mixed in the ion beam.

The process of the production of anode plasma in MID is basically considered to be as follow:11)

i) Leakage electrons emitted from cathode irradiate ion source.
ii) Sorbed molecules desorbe from the source surface and form gas cloud close to the surface.
iii) The source is charged up by the electron irradiation.12)
iv) Electric field by the charge-up causes electron avalanche in the cloud and produce an initial anode plasma.
v) Thermal and ionic bombardment of the source lead to additional desorption and vaporization of source molecule adding to neutral density in the anode plasma region.
vi) Further ionization in gas phase is lead to fully developed the anode plasma.

When an ion source is covered with sticked matter, supply of hydrogen molecules from polyethylene is reduced in process (v), which reduce the plasma density and make the average mass of ion heavier. As a results J_i is reduced by the reduction of expansion velocity of anode plasma, increase of average mass or the reduction of plasma density, which will contribute the t_d reduction.

6. Conclusion

Successively operation characteristics were evaluated experimentally. An ion current density (J_i) of 350 A/cm^2 was observed at the first shot when diode gap was 5 mm. The value decreased with increasing the number of shot and at 7th shot J_i decreased to be less than 150 A/cm^2. After 7 shots, the surface of anode was observed and found that it is covered with sticked matter of metallic materials such as Zn, Al, Fe, Cu, and it seems to be produced by the ablation of the electrode of MID. By eliminating the sticked matter form the surface, J_i was recovered to the initial value.

Reference

(1) T.H.Johnson: *Proc. of the IEEE*, **72**, 547 (1984).
(2) K.Yatsui: *Laser & Particle Beams*, **7**, 733 (1989).
(3) K.Yatsui, X.Kang, T.Sonegawa, T.Matsuoka, K.Masugata, Y.Shimotori, T.Satoh, S.Furuuchi, Y.Ohuchi, T.Takeshita and H.Yamamoto: *Phys. Plasmas*, **1**, 1730 (1994).
(4) E.L.Neau: *IEEE Trans. on Plasma Sci.*, **22**, 2 (1994).
(5) K.Yatsui, A.Tokuchi, H.Tanaka, H.Ishizuka, A.Kawai, E.Sai, K.Masugata, M.Ito and M.Matsui: *Laser & Particle Beams*, **3**, 119 (1985).
(6) R.N.Sudan and R.V.Lovelace: *Phys. Rev. Lett.*, **31**, 1174 (1973).
(7) L.Maurice, P.Duval and G.Gorinas: *J. Vac. Sci.*, **16**, 741 (1979).
(8) R.Pal and D.Hammer: *Phys. Rev. Lett.*, **50**, 732 (1983).
(9) Y.Maron, M.D.Coleman, D.A.Hammer and H.S.Peng: *Phys. Rev. Lett.*, **57**, 699 (1986).
(10)D.L.Hanson, J.L.Porter and R.R.Williams: *J. Appl. Phys.*, **70**, 2926 (1991).
(11)E.W.Gray: *J. Appl. Phys.*, **58**, 132 (1985).
(12)D.J.Johnson, J.P.Quintenz and M.A.Sweeney: *J. Appl. Phys.*, **57**, 794 (1985).

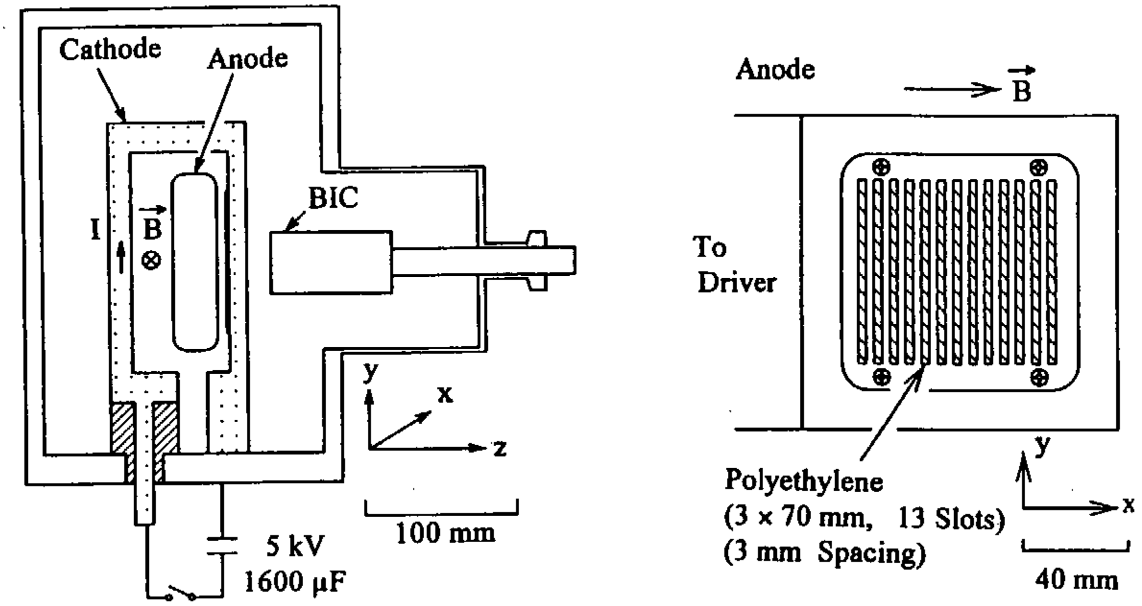

(a) (b)

Fig.1 (a) Schematic diagram of MID, (b) Frontal diagram of anode.

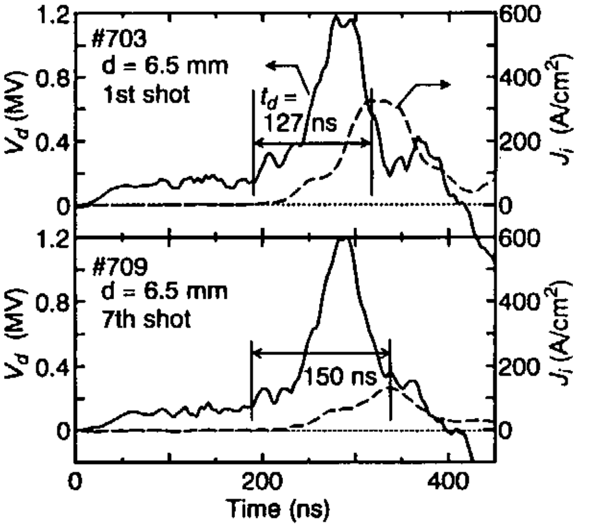

Fig. 2 Typical waveforms of diode voltage (V_d) and ion current density (J_i), where J_i was measured at z = 34 - 37 mm downsteam from the anode surface. (a) 1st shot, (b) 7th shot.

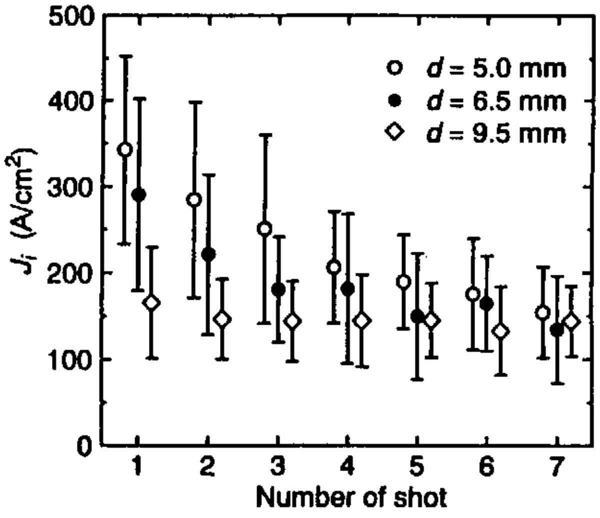

Fig. 3 Dependence of J_i on number of shot.

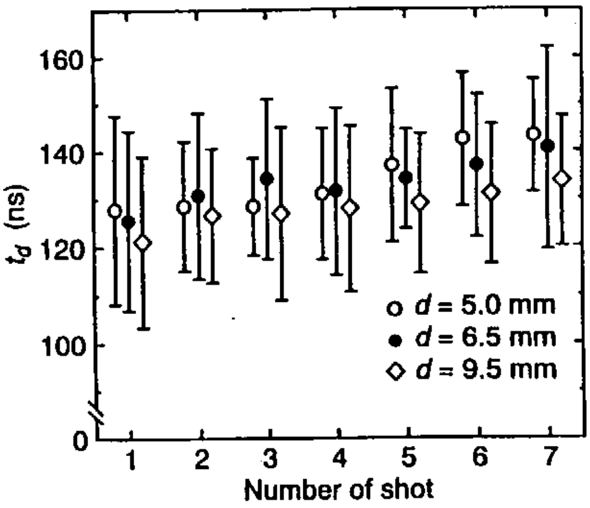

Fig. 4 Dependence of t_d on number of shot.

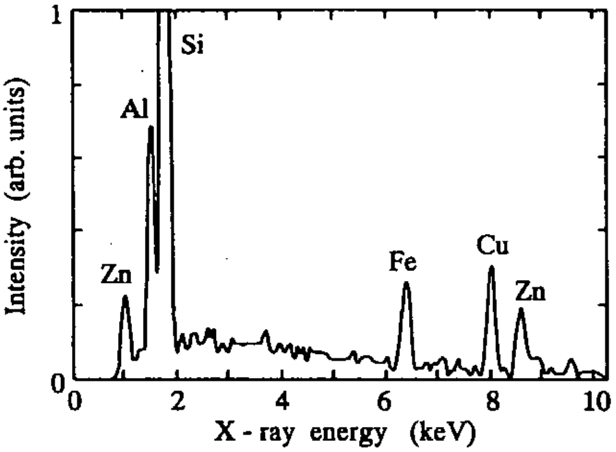

Fig. 5 Mass spectrum of Si substrate after 7 shots.

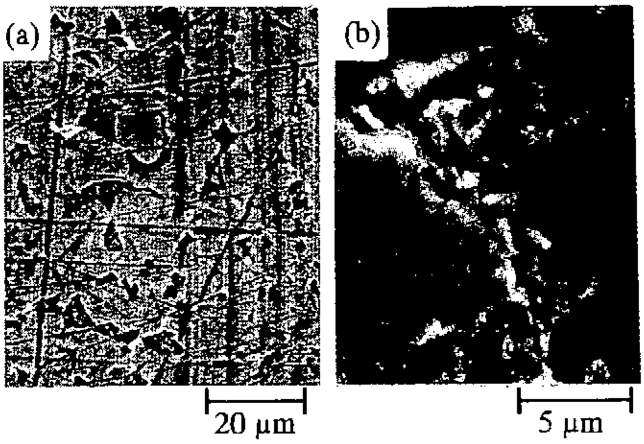

Fig. 6 Photographs of anode surface after 7 shots. (a) ×780, (b) ×3600.

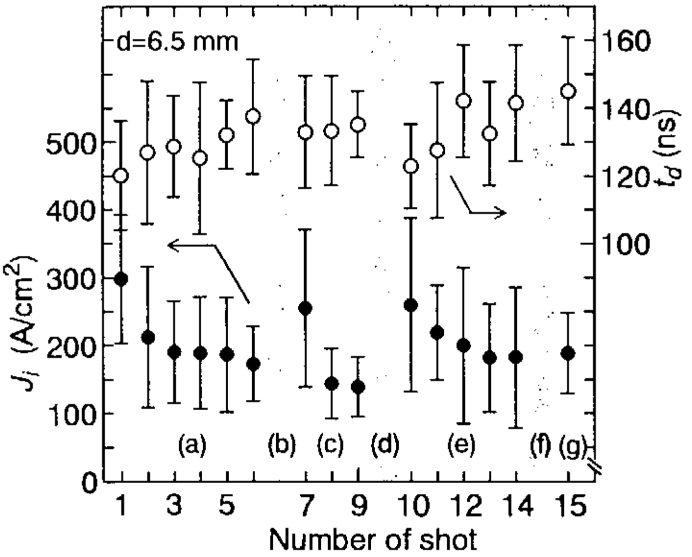

Fig. 7 Dependence of J_i and t_d on elimination or non-elimination of sticked matter.

EFFECTS OF SPACE CHARGE CURRENT ON POWER FLOW OF MAGNETICALLY INSULATED TRANSMISSION LINES

Kazuki HIRAOKA, Mitsuo NAKAJIMA and Kazuhiko HORIOKA
Department of Energy Sciences, Tokyo Institute of Technology Nagatsuta 4259,
Midoriku Yokohama, Japan 226

ABSTRACT

We have developed a new equivalent circuit model for space charge dominated MITLs(Magnetically Insulated Transmission Lines). MITLs under high power operation are dominated with space charge current flowing between anode and cathode. Conventinal equivalent circuit model does not account for space charge effects on power flow. To discuss the power transportation through the high power MITLs, we have modified the model. With this model, we can estimate the effects of space charge current on the power flow efficiency, without using complicated particle code simulations.

1. INTRODUCTION

The Magnetically Insulated Transmission Line (MITL) is a high power vacuum transmission line that insulate the field emitted electrons by bending their trajectories with self magnetic field. Thus it can transport multi-terawatt electromagnetic pulse.

In the design and parametric analysis of MITLs, the equivalent circuit modeling (Fig.1)[1] is widely used. Its advantage is that the model can describe the generator, MITL and load by one circuit, so interaction of these components can be easily discussed.

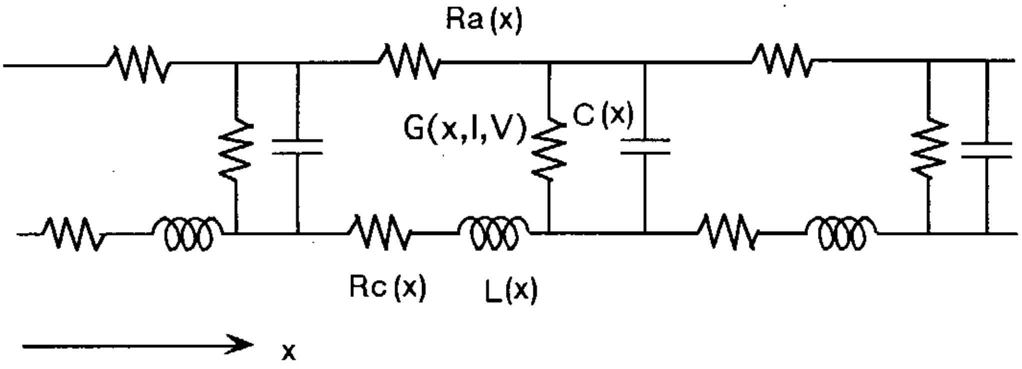

Fig.1 An Example of Equivalent Circuit Modeling of MITL

This model uses the vacuum values for the effective inductance L and the capasitance C in spite of the presence of space charge, and the current the space charge carries is not taken into account. However, the space charge electrons flowing in the gap considerably reduce the effective inductance and capasitance from vacuum value. For example as shown later, we have obtained results that the space charge electron flow carries ~50 percent of total current. So these effects are not trivial in estimation of power transport efficiency. If we use PIC(Particle-in-cell) simulation, we can estimate these effects. However, PIC code needs large amount of memory and computer time, so the survey for optimization of the power transport efficiency over a wide range of parameter is very difficult.

We have developed a new equivalent circuit model including space charge current and effective L and C by using one-dimensional laminar flow approximation(Fig.2) for coaxial structure.

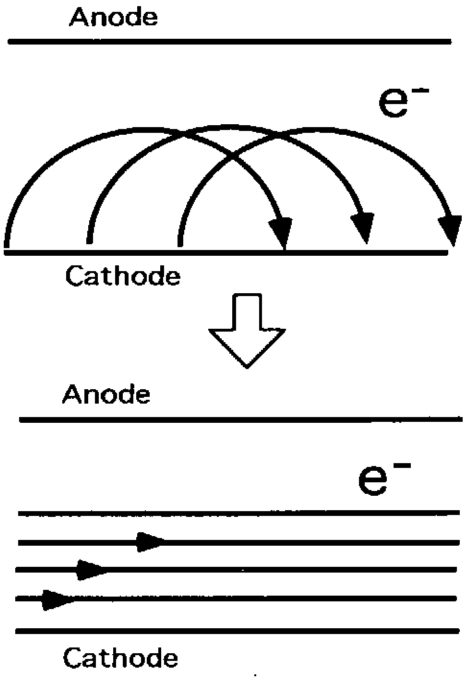

Fig.2 Schematic of Laminar Flow Modeling

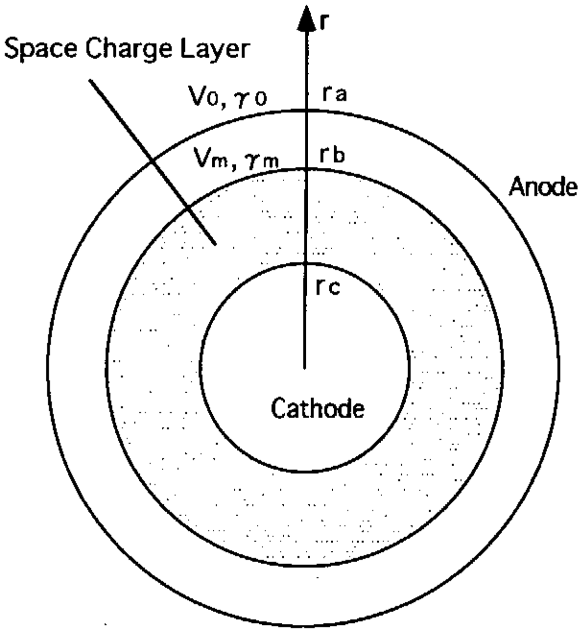

Fig.3 Cross section of cylindrical MITL

2. DEVELOPMENT OF THE MODEL

In our modeling, as shown schematically in Fig.4, once magnetic insulation is established($I>I_c$), the equivalent circuit is replaced by modified circuit that has space charge current path. Here, I_c is the critical current which makes emitted electrons' trajectories just tangent at the anode. We assumed that if the total current is below this value, electrons emitted at the cathode run into the anode; space charge limited current flows across the vacuum gap and the insulation is not achieved. This is the reason why the conductuance G is present in our model.

To determine I_c, L, M and C analytically, we use laminer flow theory of space charge flow (Relativistic Brillouin Flow model[2]). It assumes that electrons move in straight trajectories normal to the electric and magnetic field and parallel to the axis. In this theory, solutions for potential, charge desity distribution, and fraction of the current carried by the space charge are obtained self-consistently as follows,

$$I = \frac{I_\alpha}{\ln\left(\frac{r_a}{r_c}\right)}\gamma_m \cdot \left\{ \ln\left(\gamma_m + \sqrt{\gamma_m^2 - 1}\right) + \frac{\gamma_0 - \gamma_m}{\sqrt{\gamma_m^2 - 1}} \right\} \tag{1}$$

$$I_b = \frac{I}{\gamma_m} \tag{2}$$

with

$$\gamma_{0,m} = 1 + \frac{eV_{0,m}}{m_0 c^2} \tag{3}$$

$$I_\alpha = \frac{m_0 c^2}{e}\frac{2\pi}{\mu_0 c} = 8500(A) \tag{4}$$

Here I is the total (anode) current, V_0 is the anode potential, V_m is the potential at the edge of the electron sheath, and γ_m is the ratio of total (anode) current I and conduction (boundary) current I_b on the cathode. The distributing profile of space charge flow is assumed as,

$$i(r) = \frac{I}{\gamma_m}\cosh\left(\frac{I}{I_\alpha \gamma_m}\ln\frac{r}{r_c}\right) \tag{5}$$

where r is coodinate of radial direction in the cylindrical MITL, r_c and r_a is radius of the cathode and anode(Fig.3), i(r) represents the current enclosed with the cylinder of radius r.

The outer radius of space charge layer is expressed as

$$r_b = \exp\left(\ln r_a - \frac{\gamma_0 - \gamma_m}{\sqrt{\gamma_m^2 - 1}}\frac{I_\alpha \gamma_m}{I}\right) \tag{6}$$

With these functions, effective inductance L_c, L_s and mutual inductance M can be calculated analytically, as follows.

$$L_c = \frac{\mu_0 l}{2\pi}\ln\frac{r_a}{r_c} \tag{7}$$

$$L_s = \frac{\mu_0 l}{2\pi}\ln\frac{r_a}{r_b} + \frac{1}{I_s}\int_{r_c}^{rb}\frac{i(r) - I_b}{I_s}\cdot\frac{\mu_0 l}{2\pi r}\cdot\frac{i(r) - I_b}{r}dr \tag{8}$$

$$M = \frac{\mu_0 l}{2\pi}\ln\frac{r_a}{r_b} + \int_{r_c}^{rb}\frac{i(r) - I_b}{I_s}\cdot\frac{\mu_0 l}{2\pi r}dr \tag{9}$$

where, I_s is the space charge current: $I_s = I - I_b = (1-1/\gamma_m)I$, and l is the length of one unit of the equivalent circuit.

The calculation of C_a and C_c depends on some assumptions. At first, we must derive theexpression for capasitance dC at radius r and gap distance dr,

$$dC = \frac{2\pi\varepsilon_0 l\, r}{dr} \quad . \tag{10}$$

If the currents flowing in the next unit are primed, the current flowing this capasitance is i(r)-i'(r). Using this current and an assumption that the shape of the pulse is square, the voltage between the edge of electron sheath and the cathode surface is

$$V_m = \int_{r_c}^{r_b} \frac{1}{dC} \int_0^T \left(i(r) - i'(r) \right) dt \tag{11}$$

$$\approx \int_{r_c}^{r_b} \frac{1}{dC} \left(i(r) - i'(r) \right) T \tag{12}$$

$$= \int_{r_c}^{r_b} \frac{1}{2\pi\varepsilon_0 l} \cdot \frac{1}{r} \left(i(r) - i'(r) \right) T\, dr \quad . \tag{13}$$

For simplicity, we assume that the ratio i(r) and I_b is nearly equals that of i'(r) and I'_b, and C_c is calculated from the next eq.

$$\frac{1}{C_c} = \frac{V_m}{(I_b - I'_b)} \approx \int_{r_c}^{r_b} \frac{1}{2\pi\varepsilon_0 l} \cdot \frac{1}{r}\, i(r)\, dr \,/ I_b \quad . \tag{14}$$

The capasitance of the vacuum region is obtained by

$$C_a = \frac{2\pi\varepsilon_0 l}{\ln \frac{r_a}{r_b}} \quad . \tag{15}$$

The resistance R is electrode resistance when skin depth is about 10^{-5} m .

The conductance G of space charge limited current is usually the product of four functions(16). They are a space-charge-limited Langmuir-Child conductance G_{CL}which depends on voltage and geometry(17), an electric field dependent function f_1 accounting for emission turn-on, a smooth function of current f_2 which is 1 for zero current and drops to 0 when $I \geq I_c$, and correction function f_3 for relativistic effects. Generaly to say, the choice of these functions f is arbitrary. In this report, we chose $f_1, f_2 = 1$ for simplicity.

$$G = G_{CL} f_1 f_2 f_3 \tag{16}$$

$$G_{CL} = \frac{8\pi\, \varepsilon_0 r_c}{9(r_a - r_c)^2} \sqrt{\frac{2eV}{m}} \tag{17}$$

When the solutions for γ_m of equation (1) are not existing, we regard as the magnetic insulation is not achieved and the minimum value (for V) of right side of equation (1) is chosen for I_c.

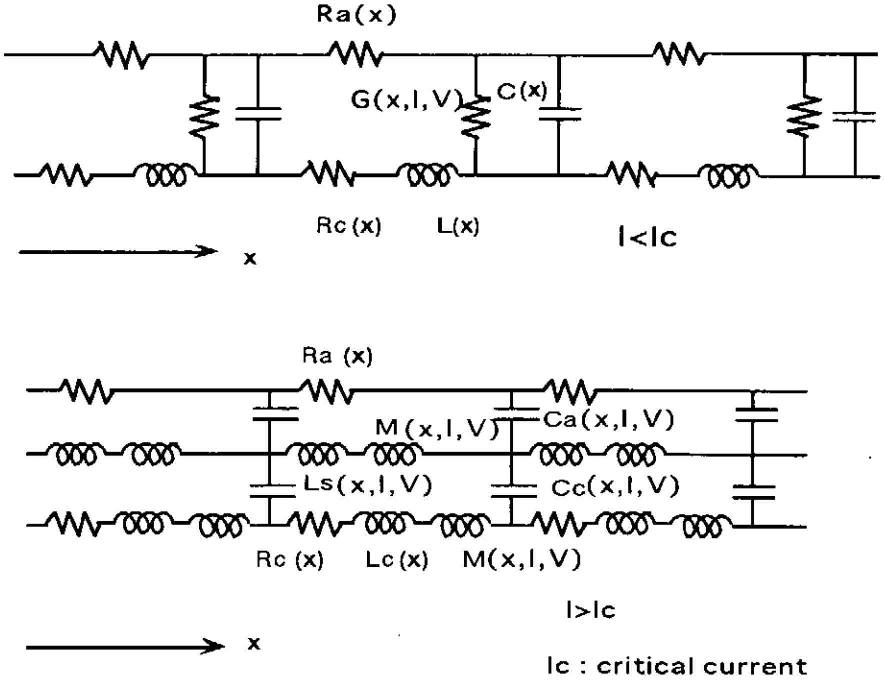

Fig. 4 Modified Equivqlent Circuit

3. RESULTS

Typical results of the simulations are shown in Fig.5~Fig.7. In Fig.5, the calculations of conventional equivalent circuit and a new equivalent circuit including space charge effects are compared under matching-load-condition. As shown in Fig.5, the effective impedance (V/I) is reduced to 78% by taking account of space charge current. The power reflection due to impedance mismatch can also be observed. Fig.6, 7 are comparisons of simulation results between the equivalent circuit calculation and the PIC simulation. Because the calculations of PIC[4] are positive polarity (the cathode is outer electrode, and anode is inner), they are not strict comparison, but qualitative characteristics are fairly expressed with our model.

4. CONCLUDING REMARKS

We have developed a new equivalent circuit model of MITLs which includes space charge effects. Results obtained with this model are compared to those by conventional equivalent circuit model and PIC simulations. The qualitative agreement between the simplified calculation and the results of PIC simulation is fairly good. The CPU time for the calculations is only a few minutes by an average personal computer (Power Macintosh).

REFERENCES

[1] Kenneth D. Bergeron, J.Appl.Phys. 48, p.3065 (1977).
[2] K.Horioka, K.Hiraoka, M.Nakajima and T.Aoki, NIFS-PROC-23, p.118 (1995)
[3] John M.Creedon, J.Appl.Phys. 46, p.2946 (1975).
[4] C. W. Mendel, Jr. and S. E. Rosenthal , Proc.10th Int.Conf.High Power Particle Beams, p276 (1994)

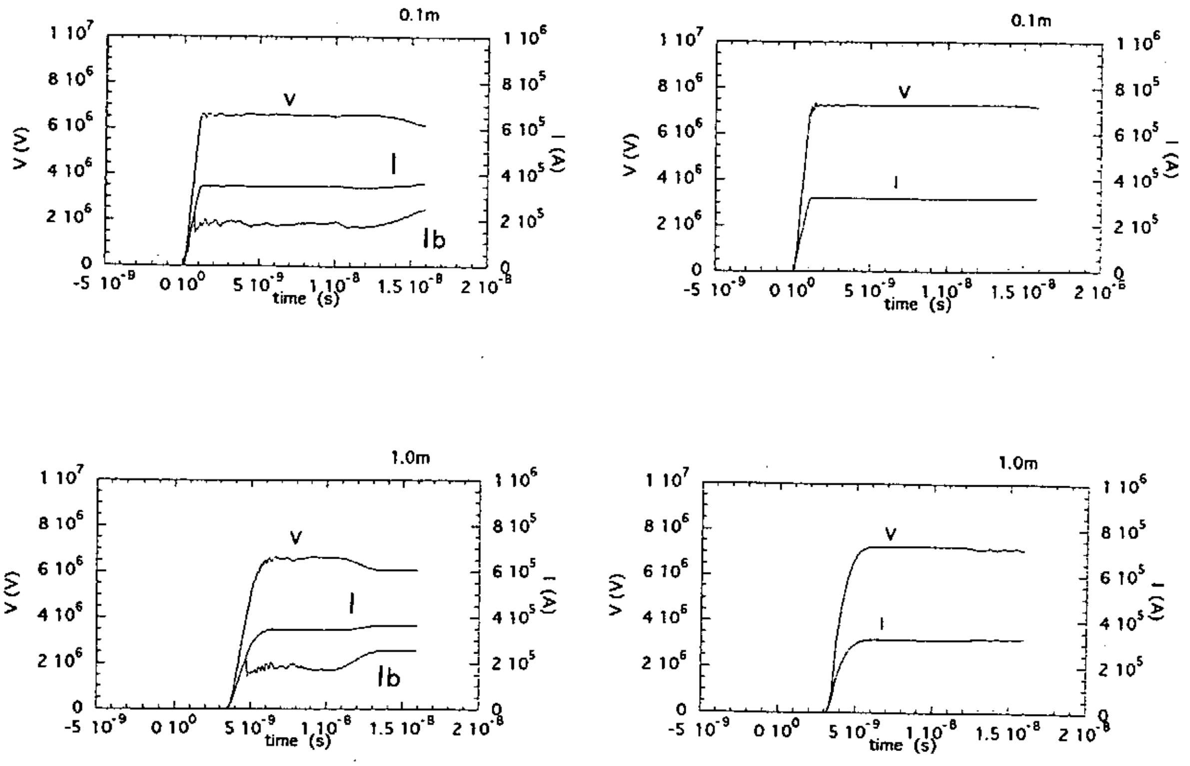

(a) (b)

Fig.5 The model(a) and usual equivalent circuit(b) calculations of of voltage V and the anode and cathode currents (I, I_b) for a step voltage in a 24.3Ω, 2m long MITL.

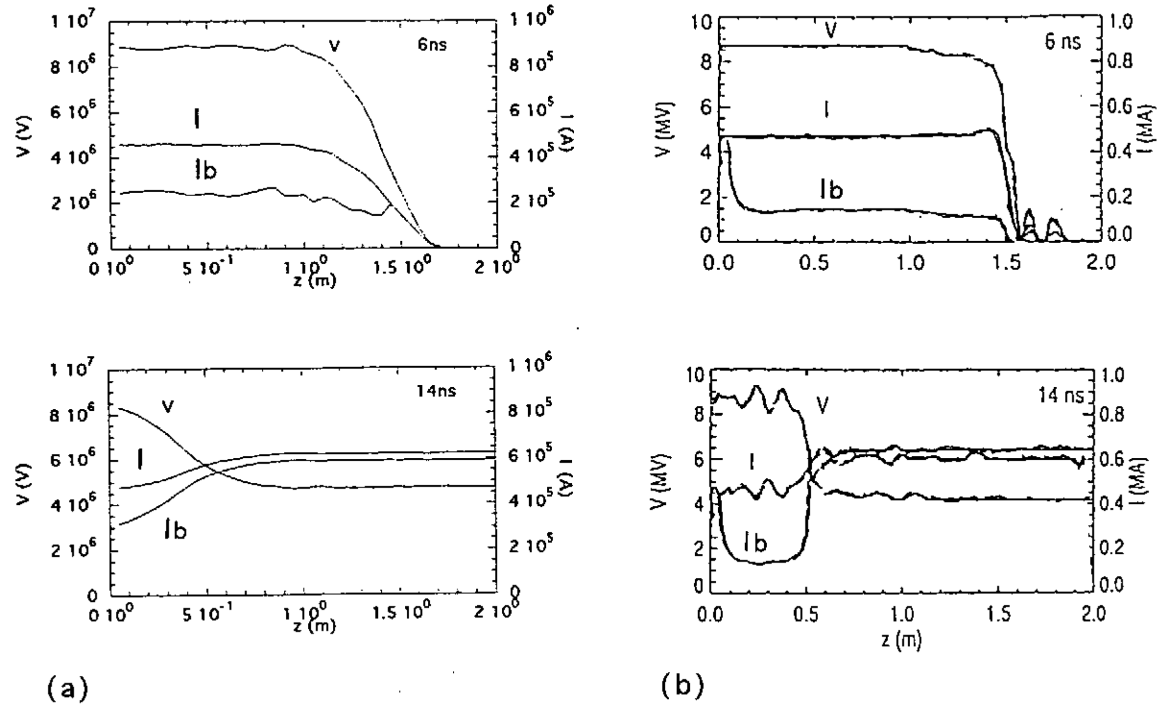

Fig.6 The model(a) and PIC(b) caluculations for a step voltage in a 24.3Ω, 2m long MITL.

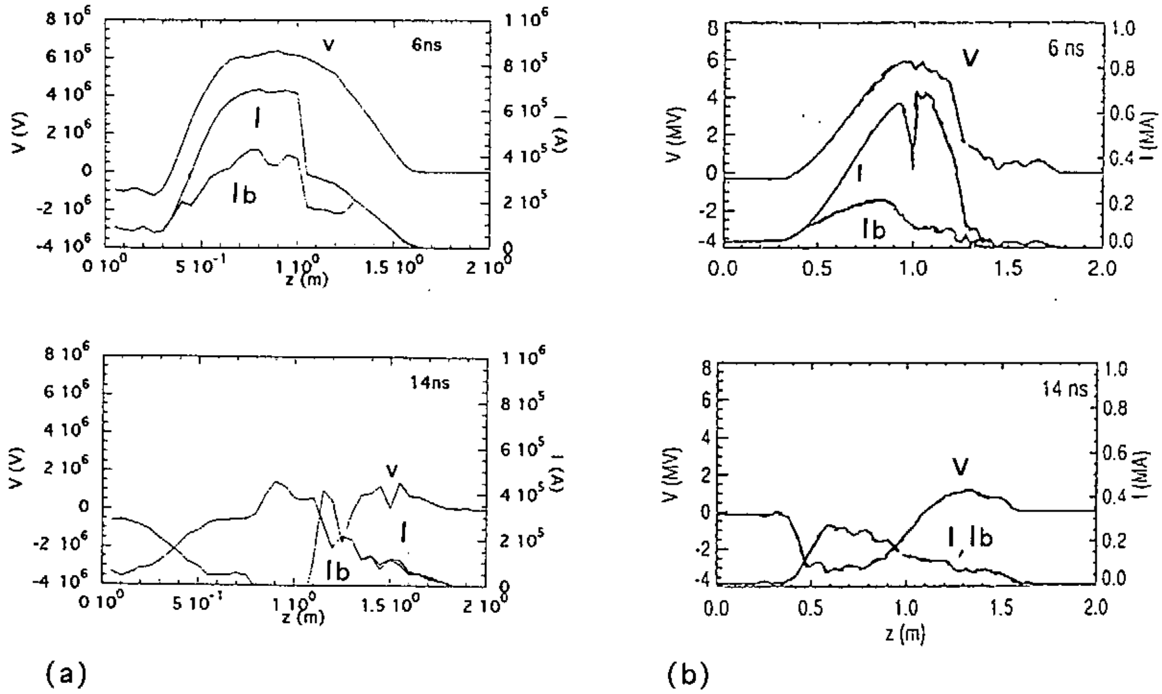

Fig.7 The model(a) and PIC(b) caluculations for a 5ns wide at base pulse voltage in a 2m long MITL that begins at 11.9Ω and changes to 24.3Ω in the middle of the line.

Time-evolution of IREB energy and angular distribution due to strong Langmuir turbulence

H. Koguchi, S. Takahata, R. Ando, K. Kamada, M. Masuzaki and M. Yoshikawa*

Faculty of Science, Department of Physics, Kanazawa University
* Plasma Research Center, University of Tsukuba

Abstract

A plasma becomes a strong turbulence state when an intense relativistic electron beam (IREB) is injected into it. In order to study this strong Langmuir turbulence state, we measured the beam properties after passing the plasma. The energy and angular spreads of the IREB were measured by a magnetic energy analyzer and an angle analyzer, respectively. The theory of transit-time interactions was applied to analyze the observed energy and angular spreads and to estimate the turbulent field strengths. These results were in good agreement with the spectroscopic measurement.

The broadband microwave radiation was also observed simultaneously with the angular spread measurement. We found correlation between the radiation and the angular spread of the IREB. The wider the angular spread, the stronger the microwave radiation.

Introduction

Recently, the beam-driven strong Langmuir turbulence has attracted much attention theoretically, computationally$^{1,2)}$ and experimentally.$^{3-15)}$ In the strong Langmuir turbulence state, generation, collapse and burnout of cavitons are repeated by the nucleation process.$^{16-19)}$ Here a caviton is a density cavity in which high intensity oscillating electrostatic fields are trapped. In our recent experiments, spectroscopic measurements of high intensity oscillating electrostatic fields in cavitons and measurements of high power broadband microwave radiation were carried out in the same experimental setup.$^{11-14)}$ For understanding the strong Langmuir turbulence state, investigation of the beam properties after passing the plasma is also important . So the energy distribution and the angular spread of the IREB were measured by means of a magnetic energy analyzer and an angle analyzer, respectively. The measured energy distribution and angular spread of the IREB were analyzed using the theory of transit-time interactions.$^{20)}$ The results of the analysis shows the presence of localized intense electric fields, and this fact is in good agreement with the spectroscopic measurements.

High power broadband microwave radiation was measured simultaneously with the angu-

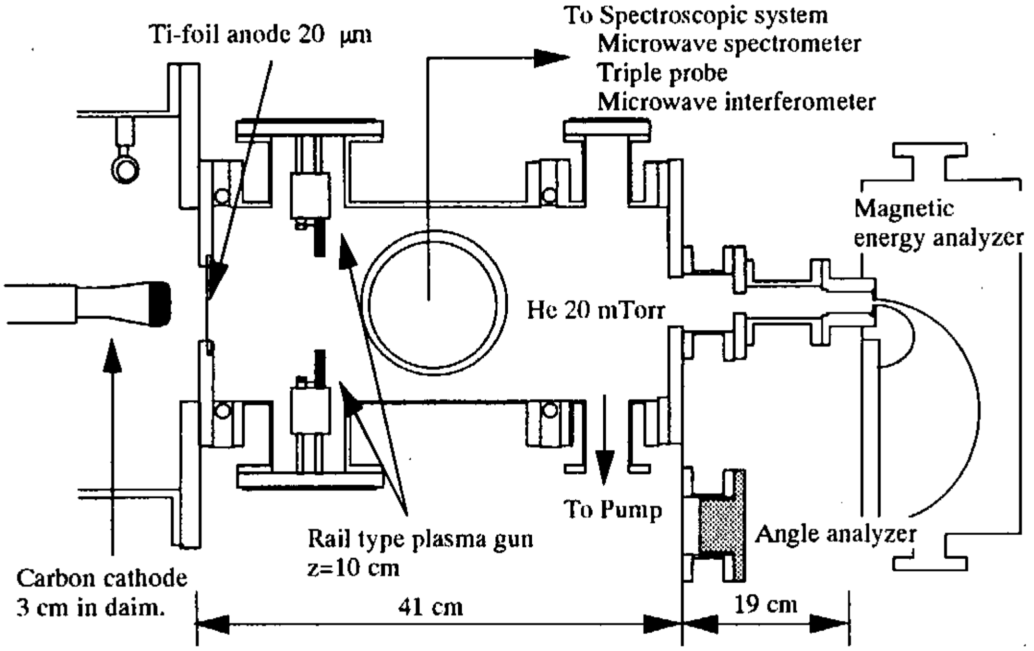

Fig. 1. The experimental setup.

lar spread measurement. The radiation was observed only during the IREB pulse as had been observed in the previous experiment. This fact shows that the radiation source was the beam electrons. There was correlation between the angular spread of the IREB and the microwave radiation.

Experimental setup

Figure 1 shows the experimental setup. Pulserad 110A produced by Physics International was used to produce an IREB. A diode consisted of a carbon cathode of 3.6 cm in diameter and a titanium foil anode of 20 μm thick. The IREB (3 cm in diameter, 1.4 MeV, 10 kA, and 30 nsec) was injected into a carbon plasma. The drift chamber, made of stainless-steel, 60 cm long and 16 cm in diameter, was filled with 20 mTorr He gas for the spectroscopic measurement. The background pressure was around 5×10^{-5} Torr. The carbon plasma was generated by two sets of rail type plasma guns set opposite to each other at 10 cm downstream of the anode foil. The plasma density was measured by a triple probe and a microwave interferometer at 17.5 cm downstream the anode. Figure 2 shows the plasma density as a function of the delay time τ of the IREB injection after the firing time of the guns. The plasma density was varied from the order of 10^{11} to the order of 10^{13} cc^{-1} by changing τ. The electron temperature without the IREB injection was measured by the triple probe, and it was 6 - 9 eV. When the IREB was injected into the plasma, the electron temperature, T_e, was estimated from the spectroscopic measurement of the intensity ratio of HeI 492.19 nm line (singlet) to HeI 471.31 nm line (triplet) by comparing the experimental results with the newly developed collisional radiative model.[21)] Figure 3 shows T_e as a

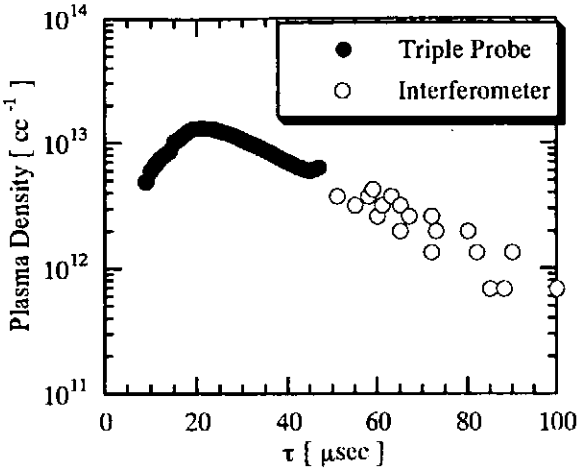

Fig. 2. The plasma density.

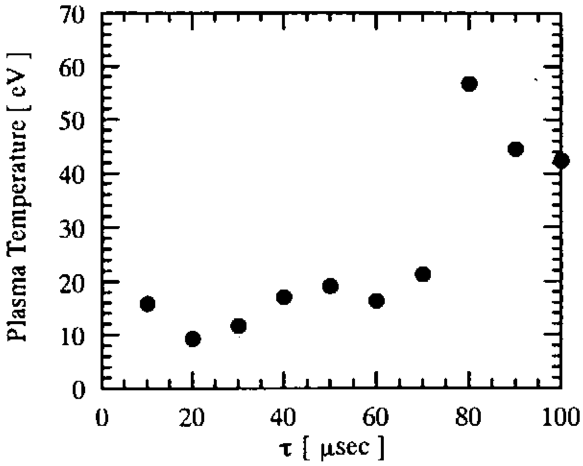

Fig. 3. The plasma temperature.

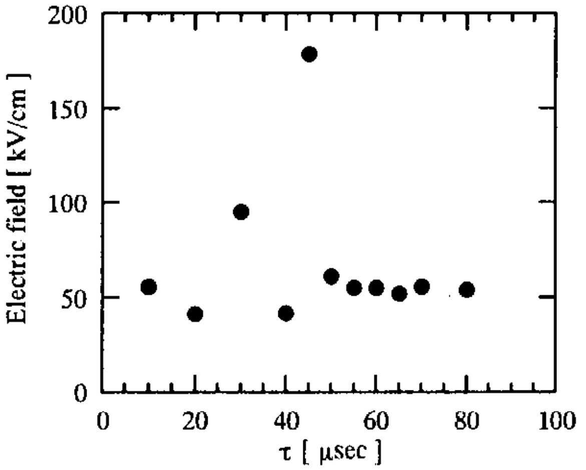

Fig. 4. The electric fields.

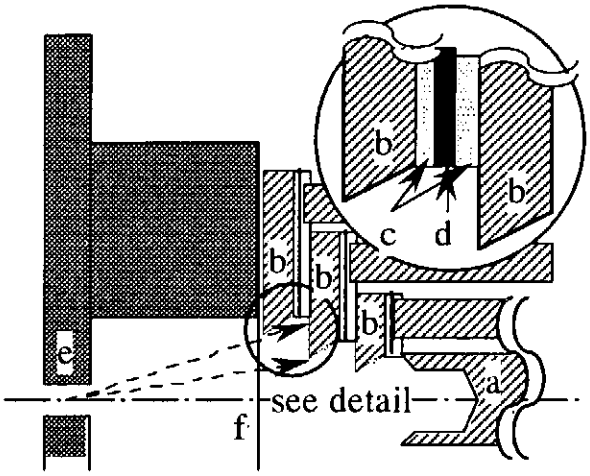

Fig. 5. The angle analyzer.

function of τ. The intensity of the high frequency turbulent electric fields was obtained using the Stark shift measurement. The HeI 501.57 nm line (3^1P_1-2^1S_0) shifts to the blue side by high frequency electric fields. Figure 4 shows the electric field strength E_s measured by the Stark shift.

The energy distribution of the IREB was measured by a magnetic energy analyzer at the end of the drift chamber. The magnetic field of 0.053 T was applied, and the observable energy ranges was 90 keV - 1.54 MeV. The width of the inlet slit was 0.1 cm. The detector was a 22 channel Faraday cup array. Each Faraday cup was made of brass and its outer diameter was 0.6 cm. The distance between neighboring cups was 1 cm. The energy resolution was 40 keV. Usually 6 - 10 channels out of 22 channels were used. Output of each Faraday cup was led to each input terminal of 1 GSa/s digitizing oscilloscopes (Hewlett-Packard HP54510A) via a 50 Ω termination. The time resolution of the analyzer was a few nsec.

The angular distribution was measured by an angle analyzer. Figure 5 shows the angle analyzer. It consisted of a Faraday cup of 0.6 cm in outer diameter (a) and three disks (b) of 0.2

cm thick which were made of brass and set coaxially. Two Mylar sheets of 125 μm thick (c) and a 100 μm thick copper foil (d) for grounding were inserted between neighboring collectors. The copper foils were directly connected to the ground. The beam electrons passing through an aperture 0.14 cm in diameter (e) were collected by these collectors. These collectors are insulated from the plasma by a 10 μm thick Ti-foil (f). The center Faraday cup covered the sinusoidal range of the scattering angle 0 - 0.1, and three disks covered 0.1 - 0.2, 0.2 - 0.3, and 0.3 - 0.4, respectively. The angle analyzer was placed in the axis at the end of the chamber. Output of each Faraday cup was led to each input terminal of 1 GSa/s digitizing oscilloscopes (Hewlett-Packard HP54510A) via a 50 Ω termination. The time-evolved expected value of the sine of the scattering angle was calculated from these output signals.

The high power broadband microwave radiation was measured at 17.5 cm downstream of the anode by a 5 channels microwave spectrometer of filter-bank type. A K-band and a Ka-band horn antennae were set facing each other at the observation ports for radial observation. The received microwaves were distributed into each channel (18.0 - 22.2 GHz, 22.2 - 26.5 GHz, 26.5 - 31.5 GHz, 30.7 - 35.7 GHz, and 35.5 - 40.0 GHz) by directional-couplers, and passed through the band-pass filters. The signal of each channel was detected by a crystal detector.

Experimental Results

Figure 6 shows typical time-evolution of energy distributions in one shot. Time interval of each spectra was 5 nsec. In this case 6 channels out of 22 channels were used. The data in Fig. 6 a) were obtained for the case of the IREB injection into 20 mTorr He gas only. These energy distributions show that the rise time of the IREB is about 10 nsec. The energy distributions are

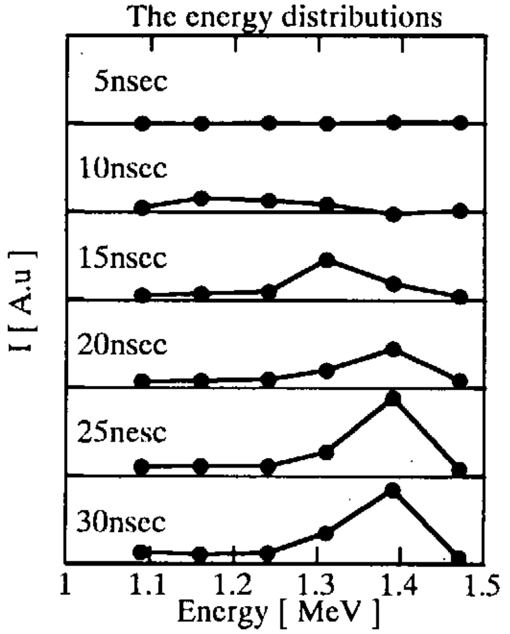

Fig. 6 a). He 20 mTorr

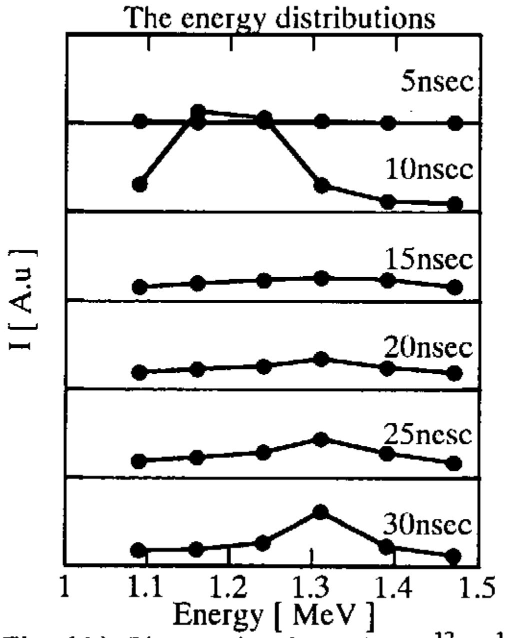

Fig. 6 b). Plasma density 1.6 x 10^{12} cc^{-1}

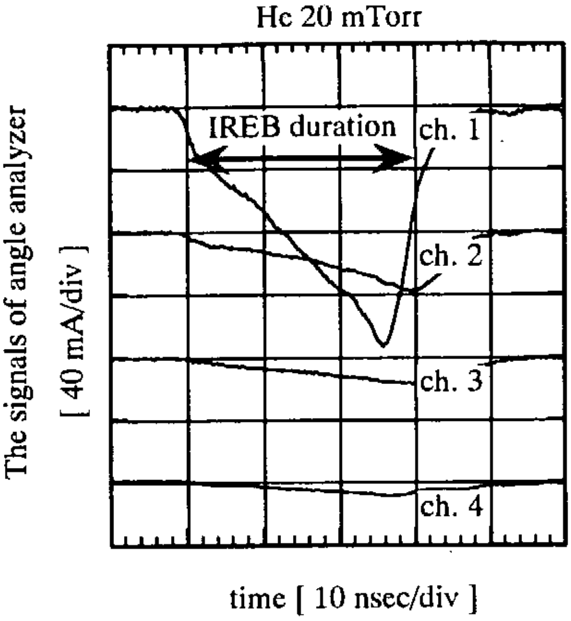

Fig. 7 a). The signals of angle analyzer.

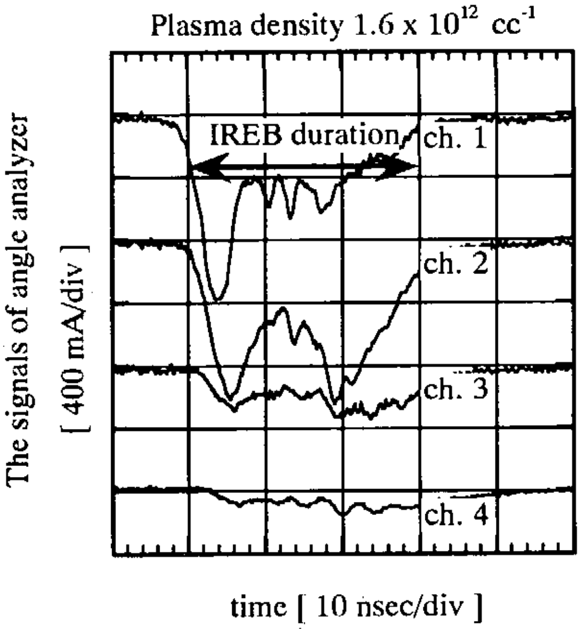

Fig. 7 c). The signals of angle analyzer.

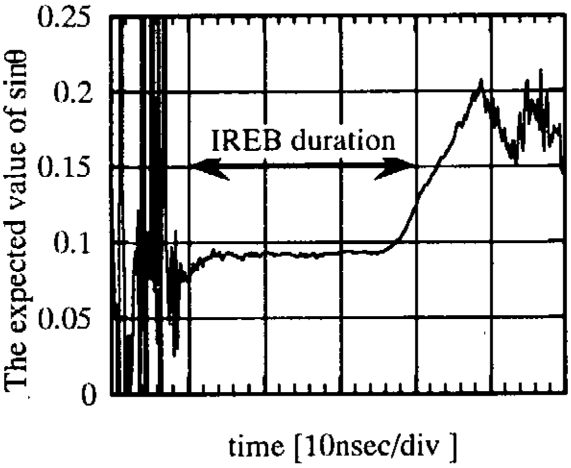

Fig. 7 b). The expected value of sin θ.

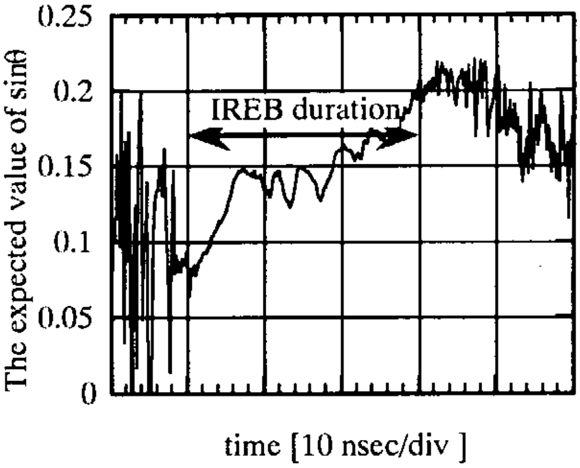

Fig. 7 d). The expected value of sinθ.

the same form and are Gaussian during 15 - 30 nsec in the beam pulse. The FWHM averaged over 15 - 30 nsec is 58 keV. The data in Fig. 6 b) were obtained for the case $\tau = 80$ μsec. The plasma density n_p was 1.6×10^{12} cc^{-1}. During 15 - 30 nsec in the beam pulse, the energy distributions show Gaussian spectra too, and have the wider spread than Fig. 6 a). The FWHM averaged over these duration is 160 keV, where the initial spread 58 keV is took into account.

We simultaneously measured the angular spread of the IREB and the high power broadband microwave radiation. Figure7 a) shows the signals of the angle analyzer measured for the case of injection of the IREB into 20 mTorr He gas only, and Fig. 7 c) shows the signals for the case of injection of the IREB into the plasma with the density 1.6×10^{12}cc^{-1}. The time-evolved expected values of sine obtained from signals in Fig. 7 a) and c), respectively, are given in Fig. 7 b) and d), respectively. For the case of He gas only, the expected value of the sine of the scattering angles does not vary much during the IREB pulse (30 nsec) as shown in Fig. 7 b). The averaged expected values of the sine of the scattering angles is 0.09. For the case of the plasma, the averaged value is 0.12. We can see that the angular spread is larger due to the beam-plasma interaction.

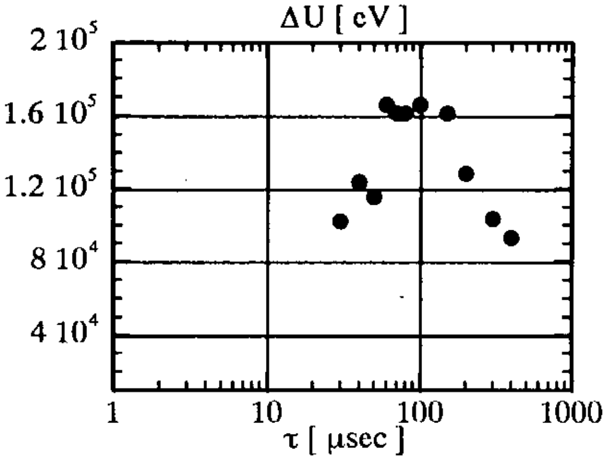

Fig. 8 a). The energy spread.

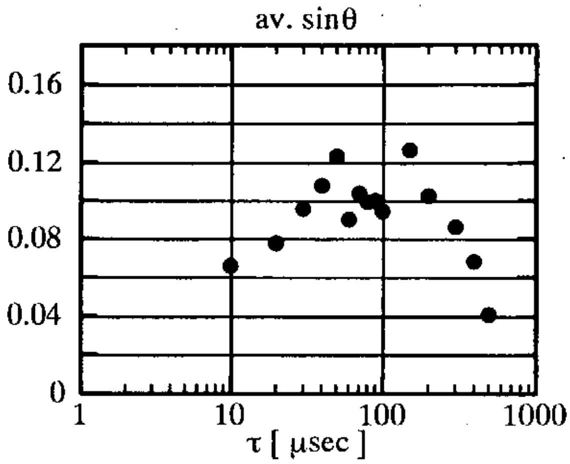

Fig. 8 b). The expected value of sin θ.

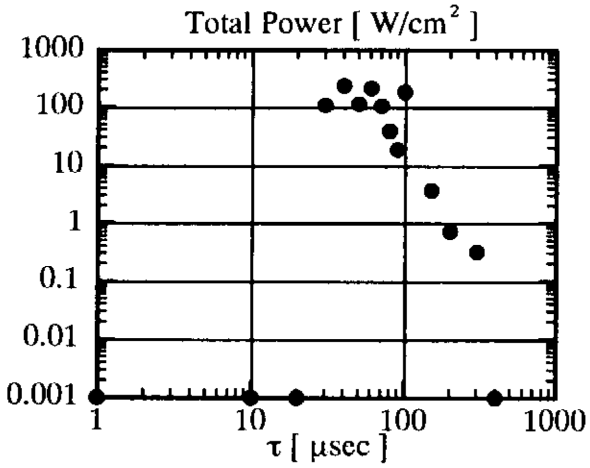

Fig. 8 c). The microwave total power.

In Fig. 8 a) the averaged FWHM of the energy distribution is shown as a function of τ. The averaged expected value of the sine of the scattering angles is also shown as a function of τ in Fig. 8 b). The total power of microwave radiation is calculated from signals of 5 channels microwave spectrometer, and shown in Fig. 8 c) as also a function of τ.

Discussion

The energy spread is caused by scattering of beam electrons in energy and in angle during interaction with cavitons. We applied the theory of multidimensional transit-time interactions$^{20)}$

to calculate the scattering. We calculate the electron trajectory during a single transit on a caviton. The caviton is assumed to be described by a dipole potential of the form,[1)]

$$\Phi\left(\boldsymbol{r},t\right)=\Phi_0\, l\left(\boldsymbol{r}\cdot\boldsymbol{u}\right)\cos\left(\omega\cdot t+\phi\right)/\left(l^2+r^2\right)$$

where Φ_0 is constant, l the characteristic length scale of the caviton, r the distance from the center, ϕ a phase factor, and ω_p the plasma frequency. And $\boldsymbol{u}$ is an unit vector along the dipole direction which is assumed to coincide with the direction of the IREB propagation. The electric field is given as

$$\begin{aligned}\boldsymbol{E}\left(\boldsymbol{r},t\right)&=-\operatorname{grad}\Phi\left(\boldsymbol{r},t\right)\\&=E_0\left(l^2+r^2-2x^2,-2xy,-2xz\right)\left(l^2+r^2\right)^{-2}\cos\left(\omega\cdot t+\phi\right)\end{aligned}$$

An electron with velocity $\boldsymbol{v}$ gains an energy

$$U\left(\boldsymbol{v},\phi\right)=-e\int \mathrm{d}\boldsymbol{r}\cdot\boldsymbol{E}\left(\boldsymbol{r},t\right)$$

A Born approximation is introduced, and we get the first-order gain in energy given as

$$U^{(1)}\left(v,\phi\right)=-e\,\mathrm{Re}\left[\left(E_x\right)_k e^{-i\phi}\right]$$

where the subscript k denotes the Fourier component having wavenumber $k=\omega_p/v$, and the direction of the beam propagation is taken as the x-direction. This first-order energy gain becomes zero when phase-averaged but dominates the electron scattering in energy. And

$$\Delta U^2=\int \mathrm{d}\phi\left[U^{(1)}\left(v,\phi\right)\right]^2 \qquad (1)$$

gives measure of the energy spread per single transit. The second order gain in energy is given by

$$\begin{aligned}L\left(v\right)=\frac{e^2}{4\gamma^3 m v^2}\Bigg[&-k\frac{\mathrm{d}}{\mathrm{d}k}\left|\left(E_x\right)_k\right|^2+\gamma^2\left\{\left|\left(E_y\right)_k\right|^2+\left|\left(E_z\right)_k\right|^2\right\}\\&-\gamma^2\frac{\mathrm{d}}{\mathrm{d}k}\mathrm{Im}\left\{\left[\left(E_y\right)_k\right]^*\left(\frac{\partial E_x}{\partial y}\right)_k+\left[\left(E_z\right)_k\right]^*\left(\frac{\partial E_x}{\partial z}\right)_k\right\}\Bigg] \qquad (2)\end{aligned}$$

where γ is the Lorentz factor of the IREB, and m is electron-mass. The second term of eq. (2) gives the phase-averaged perpendicular scattering $\delta v/v_b$,

$$\left\langle \left[\frac{\delta v_{\perp}}{v_{\mathrm{b}}} \right]^2 \right\rangle = \frac{1}{2} \left(\frac{e}{\gamma m v_{\mathrm{b}}^2} \right)^2 \left[\left| (E_y)_k \right|^2 + \left| (E_z)_k \right|^2 \right] \tag{3}$$

which corresponds to the expected value of the sine of the scattering angles measured by angle analyzer.

As the parameter ranges in the experiment were 10 - 60 eV in T_e, 25 - 180 kV/cm in E_s, 40 - 160 keV in ΔU, and 0.09 - 0.17 in $\delta v/v_b$, the parameter ranges needed for calculation of ΔU and $\delta v/v_b$ are chosen as 0 - 430 eV in T_e and 0 - 150 kV/cm in E_s, respectively, for each plasma density. Figure 9 shows ΔU and $\delta v/v_b$ for the plasma density $n_p = 1.6 \times 10^{12}\,\mathrm{cc}^{-1}$. In this case, the experimental values of T_e and E_s are 58 eV and 54 kV/cm, respectively. These parameters give the $\Delta U = 60$ keV and $\delta v/v_b = 0.025$. The experimental results are $\Delta U = 160$ keV and $\delta v/v_b = 0.10$. The experimental values of ΔU and $\delta v/v_b$ are wider than the calculation. These differences may be caused by the assumption that the dipole axes of all cavitons are aligned on the IREB direction. Besides, we neglect the beam energy loss associated with the generation of the cavitons. However, these results suggest the existence of strong turbulent fields of at least 26 kV/cm. The same tendency is obtained for the other plasma densities.

From Fig. 8 we can see that the dependence on τ of the microwave radiation is almost the same as these of the energy and angular spreads. The wider the energy and angular spreads, the stronger the total power of the microwave radiation. Yoshikawa et al. found that the microwave radiation was not necessarily observed when the turbulent field strength was high.[14)] Comparing Figures 4 and 8, we can say that the turbulent field is needed for the microwave radiation and the scattering of the IREB. However, the radiation and the IREB scattering are not necessarily observed when the plasma was in a strong Langmuir turbulence state. It is one of the conditions for the microwave radiation and the IREB scattering for the plasma to be strong Langmuir turbulence state.

Conclusions

We measure the energy distribution and angular spread of the beam electrons in order to investigate the beam-driven strong Langmuir turbulence state. The theory of transit-time interactions was applied to analyze the measured energy and angular spreads. The high frequency electric fields obtained were compared with those obtained from the spectroscopic measurements. The results of analysis suggest the existence of strong turbulent field. However, the measured energy and angular spreads are wider than the calculations which uses the electron temperature and the turbulent fields obtained from the spectroscopic measurements. If the effect of variety of the direction of the dipole axes and the beam energy loss associated with the generation of the cavitons could be taken into account, the more accurate calculation would become possible.

Fig. 9 a). The energy spread.

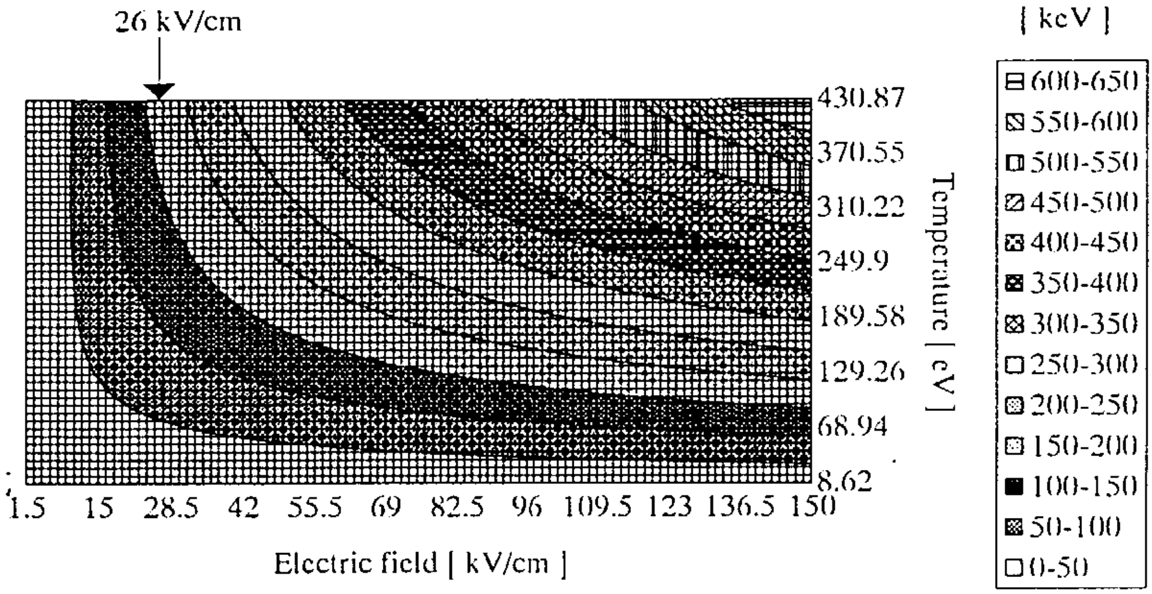

Fig. 9 b). $\delta v / v$.

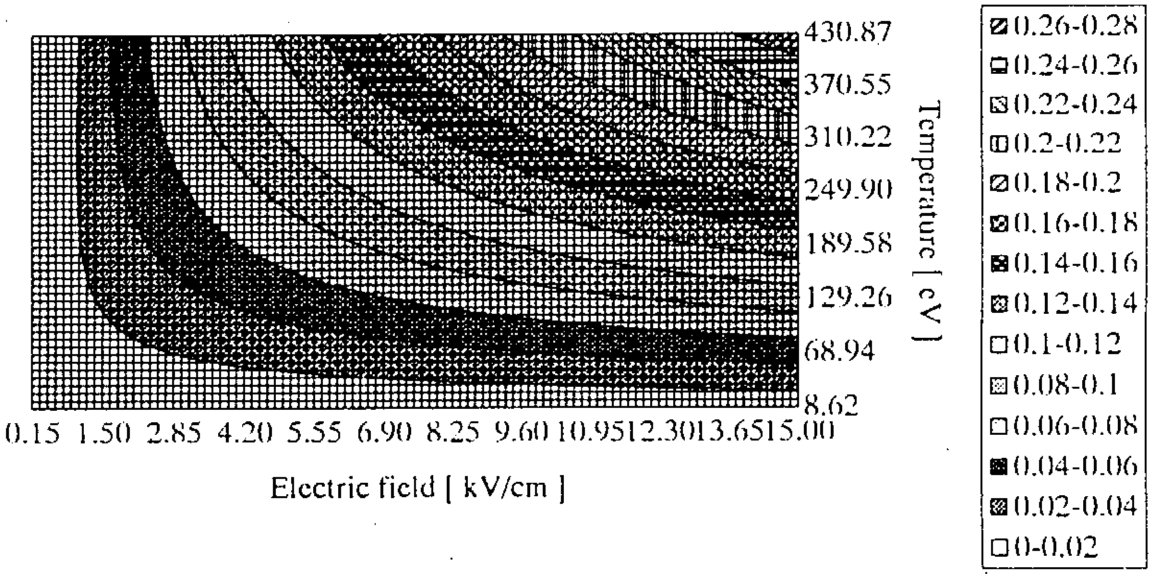

The microwave radiation is observed simultaneously with the angular spread measurement. The microwave radiation has the same dependence on the plasma density as the energy and the angular spreads. The wider the energy and angular spreads, the stronger the total power of the microwave radiation.

Part of this work was supported by Grant-in-Aid for Scientific Research from the Ministry of Education, Science and Culture.

References

1) P. A. Robinson and D. L. Newman: Phys. Fluids **B1** (1989) 2319.
2) P. A. Robinson and D. L. Newman: Phys. Fluids **B2** (1990) 3120.
3) G. C. A. M. Janssen, J. H. M. Bonnie, E. H. A. Granneman, V. I. Krementsov, and H. J. Hopman: Phys. Fluids **27** (1984) 726.
4) G. C. A. M. Janssen, E. H. A. Granneman, V. I. Krementsov, and H. J. Hopman: Phys. Fluids **27** (1984) 726.
5) H. J. Hopman and G. C. A. M. Janssen: Phys. Rev. Lett. **52** (1984) 1613.
6) D.Levron, G. Benford and D.Tzach: Phys. Rev. Lett. **58** (1987) 1336.
7) G. Benford, X. Zhai and D.Levron: Phys. Fluids **B3** (1991) 560.
8) D.Levron, G. Benford, A. Ben-Amar Baranga and J. Means: Phys. Fluids **31** (1988) 2026.
9) A.Dovrat and G. Benford: Phys. Fluids **B1** (1989) 2488.
10) K. G. Kato, G. Benford and D.Tzach: Phys. Fluids **26** (1983) 3636.
11) M. Masuzaki, R. Ando, A. Yoshimoto, M. Ishikawa, M. Yoshikawa, K. Kitawada, H. Morita and K. Kamada: *Proceedings of 8 th International Conference on High-Power Particle Beams*, eds. B. N. Breizman and B. A. Knyazev (World Scientific, Singapore,1991) Vol. 2, p.683.
12) M. Masuzaki, R. Ando, M. Yoshikawa, H. Morita, J. Yasuoka and K. Kamada: *Proceedings of 9 th International Conference on High-Power Particle Beams*, eds. D. Mosher and G. Cooperstein (Washington,DC.,1992) Vol. 2, p.1227.
13) M. Yoshikawa, R. Ando and M. Masuzaki: Jpn. J. Appl. Phys. **32** (1993) 969.
14) M. Yoshikawa, M. Masuzaki and R.Ando: J. Phys. Soc. Jpn **63** (1994) 3303.
15) G. Benford and J. C. Weatherall: Phys. Fluids **B4** (1992) 4111.
16) G. D. Doolen, D. F. DuBois and H. A. Rose: Phys. Rev. Lett. **54** (1985) 804.
17) D. Russel, D. F. DuBois and H. A. Rose: Phys. Rev. Lett. **56** (1986) 838.
18) D. Russel, D. F. DuBois and H. A. Rose: Phys. Rev. Lett. **60** (1988) 581.
19) D. F. DuBois, H. A. Rose and D. Russel: Phys. Rev. Lett. **61** (1988) 2209.
20) P. A. Robinson: Phys. Fluids **B1** (1989) 490.
21) S. Sasaki, Research Report NIFS-346 (1995).

Preparation of Thin Films and Nanosize Powders by Intense Pulsed Light Ion Beam Evaporation

Constantin Grigoriu, Yukio Nakagawa, E.P.Achmad Chamdani,
Tomihiro Sonegawa, Koji Nishiura, K.Shanmuga Nathan, Katsumi Masugata
and Kiyoshi Yatsui

Laboratory of Beam Technology
Nagaoka University of Technology
Nagaoka, Niigata 940-21

Abstract

The ion beam evaporation method (IBE), for high T_c thin films deposition and nanosize powders preparation is presented.

We have investigated the properties of the $YBa_2Cu_3O_{7-x}$ (YBCO) films by the IBE method, comparing standard deposition configuration, front side deposition (IBE/FS), with a new one, back side deposition (IBE/BS). The study reveals possibility of production of thin films, with c-⊥-type orientation, from $YBa_2Cu_3O_{7-x}$ target, by single shot, IBE/FS. Multishot IBE/FS depositions, create off-stoichiometric films, Cu and Ba depleted, due to selective reevaporation of Cu and Ba. In contrast to IBE/FS deposition, IBE/BS method, permitted obtaining of high quality films, even in the multishot case, with a much improved surface morphology too. The films deposited on $LaSrGaO_4$ substrate have a significant improved crystallinity in comparison with those deposited on MgO.

In addition, we have studied preparation of fine and ultra-fine powders by IBE. We prepared nanosize Al_2O_3, TiO_2, TiN and AlN powders. The influence of experimental parameters, on size, size distribution, form and particle structure have been investigated.

1 Introduction

The present report describes some applications of the ion beam evaporation technique. It consists in two parts:

a) Deposition of $YBa_2Cu_3O_{7-x}$ thin films on MgO and $LaSrGaO_4$ substrates, and investigation of the film properties dependence on experimental conditions. A new advantageous deposition configuration , back side deposition (IBE/BS) have been proposed.

b) Preparation of fine and ultrafine powders as Al_2O_3, TiN, TiO_2 and AlN. We have investigated the influence of the experimental conditions on particles structure, form and size.

2 Experimental setup

The experiments have been carried out by the light ion beam accelerator , ETIGO-II [1,2]. The ion beam, (mainly represented by protons) was delivered by a magnetically insulated ion diode with spherically shaped anode and cathode. The typical parameters: diode voltage ~1.1 MV, diode current ~ 80 kA, pulse width ~70 ns and ion current density ~0.5 kA/cm^2. The ion beam is focused onto a target, interaction area diameter being 2 cm. Thus, occurs an evaporation of the surface and a high density plasma is produced in a perpendicular direction on the target surface (plasma density $10^{19} \sim 10^{20}\,cm^{-3}$, plasma temperature 1 ~ 4 eV, plasma expansion velocity 10^{6} cm/s) [3]. The ablation plasma is propagating either to a substrate in the case of thin films deposition, or to a mesh collector in the case of the powders preparation.

Experimental conditions are given in Table I.

Table I. Experimental conditions.

YBCO films

Target	Substrate	Deposition in vacuum	Target-substrate distance
$YBa_2Cu_3O_{7-x}$	MgO ; $SrLaGaO_4$	3×10^{-2} Pa	60 mm

Powders

Target	Ambient gas	Gas pressure	Target-mesh distance
Ti; Al; TiN; AlN	Oxygen ; Nitrogen	1 ~ 100 Torr	60 mm ~ 330 mm

3 Results

3.1 YBCO thin films

We have investigated the properties of YBCO films by the IBE method, comparing standard deposition configuration (front side deposition, IBE/FS), with a new proposed one, back side deposition (IBE/BS).

Figure 1 schematically illustrates the two geometrical configurations.

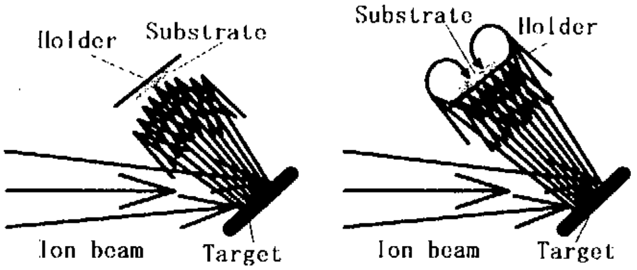

Front side
IBE/FS

Back side
IBE/BS

Fig. 1 IBE/FS and IBE/BS deposition configurations.

In standard IBE/FS method, the deposition takes place on the frontal side of the substrate, while in the IBE/BS method, the substrate is placed on the reverse side of the holder, deposition being due to diffusion process. We have proposed IBE/BS method in order to avoid some drawbacks present in the IBE/FS method.

Firstly, the morphology of the films deposited by IBE/FS is not satisfactorily; in general, the surface of the film have some irregularities, the surface is pretty rough, and also, one can be found droplets with diameters above 1.5 μm. The films deposited by the new method, IBE/BS, exhibit an improved roughness, with no droplets. For comparison, in Fig. 2 are shown two micrographs obtained by atomic force microscopy: (a) for a film deposited by IBE/FS, one shot, and (b) for a film deposited by IBE/BS, one shot.

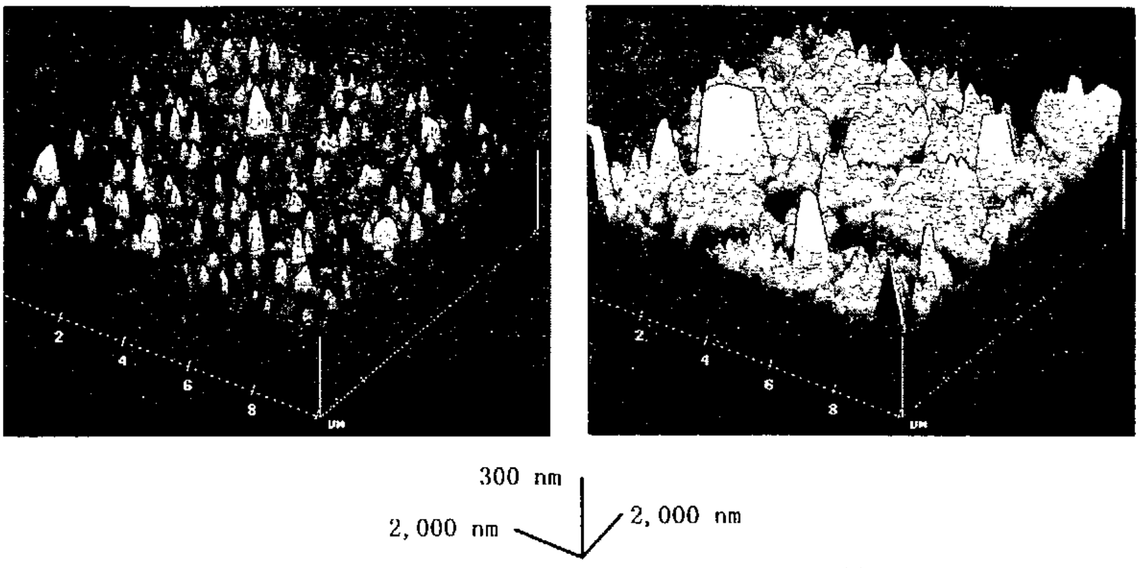

(a) (b)

Fig. 2 AFM micrographs of YBCO films deposited in vacuum, on MgO (100), one shot, substrate temperature 700 ^{0}C, annealed films: (a) by IBE/BS, (b) by IBE/FS.

In Table II is presented roughness calculated as arithmetical average of the surface deviation from the mean line R_a, and root mean square average R_{ms}, for the two deposition methods. One can notice the significant improvement of the roughness, about five times, for the IBE/BS deposited films.

Table II. The roughness of the films deposited by IBE/FS and IBE/BS.

	IBE/FS	IBE/BS
R_a	55.47 nm	10.35 nm
R_{ms}	84.23 nm	17.93 nm

Another drawback of the IBE/FS method, is related to the film stoichiometry. In the case of multishot deposition, the XRD patterns for these films were inadequate, with many extra-peaks of unidentified phases.

These results, correlated with electron probe microanalysis [4] and Rutherford backscattering spectroscopy, reveal that our layers are off-stoichiometrically, depleted in barium and copper, in comparison with initial target. It can be explained by the fact that the plume that impinges the substrate, consisting of huge amount of very energetic particles, produces a strong bombardment of the previous layer. Consequently, occurs a selective reevaporation, particularly valid for barium and copper, which have much lower boiling points in comparison with yttrium.

By the indirect deposition method, IBE/BS, we mainly intended to eliminate the strong bombardment of the film by energetic particles, and thus to avoid the reevaporation of Ba and Cu. We have been successfully obtaining good films for multishot depositions too. The best crystallinity was obtained for the substrate temperature of 700 ^{0}C. Figure 3 (a), (b) presents XRD patterns for IBE/FS and IBE/BS deposited films. We see a strong c axis ⊥ orientation to substrate surface, for the films deposited by IBE/BS in comparison with IBE/FS.

The above mentioned depositions have been made on MgO (100). We also deposited YBCO films on $LaSrGaO_4$ (100) substrate. As can be observed from Fig. 3 (c), the films deposited on $LaSrGaO_4$ substrate, have a significant improved crystallinity in comparison with MgO. This is due to the small lattice mismatch between YBCO and $LaSrGaO_4$ (YBCO a=0.382 nm, b=0.389 nm; MgO a=0.42 nm ; $LaSrGaO_4$ a=0.384 nm). Also, because $LaSrGaO_4$ shows no phase transformation below 1520 ^{0}C unlike 850~900^{0}C for MgO, the annealing process for the films that is necessary after deposition, does not perturb the interface substrate-film.

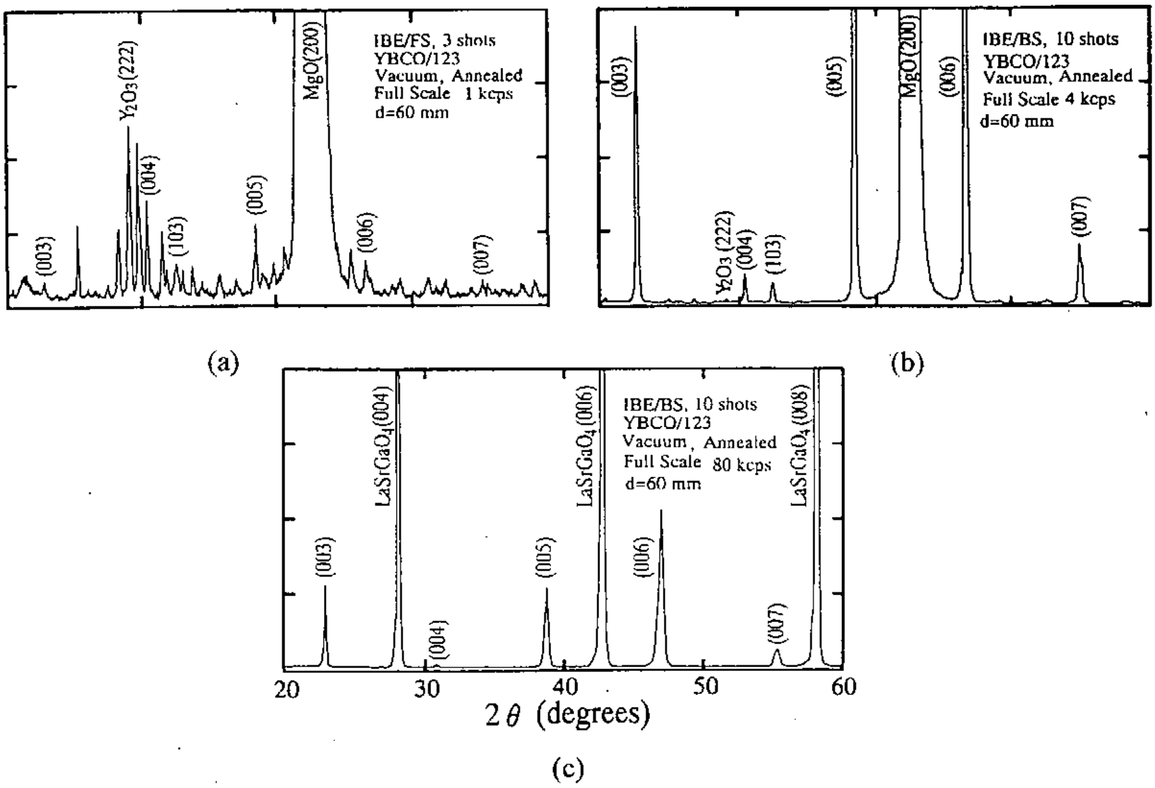

Fig. 3 XRD patterns for films deposited by IBE/FS on MgO , full scale 1 kcps, (a); by IBE/BS on MgO, full scale 4 kcps, (b); by IBE/BS on $LaSrGaO_4$, full scale 80 kcps (c).

Concerning deposition rate, IBE is a very attractive method due to its high deposition rate. Thus, in the case of the IBE/FS we measured a deposition rate in vacuum, of 300~400 nm/shot, for a beam energy density of 50 J/cm^2, power density of 1 GW/cm^2 and a target-substrate distance of 6 cm. In the case of IBE/BS deposition, the rate was around 30 nm/shot, that is an order of magnitude lower. If we compare with other methods (for example laser ablation), the deposition rate of IBE/BS is still much higher, so IBE/BS remains an attractive deposition technique.

In conclusion, in comparison with IBE/FS method , IBE/BS deposition method is highly recommended for deposition of high quality epitaxial YBCO films; IBE/BS deposited films have an improved roughness (5 times better), without droplets and a higher crystallinity. Because IBE/BS method avoids strong bombardment of the film by high energetic particles , the multishot deposited films are stoichiometric. Substrate made of $LaSrGaO_4$ are suitable for YBCO films deposited by IBE technique.

3.2 Nanosize powders

IBE method may be suited for synthesizing some nanosize powders. In comparison with lasers methods [5,6], the IBE has significant advantages: metallic targets, which generally reflect laser light, readily absorb ion beam, allowing the efficient production of powders; ions penetrate the plasma deeper than the laser beam; ion beam accelerators are efficient and less-expense. We have tried to demonstrate the process feasibility and to investigate the relation between the powder characteristics and the process parameters.

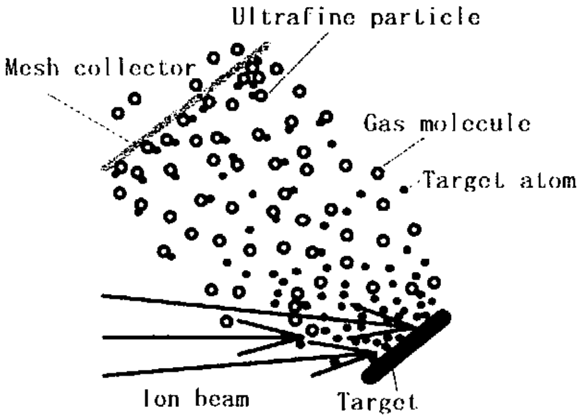

Fig. 4 Experimental schematic for the powders preparation.

A schematic of the experimental configuration is shown in Fig. 4. As one can see a metal target is irradiated by an intense ion beam . The ablated material expands in a plume

Table III. The characteristics of the powders produced by IBE method.

Target material	**Ambient gas**	**Gas pressure (Torr)**	**Target collector distance (mm)**	**Particle**	**Particle size, Min -Max (nm)**
Ti 99.5%	Oxygen 99.5%	1	100	**$TiO + TiO_2$**	380 ~ 2,410
			330	**$TiO + TiO_2$**	4 ~ 40
		10	100	**TiO_2**	320 ~2,000
			330	**TiO_2**	4 ~ 45
	Nitrogen 99.5%	1	100	**TiO + TiN**	5 ~ 1,800
			330	**TiN**	5 ~38
		10	100	**TiN**	380 ~ 1,420
			330	**TiN**	5 ~ 23
TiN 99.5%	Nitrogen 99.5%	1	100	**TiN**	350~2,270
			330	**TiN**	350~1,050
		10	100	**TiN**	350~3,850
			330	**TiN**	350~700
Al 99.5%	Oxygen 99.55	1	330	**Al_2O_3**	5 ~ 50
		10	330	**Al_2O_3**	5 ~ 65
	Nitrogen 99.5%	1	330	**Al**	-
		10	330	**Al**	-
AlN 99.5%	Nitrogen 99.5%	1	330	**AlN**	150 ~ 1,600
		10	330	**AlN**	70 ~ 550

normal to the target surface and collides with the ambient gas. As a result of the interaction, fine and ultrafine powders are synthesized.

Firstly, in Table III we present an overview of the powders produced by IBE technique. We have attempted to produce ultrafine particles from Ti, Al , TiN and AlN targets. The irradiation was performed in oxygen or nitrogen atmosphere, 1~10 Torr pressure, at different target-collector distances, from 100 mm to 330 mm. The powders were characterized by scanning (SEM) and transmission electron microscopy (TEM).

In Fig. 5 are presented the SEM photographs of powders collected on stainless steal mesh at different distances, produced in 10 Torr oxygen, from a Ti target. It is clear that at shorter distances the powder diameters are in the μm range.

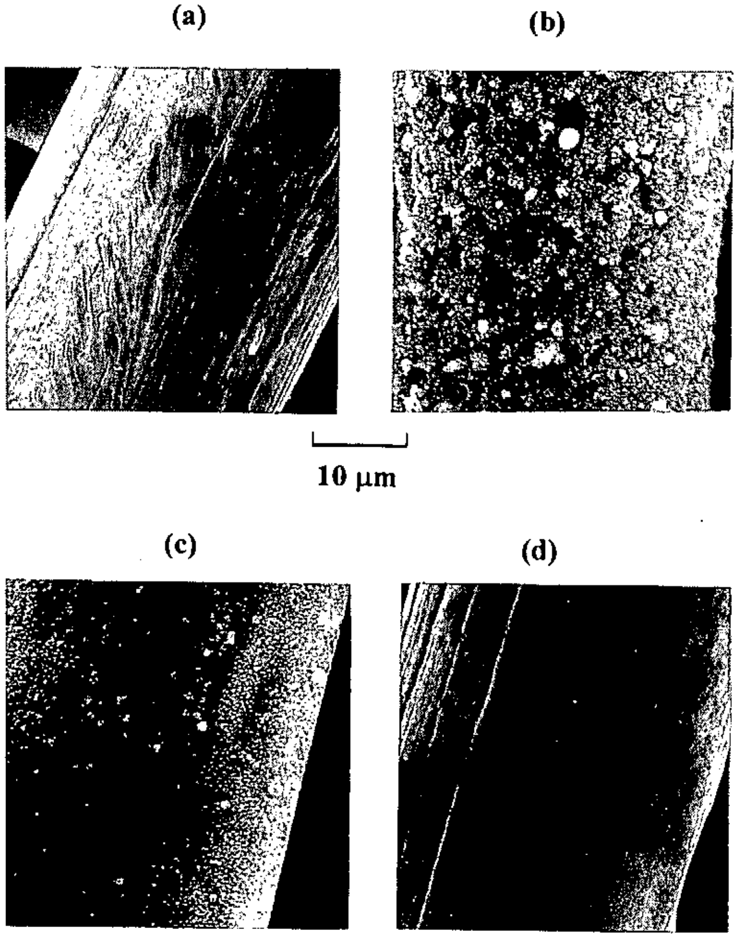

Fig. 5 SEM photographs of the powders deposited on stainless steal mesh, in oxygen atmosphere, 10 Torr, Ti target; (a) before irradiation, (b) collected at 100 mm, (c) at 200 mm, (d) at 330 mm.

Figure 6 illustrates the size distribution of the TiO_2 particles for two collecting distances: 100 mm and 330 mm. At 100 mm the TiO_2 powder is represented by larger particles, that have diameters 0.3~2 μm ranged. It is obvious that ultrafine powders with diameters of 5~25 nm could be collected only at 330 mm distance.

In fig. 7 (a) and (b) is shown the TEM photograph of TiO_2 powder prepared in oxygen, from a Ti target, and collected at 330 mm. The particles are in globular shape.

Figure 7 (c) and (d) shows the TiN nanosize powders, prepared in the same way as TiO_2, only the gas is different. For this material the particles are not any more of spherical form, TiN particles being nanocrystallites with typical cubic form.

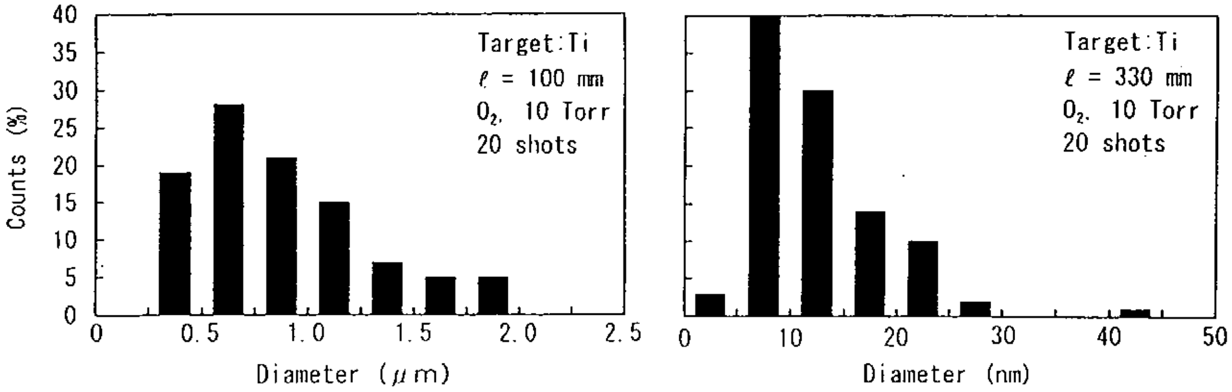

Fig. 6 Size distribution of TiO_2 powder prepared in oxygen, 10 Torr, from a Ti target, collected at two distances: 100 mm and 330 mm.

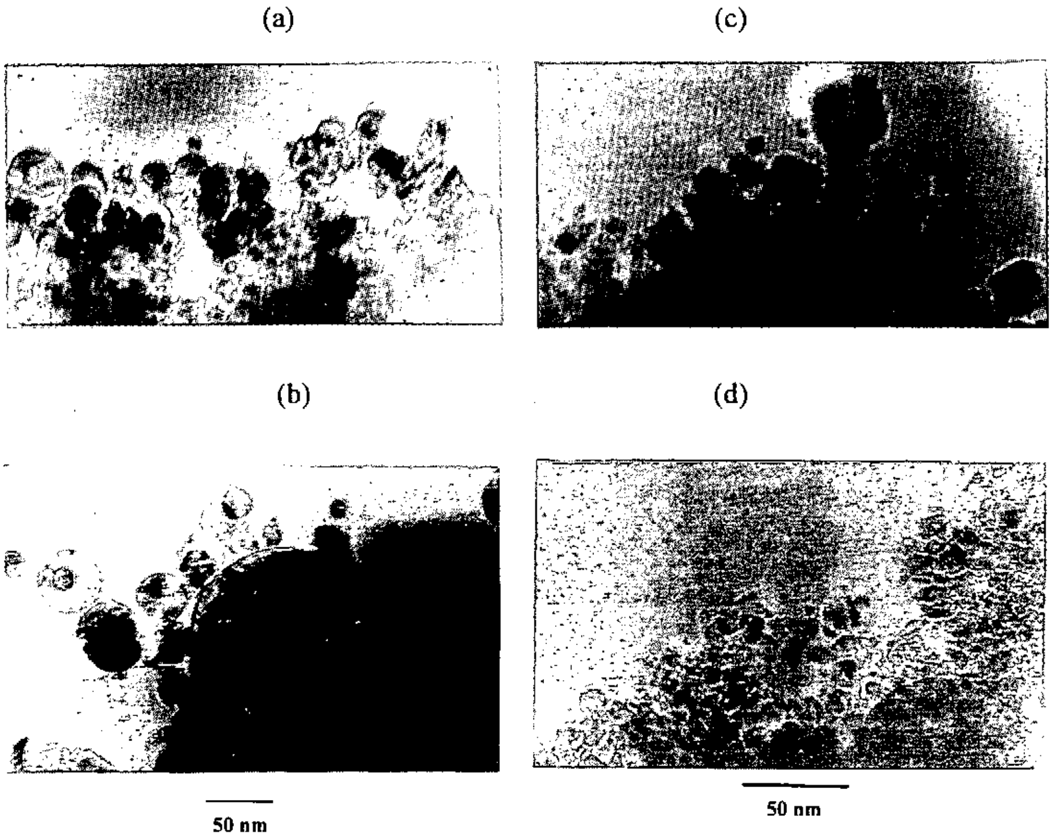

Fig. 7 TEM photographs of TiO_2 and TiN nanosize powders, produced from Ti target and collected at 330 mm; (a) 1 Torr oxygen, (b) 10 Torr oxygen, (c) 1 Torr nitrogen, (d) 10 Torr nitrogen.

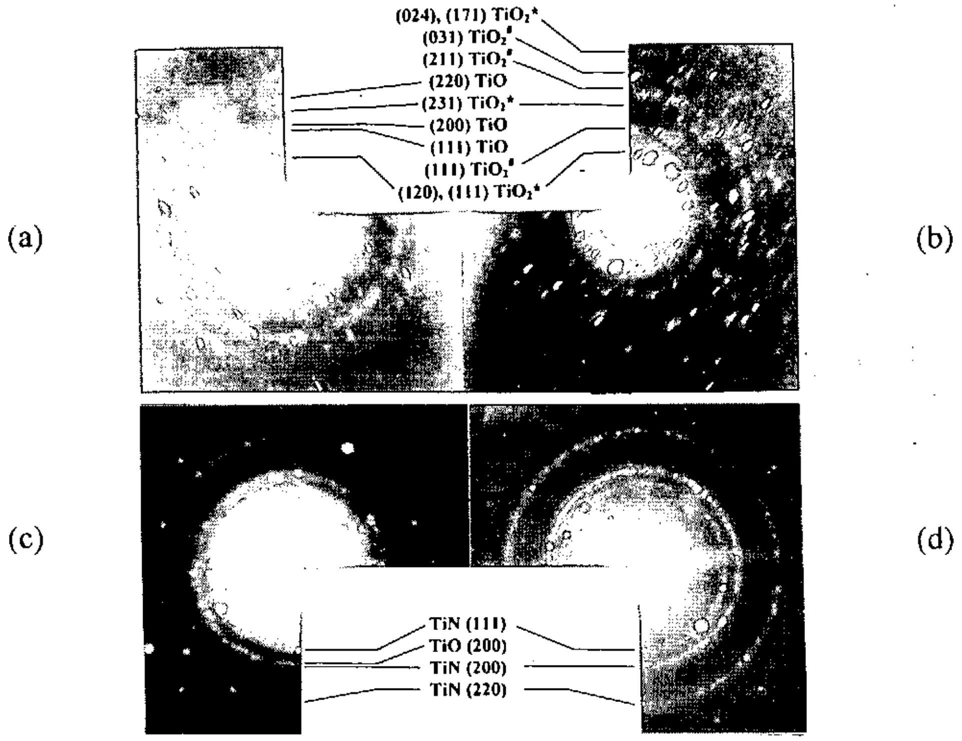

Fig. 8 Electron diffraction patterns of powders prepared from Ti target and collected at 330 mm;
- TiO$_2$: (a) 1 Torr, (b) 10 Torr; - TiN: (c) 1 Torr, (d) 10 Torr;
JCPDS: *29-1360, #21-1276

Electron diffraction patterns of TiO$_2$ and TiN are presented in Fig. 8 (a), (b), (c) and (d). One can notice that at 1 Torr oxygen, besides the TO$_2$ appears TiO too. This situation can be explained by lack of oxygen for the given ablated material.

Also, in the case of TiN powders prepared in nitrogen at 1 Torr pressure, TiO have been identificated; this is due to the reaction between residual oxygen adsorbed on the chamber walls and the ablated Ti atoms.

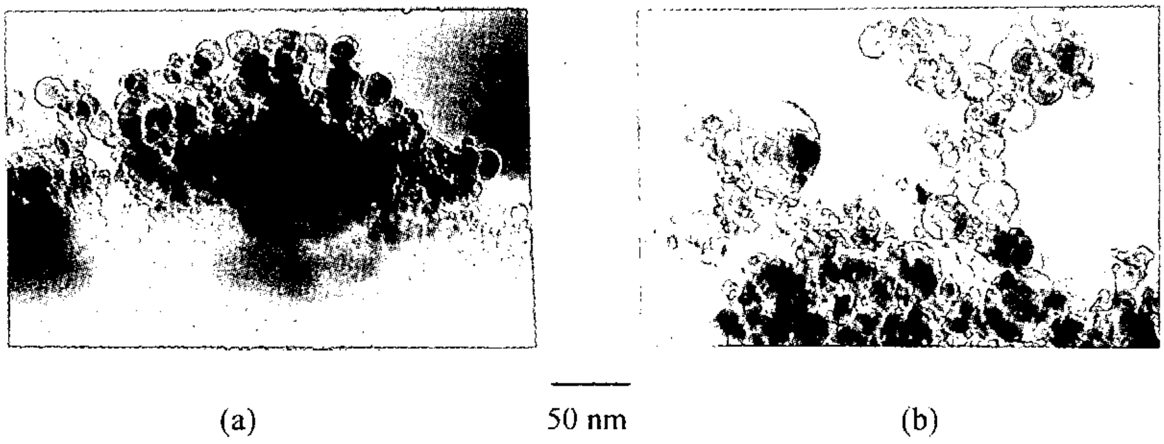

Fig. 9 TEM photographs of Al$_2$O$_3$ powder, prepared in oxygen, Al target; (a) 1 Torr, (b) 10 Torr.

Concerning the Al based powders, nanosize Al_2O_3 , namely γ-alumina, can be readily prepared [7]. The shape is spherical, and diameters of the powders are mostly 5~25 nm. Figure 9 illustrates TEM photographs for Al_2O_3 powders.

On the contrary, in the case of Al ablation in nitrogen atmosphere (1~10 Torr), one can not produce AlN.

Related to powders produced by irradiation of TiN or AlN targets in nitrogen atmosphere, our experiments have shown powders with relatively large diameters 0.07~3.85 μm ranged.

4 Conclusions

From the above experimental studies we have drawn the following conclusions:

4.1 YBCO films

1) IBE/BS deposition method is highly recommended for deposition of high quality epitaxial YBCO films;
2) IBE/BS deposited films have an improved roughness (5 times better), without droplets and a higher crystallinity;
3) Because IBE/BS method avoids strong bombardment of the film by high energetic particles , the multishot deposited films are stoichiometric;
4) Substrate made of $LaSrGaO_4$ are suitable for YBCO films deposited by IBE technique.

4.2 Powders

1) Generally, at higher pressure and longer target-collector distances, the particles of the plume react completely with the ambient gas;
2) Powders collected at shorter distances are fine particles (xμm) covered with nanosize particles;
3) Powders collected at longer distances , are nanosize particles, 5~40 nm in diameter;
4) Nanosize alumina powders are readily produced irradiating Al target in oxygen atmosphere;
5) AlN one can not be prepared at 1~10 Torr nitrogen, because the ablated Al plume does not react with the nitrogen;
6) AlN and TiN powders prepared by ablation of the same material , in nitrogen atmosphere, have larger size , with diameters in the range 0.07~3.85 μm.

References

[1] K.Yatsui, A.Tokuchi, H.Tanak, H.Ishizuka, A.Kawai, E.Sai, K.Masugata, M.Ito and M.Matsui, Laser Particle Beams **3**, 119 (1985).

[2] A.Tokuchi, N.Nakamura, T.Kunimatsu, N.Ninomiya, M.Den, A.Araki, K.Masugata, and K.Yatsui, *Proceedings of the 2nd International Topical Symposium on Inertial Confinement Fusion Research by High-Power Particle Beams*, edited by K.Yatsui (Nagaoka University of Technology, Nagaoka, Japan, 1986), p. 430.

[3] K.Yatsui, N.Yumino and K.Masugata, *Laser Interaction and Related Plasma Phenomena*, (Plenum Press, New York, 1992), p. 567.

[4] C.Grigoriu, E.P.Achmad Chamdani, T.Sonegawa, K.Masugata, and K.Yatsui, *Proceedings on New Applications of Pulsed High-Energy Density Plasmas*, edited by K.Yatsui (Nagoya, Japan 1995), NIFS-PROC-23, National Institute for Fusion Science, p. 10.

[5] A.Matsunawa and S.Katayama, Transactions of JWRI **19** (1), 137.(1990).

[6] G.P.Johnston, R.Muenchausen, D.M.Smith, W.Fahrenholtz and S.Foltyn, J.Am.Ceram.Soc. **75** (12), 3293 (1992).

[7] K.Yatsui, C.Grigoriu, H.Kubo, K.Masugata and Y.Shimotori, Appl.Phys.Lett. **67** (9), 1214 (1995).

Effects of Pulsed REB Irradiation on Nitriding in Surface Layers of Irons

M. Sato
Department of Electronic Engineering,
Gunma University, Kiryu 376, Japan

H. Matsushita, H. Iwasaki* and S. Nobuhara
Department of Electrical Engineering,
*Department of Materials Science and Engineering,
Himeji Institute of Technology, Himeji 671-22, Japan

R. Ando and M. Masuzaki
Department of Physics, Faculty of Science,
Kanazawa University, Kanazawa 920, Japan

Abstract

Various nitriding methods have been popularly used to make hard in surface layers of steels, but they require long processing times to obtain thick nitriding layers. In order to reduce these processing times, we tried irradiation of a pulsed relativistic electron beam (REB) to the surfaces of pure irons before they were processed by nitrogen plasmas. By this irradiation, many lattice defects may be formed in the pure iron. Along these defects nitrogen penetrates fast and forms thicker nitriding layers.

Irradiation of pulsed REB to the pure irons was carried out with a pulse power generator. The energy, the pulse width and the current density of pulsed REB were 1.4 MeV, 30 ns and 35~200 A/cm^2, respectively. After a shot, the iron was processed by a nitrogen plasma, and was analyzed with several analyzed methods. The maximum thickness of the nitrided layer was 40 μm, and this value was 1.5 times longer than that obtained without irradiation of pulsed REB.

1 Introduction

Surface nitriding treatments have been developed as one of methods hardening the surfaces of steels, and have already applied to automobile parts, machining tools and hydraulic parts, because they increase wear and corrosion resistance [1]. However these treatments require long processing times to obtain thick nitriding layers because nitrogen is put into the steel by diffusion from the surface. As one of applications with pulse power technologies, we propose the method to promote growth of nitrided layers with irradiation of a pulsed relativistic electron beam (REB). In this method, a role of pulsed REB is as like a catalyst. Irradiated pulsed REB produces many lattice defects in a target material. Along these defects nitrogen penetrates fast and forms thicker nitriding layers.

This method originates the experiments with a heavy ion beam [2,3] and 20 MeV REB [4]. In both cases, promotion for growth of the nitrided layers was verified, but there were some problems. With the heavy ion beam, several hours are required for irradiation of the ion beam because the current of it is small. In the case of 20 MeV REB, a long irradiation time also induces activation of a target material. Irradiation to a large area of a target material is difficult because the diameters of the heavy ion beam and 20 MeV REB are small. By using a pulsed power generator, there is capability to promote growth of nitrided layers by one shot irradiation of pulsed REB. Irradiation to a relatively large area of a target material is capable because pulsed REB is generated with a simple diode which consists of an anode and a cathode [5].

In this paper, the experimental results for the proposed method are reported. In the experiments, a pure iron was used as the specimen, and irradiation of pulsed REB to the specimen was carried out with a pulse power generator. The energy, the pulse width and the current density of pulsed REB were 1.4 MeV, 30 ns and 35 - 200 A/cm^2, respectively.

2 Experimental procedure

A pure iron (99.99%) of which thickness was 1 mm was used as a specimen. The specimen was cut 10 × 10 mm, and was polished mechanically with emery papers and aluminum oxide powder. The polished specimen was washed and was annealed at 550 ℃ by 2 hours in vacuum. After annealing a pulsed REB was irradiated to the specimen. Irradiation of pulsed REB was performed at Kanazawa University with a pulsed power generator called modified Pulserad 110A (1.5 MV, 25 kA, 30 ns) produced by Physics International. Figure 1 shows an experimental setup at the end of the generator. An utilized diode consisted of a carbon cathode and a 27 μm thick titanium foil. The diameters of the cathode and the anode were 36 and 60 mm, respectively. An anode-cathode gap length was set by 30 mm. When a pulsed high voltage is supplied to the diode, electrons emitted from the carbon cathode are accelerated to the anode. The accelerated electrons pass through the foil anode, and loses an average energy of about 0.1 MeV. As a result, the electrons irradiated to the specimen have the energy of about 1.4 MeV. The current densities of the pulsed REB were measured with Faraday cups. Since the radial profile of the current densities was not uniform, one specimen was placed on a center axis of the setup. The current density irradiated to the specimen was varied with changing the axial position of the specimen. Its peak value ranged from 35 to 200 A/cm^2.

After one shot irradiation, the specimen was nitrided with an apparatus called plasma source nitrider [6] as shown in Fig. 2. The apparatus consisted of a plasma source and a specimen holder. The plasma source had a filament (cathode), an anode and an anti-cathode. The anode and the cathode were ring shape, and their radii were approximately 5 mm. Electrons emitted from the filament were accelerated by the DC voltage of about 100 V, and moved back and forth between the filament and the anti- cathode. By these reciprocating motions of the electrons, nitrogen and hydrogen gas were ionized. Preset mixture of N_2 and H_2 (N_2:H_2=5:2) was used as working gas. A pressure inside a vacuum vessel was kept at 5×10^{-4} torr. The specimen holder was insulated from the vacuum vessel. The DC bias voltage of about - 1 kV was applied between the anti-cathode and the specimen holder. This voltage accelerated nitrogen ions and protons, and the ions bombarded to the specimen. By bombardment of the ions, the temperature of the specimen became high and kept at about 550℃ without an external heating device. The temperature of 550℃ was required by formation of nitride. The temperature of the specimen was monitored with a chromel- alumel thermocouple set behind the specimen. After nitriding, the specimen was cut and its cross section was polished and etched by dilute nitric acid. The cross section was observed and analyzed with a optical microscope, a scanning electron microscope (SEM), a micro Vicker's hardness tester, an electron probe micro analyzer (EPMA), an Auger electron spectroscopy (AES) and the X-ray diffraction method (XRD).

3 Experimental results

After nitriding for irons, ϵ- phase layers ($Fe_{2\text{-}3}N$) and γ'-phase layers (Fe_4N) are formed near the surface of the irons. It is well known that the γ'- phase layer is suitable for industrial applications because the hardness for the γ'-phase layer is approximately five times higher than that for a pure iron. Figures 3 show the cross-sectional photographs obtained with the optical microscope. The specimens shown in Figs. 3 (a) and (b) were obtained without and with irradiation of pulsed REB, respectively. Since the cross sections were etched by dilute nitric acid to exhibit grain boundaries, the ϵ-, the γ'- and the α-phase layers can be distinguished. Here the α- phase layer is a nitrogen diffused layer (Fe_8N) and is not nitride. In Fig. 3 (a), these layers are clearly distinguished and the sum of the thicknesses for the ϵ and the γ'-phase layer is 27 μm. Meanwhile the ϵ- phase layer is not distinguished in Fig 3 (b). This is caused by promotion for diffusion of nitrogen by irradiation of pulsed REB. That is, the ϵ-phase layer becomes very thin by decrease of nitrogen in the surface layer of the specimen. The maximum thickness of the γ'-phase layer is 40 μm in Fig. 3 (b). As a result, the thickness with irradiation of pulsed REB is approximately 1.5 times longer than that without irradiation of pulsed REB.

A hardness was estimated with the micro Vicker's hardness tester. Figures 4 show the hardness as a function of the depth from the surface of the specimen. The data shown in Figs. 4 (a) and (b) were obtained by the current densities of 70 and 160 A/cm^2, respectively. In these figures, the regions in which the hardnesses are high correspond to the nitrided layers. The hardnesses in the nitrided layers are three to four times higher than that in the pure iron because the hardness for the annealed pure iron is 88. The depths where the hardnesses become low agree with the boundaries between the γ'- and the α- phase layers observed with the optical microscope and SEM. These depths are 27 and 33 μm and displayed by dotted line in Figs. 4. From comparison of these two values, it is expected that the thickness of the nitrided layer becomes longer with increase of the current density. To make clear this correlation, the thicknesses of nitrided layers are plotted as a function of the current density in Fig. 5. The thicknesses shown in Fig. 5 were measured with SEM. A dotted line in the figure shows the maximum thickness of the nitrided layer obtained without irradiation of pulsed REB. The effect by irradiation of pulsed REB is not seen at the low current density, but a thicker nitrided layer is obtained by a higher current density. The thickness of the nitrided layer increases with increase of the current density. These facts are explained by a number of the lattice defect. By irradiation of pulsed REB, the number of the lattice defect increases. These lattice defects promote diffusion of nitrogen and the thick nitrided layer is obtained. Increase of the thickness seen in Fig. 5 agrees with this explanation, but increase of the lattice defect was not verified due to difficulty in direct measurement for the lattice defect.

Figure 6 shows the analyzed results with the Auger electron spectroscopy for the specimen with irradiation of pulsed REB (200 A/cm^2). In Fig. 6, the vertical and the transverse axis correspond to a concentration and a depth from the surface of the specimen, respectively. Here the concentration means the percentage of each element and is not transferred to the weight concentration. A deep region of the specimen was analyzed with sputtering by an argon ions accelerated with the voltage of 15 kV. From this analysis, it is verified that nitrogen is contained near the surface of the specimen and the concentration for nitrogen is approximately 9.0 % in average. The reason why this value is lower than that for Fe_4N may be caused by estimation without absolute calibration. Oxygen is only detected from the surface to 15 Å. This fact means that oxygen is contained by oxidation of the surface.

Since AES could not analyze the deeper region of the specimen, analysis with the electron probe micro analyzer was carried out. Figures 7 show the results of the qualitative analysis with EPMA for the same specimen analyzed with AES. Figures 7 (a), (b) and (c) show intensities for reflected electrons by SEM and X- ray signals corresponding to the wave lengths of iron and nitrogen. Here the intensities are shown by counts of detected signals and are arbitrary units. In Fig. 7 (a), the peaks appeared at 1 and 37 μm correspond to the surface of the specimen and the boundary between nitride and iron, respectively. In Fig. 7 (b), there is few difference in the intensity over an analyzed region, but the intensity slightly decreases in the nitrided layer. The intensity for nitrogen increases considerably in the nitrided layer in Fig. 7 (c). It is considered that a peak appeared at 37 μm is incorrect data. The reason why a peak appears at 37 μm is that the analyzed position gets out of the Rowland circle for a X- ray spectroscopy in an etched groove, and the incorrect data is obtained. By absolute calibration, the concentrations were estimated at 20 μm from the surface. Their values for iron and nitrogen were 79.9 and 11.7 %, respectively. The rest of the concentration is mainly occupied by oxygen. In analysis with EPMA, the specimen is cut and its cross section is analyzed. It is considered that oxygen may be contained by oxidation of the cross section.

By analysis with AES and EPMA, it was verified that nitrogen is contained near the surface of the specimen. However formation of nitride was not verified by these analyses, so we carried out analysis with the X- ray diffraction method. Figures 8 (a), (b) and (c) show the analyzed data obtained by specimens with irradiation of pulsed REB (160 A/cm^2), without irradiation and only annealing, respectively. Nitriding for specimens was performed in the case of Figs. 8 (a) and (b). The vertical and the transverse axes correspond to intensities of X- rays and diffraction angles 2θ, respectively. From Figs. 8 (a) and (b), formation of Fe_4N is verified by good agreement between the angles where peaks appear and the angles from a database for Fe_4N. The difference between Figs. 8 (a) and (b) is a ratio of the intensities for the peaks appeared at 42 and 50 degrees. For the peak at 42 degrees, the signal by $Fe_{2\text{-}3}N$ is superimposed. It is considered that the thick layer of $Fe_{2\text{-}3}N$ is formed without irradiation of pulsed REB, and the signal from this layer changes the ratio of the counts. In Fig. 8 (c), peaks appear at the angles from a database for Fe, and not appeare at the angles from the database for Fe_4N.

4 Summary

In order to promote growth of nitrided layers, a nitriding method with irradiation of pulsed REB was proposed and tested. The results are summarized as follows. The maximum thickness of the γ'- phase layer (Fe_4N) was 40 μm with irradiation of pulsed REB. Under the same condition, the thickness of the nitrided layer was 27 μm without irradiation of pulsed REB. As a result, the 1.5 times thicker nitrided layer was obtained by irradiation of pulsed REB. This fact also means that growth of the nitrided layer was promoted by the proposed method. By analysis with EPMA and XRD, it was verified that nitrogen was contained near the surface of the specimen and nitride was formed in the surface of it. From the dependence of the thickness of the nitrided layer on the current density of pulsed REB, it was made clear that thicker nitriding layers were obtained with higher current densities of pulsed REB. An optimized condition for the current density was not obtained, because it is difficult for the pulse power generator that the current density of pulsed REB becomes high without increase of an acceleration voltage. However it is expected that the proposed method will be one of the applications with a pulse power generator which easily generates the relativistic electron beam for a relatively large area with the current density of hundreds of amperes per square centimeters.

References

[1] H. Yamanaka: "Ion nitriding method" Nikkan Kogyo Shinbunsha (1976) [in Japanese].

[2] M. Nunogaki, H. Suezawa, Y. Kuratomi and K. Miyazaki: Vacuum, **39** (1989) 281.

[2] M. Nunogaki, H. Suezawa, Y. Kuratomi and K. Miyazaki: Nucl. Instrm. Methods, **B39** (1989) 591.

[4] M. Nunogaki, Y. Simaoka, D. Ishiko and T. Okada: Proc. 3rd Symp. Beam Engineering of Advanced Material Syntheses, Tokyo, 1992 p.331 [in Japanese].

[5] for example:
J. Nation: Particle Accelerators, **10** (1979) 1.

[6] M. Nunogaki, H. Suezawa, K. Hayashi and K. Miyazaki: Applied Surface Science, **33** (1988) 1135.

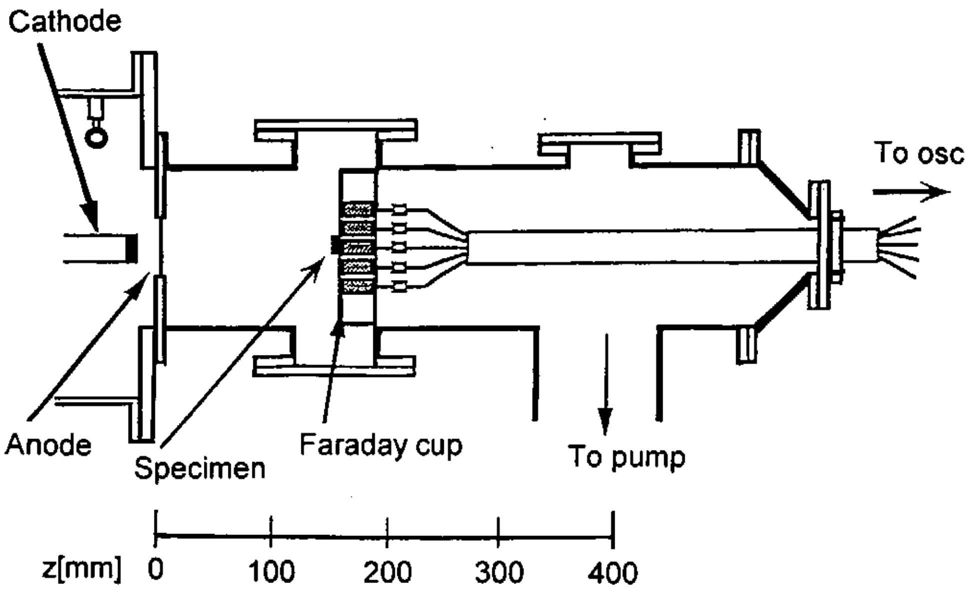

Fig. 1 Experimental setup at the end of the pulsed power generator "modified pulserad 110A".

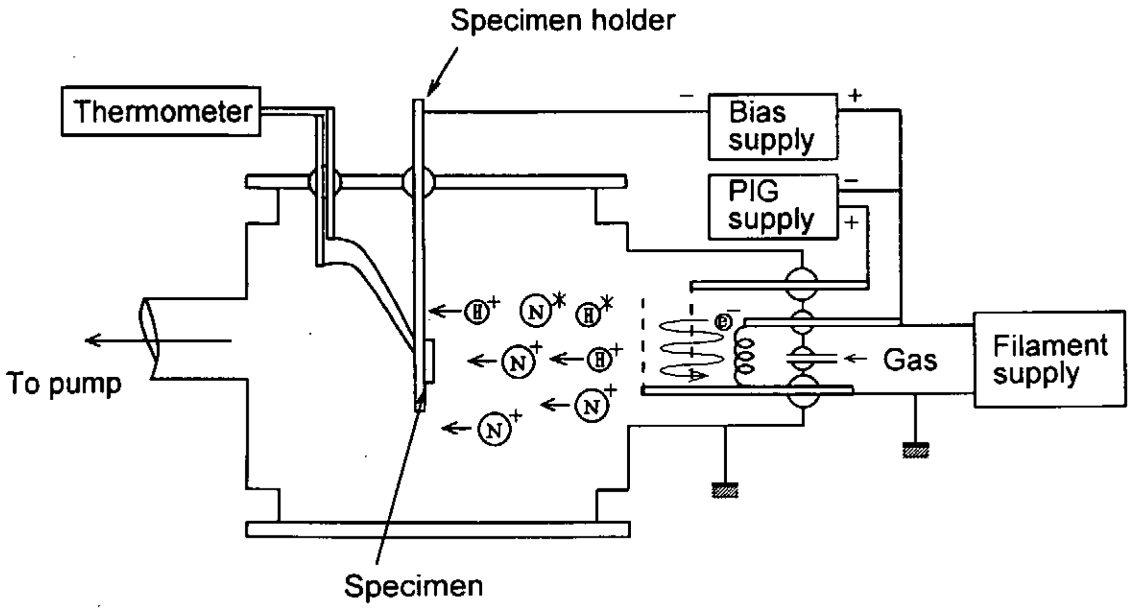

Fig. 2 Schematic drawing of nitriding apparatus called plasma source nitrider.

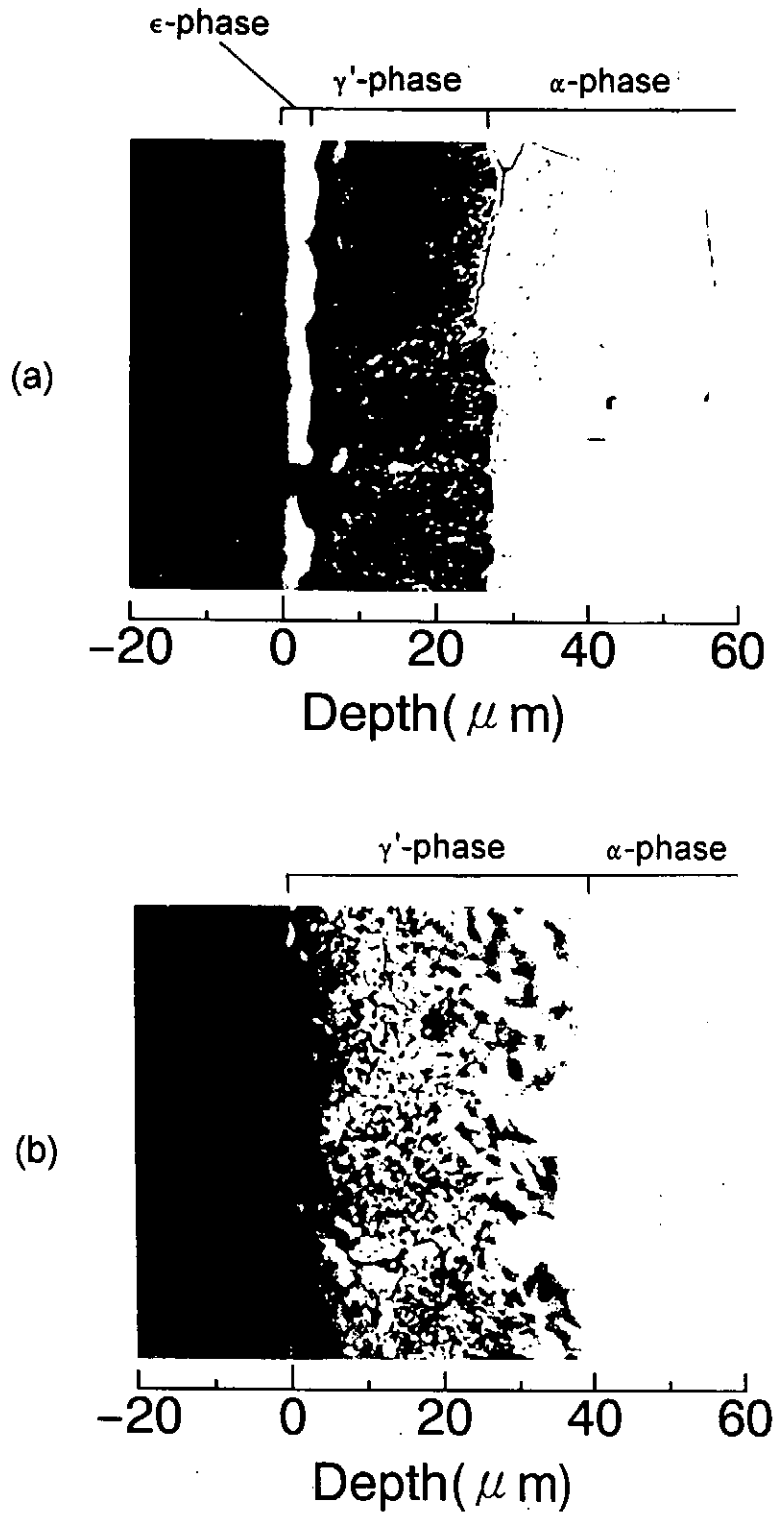

Fig. 3 The cross-sectional photographs for nitrided irons obtained with the optical microscope; (a) without irradiation of pulsed REB, (b) with irradiation of pulsed REB (200 A/cm ^{2}). The magnification by the microscope was 400.

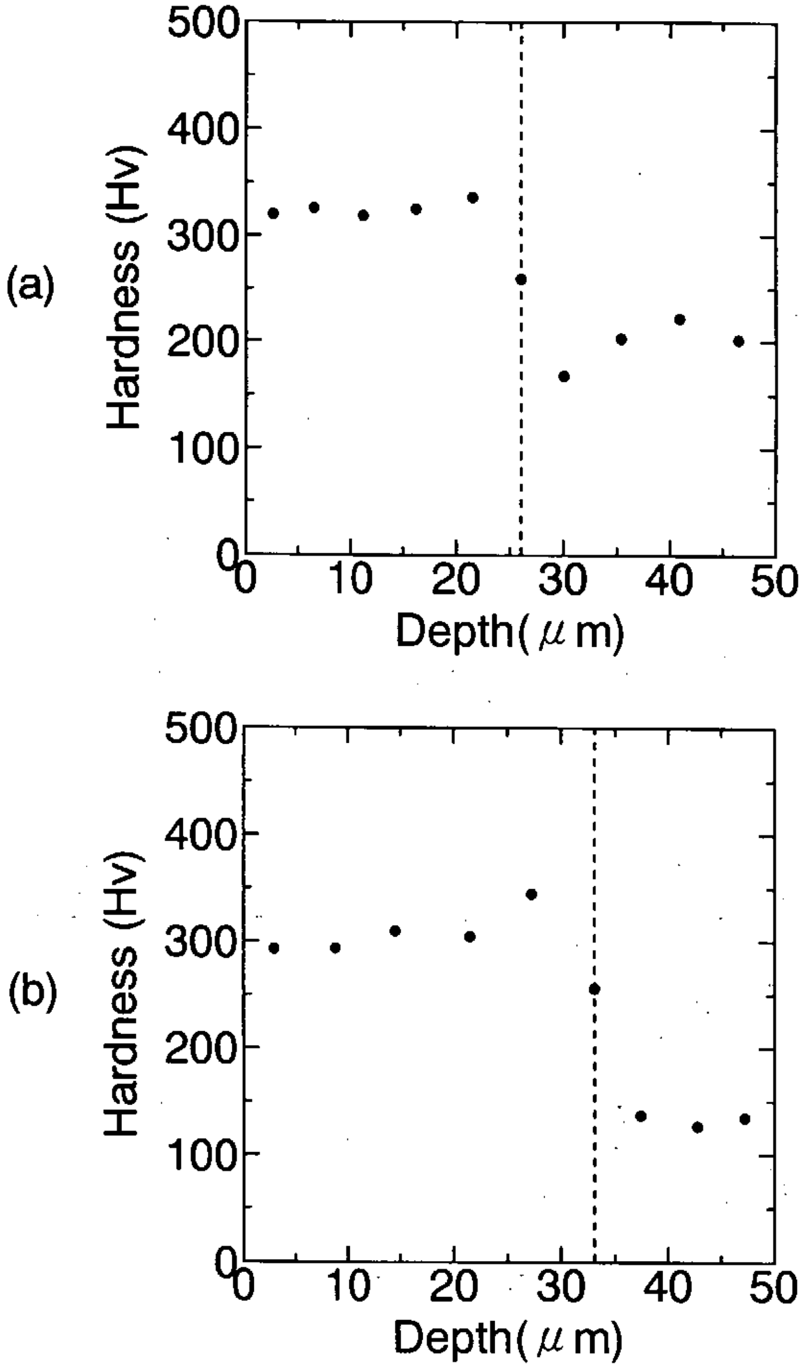

Fig. 4 The hardness as a function of the depth from the surface of the specimen. The data shown in (a) and (b) were obtained by irradiation of pulsed REB with the current densities of 70 and 160 A/cm ^{2}, respectively.

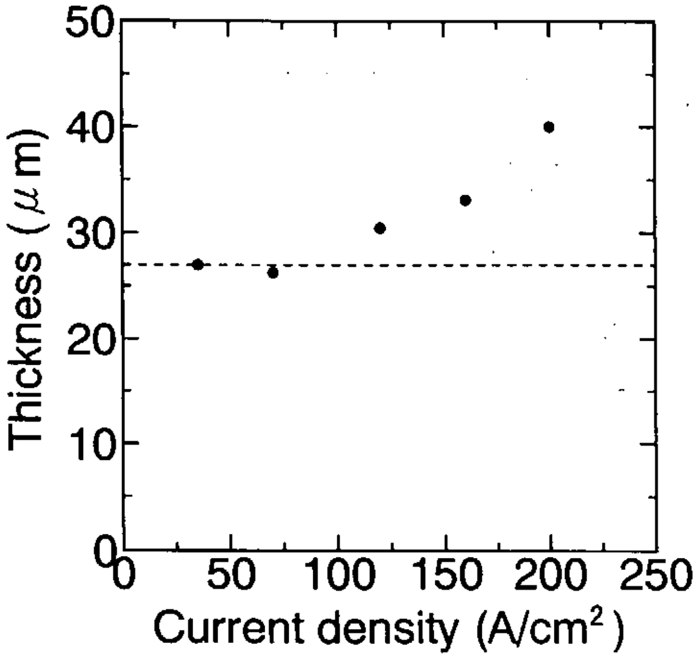

Fig. 5 The dependence of the thickness of the nitrided layer on the current density of pulsed REB.

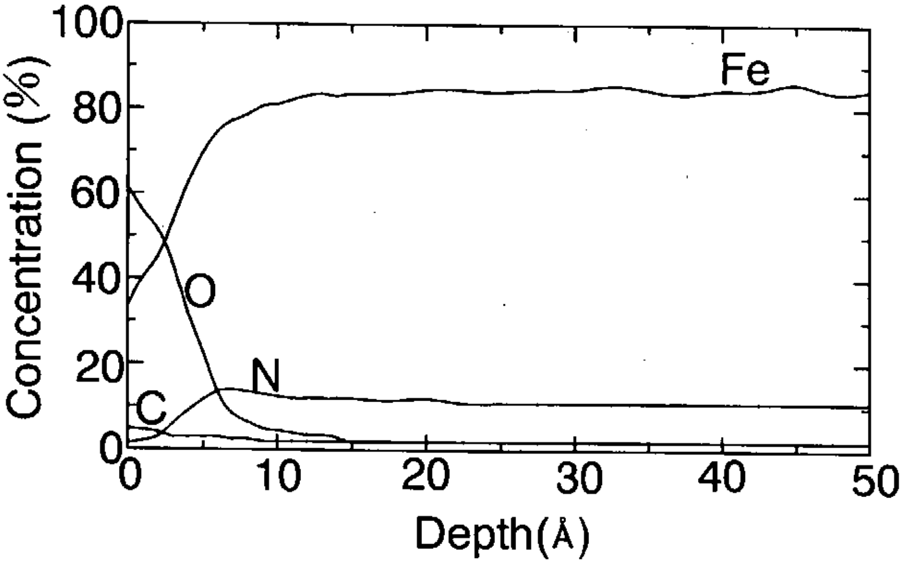

Fig. 6 The analyzed results by AES for the nitrided specimen with irradiation of pulsed REB (200 A/cm ^{2}).

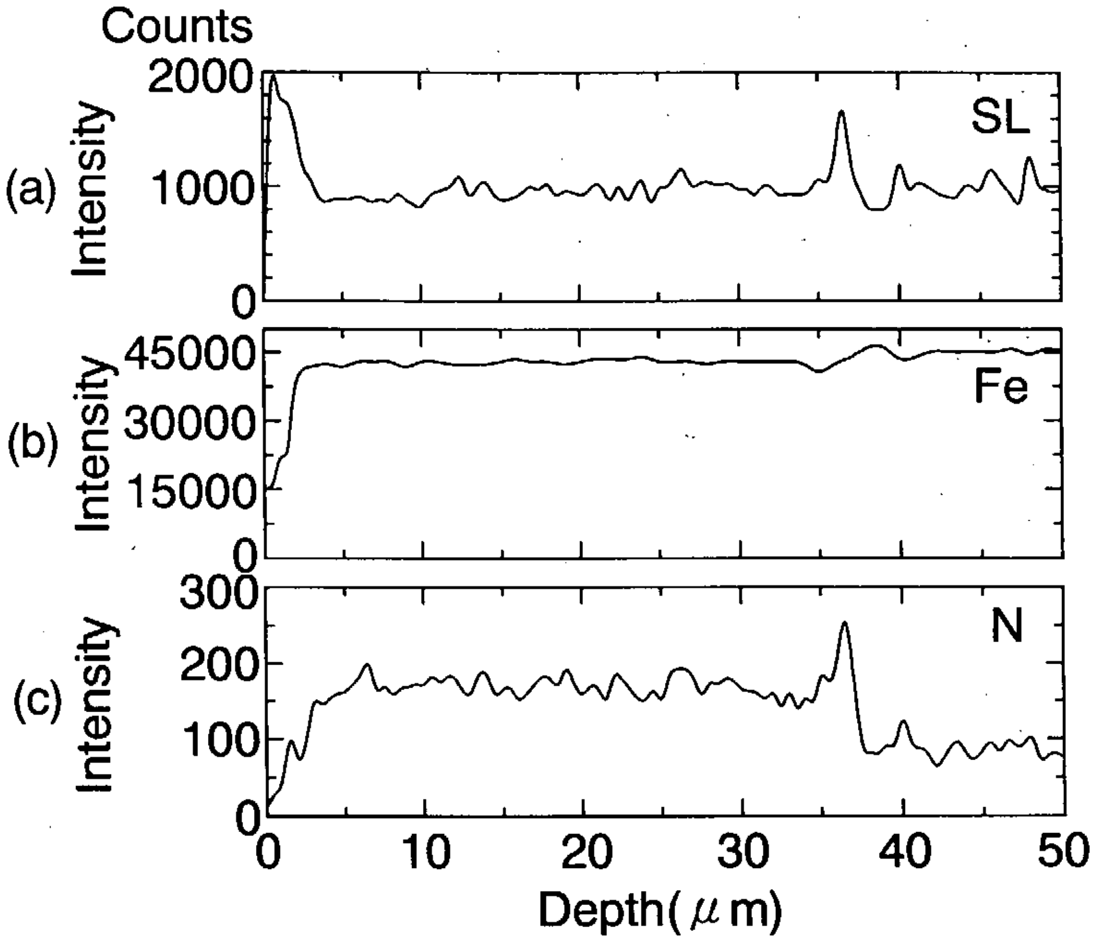

Fig. 7 The results of the qualitative analysis with EPMA; the intensities for reflected electrons by SEM (a) and X-ray signals corresponding to the wave lengths of iron (b) and nitrogen (c).

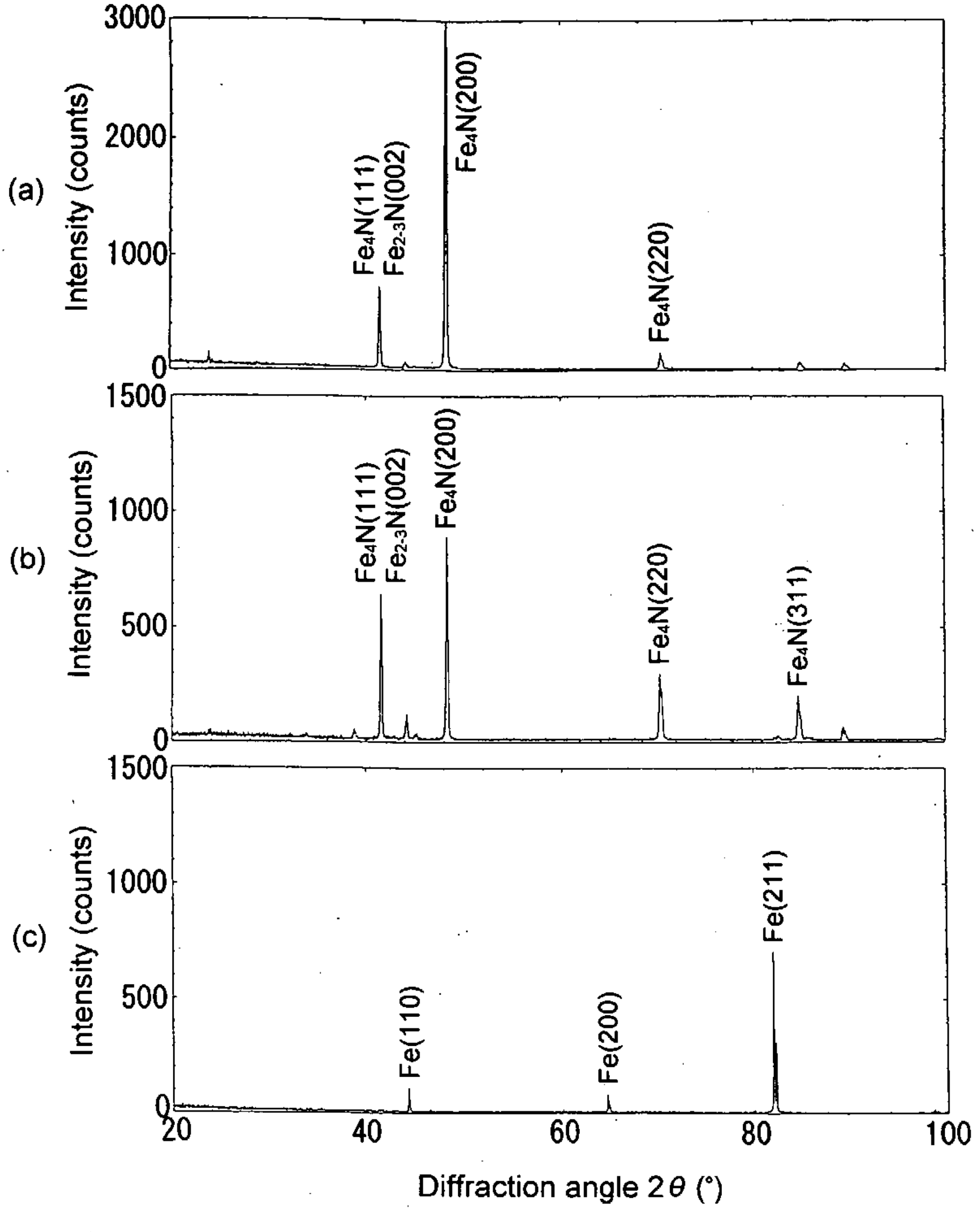

Fig. 8 The analyzed data for iron obtained by the X-ray diffraction method; (a) with nitriding and irradiation of pulsed REB (160 A/cm ^{2}), (b) with nitriding but without irradiation of pulsed REB, (c) only annealing.

Characterization of $BaTiO_3$ Thin Films prepared by Intense, Pulsed, Ion-Beam Evaporation

Tomihiro Sonegawa, Constantin Grigoriu, Katsumi Masugata, Kiyoshi Yatsui,
Yutaka Shimotori[a], Sigemasa Furuuchi[a] and Hiroshi Yamamoto[b]

Laboratory of Beam Technology, Nagaoka University of Technology,
Nagaoka, Niigata 940-21
[a] R & D Center, Nippon Seiki Co. Ltd., Nagaoka, Niigata 940-21
[b] Nichicon Co. Ltd., Nakagyo-ku, Kyoto 604

Abstract

Cubic barium titanate ($BaTiO_3$) thin films have been prepared *in situ*, on $A\ell/SiO_2/Si(100)$ substrate at ≤ 200 °C, by intense, pulsed, ion-beam evaporation (IBE). We have proposed a new deposition configuration, back side deposition (IBE/BS), which in comparison with standard front side deposition (IBE/FS) proved to be advantageously. Very smooth thin films, without any droplets, with a dielectric constant value of 90 at 1 kHz, have been obtained by IBE/BS and substrate temperature at 200 °C. The deposition rate was 50 ~ 100 nm/shot, 10 ~ 20 % of the IBE/FS.

1. Introduction

Barium titanate ($BaTiO_3$), which is a perovskite-type ferroelectric material possessing a high dielectric constant, is promising for application in electronic devices. Because of interests in $BaTiO_3$ thin films many different preparation techniques have been developed, which include sputtering,[1] metal organic chemical vapor deposition (MOCVD),[2] sol-gel process,[3] pulsed laser deposition (PLD).[4,5] Some of them need heating processing in order to crystallize the film. Considering the fabrication of ferroelectric films on semiconductors, processing temperatures below 500 °C are desirable.

In this work, we studied *in situ* deposition of crystalline $BaTiO_3$ thin films, on low temperature substrate, using an intense, pulsed, ion-beam evaporation (IBE) technique.[6~13] The IBE technique is advantageous in comparison with other techniques because of the high-rate growth and transfer of the composition from the target to film. However, it suffers from the problem of droplets which are scattered on the grown film surface. Therefore, we have investigated the properties of low temperature deposited film by the IBE technique, for two geometrical configurations: conventional IBE (front side deposition: IBE/FS) and new configuration IBE (back side deposition: IBE/BS).

2. Experimental

Figure 1 (a) and 1 (b) shows the two geometrical configurations, IBE/FS and IBE/BS, respectively. In the conventional IBE/FS technique, the deposition takes place on the frontal side of the substrate, while in the IBE/BS technique the deposition on the substrate placed on the reverse side of the holder. The target-substrate distance was approximately 40 mm, in both cases.

The intense, pulsed, ion beam (1.3 MeV, 0.6 kA/cm^2, mainly protons) is delivered by "ETIGO-II" accelerator. [14] The ion beam was focused onto a $BaTiO_3$ target. The typical ion beam parameters are: energy density 25 J/cm^2, pulse duration 50 ns (FWHM), and the beam-target interaction area 2 cm diameter.

We have used a tetragonal, sintered, polycrystalline $BaTiO_3$ disc target, 40 mm diameter, 5 mm thick, 99.9 % purity. The substrate consisted of a (100) oriented silicon wafer, coated with a thermally grown SiO_2 layer (300 nm thick), on which, through a mask, an $A\ell$ bottom electrode of 100 nm thickness was thermally evaporated ($A\ell/SiO_2/Si(100)$ substrate). The substrate was heated, at 25 °C ~ 200 °C, by a Ni-Cr alloy sheet. The chamber pressure during the deposition was 3×10^{-2} Pa.

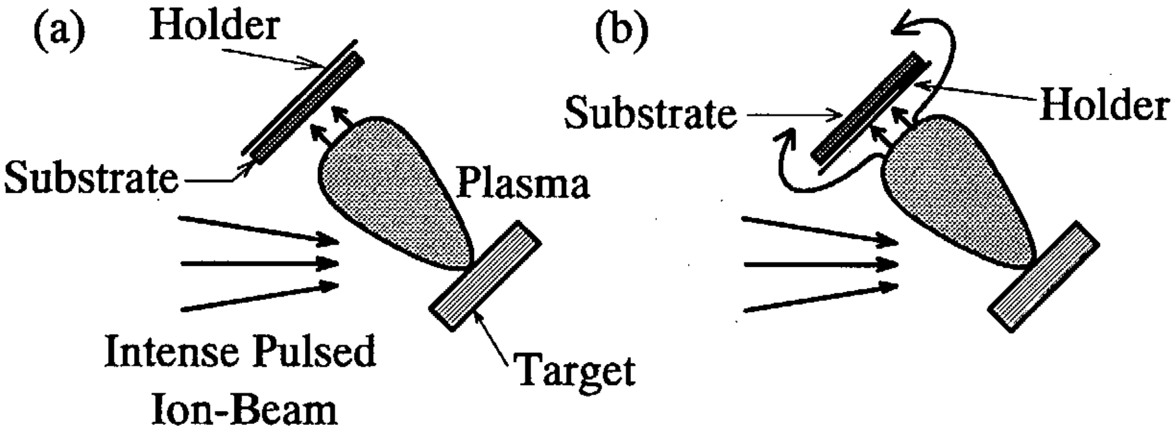

Fig. 1 Schematic drawing of IBE technique: (a) front side configuration (IBE/FS) and (b) back side configuration (IBE/BS).

By X-ray diffraction (XRD) with Cu-K_α emission, the crystalline structure of $BaTiO_3$ thin films have been studied. The surface morphology and thickness of the deposited films were observed by scanning electron microscope (SEM) and atomic force microscope (AFM). In order to investigate the electrical characteristics, we evaporated an $A\ell$ top electrode with the size of 10 mm^2 on $BaTiO_3$ thin film. We have used a Sawyer-Tower circuit to measure the dielectric constant, at 10 ~ 10^5 Hz.

3. Results and discussion

Figure 2 (a) and 2 (b) shows respectively the SEM images from surface morphology and the cross sectional view of the thin film deposited by one shot IBE/FS. As shown in fig. 2 (a) on the surface we can see a lot of spherical droplets. The droplets diameter varied from less than 1 μm to 8 μm. These droplets are generally thought to be introduced directly from the target or to be condensed during expansion in the ambient. Moreover, some samples exhibit pinholes on the surface. The droplets were condensed on the thin film because of the shrinkage phenomenon, peel the film and afterwards fall.

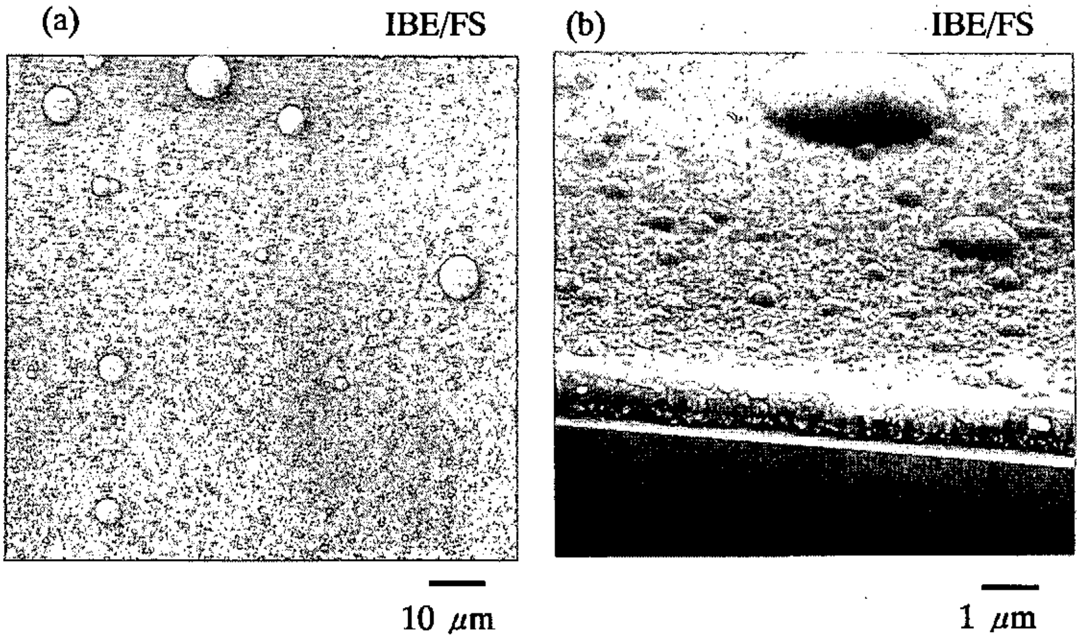

Fig. 2 SEM images of $BaTiO_3$ film deposited on $A\ell/SiO_2/Si(100)$, by IBE/FS, one shot, substrate temperature 25 °C: (a) typical morphology showing droplets and (b) film cross sectional view.

As shown in Fig. 2 (b), the film thickness deposited by IBE/FS was 600 nm, corresponding to the high deposition rate of 600 nm/shot.

So as to avoid droplets, we have proposed a new geometrical configuration, IBE/BS, as shown in Fig. 1 (b). Figure 3 (a) and (b) show respectively the SEM images of the surface morphology and the cross sectional view of the thin film deposited by IBE/BS, one shot, substrate temperature at 25 °C. As shown in Fig. 3 (a), the surface does not show any droplets or pinholes. The most of the melted balls, are impinging on the front side of the substrate holder, being deposited on it, while backside, is coated with a very smooth film. As shown in Fig. 3 (b), the measured thickness has been 100 nm.

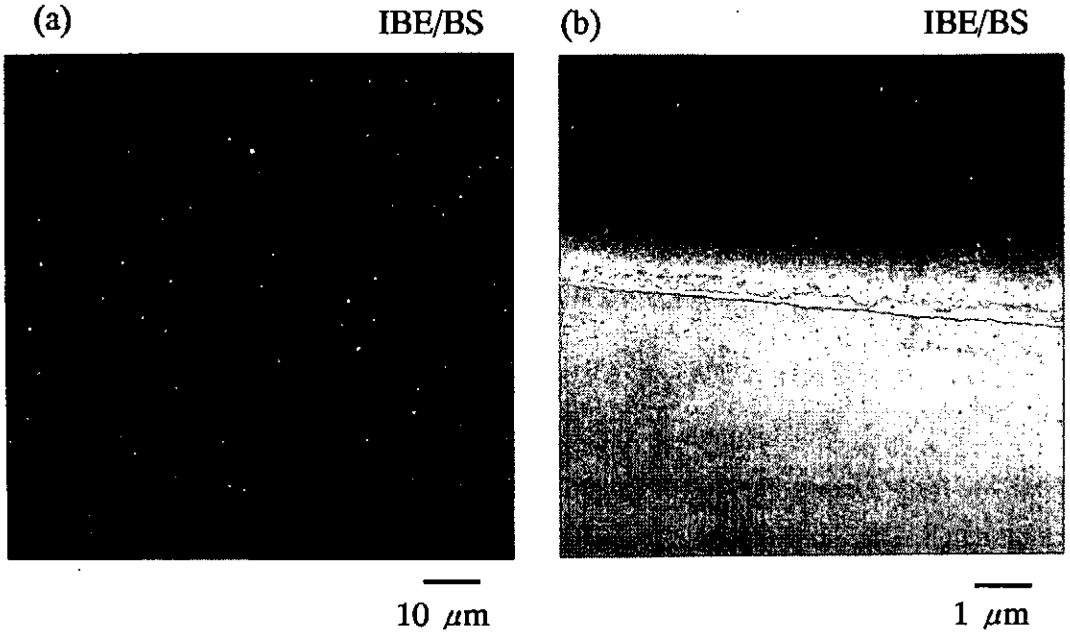

Fig. 3 SEM images of $BaTiO_3$ film deposited on $A\ell/SiO_2/Si(100)$, by IBE/BS, one shot, substrate temperature 25 °C: (a) film surface, (b) film cross sectional view.

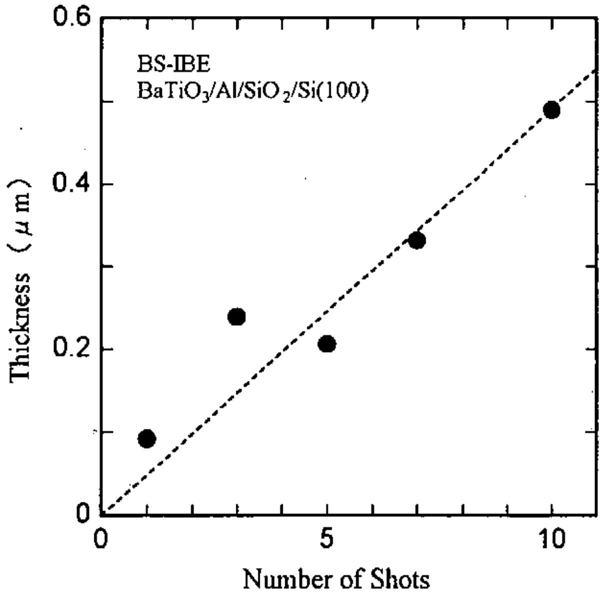

Fig. 4 Film thickness vs. number of shots, by IBE/BS.

Figure 4 shows the thickness of the $BaTiO_3$ films deposited by IBE/BS plotted against the number of shots of the beam. A deposition rate is 50 ~ 100 nm/shot, which is 10 ~ 20 % of that in the IBE/FS.

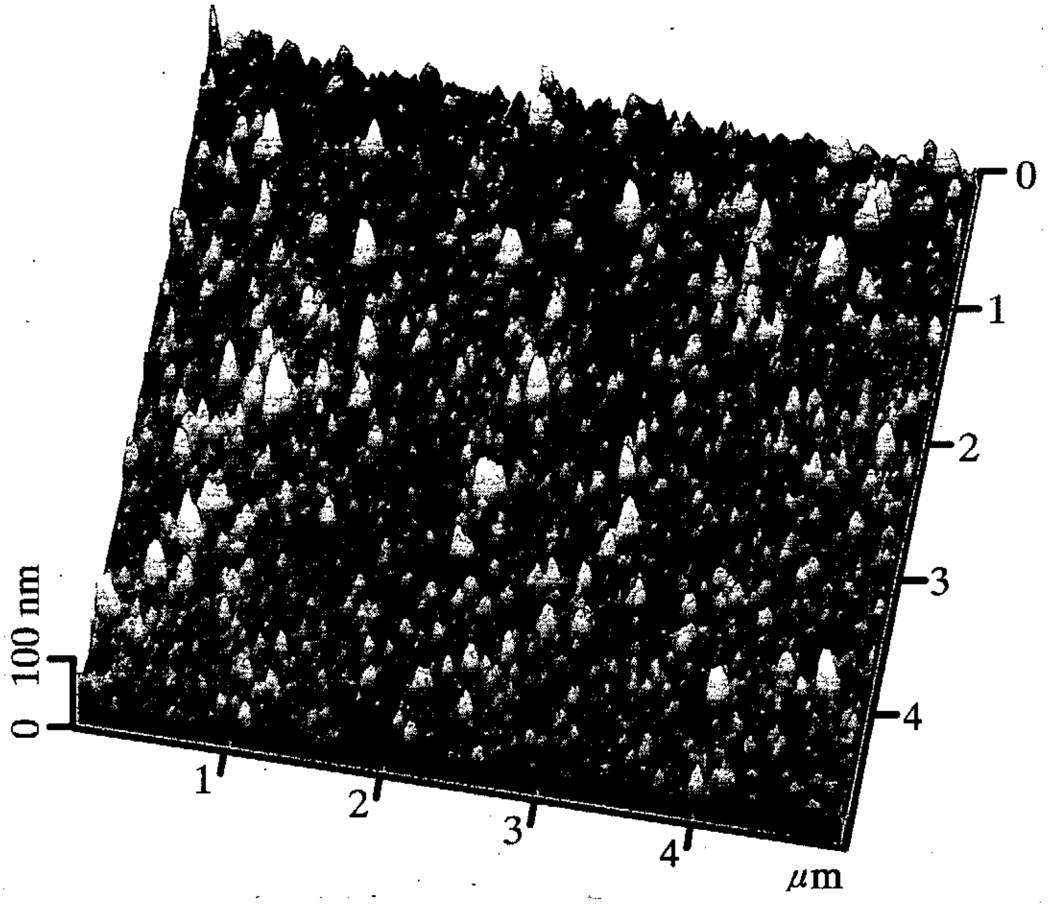

Fig. 5 AFM images of $BaTiO_3$ film deposited on Aℓ/SiO_2/Si(100), by IBE/BS, one shot, substrate temperature 25 °C.

Figure 5 presents the AFM images of $BaTiO_3$ film deposited on Aℓ/SiO_2/Si(100), by IBE/BS, one shot, at the substrate temperature of 25 °C. As shown in Fig. 5, the surface is found to be flat with a surface roughness in the following:

R_a (mean roughness) = 8.9 nm

R_{ms} (root mean square average roughness) = 11.9 nm.

In the case of higher substrate temperature, 200 °C, the roughness was significantly improved:

R_a = 3.1 nm

R_{ms} = 4.0 nm.

It is very clear that in comparison with IBE/FS technique, by IBE/BS droplets have been cleared, and that a significant improvement of the roughness has been achieved.

XRD patterns from the $BaTiO_3$ film grown by IBE/BS and IBE/FS are shown in Fig. 6 (a) and (b), respectively. Comparison between Fig. 6 (a) and (b) shows that both film structures are very similar. The XRD peaks exactly correspond to cubic perovskite $BaTiO_3$ crystal. Although splitting for tetragonal $BaTiO_3$ materials, near (200) and (002), was reported[15)], we could not observe it at the present experiment. The peak at 2θ = 24° corresponds to the orthorhombic $BaCO_3$ (111), that probably appears due to contamination in air, or from the diffusion pump oil used.

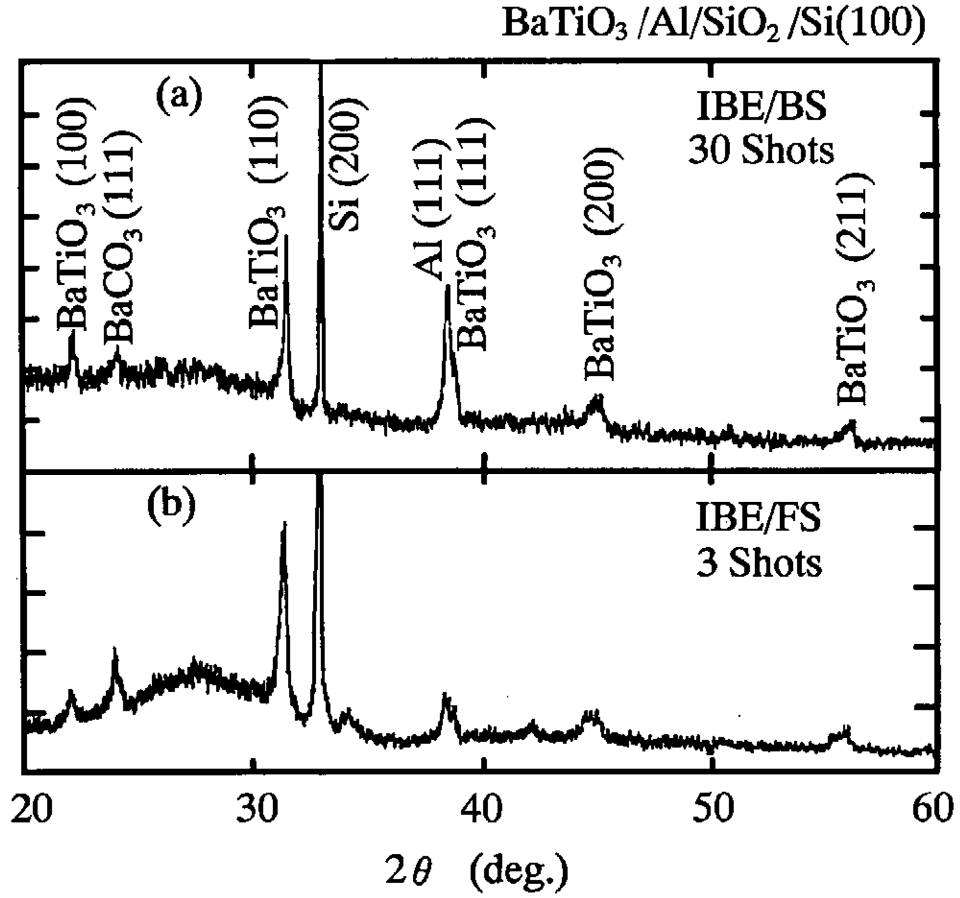

Fig. 6 XRD patterns of films deposited at substrate temperature of 25 °C by:
(a) IBE/BS, 30 shots and (b) IBE/FS, 3 shots.

Figure 7 (a) shows the dielectric constant of $BaTiO_3$ films deposited by IBE/FS and IBE/BS, one shot, substrate temperature at 25 °C, as a function of frequency. The dielectric constant of the film deposited by IBE/FS increases at low frequency. On the other hand, the dielectric constant of the film deposited by IBE/BS is pretty much the same for all the frequency range studied.

Figure 7 (b) shows the dielectric constant of $BaTiO_3$ films prepared by IBE/BS one shot at substrate temperature 25 °C and 200 °C. The film thickness was 100 nm. The dielectric constant at 200 °C was higher than at 25 °C. For example, at 1 kHz, the dielectric constant increases from 35 (25 °C) to 90 (200 °C).

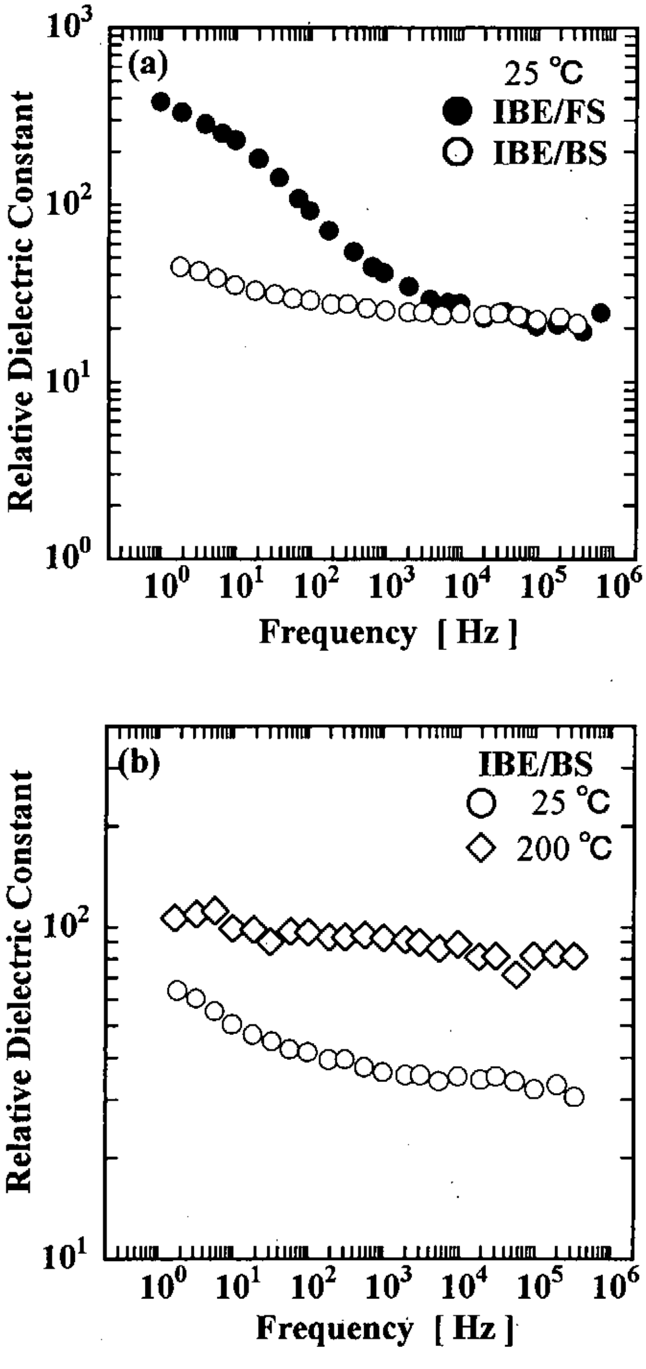

Fig. 7 Dielectric constant as a function of frequency for (a) IBE/FS and IBE/BS deposition, one shot, 25 °C, and (b) IBE/BS deposition at 25 °C and 200 °C.

4. Conclusions

In summary, we have investigated the properties of low temperature ($\leqq$ 200 °C) deposited $BaTiO_3$ films by the ion beam evaporation technique, for two geometrical configurations: front side and back side configuration. The back side deposition technique avoids droplets formation and provides a significant improvement of the roughness, R_a = 3.1 (at the substrate temperature of 25°C) ~ 8.9 nm (200° C) and R_{ms} = 4 (25 °C) ~ 11.9 nm (200 °C). The films deposited on $A\ell/SiO_2/Si(100)$ substrates were cubic perovskite polycrystals, with the relative dielectric constant of about 90, at 200 °C substrate temperature.

References

1) Q. Shi, Q. X. Jia and W. A. Anderson, J. Vac. Sci. & Technol. **A10**, 733 (1992).
2) I. T. Kim, C. H. Lee and S. J. Park, Jpn. J. Appl. Phys. **33**, 5125 (1994).
3) T. Hayashi, N. Oji and H. Maiwa, Jpn. J. Appl. Phys. **33**, 5277 (1994).
4) H. F. Cheng, M. H. Yeh, K. S. Liu and I. N, Lin, Jpn. J. Appl. Phys. **32**, 5656 (1993).
5) T. Nose, H. T. Kim and H. Uwe, Jpn. J. Appl. Phys. **33**, 5259 (1994).
6) Y. Shimotori, M. Yokoyama, S. Harada, K. Masugata and K. Yatsui, J. Appl. Phys. **63**, 968 (1988).
7) Y. Shimotori, M. Yokoyama, S. Harada, K. Masugata and K. Yatsui: Jpn. J. Appl. Phys. **28**, 468 (1989).
8) K. Yatsui: Laser and Particle Beams **7**, 733 (1989).
9) X. D. Kang, K. Masugata and K. Yatsui, Jpn. J. Appl. Phys. **33**, 1155 (1994).
10) X. D. Kang, K. Masugata and K. Yatsui, Jpn. J. Appl. Phys. **33**, L1041 (1994).
11) K. Yatsui, X. D. Kang, T. Sonegawa, T. Matsuoka, K. Masugata, Y. Shimotori, T. Satoh, S. Furuuchi, Y. Ohuchi, T. Takeshita and H. Yamamoto: Phys. Plasmas **1**, 1730 (1994).
12) G. P. Johnston, P. Tiwari, D. J. Rej, H. A. Davis, W. J. Waganaar, R. E. Muenchausen, K. C. Walter, M. Nastasi, H. K. Schmidt, N. Kumar, B. Li, D. R. Tallant, R. L. Simpson, D. B. Williams and X. Qiu, J. Appl. Phys. **76**, 5949 (1994).
13) K. Yatsui, C. Grigoriu, H. Kubo, K. Masugata and Y. Shimotori, Appl. Phys. Lett. **67**, 1214 (1995).
14) A. Tokuchi, N. Nakamura, T. Kunimatsu, N. Ninomiya, M. Den, A, Araki, K. Masugata and K. Yatsui: Proc. 2nd Int'l Top. Symp. Inertial Confinement Fusion Res. by High-Power Particle Beams, ed. by K. Yatsui (Lab. of Beam Tech., Nagaoka Univ. of Tech.) 430 (1986).
15) S. Naka, F. Nakakita, Y. Suwa and M. Inagaki: Bull. Chem. Soc. Jpn. **47**, 1168 (1974).

A Study of Material Processing using an Intense Pulsed Ion Beam

Yoshiyuki Hashimoto, Mitsuyasu Yatsuzuka[A], Tohru Yamasaki[B]
and Hitoshi Uchida[C]

Department of Electronic Engineering
Kobe City College of Technology,
8-3 Gakuen-Higashimachi Nishiku, Kobe, Hyogo 651-21

[A] Department of Electrical Engineering,
[B] Department of Material Science and Engineering,
[C] Department of Mechanical and Intelligent Engineering,
Himeji Institute of Technology,
2167 Shosha, Himeji, Hyogo 671-22

Abstract

Material surface characterization by irradiation of an intense pulsed ion beam (IPIB) with power density of 34MW/cm^2 and pulse duration of 30 ns has been studied experimentally. The IPIB irradiations to a target result in formation of an amorphous layer on the $Ni_{65}Cr_{15}P_{16}B_4$ alloy surface. They also the IPIB irradiation to a titanium produce the nanostructured phase and remove its roughness on the titanium surface. According to an estimation of nickel surface temperature, an IPIB irradiation leads to a rapid heating of the sample surface up to its boiling point, resulting in cooling rate of be 2.2×10^9 °C/s.

1. Introduction

Recently, intense pulse ion beams (IPIBs) with a high power density (~GW/cm^2) and a short pulse duration (~10ns) have attracted as a new heat-source instead of a laser in a material development field. Since ion ranges are extremely shorter than electron ones, the beam energy is deposited to a surface layer, typically, within a few µm. As a result, a target surface is heated above melting point in a short time of several nanosecond, and is immediately followed by rapid cooling and resolidification. Solidification of metals at the rapid cooling rate results in production of non-equilibrium microstructures such as amorphous and nanocrystalline phases[1-6].

In this paper, the formation of an amorphous layer on the $Ni_{65}Cr_{15}P_{16}B_4$ alloy and the production of nanocrystalline phase and the reduction of machining roughness on a titanium surface are successfully demonstrated. The experimental setup and the characteristics of the IPIB are introduced in section 2. Experimental results and discussion are described in section 3, and some conclusions are summerized in section 4.

2. Apparatus

2.1 *Experimental setup and measurement*

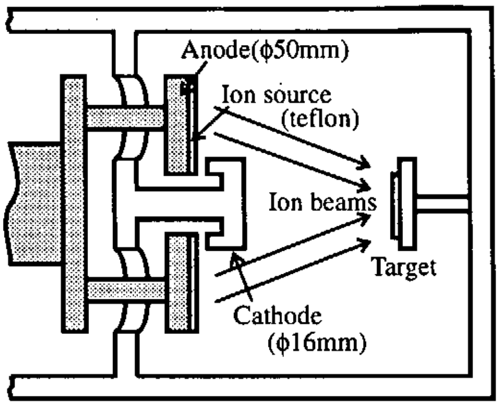

Fig. 1 Experimental setup of an inverse pinch ion diode and a target.

Figure 1 shows a schematic drawing of experimental setup. An IPIB was generated by an inverse pinch ion diode (IPD)[7,8] with the pulsed power generator "HARIMA-II" (400kV, 3Ω and 50ns) at Himeji Institute of Technology. The IPD consisted with a ring anode (diameter:50mm) and an annular cathode (diameter:16mm). A Teflon plate (thickness:2mm) was attached to the anode surface as an ion source. The anode-cathode (A-K) gap length was 3 mm. A target material for IPIB irradiation was located at the focal point 120 mm from anode. The typical pressure for diode operation was in the range of $2.0\sim8.0\times10^{-5}$ Torr. A diode voltage was measured with a resistive voltage divider placed close to the anode. A current density of the IPIB was measured with a single-pinhole biased ion collector (BIC) movable in radial and axial directions. Energies and species of the ion beams were estimated by the Thomson-parabola ion spectrometer. The characteristics of the IPIB-irradiated surface were analyzed using the X-ray diffractometer (CuKα, 50kV and 200mA). The lattice fringes of the IPIB-irradiated specimen were directly observed by a high resolution transmission electron microscope (HR-TEM). The specimen for HR-TEM was cut down from the top surface of IPIB-irradiated materials using a microtome with a diamond cutter. The topography and the microstructure of the cross section of the targets were observed with Scanning Electron Microscope (SEM). Here, the cross section was obtained by subjecting the specimen to the mechanically bending fracture.

2.2 *Characteristics of IPIB*

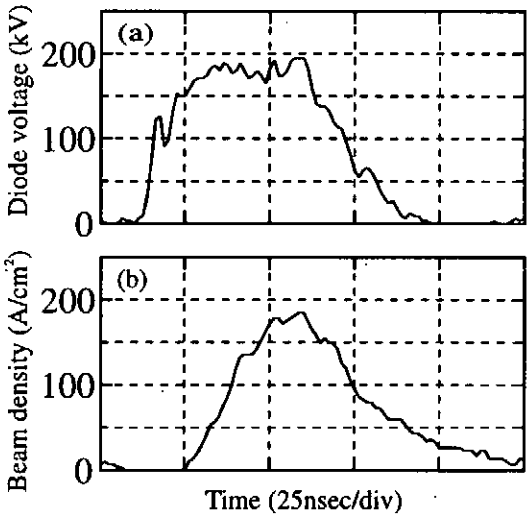

Fig. 2 Typical time history of diode voltage and ion beam current density.

Figure 2 shows the typical time history of (a) a diode voltage and (b) a current density of an ion beam measured with the BIC located at 120 mm behind the anode. As seen in Fig.2, the maximum accelerating voltage, current density and pulse duration of ion beams were 180 kV, 180 A/cm^2 and 30 ns, respectively.

Figure 3 shows the time evolution of beam power density obtained from the results of diode voltage and current density in Fig.2. The power density is not constant in time and has the largest value of 37 MW/cm^2. The total beam energy is estimated to be 1.02 J/cm^2 by integrating the power density with respect to time. We assume the ideal rectangular beam with the same total beam energy as 1.02 J/cm^2 estimated above. Supposing that the pulse duration equals to the FWHM value of 30 ns in Fig.3, we obtain the uniform power density of 34 MW/cm^2.

The main components of the ion beam were confirmed carbon (C^{2+}, C^{3+} and C^{4+}) and fluorine (F^{+} and F^{2+}) ions by the Thomson-parabola ion spectrometer.

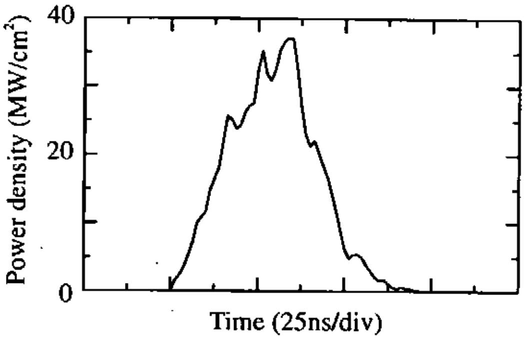

Fig. 3 The time evolution of beam power density estimated with the results in Fig. 2.

3 Results and Discussion

3.1 *Amorphous layer formation on $Ni_{65}Cr_{15}P_{16}B_4$ alloy*[5,6]

The IPIB was irradiated to a $Ni_{65}Cr_{15}P_{16}B_4$ alloy for an amorphous layer formation. Typical X-ray diffraction pattern of a non-irradiated $Ni_{65}Cr_{15}P_{16}B_4$ alloy is shown in Fig.4(a), where the maximum X-ray diffraction depth from the surface is estimated to be approximately 1.3 μm. Figure 4(b) shows the X-ray diffraction patterns of the IPIB irradiated $Ni_{65}Cr_{15}P_{16}B_4$ alloy for various incident angle α of X-rays to the target, and α = 1.0°, 1.5° and 2.0° correspond to the maximum X-ray diffraction depth of 0.66, 0.99 and 1.3 μm, respectively. The diffraction pattern of the non-irradiated substrate reveals the crystalline phase which is characterized by the narrow diffraction peak in Fig.4(a). In contrast, the IPIB-irradiated $Ni_{65}Cr_{15}P_{16}B_4$ alloy surface exhibits diffraction pattern typical of an amorphous structure. The diffraction patterns for α = 1.5° and α = 2.0° reveal the formation of a mixture of major amorphous and a minor crystalline phases. For α = 1.0°, however, the narrow diffraction peak indicating the crystalline phase disappears, suggesting that IPIB irradiation of the $Ni_{65}Cr_{15}P_{16}B_4$ alloy produces an amorphous layer with depth less than 0.66 μm from the surface.

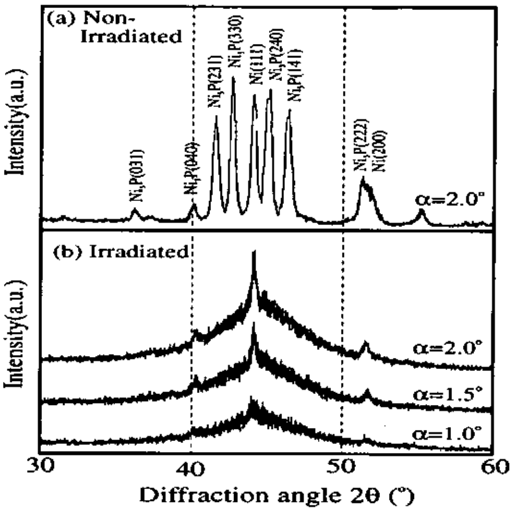

Fig. 4 X-ray diffraction patterns of IPIB (a) non-irradiated $Ni_{65}Cr_{15}P_{16}B_4$ alloy and (b) irradiated $Ni_{65}Cr_{15}P_{16}B_4$ alloy, where α is the angle of the incident X-ray to the target.

Figure 5 shows a HR-TEM micrograph and the corresponding selected area diffraction pattern of the IPIB-irradiated $Ni_{65}Cr_{15}P_{16}B_4$ alloy. Randomly oriented lattice fringes as well as a halo diffraction pattern are observed in the entire field of the micrograph except in some small area. These results indicate the formation of a homogeneous amorphous layer by IPIB irradiation.

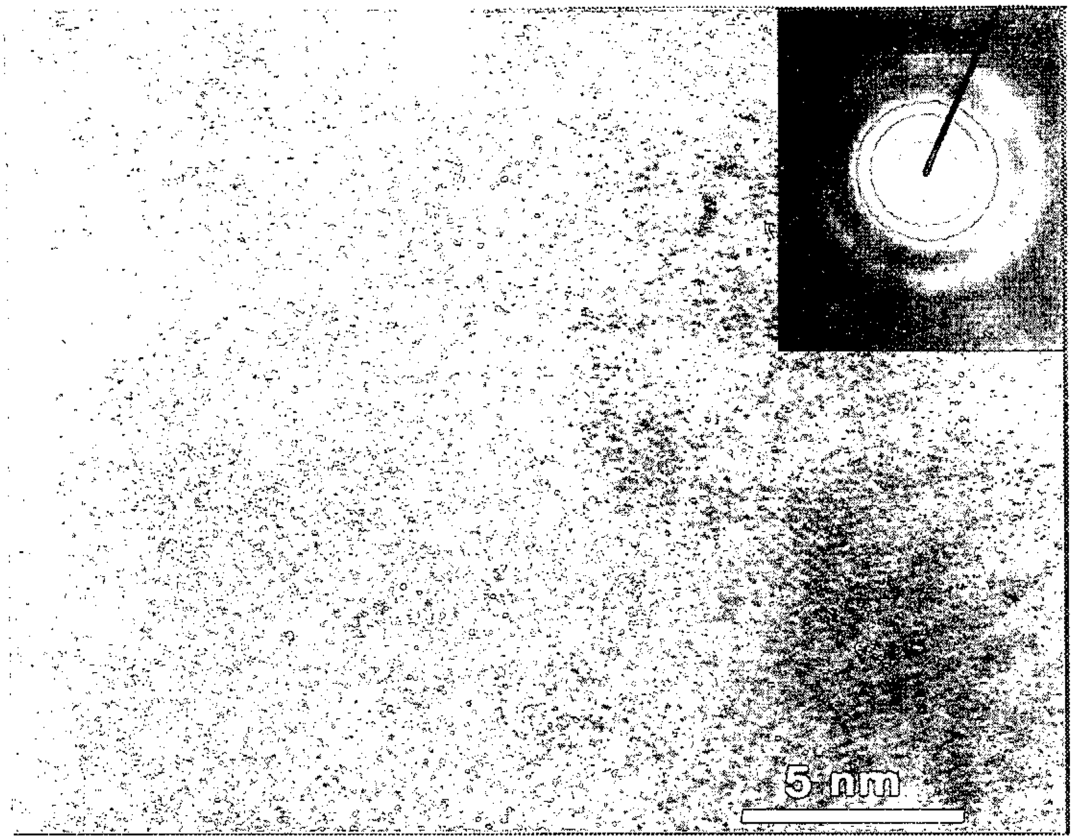

Fig. 5 HR-TEM micrograph and selected area diffraction of IPIB-irradiated $Ni_{65}Cr_{15}P_{16}B_4$ alloy.

The effect of repeated irradiations of IPIB on amorphous formation was studied experimentally. Figure 6 shows the X-ray diffraction patterns of the $Ni_{65}Cr_{15}P_{16}B_4$ alloys processed by IPIB-irradiation of 1, 3 or 10 shots, where the incident angle of X-ray is 2.0°. An increase in the number of IPIB-irradiation reduces the height of sharp diffraction peak that indicates the existence of a crystalline phase. After the IPIB-irradiation of 10 shots, the sharp peak in the X-ray diffraction pattern is almost completely lost, indicating the amorphous layer formation in a deep region from the surface.

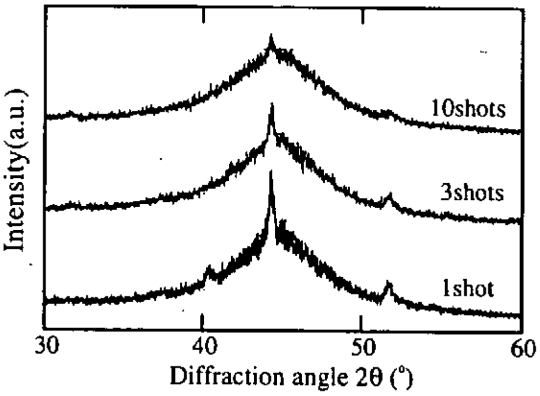

Fig.6 Effect of repeated irradiations of IPIB for amorphous layer formation.

The SEM micrograph of the cross section of a IPIB-irradiated $Ni_{65}Cr_{15}P_{16}B_4$ alloy is shown in Fig.7. The heat-affected depth of the sample is approximately 2 μm, which is comparable to the microstructural scale of the sample. Although not shown here, no crack was observed on the top surface irradiated by IPIB, while laser irradiation often resulted in cracks at the border of the neighboring laser irradiation traces.

Thermal diffusion length z_D during time t is approximately given by $z_D = \sqrt{\kappa t}$, where κ is the thermal diffusivity. Using κ = 0.133 cm^2/s for nickel and t = 30 ns, we obtain z_D = 0.63 μm, which is larger than both ion ranges of carbon and fluorine. Then, under the present conditions, the time evolution of surface temperature and cooling rate are estimated from the solution of the differential equation for heat conduction, so that the temperature rise depends little on ion spices and ranges.

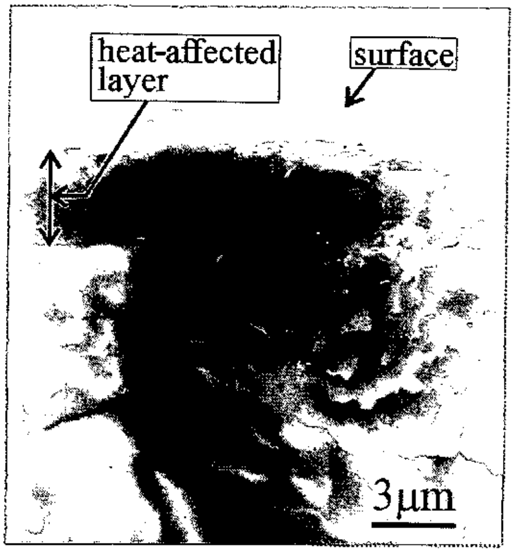

Fig.7 SEM micrograph of cross-section of the $Ni_{65}Cr_{15}P_{16}B_4$ alloy after one shot of IPIB irradiation.

Since the beam area is sufficiently larger than the target area, heat diffusion in the target is considered to be the one-dimensional. Assuming an ideal rectangular beam with constant power p and pulse duration τ, the temperature rise of the target surface is written as :

i) $0<t<\tau$ $$T(t) = \frac{2p}{K}\sqrt{\frac{\kappa}{\pi}t} \quad (^\circ C) \tag{1}$$

ii) $t>\tau$ $$T(t) = \frac{2p}{K}\sqrt{\frac{\kappa}{\pi}}\left(\sqrt{t} - \sqrt{t-\tau}\right) \quad (^\circ C), \tag{2}$$

where κ is the thermal diffusion rate, K is the thermal conductivity and the radiation loss from the surface is ignored. Substituting the present conditions (p = 34 MW/cm^2 and K = 0.67 W/(cm·K) for nickel) into eqs.(1) and (2), we obtain the time evolution of temperature on the nickel surface as shown in Fig.8, where the effects of the latent heat for fusion and vaporization are considered. The

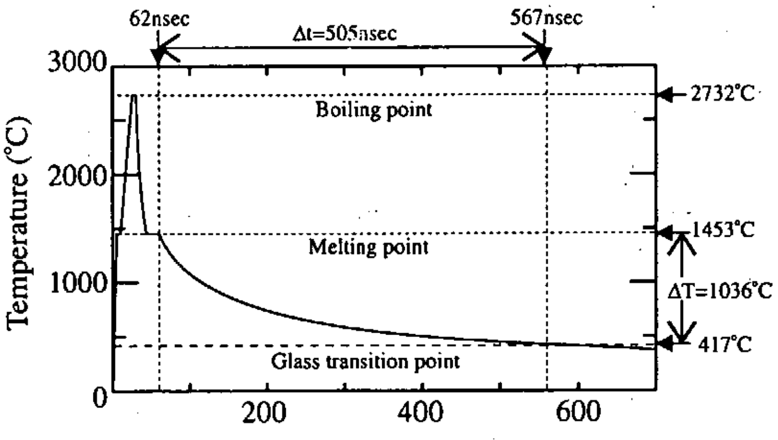

Fig. 8 Temperature rise and cooling rate of the nickel target surface for an irradiation of IPIB with the uniform power density of 34 MW/cm^2 and pulse width of 30 ns.

nickel surface is heated to its boiling point of 2732 °C, but dose not exceed the boiling point because of the large latent heat of vaporization. The cooling rate from the melting point (1453 °C for nickel) to the glass transition point (417 °C for the $Ni_{65}Cr_{15}P_{16}B_4$ alloy[9]) is found to be $dT/dt=2.2\times10^9$ °C/s in Fig.8. The estimated cooling rate is larger than the critical cooling rate(10^5~10^6 °C/s) for amorphous layer formation of nickel alloys. The temperature rise and cooling rate shown in Fig.8 were estimated using the physical parameters of pure nickel. However, since the difference in the physical parameters between pure nickel and nickel alloys is small, the results estimated using the physical parameters of pure nickel give rise to a good approximation of the experiments.

3.2 *Surface modification of titanium*

The IPIB was irradiated to a titanium target (15mm×15mm×0.5mm) for surface modification. The titanium target was polished with the emery paper (#1000) and annealed in a vacuum. The target was irradiated with the IPIB of 5 shots for the more uniform irradiation. Figure 9 shows the X-ray diffraction patterns of (a) non-irradiated and (b) irradiated titanium, where the incident angle of X-ray α is 2° which corresponds to the maximum diffraction depth of 0.85 μm from the surface. The X-ray diffraction peaks of IPIB-irradiated titanium are broaden compared with that of non-irradiated titanium. The width of X-ray diffraction peaks are similar to that of amorphous phase. The width B of X-ray diffraction peak is dependent on the grain size d in Scherrer's formula :

$$d = \frac{0.9\lambda}{B\cos\theta_B} \qquad (3)$$

where λ is the wavelength of X-ray and θ_B is Bragg angle[10]. Substituting the present conditions to eq.(3), the grain size of IPIB non-irradiated titanium was calculated to be approximately 32 nm. On the other hand, the grain size of

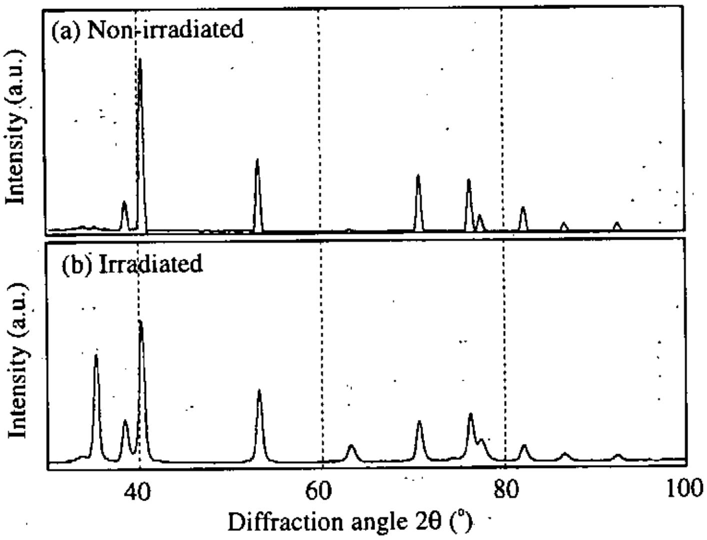

Fig. 9 X-ray diffraction patterns of (a) non-irradiated and (b) irradiated titanium.

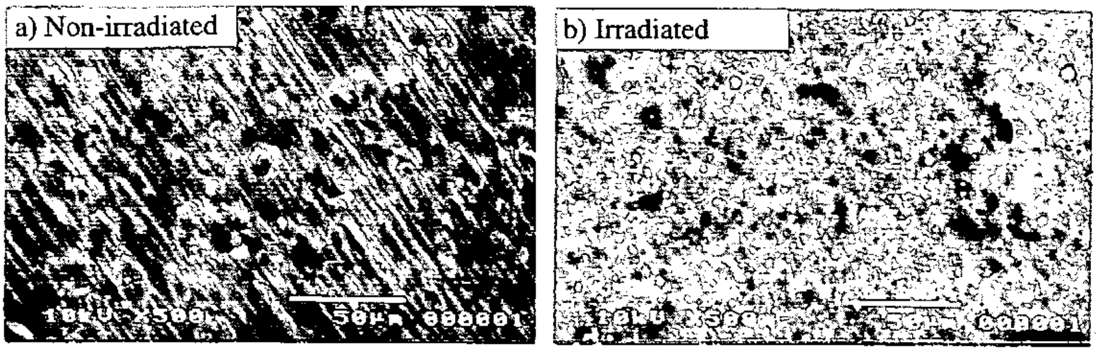

Fig.10 The topography of (a) non-irradiated and (b) irradiated titanium.

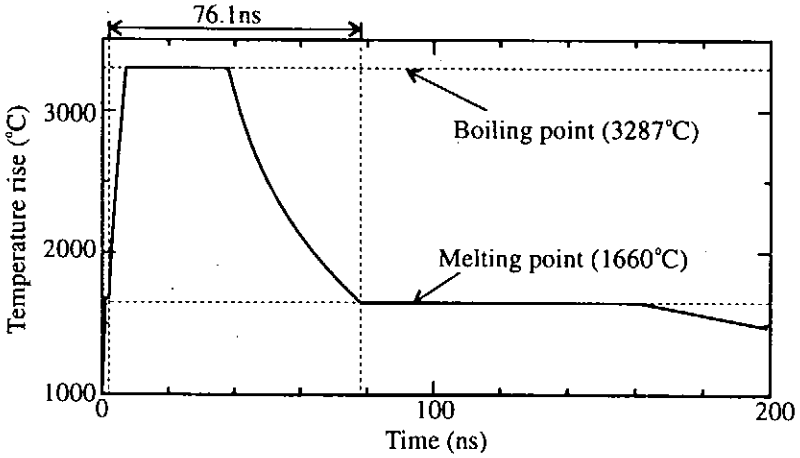

Fig. 11 Temperature rise of titanium surface for an irradiation of IPIB with the uniform power density of 34 MW/cm^2 and pulse width of 30 ns.

IPIB-irradiated titanium was calculated to be approximately 11 nm. These results demonstrate the formation of formation of nanostructured titanium surface by IPIB irradiation.

Figure 10 shows the topography of (a) non-irradiated and (b) irradiated titanium. In Fig.10(a), the machining roughness produced by polishing is found on the surface of the non-irradiated titanium. After IPIB irradiation, such roughness almost disappears as shown in Fig.10(b). From this fact result, it is possible to smooth the titanium surface by IPIB-irradiation.

Assuming the IPIB composes a single ion spice of carbon, we calculate the temperature rise of a target surface by IPIB-irradiation. The temperature rise of titanium surface by IPIB irradiation is also given by eqs.(1) and (2). Substituting the present parameters (p = 34 MW/cm^2 and τ = 30 ns) into eqs.(1) and (2), we obtain the time evolution of temperature rise on titanium surface as shown in Fig. 11, where the effect of the latent heat is considered. The titanium surface is heated to its boiling point of 3278 °C in a very short time of 2 ns. The holding time above the melting point is 76 ns in Fig.11, and might be enough to remove the machining roughness. After IPIB is turned off, the titanium surface is rapidly cooled by thermal diffusion, producing the nanostructured phase on the titanium surface.

4. Conclusion

A mixed carbon and fluorine IPIB with the power density of 34 MW/cm^2 and the pulse duration of 30 ns was irradiated to the target materials. The IPIB irradiation to $Ni_{65}Cr_{15}P_{16}B_4$ alloy results in amorphous structure on the surface within 0.66 μm in depth. The repeated irradiations of IPIB produce the amorphous phase in the deeper region from the surface. The IPIB irradiation heats the nickel surface up to its boling point of 2732 ℃. The cooling rate from the melting point to the glass transition point is estimated to be 2.2×10^9 ℃/s, which is sufficiently larger than the critical cooling rate for amorphous formation of nickel alloys. The IPIB irradiation to the titanium surface leads to the nanostructured phase on the titanium surface. After IPIB irradiation, the machining roughness on titanium surface is removed sufficiently.

Acknowledgment

A part of this work was supported by the Sasakawa Scientific Research Grant from the Japan Science Society.

References

1) Y.Shimotori, M.Yokoyama, S.Harada, H.Isobe, K.Masugata and K.Yatsui : J. Appl. Phys. **63**(1988)968.
2) K.Yatsui : Laser & Particle Beams, **7**(1989)733.
3) G.E.Remnev and V.A.Shulov : Laser & Particle Beams, **11**(1993)707.
4) E.L.Neau : IEEE Trans. on Plasma Science, **22**(1994)2.
5) M.Yatsuzuka, T.Yamasaki, H.Uchida and Y.Hashimoto: Appl. Phys. Lett., **67**(1995)206.
6) M.Yatsuzuka, T.Yamasaki, Y.Hashimoto and H.Uchida: Trans. I.J.E.E Jpn., **115A**(1995)1030 [in Japanese].
7) Y.Hashimoto, M.Sato, M.Yatsuzuka and S.Nobuhara : Jpn. J. Appl. Phys., **31**(1992)1922.
8) Y.Hashimoto, M.Yatsuzuka and S.Nobuhara : Jpn. J. Appl. Phys., **32**(1993)4838.
9) H.Yoshioka, K.Asami, A.Kawashima and K.Hashimoto: Corrosion Science, **27**(1987) 981.
10) B.D.Cullity: "*Elements of X-ray Diffraction*", (Addison-Wesley Pub.,1978) p.101.

Removal of NO_X by Pulsed Power

Tomohiro Takeshita, Shunsuke Tsukamoto*
Sunao Katsuki, Hidenori Akiyama

Department of Electrical Engineering and Computer Science, Kumamoto University, Kumamoto 860, JAPAN
*Department of Electrical Engineering, Ariake National College of Technology, Ohmuta 836, JAPAN

ABSTRACT

A corona streamer discharge system has been developed for the removal of NO_X from flue gas. The system consists of a Blumlein line generator and a discharge tube with coaxial geometry. A voltage pulse with a duration of 120 nsec and with an amplitude of 35 to 50 kV is used for the generation of streamer discharges. Trial gases for the pollution control experiment are composed of N_2, NO, O_2, and H_2O. The flow rate is 1.2 l/min. Preliminary results show a NO removal of 100% with a removal efficiency 250 μmol/Wh; 98% is removed with an efficiency of 300 μmol/Wh. The removal ratios of NO and NO_x are increased when H_2O molecules are added to the flue gas prior to the streamer discharge.

1. Introduction

Recent emission standards require that the amount of nitrogen oxides (NO_X) in flue gases, mainly emitted from fossil fueled electric power plants and automobiles, is reduced. Current systems can be catagorized as chemical or electrical NO_x removal systems. Chemical systems include wet scrubbing systems based on limestone, lime, and sodium carbonate, spray drying systems using alkali sorbents, as well as ammonia injection systems in combination with flue gas heaters. Electrical systems utilize e-beams, silient discharges, and corona streamer discharges.

Chemical systems have the advantages of low cost and reliable technology. Although electrical systems tend to be more expensive at the current state of development, they have the advantage of higher removal ratios. Moreover, most of the undesired NO_x is converted to N_2 and O_2, which require no special disposal. The corona streamer discharge system promises high removal ratios with a relatively high removal efficiency. Specifically, this system offers the following features:

- homogeneous discharges at atmospheric pressure,
- generation of electrons with energies of 10 eV or more which can dissociate NO_x molecules directly,
- streamer discharges can treat large volumes of flue gases, and
- applied energy mainly creates energetic electrons, with little energy wasted in heating ions and neutral gas molecules.

2. Experimental Apparatus

The schematic diagram of the experimental apparatus for the pollution control by pulsed power is shown in Fig. 1. The simulated gas, a mixture of NO, N_2, O_2, and H_2O is introduced into the discharge tube at room temperature. The NO concentration is 200 ppm, the O_2 concentration is 11%, the H_2O concentration is about 4%, and the flow rate of the simulated flue gas is 1.2 l/min.

Fig. 2 shows a schematic diagram of the Blumlein line generator, which is used as a pulsed voltage source. This Blumlein line generator consists of a trigatron switch and six coaxial transmission lines, each with a length of $l = 12$ m, and with a characteristic impedance of $Z_0 = 50$ ohm. Under matched conditions, this generator provides a square pulses with an amplitude equivalent to 3 times the charging voltage and with a duration of 120 nsec.

The discharge tube used in this experiment is shown in Fig. 3. The voltage pulse with a positive polarity is supplied to the inner electrode with a diameter of 1 mm, and the outer electrode with an inner diameter of 76 mm is grounded. The length of the tube is 500 mm. Current and voltage waveforms are measured by a Rogowski coil and a resistive voltage divider, respectively. The gases exiting in the discharge tube are analyzed by the gas analyzer.

3. Experimental Results and Discussion

Typical voltage and current waveforms during a corona streamer discharge are shown in Fig. 4. In this case, the charging voltage of the Blumlein line generator, V_{ch}, is 20 kV, resulting in a output voltage of about 36 kV at the discharge tube. Fig. 5 shows the open-shutter picture of the discharge. Homogeneous streamer discharges are observed clearly.

The removal ratios of NO and NO_X in a N_2+NO mixture are plotted versus the repetition rate of the applied voltage pulse in Fig. 6. For the maximum applied pulse repetition rate of 7 pps, the removal ratios of NO and NO_X are 68 % and 59 %, respectively. In these

In this case, three NO_2 molecules produce one additional NO molecule. Consequently, the removal ratio of NO_X is increased but the removal ratio of NO is decreased compared to the case with H_2O molecules in the streamer discharge. From these results it appears that the OH and HO_2 radicals are very helpful in the removal of NO.

In addition, the performance of the NO_x removal has been investigated for different electric field amplitudes in the discharge tube. A Blumlein line charging voltage of 15 kV and 25 kV resulted in an average applied electric field strength of 1 MV/m and 1.3 MV/m, respectively. Typical voltage and current waveforms during a corona streamer discharge with V_{ch} = 15 kV and 25 kV are shown in Figs. 11 and 12. Figs. 13 and 14 show the removal ratios of NO and NO_X for those cases. The trial gas is a N_2+NO+O_2+H_2O mixture. In the case of V_{ch} = 25 kV, a NO removal ratio of 100% is already achieved at a pulse repetition rate of 4 pps. The NO removal efficiency is given in Fig. 15. In general, the following trend is seen: applied voltage pulses with higher amplitudes lead to an increase of the NO and NO_x removal but, on the other hand, decreases the removal efficiency. Therefore, the voltage amplitudes should be adjusted according to the needed NO removal ratio in order to optimize the removal efficiency.

4. Conclusion

The performance of NO_X removal using corona streamer discharges has been evaluated. It seems that this is an attractive method, and it has a possibility to solve the problem of NO removal from flue gas. With the simple discharge tube used in this experiment, NO gas in a N_2+NO+O_2+H_2O mixture is removed to 100% with a removal efficiency 250 μmol/Wh, 98% is removed with an efficiency of 300 μmol/Wh. The measurements showed that H_2O molecules in the flue gas enhance the removal of NO_2 gas. Future works lie in the investigation of the effect of additives which could significantly increase the NO_X removal efficiency, and in the development of high repetitive, economical, light and compact pulsed power generators in order to realize the industrial applicability of this technique.

measurements, the concentration of NO_2 stays nearly constant, indicating that the NO gas does not convert to NO_2.

Fig. 7 shows the removal ratio of NO and NO_X in a N_2+NO+O_2 mixture. The removal ratio of NO increases up to 93 % and the removal ratio of NO_X decreases to -13 %. Since O_2 is included in the gas mixture, O radicals are produced. The plasma chemical reactions during/after a corona streamer discharge are written as:

$$NO + N \rightarrow N_2 + O \qquad (1)$$

$$NO + O + M \rightarrow NO_2 + M \qquad (2)$$

$$N + O + M \rightarrow NO + M \qquad (3)$$

where M is an inert molecule.

Fig. 8 shows the removal ratio in a N_2+NO+O_2+H_2O mixture. In this case, NO is totally removed, and the overall NO_X removal ratio increases significantly compared to the case without H_2O. With the addition of H_2O molecules, OH and HO_2 radicals are produced. They lead to the following plasma chemical reactions:

$$NO + HO_2 \rightarrow NO_2 + OH \qquad (4)$$

$$NO + OH \rightarrow HNO_2 \qquad (5)$$

$$OH + NO_2 + M \rightarrow HNO_3 + M \qquad (6)$$

$$HO_2 + NO_2 + M \rightarrow HO_2NO_2 + M \qquad (7)$$

From these reactions, NO_2 is converted to HNO_3, which increases the removal ratio of NO_X. This result indicates that H_2O plays an important role in the removal of NO_2. In order to further investigate the role of H_2O, the position of the water vessel has been changed as shown in Fig. 9. In Fig. 9 (a) the water vessel is placed prior to the discharge tube, Fig. 9 (b) shows the case where water is added to the flue gas after it has passed through the discharge tube. Fig. 10 shows the results of this experiment. In the case of (a), the plasma chemical reactions (4), (5), (6), and (7) most likely occur. Therefore, both the removal ratios of NO and NO_X are higher compared to the case without H_2O. In the case of (b), there are no H_2O molecules presents during the streamer discharge. Since no OH and HO_2 radicals are produced, the following chemical reaction is expected:

$$3NO_2 + H_2O \rightarrow 2HNO_3 + NO \qquad (8)$$

REFERENCES

[1] G. Dinelli, et. al., IEEE Trans. Ind. Appl., vol. 26, no. 3, pp. 535-541, 1990.

[2] J. S. Clements, et. al., IEEE Trans. Ind. Appl., vol. 25, no. 1, pp. 62-69, 1989.

[3] A. Mizuno, et. al., IEEE Trans. Ind. Appl., vol. IA-22, no. 3, pp. 516-522, 1986.

[4] S. Masuda, et. al., IEEE Trans. Ind. Appl., vol. 26, no. 2, pp. 374-383, 1990.

[5] R. P. Dahiya, et. al., IEEE Trans. Plasma Sci., vol. 21, no. 3, pp. 346-348, 1993.

[6] J. C. Person, et. al., Radiat. Phys. Chem., vol. 31, pp. 1-8, 1988.

[7] T. Ohkubo, et. al., IEEE Trans. Ind. Appl., vol. 30, no. 4, pp. 856-861, 1994.

[8] H. Akiyama, 1995 International Power Electronics Conf., pp. 1397-1400, 1995.

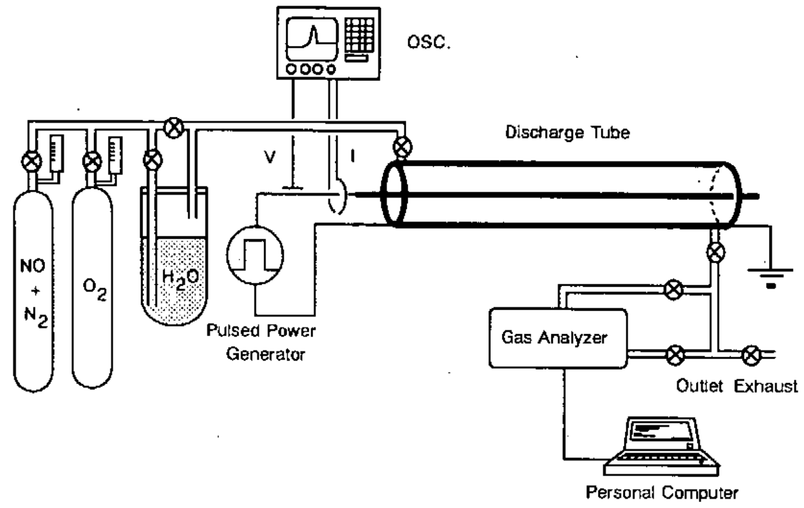

Fig. 1 Schematic diagram of experimental apparatus

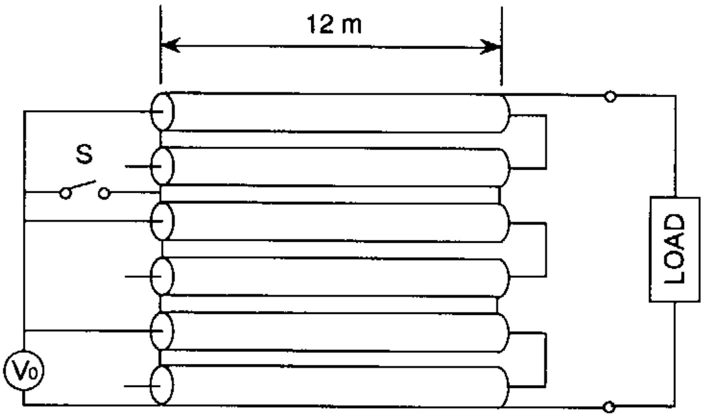

Fig. 2 Schematic diagram of Blumlein line generator

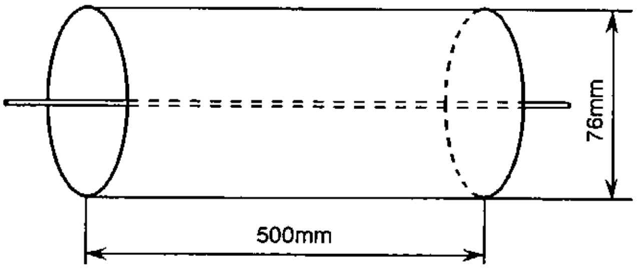

Fig. 3 Schematic diagram of the discharge tube

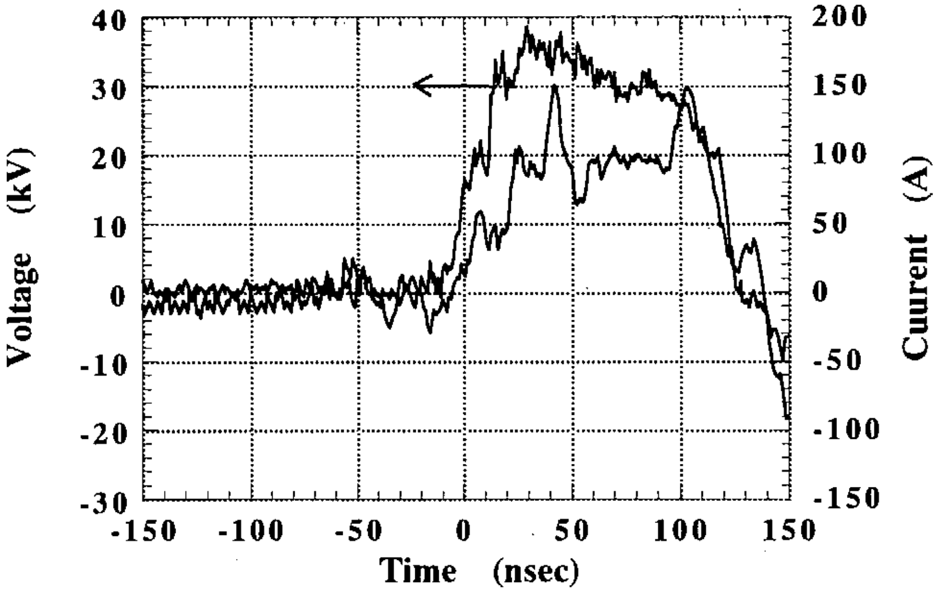

Fig. 4 waveforms of voltage and current

(V_{ch} = 20 kV)

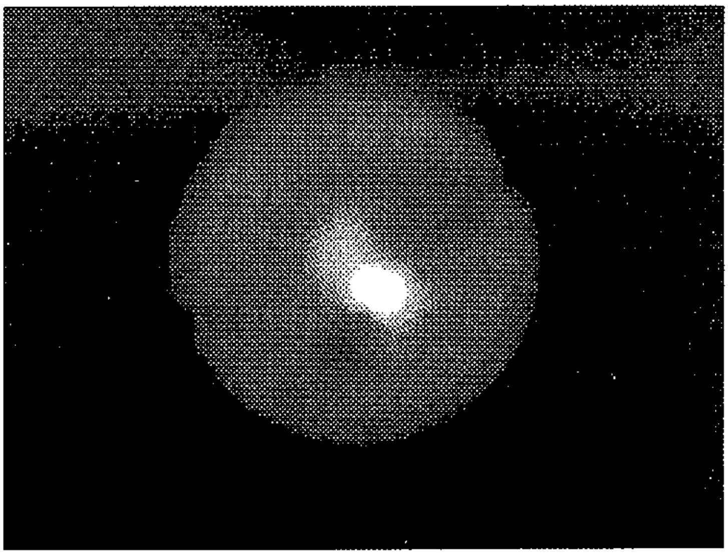

Fig. 5 Picture of the discharge

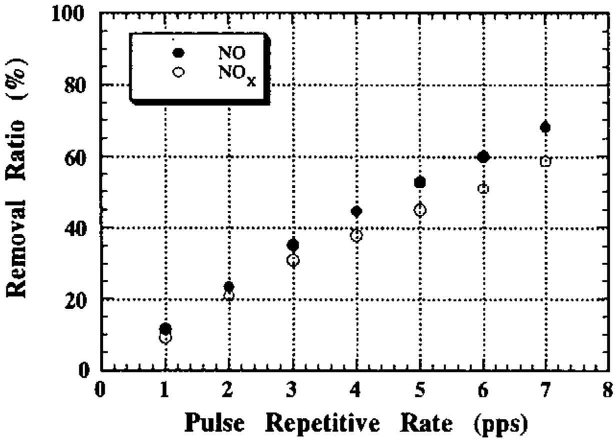

Fig. 6 Removal ratio of NO and NO_X in N_2+NO mixture

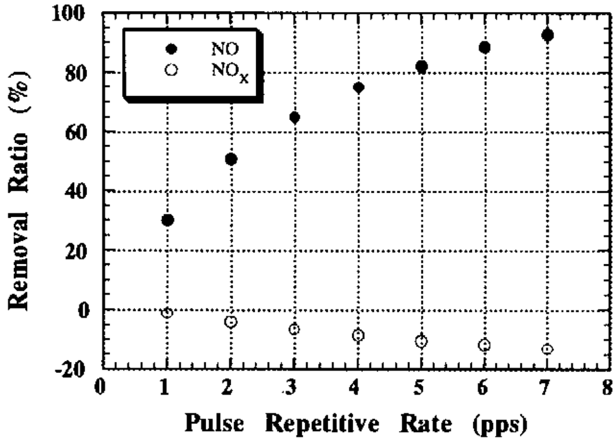

Fig. 7 Removal ratio of NO and NO_X in N_2+NO+O_2 mixture

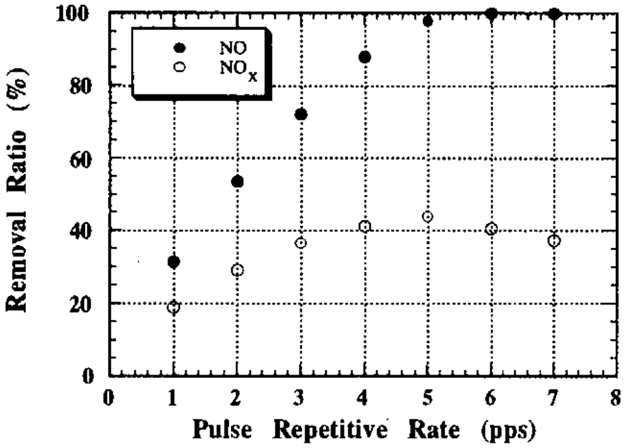

Fig. 8 Removal ratio of NO and NO_X in N_2+NO+O_2+H_2O mixture

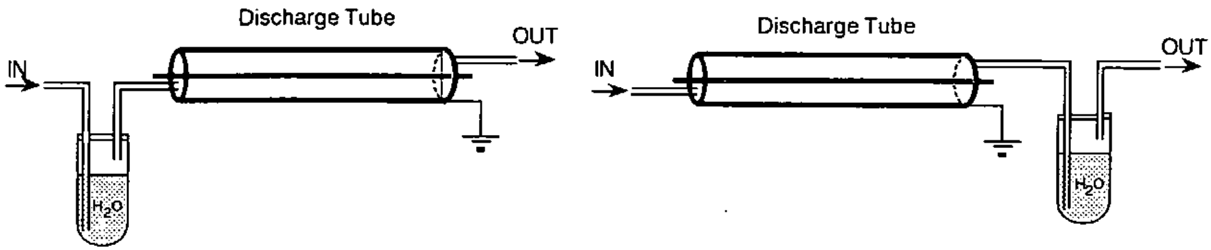

(a) (b)

Fig. 9 Position of the water vessel

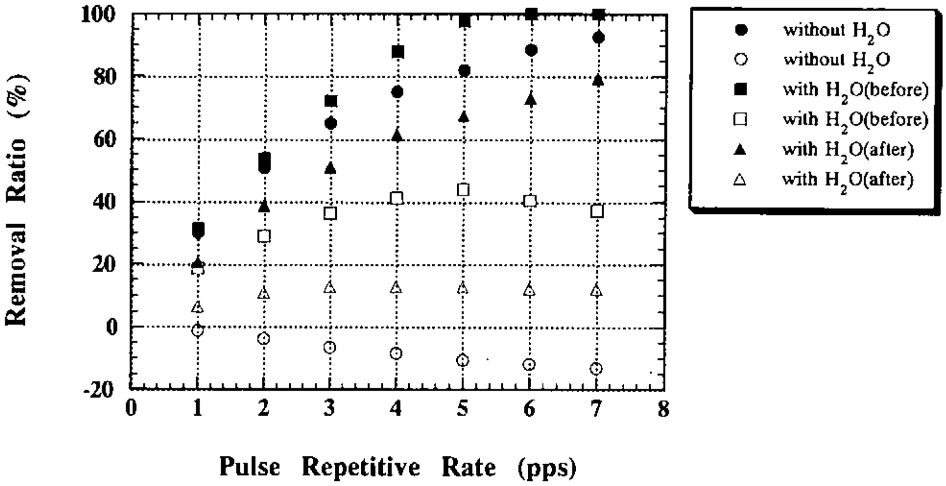

Fig. 10 Removal ratio of NO and NO_X changing the position of the water vessel

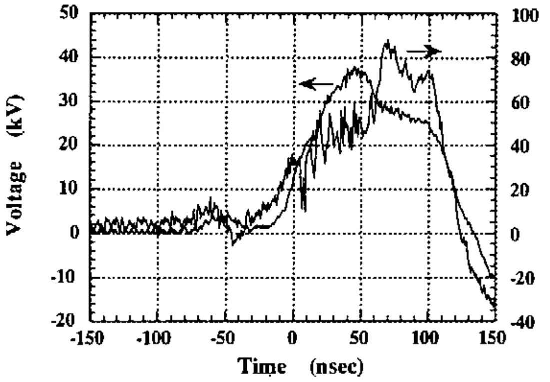

Fig. 11 Waveforms of voltage and current (V_{ch} = 15 kV)

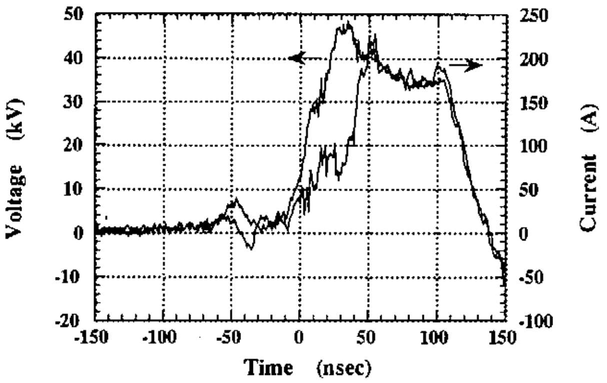

Fig. 12 Waveforms of voltage and current (V_{ch} = 25 kV)

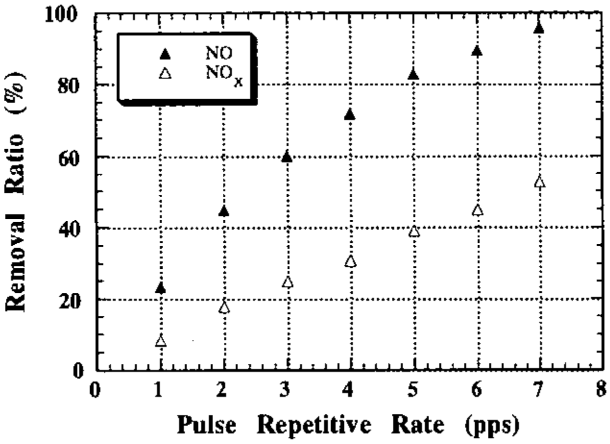

Fig. 13 Removal ratio of NO and NO_X
(V_{ch} = 15 kV)

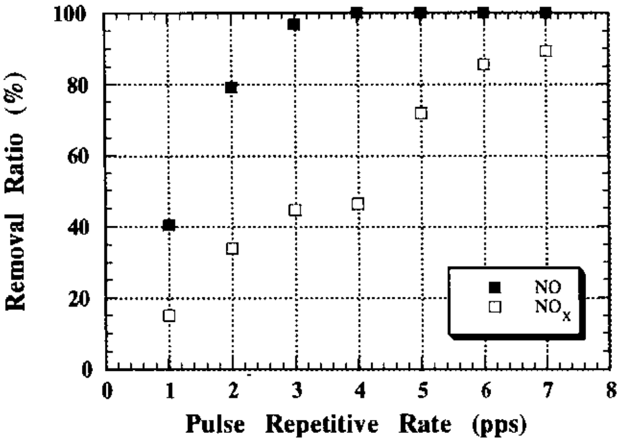

Fig. 14 Removal ratio of NO and NO_X
(V_{ch} = 25 kV)

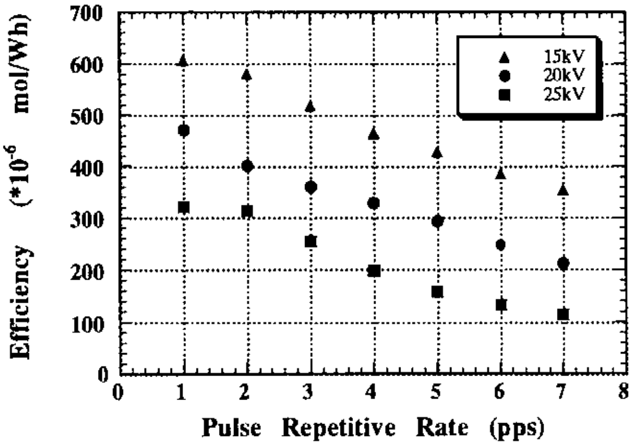

Fig. 15 Energy efficiency of NO removal

FUSION APPROACHES BASED ON SELF-MAGNETIC FIELD CONFINEMENT

T. Miyamoto

Atomic Energy Research Institute, Nihon University
Kanda-Surugadai, Chiyoda-ku, Tokyo

1. INTRODUCTION

It was realized in the early phases that the peaceful use of nuclear fusion energy must be based on thermonuclear reactions in hot plasma confined magnetically. Hot plasma has to satisfy the conditions of temperature T and the product nt – density n and sustaining time t, the so called Lawson conditions (1), which permit choosing either density or sustaining time, independently. The fusion reactor is restricted by several additional conditions. For example, the energy that passes through the reactor wall is limited to less than 1-10 MW/m^2 for conventional wall material, and the available confinement field strength is also limited to less than several 10 T when solenoid coils are used. Hence, it had been believed that the density had to be the order of 10^{20} – 10^{22} m^{-3} (depending on D-D or D-T fuels) in magnetic fusion where the use of solenoid coils had been assumed implicitly. The limitation on density was removed after the laser fusion approach appeared at the end of the 1960's. The additional conditions depend on the scheme of fusion approach. At present we can classify the fusion approach into three types, depending on the density (or the sustaining time) (2).

1) External magnetic confinement (Steady or Quasi-steady reactor)
   $n \sim 10^{20} - 10^{22}$ m^{-3}
2) Self magnetic confinement (Pulsed reactor)
   $n > 10^{26} - 10^{28}$ m^{-3}
3) Inertia confinement (Pulsed reactor)
   $n > 10^{31} - 10^{32}$ m^{-3}

Besides these three approaches we have to point out the wide density region where no fusion scenario exists :

$$10^{20} - 10^{22} < n < 10^{26} - 10^{28} \text{ m}^{-3} \quad .$$

As is well known, magnetic confinement (precisely, the external magnetic confinement) has been the main fusion approach since the early phase of fusion research. It is important to distinguish self magnetic field confinement from external magnetic fusion confinement. A magnetic field is used in both approaches. In the former, however, no solenoid coil are needed, so the magnetic field and density are not limited. As a result, the reactor concept is rather similar to the inertia confinement approach, thus differing essentially from the latter. The progress of pulsed power technologies has given new prospects for the self magnetic field confinement approach. The outline of fusion research and the typical methods and devices that have been investigated so far, are summarized in Fig.1.

2. FUSION RESEARCH BASED ON Z-PINCHES AND RELATED APPROACHES

2.1 First Period (searching period : before 1960)

We are able to classify the research into four periods. In the first period many methods were investigated to produce fusion plasma. The main trend was to investigate the steady or quasi-steady magnetic confinement fusion approach. The differences between external and self magnetic fusion mentioned in Sec.1 had not been realized yet, and inertia fusion had not yet appeared on the stage.

The simple Z-pinch gave a large amount of neutron yield. It was shown, however, that most neutrons were not generated in thermonuclear reactions, but in reactions with ions accelerated by instabilities. Hence, main efforts were devoted to stabilizing the simple Z-pinch plasma by axial magnetic and conductive shells (stabilizing Z-pinches). The conclusions obtained from these Z-pinches in this period are summarized as following :

i) The plasma column is highly unstable, and density is limited. As a result, the product nt is limited to less than 10^{18} m^{-3}.

ii) Several stabilizing methods decrease the nt-value in spite of the prolongation of life time, because of decreasing density.

iii) The emitted neutrons mostly originate from non-thermal reactions due to accelerated deuterium rather than from thermonuclear reactions.

Toroidal Z-pinch devices (for example, "Zeta") were also investigated for eliminating the end loss in the straight geometry. Afterwards, this trend developed to RFP (the reverse field pinch), and Tokamak in which a stronger toroidal magnetic field was applied to avoid the pinch of plasma.

2 . 2 Second Period (after the fusion approach based on a simple Z–pinch and its modification failed, and until early 1970s)

After the Z–pinch fusion approach failed, several pulsed systems were investigated :

(1) Theta pinch
(2) Plasma focus
(3) Liner compression

In this period a leading approach was theta pinches, because they were stabler than Z–pinches. Toroidal theta pinches (for example, the Scyllac project (3)) could not, however, achieve the aim due to instabilities. The pulsed approach had not yet been established distinguishing it from the steady one as well as the first period. The theta pinch plasma was confined by an external field produced by solenoid coils, and so has an upper limit in its density. From this point of view, the theta pinch was a pulsed device that needed higher density, and thus had a disadvantage in comparison with other steady devices.

In this period the focusing of plasma was also discovered in vicinity of the inner electrode in a coaxial plasma gun geometry (4) . This plasma focus gave a large yield of neutrons. It was shown that the scaling of neutron yield to the bank energy existed under the optimized conditions of each focus device (5) . It was expected that the plasma focus device might produce the fusion plasma, if this scaling holds in large bank energy. An inertia fusion (i.e. a laser fusion) approach also appeared at the end of this period.

2 . 3 Third Period (after the Scyllac project was shut down)

The laser implosive fusion approach had been established. It was recognized that the pulsed fusion approach must aim at a completely different regime and be based on a standpoint different from those of the steady fusion approach in the early phase of this period. In the pulsed approach a high density was generally required because of the short sustaining time. Hence, the pulsed approaches can not be materialized on the basis of the external magnetic field produced by coils, but only the self magnetic field. The pulsed systems using a solenoid coil such as theta pinches are essentially within the framework of the steady fusion approach. A profound gap exists between the fusion approach based on the self magnetic field and that based on the external field, as shown in Sec. 1.

After the Scyllac project was shut down, many approaches were proposed. Except for the proposals related to the theta pinch, those based on self magnetic confinement were

(1) Dense, slender Z-pinches (the target is clear and simple)
(2) Fast liner compression
(3) Plasma focus.

In this period a leading approach was to produce a dense slender pinched plasma column by a laser initiated, gas-embedded Z-pinch, a capillary Z-pinch and a fiber Z-pinch. The results for these Z-pinches has been compiled. On the other hand, the plasma focus experiments were carried out using the capacitor bank up to 1 MJ. The neutron yield did not, however, satisfy the scaling law to the bank energy, but that to the current flowed into the pinch plasma channel. That is, the leakage current increases with the bank energy. The fast liner compression experiments were proposed, but were not examined experimentally.

2.4 Fourth Period (up to present)

The dense slender Z-pinch experiments seem to be facing several difficulties at present, as described in Sec.3. They will have to be reexamined. The pulsed fusion approaches based on the self magnetic field are in the investigating phase again. The candidates are still :

(1) Dense, slender Z-pinches
(2) Fast liner compressions
(3) Plasma focus

In all the approaches, however, new ideas and methods are required for further developments.

3. DENSE Z-PINCHES

3.1 Fusion Criterion by Dense, Slender Z-Pinches

The pressure balance of current-curring pinch plasma is given by the Bennett condition

$$\mu_0 I^2 = 16\pi NT \qquad (1)$$

The steady state is established in the Z-pinches only when the energy balance is satisfied. In an isolated Z-pinch the energy losses result from radiations, especially the Bremsstrahlung radiation in fully ionized, hot plasma, which has to be equal to the joule heating. This energy and the pressure balance relations give the result that the steady state is established at a constant current, the so called Pease-Braginskii current

$$I = I_{PB} \approx 1.4 \times 10^6 \text{ (A)} \qquad (2)$$

The corresponding internal energy per unit length is given as

$$NT = \frac{\mu_0 I_{PB}{}^2}{16\pi} \approx 5 \times 10^4 \quad (\text{J}/\text{m}) \qquad (3)$$

Hence, the line density and the radius for temperature $T_f = 5 \times 10^4$ K and density $n_{solid} = 10^{28}$ m^{-3} reduces to

$$N = \pi r_p{}^2 n = \frac{\mu_0 I_{PB}{}^2}{16\pi T_{fusion}} \approx 7 \times 10^{18} \text{ (m}^{-1}\text{)}$$

$$r_p = \frac{N}{\pi n_{solid}} \approx 15 \times 10^{-6} \text{ (m)}$$

The sustaining time corresponding to the solid density has to be $t > 10^{-8}$ s. The length of plasma is determined by the axial energy loss and have to be more than about 0.1 m. This scheme is attractive, because a fusion reactor will be remarkably compact. At the same time we notice that the scheme requires a very fast rising current, that is, very high voltage (more than MV). If not so, the discharge reduces to a conventional wire-explosion.

3 . 2 Problems in Dense Slender Z-pinch

So far several types of fusion oriented experiments have been carried out using high voltage pulse power devices, and the important results are summarized in the following.

(1) Laser initiated, gas-embedded Z-Pinch

The pinch discharge was fired along a weakly ionized plasma channel generated by irradiating an intensive laser beam (8) . The pinched plasma column was accompanied with irreguralities due to instabilities. However, their growth rate was not so high, and the current flowed along the plasma column throughout the discharge. This experiment showed that a pinch plasma column with a density exceeding 10^{26} m^{-3} was produced. It was difficult to produce such a dense plasma column by means of a conventional dynamic pinch. In addition, the gas-embedded Z-pinch has several features that it makes repeated discharges easy, and that a unique reactor concept similar to a light water fission reactor is possible (9). However, the produced plasma column expanded rapidly, because the surrounding gas flowed into the column. This accretion meant that it was difficult to sustain a slender dense plasma channel for the required period in a gas atmosphere.

(2) Fiber Z-pinch

To avoid the accretion in the gas-embedded Z-pinch the fiber Z-pinches hve been investigated by many authors. In the experiment using a D_2 fiber, neutron emissions which resulted from instabilities were not observed during the current rising phase. So it was stressed that no MHD instability grew during the current rising phase (10). However, this result has not been confirmed.

Recently, it have been shown that as the m=0 instability developed, the current was almost completely displaced from the constriction to the periphery of the pinch (11). It was also reported that the growth rate of m=0 mode was high enough in the polyethylene fiber Z-pinch with a diameter 15 μm. The experimental results show the radial ejection of plasma by m=0 cusps, the transition of current from the pinch column to the outside of the column and the contraction of the outside plasma. As a result of these processes, the ions were turbulently heated, and the plasma radius was determined by this heating (12). These experimental results seem to be opposite to the fusion scenario described in Sec.3.1.

(3) Instabilities and Stabilizing effects

So far many authors have reported that the experimental growth rate of instabilities was slower than that predicted by the ideal MHD theory except for the above mentioned results. It was also pointed out that there were wide regions in which non-ideal MHD theory was required (13). Hence, several effects neglected in the ideal MHD theory (for example, finite Larmor radius effects, large Larmor radius effects, viscosity, etc.) were examined. These theoretical investigations were carried out only near the ideal MHD plasma, and were failed to obtain drastic stabilizing effects so far.

4. PLASMA FOCUS

4.1 Target and Difficulties of Plasma Focus

It was suggested that the neutron yield was proportional to $E^{2.1}$ in plasma focus devices using a small capacitor bank of energy E under conditions optimized in each device (6). If this scaling holds true for higher bank energy, the fusion reactor can be realized in a scaled-up focus device. Unfortunately, large scale focus experiments failed to prove the scaling on the discharge energy. In the plasma focus devices the scaling law holds rather on the plasma current, which does not increase with the discharge energy, because the current is excluded from the constricted column.

4.2 Problems of Plasma Focus as the Fusion Approach

Plasma focus is characterized as kind of dynamic Z-pinches accompanying the radiation collapse (14). The focus device is also considered as an impedance convertor, which gives a fast rising high current at the final pinch phase. In spite of these special features, it is questionable whether the plasma focus can be revived as a fusion approach. The impedance of pinched plasma becomes higher with stronger pinch. The higher impedance tends to increase the leakage of current through several mechanisums (15). The future of the plasma focus depends on whether the leakage current which increases with the discharge energy is intrinsic in the plasma focus device. It is necessary to find out methods to diminish the current leaking from the plasma column in large scale focus devices to overcome this tendency. The role of radiation collapse in the plasma focus device and theoretical explanations to the scaling law obtained experimentally will be important subjects to study.

5. Liner Compression

5.1 Classification of Liner Compression

The liner compression is classified as the following, depending on the imploding speed of liner (16).

(1) Passive liner (zero implosion speed)

Wall confinement of a magnetically confined plasma

(2) Slow liner (the imploding speed $v = 10^2 - 10^3$ m/s)

Most liner compression experiments fall into this category of liner. For example, this liner speed has been used for generating high magnetic fields and for compressing a magnetically confined plasma. We need well confined plasma to produce a hot plasma by the liner with this speed. It is difficult to obtain fusion plasma. This type of liner compression is essentially pulsive, but could be classified to the external magnetic confinement approach as well as theta pinches.

(3) Fast liner ($v = 10^3 - 10^5$ m/s)

Hot plasma is produced by compressing wall-confined plasma when it is insulated thermally by magnetic field.

(4) Extremely fast liner ($v = 10^6$ m/s)

A magnetic field is not necessary required for this liner speed, which is corresponding to about 10 keV for D. A dense plasma compressed directly by a wall can be fusion plasma.

5 . 2 Fast Liner Compression

In the beginning of the third period, several experiments on fast liner compression were proposed just after the theta pinch approaches were shut down (16) (17) . These early proposals were based on rapidly compressing plasma confined magnetically of several 10^6 degrees and several 10^{18} m^{-3} in density. The compression ratio of 50 – 10^2 can give a plasma of several 100 million degrees and 10^{26} m^{-3}, if this initial plasma is produced in the magnetic field with the order of several Tesler. The difficult problem in this approach is to produce such a dense, hot, initial plasma. For this reason the proposal was not investigated experimentally.

Recently, several attempts on the fast liner were proposed (18) (19) . One of them related to methods of how to produce the initial plasma. The fast liner approach will be revived, if this problem is solved. The generation of extermely high liner speed is an interesting subject.

6. CONCLUDING REMARKS

The fiber Z-pinch was a leading approach in the last decade, and its scenario for fusion was quite simple, if the plasma column was stable for the short period required. However, it is not still possible to keep the dense plasma stable for the necessary sustaining time. Both fiber Z-pinch and plasma focus seem to meet similar difficulties, that is, the plasma impedance increases extremely with a strong pinch. History progresses like climbing a spiral staircase. Now we may stand at the new period to search for and examine new methods based on the self magnetic fusion approach.

We did not examine the pulsed approaches in the view of reactor feasibility. It will naturally be difficult to construct a pulsed reactor borrowing the concepts of the steady reactor. It is important to create reactor technologies appropriate to the pulsed approach. We can point out the wetted wall, the liquid wall and the reactor concept similar to light water fission reactor as these examples.

References

(1) J.D.Lawson, Proc.Phys.Soc. B70(1957)1−5.
(2) T. Miyamoto, Pulse Power Tech. and Fusion, Symp. on Plasma Prod. and Its Appl. Pulsed Power Tech. (S1) (in Japanese,1990 Nat. Convention Record I.E.E Japan) pp.15−18 (1990).
(3) S.Burnett, et al. LA−5121−MS(1972);F.Ribe et al., LA−UA−73−1780 (1974)
(4) N.V.Filippov,T.I.Filippova and V.P.Vinogradov, Nucl. Fusion, Suppl.Pt.2, (1962)577 ; J.W.Mather, Phys. Fluids 8 (1965)366.
(5) L.Michel, K.H.Schonbach and H.Fisher, Appl.Phys.Lett., 24 (1974)57 .
(6) O.Zucker, W.Bostick et al., Nucl. Instrum. & Methods, 145 (1977)185.
(7) H.Krompholz et al., Phys.Rev.Lett. 82A (1981)82.
(8) J.E.Hammel, D.W.Scudder and J.S.Schlachter, Nucl. Instrum.& Meth. 207(1983)161.
(9) H.R.Bolton, P.Choi, et al., Nucl. Fusion Suppl. Vol.3(1987)367.
(10) J.D.Sethian A.E.Robson, K.A.Gerber and A.W.Desilva, Phys. Rev. Lett. 59(1987)892.
(11) G.S.Sarkisov and A.S.Shikanov, ZETP 108 (1995) 1355.
(12) R. Relay et.al., To be published in Phys.of Plasma.
(13) M.G.Haines and M.Coppins, Phys.Rev.Lett. 66(1991)1462.
(14) J.W.Shearer, Phys.Fluid 19(1976)1426.
(15) R.E.Terry and N.R.Pereira, Phys.Fluids B3(1991)195.
(16) A.R.Sherwood et al., "Fast Liner Proposal", LA−6707−P (1977) .
(17) Yu.B.Khariton et al., Sov.Phy.Usp. 19, 1032(1976) : V.N.Mokhov et al., Sov.Phys.Dokl. 24, 557(1979).
(18) J.H.Degnan et al., Phys.Rev.Lett. 74, 98(1995).
(19) I.R.Lindemuth et al., Phys.Rev.Lett. 75, 1953(1995).

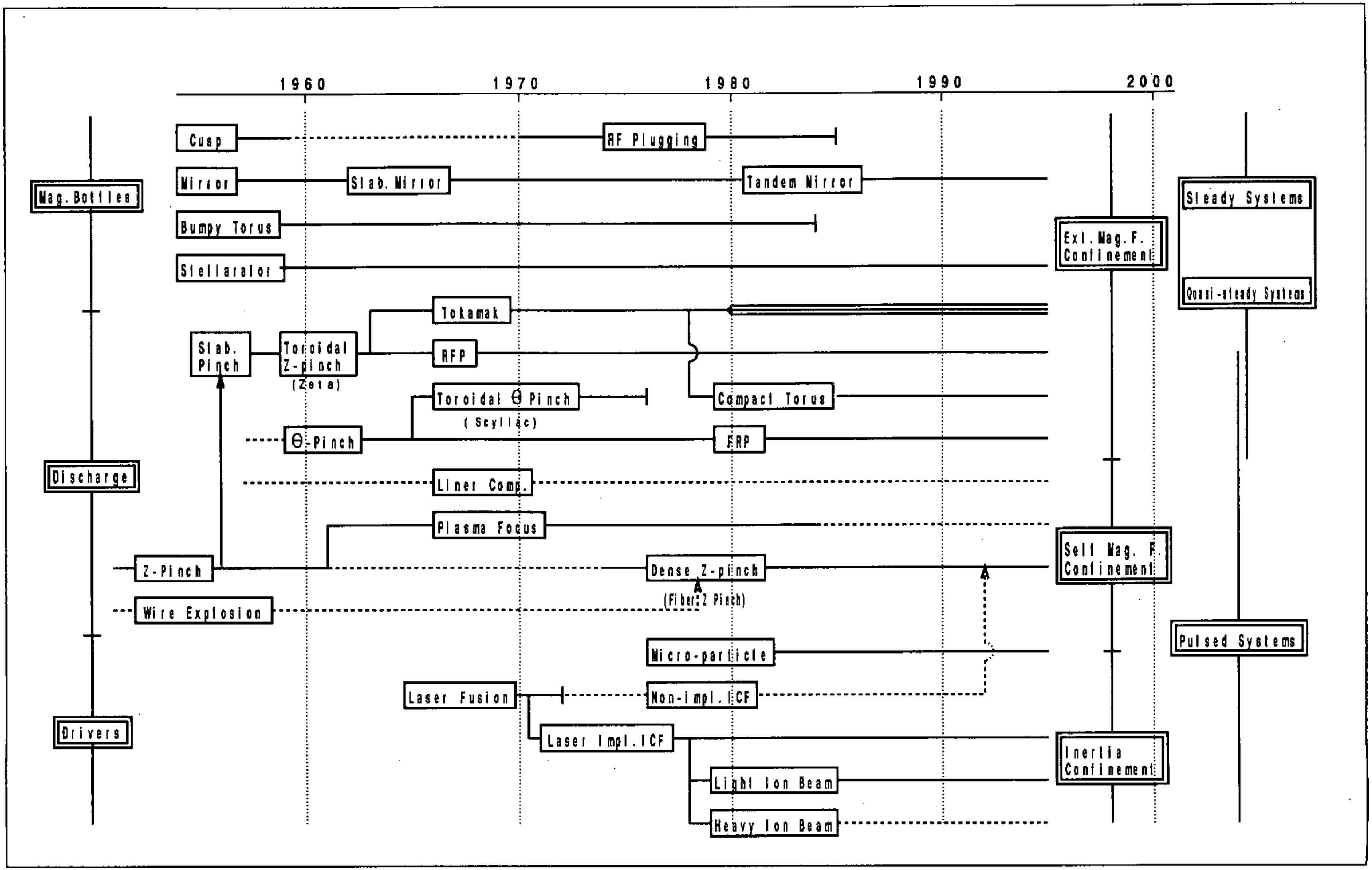

Fig.1 History of Fusion Approaches & Devices

Measurement of Beam Energy of Spherical Plasma Focus Diode and Its PIC Code Simulations

Kazuo Imanari, Kozue Sasaki, Weihua Jiang,
Katsumi Masugata, and Kiyoshi Yatsui

Laboratory of Beam Technology and Department of Electrical Engineering,
Nagaoka University of Technology, Nagaoka, Niigata 940-21

Abstract

We have evaluated dynamic characteristics of spherical plasma focus diode (SPFD) by experiments and simulations. Using a caloriemeter, there was a peak of 84 J/cm^2 on z-axis of an intense, pulsed, light-ion beam energy density. To evaluate the species and energy, Thomson parabola energy spectrometer measurement was carried out. To obtain beam flux, new types of electrodes were used; grooveless high flux anode and highly transparent, webbed cathode. We found that the protonic ratio, defined by the ratio of protons over heavy ions (C^+, C^{++}, O^+, and O^{++}), is 8.2. The energy of protons, which had a peak at 300 keV, distributed in the range of 230 ~ 600 keV. In PIC code simulations, we proposed initial thermal energy model to express the local divergence of LIB. We assumed that the initial thermal energy models takes half vector space. The vector had a constant magnitude and random direction. When the initial energy is 20 eV, the ion beam focused in a cylindrical area of 0.4 mm$^\phi$ × 2.4 mm. This focusing size was much tighter than the experimental results (6.0 mm$^\phi$ × 4.5 mm) measured by time-integrated backward Rutherford scattering pinhole camera. Above 20 eV, simulation results gave better focusing. The local divergence , however, could not be expressed by the above models.

1. Introduction

In practical applications, tight focusing an intense pulsed light ion beam (LIB) within a small area is very important to achieve high power density. In most cases, the LIB has been focused geometrically, where both the anode and the cathode of the ion diodes are shaped in concave. However, the solid angle of the spherical diode is strongly limited since a magnetic field is transversely applied in the anode-cathode gap to prevent electron flow. To obtain large solid angle, we have proposed a new type of self-magnetically insulated vacuum ion beam diode, spherical plasma focus diode (SPFD) [1 - 4].

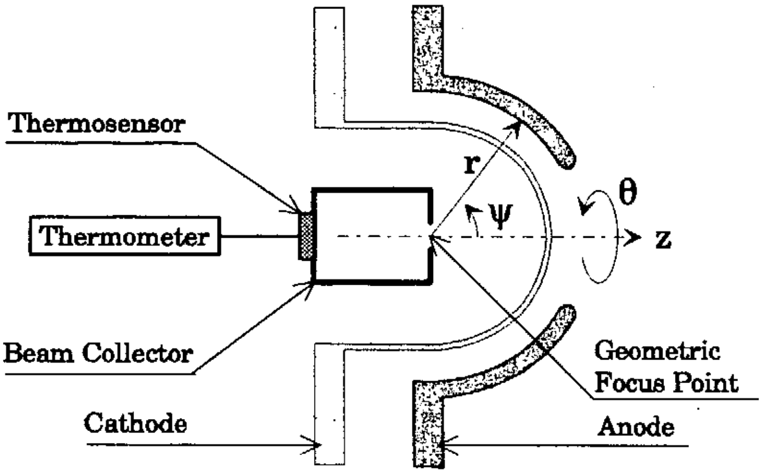

Fig. 1 Schematic of SPFD together with caloriemeter.

The SPFD is three-dimensionally focused, self-magnetically insulated diode. It consists of two concentric spherical electrodes, anode and cathode, as shown in Figure 1. The anode has grooves filled with epoxy for the ion source. The solid angle covered is 0 - 2π and π/6 - π/2 in the θ and ϕ directions, respectively. The cathode have many drilled holes (1 mm diameter) and has a transparency of ~5 %. It has been designed so that the LIB extracted from the anode plasma tends to focus on the same geometric focusing point as the center of the electrodes. The features of the SPFD are summarized as 1) very simple and compact structure (we do not need external magnetic field coils), 2) large solid angle of focusing, and 3) axial symmetry.

2. Experimental setup

Using a calorie meter, we evaluated the LIB energy density. Figure 1 shows the experimental setup. Cylindrical beam collector (inner cup size : 20 mm^{ϕ} × 20 mm) is made of brass with the weight of 87.26 g. To collimate the incident LIB, a copper aperture plate (1 mm^{t}) was arranged in front of the collector. Supporting parts are made of polypropylene to prevent thermal conduction. A thermistor sensor is bolted onto the end of the collector, and is connected with a digital thermometer. Resolution of the digital thermometer is 0.01 degree, which corresponds to 0.35 J.

To analyze ion species and its energy, Thomson parabola energy spectrometer (TPES) measurement was carried out. Figure 2 shows the arrangement of TPES. The TPES was placed on ϕ = 40 degree axis in the diode chamber. Direct measurement was available without any scatterer. To obtain beam flux, new type of electrodes was used; highly transparent webbed cathode and grooveless anode. The cathode was made of 0.1 mm$^{\phi}$ copper wire, and has 95 % beam transparency. There were no grooves on the anode, on which a mixture of nitro-cellulose and alkyd resin was sprayed (~10 μm thick) as an ion source.

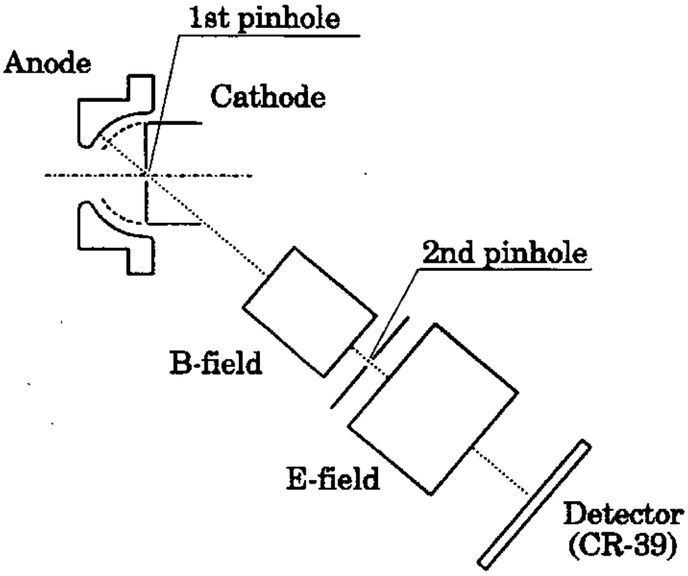

Fig. 2 Arrangement of Thomson parabola energy spectrometer.

3. Experimental results and discussions

The SPFD was operated on the pulse power generator, "ETIGO-II" [5]. Figure 3 shows typical waveforms of the inductively calibrated diode voltage (V_d), diode current (I_d) and diode impedance (Z_d). The diode impedance is 6.8 Ω in the high voltage region, being good impedance matching with output impedance (6.5 Ω) of ETIGO-II.

Figure 4 shows the LIB energy density measured by the calorimeter on the z-axis. The circles show the averaged value of two shots, where an error bar is less than 10 %. Figure 4 (a) shows the dependence of aperture diameter on the energy. The aperture was placed at z = 0 mm of the geometric focus point. We may evaluate the incident ion beam diameter to be ~ 3 mm. Hereafter, the aperture diameter of 3 mm$^{\phi}$ was used. Figure 4 (b) shows the energy density profile along the z-axis. The beam energy density has the peak of 84 J/cm^2 at z = 1 mm.

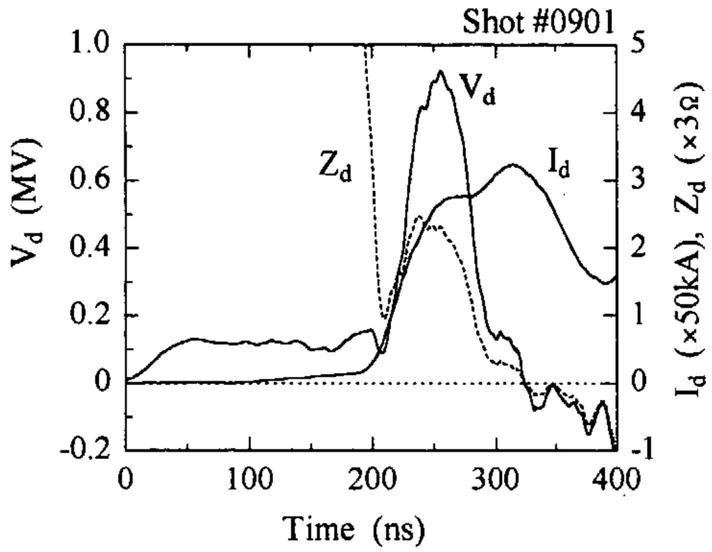

Fig. 3 Typical waveforms of inductively-calibrated diode voltage (*V_d*), diode current (*I_d*), and diode impedance (*Z_d*).

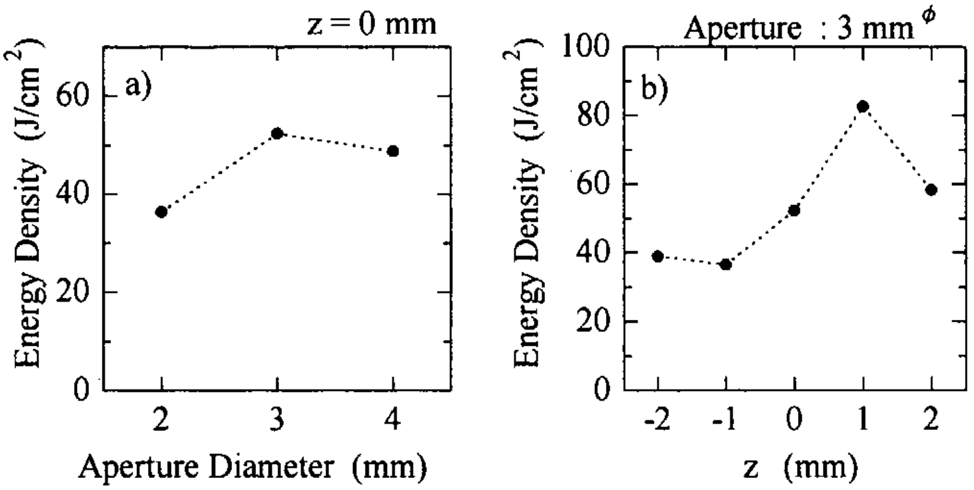

Fig. 4 Energy density a) as a function of aperture diameter at z=0, and b) distribution along the z-axis with the aperture 3 mm$^\phi$.

Figure 5 shows the result obtained by TPES measurement. Heavy ion contains C^+, C^{++}, O^+ and O^{++} ions. We see the protonic ratio defined by the protons over the heavy ions is about 8.2. The energy of protons, which had a peak at 300 keV, distributed in the range of 230 ~ 600 keV. The protons are produced at a later stage of the pulse where the diode voltage starts to drop.

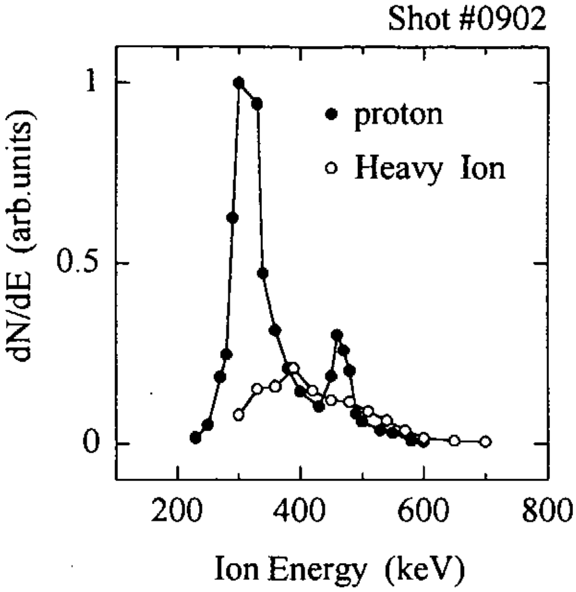

Fig. 5 Energy distribution of protons and heavy ions (C^+, C^{++}, O^+, and O^{++}).

4. Two-dimensional PIC code with initial thermal energy model

Utilizing a time-integrated backward Rutherford scattering pinhole camera with CR-39 track detector, we have evaluated the focusing size of the beam. The LIB was focused radically within 4.5 mm (FWHM) in diameter. Axially, on the other hand, we found 6.0 mm (FWHM) in the z direction, which deviates 2.5 mm downstream from the geometric focusing point [6]. Since the averaged deflection angle measured by shadow box is only 1 ~ 7 degrees in the elevation angle of ϕ and 1 ~ 2 degrees in the rotation angle of ϕ [2, 3], it is considered that the LIB seems to have considerably large local divergence. The local divergence will be induced by initial thermal energy of ions, nonuniformity of anode plasma, and plasma expansion to the acceleration gap. To evaluate the contribution of the initial thermal energy on the local divergence, we proposed initial thermal energy model on PIC code simulation.

Considering rotationally symmetric structure of the SPFD, we have designed and developed particle in cell (PIC) code in two-dimensional coordinate. The uniform mesh is square with the size of 0.2 mm. The code contains Maxwell's equations and relativistic particle kinematics. Electric- and magnetic-field strength, and simulation particles' position and velocities are calculated once in every computational time step of 0.3 ps. The simulation particles are used to simulate the electron and proton flows and provide self-consistent sources for the field equations. Electrons kinetic motion are treated as relativistic, while not for protons.

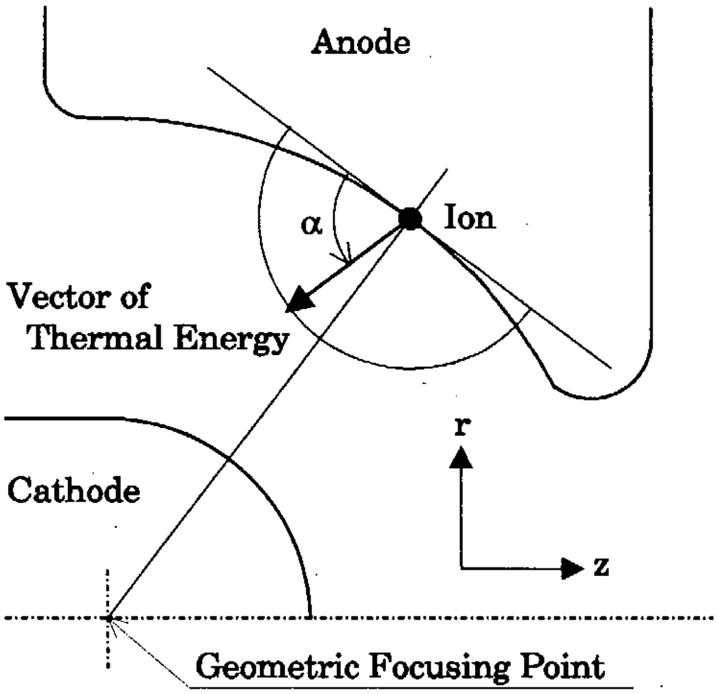

Fig. 6 Model of initial thermal energy assigned.

Figure 6 shows the initial thermal energy model. We considered the half vector space. Its boundary is decided by a tangent line of circle having a radius with distance from the position of the particles toward the geometric focusing point. After some computational steps, the initial thermal energy is given to protons. Otherwise, many protons will disappear by the collisions with the anode surface. In the initial thermal energy, some probability function should be taken into account. Here, we assume a constant magnitude of the energy vector. The direction of the vector is given by considering uniform random probability.

The simulation model is different from the experimental configuration of the SPFD from the following aspects.

1) There are many grooves in the actual anode, whereas no grooves in the simulations. The anode is treated as a surface ion source. Protons are produced from all the active area of the anode surface.

2) The actual cathode is transparent due to the presence of a lot of drilled holes, while the simulated cathode is fully transparency. The ions come from all active ϕ direction.

3) The simulation is PIC code. The feature of plasma as a fluid is not considered, and hence we do not take plasma expansion phenomenon into account.

5. Simulation results and discussions

Figure 7 shows the typical waveforms of diode voltage (V_d) and current (I_d). Their peaks are $V_d \sim 940$ kV and $I_d \sim 160$ kA, respectively, resulting in the diode impedance to be 5.9 Ω. These parameters are well matched with those of the experiments.

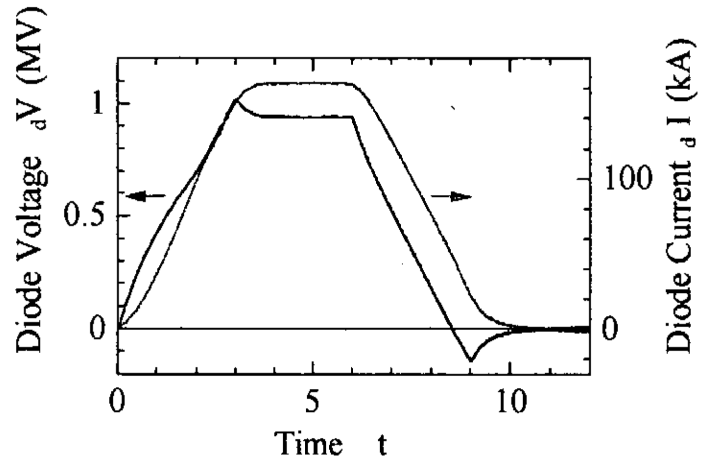

Fig. 7 Simulation waveforms of diode voltage (V_d) and diode current (I_d) with 20-eV initial thermal energy.

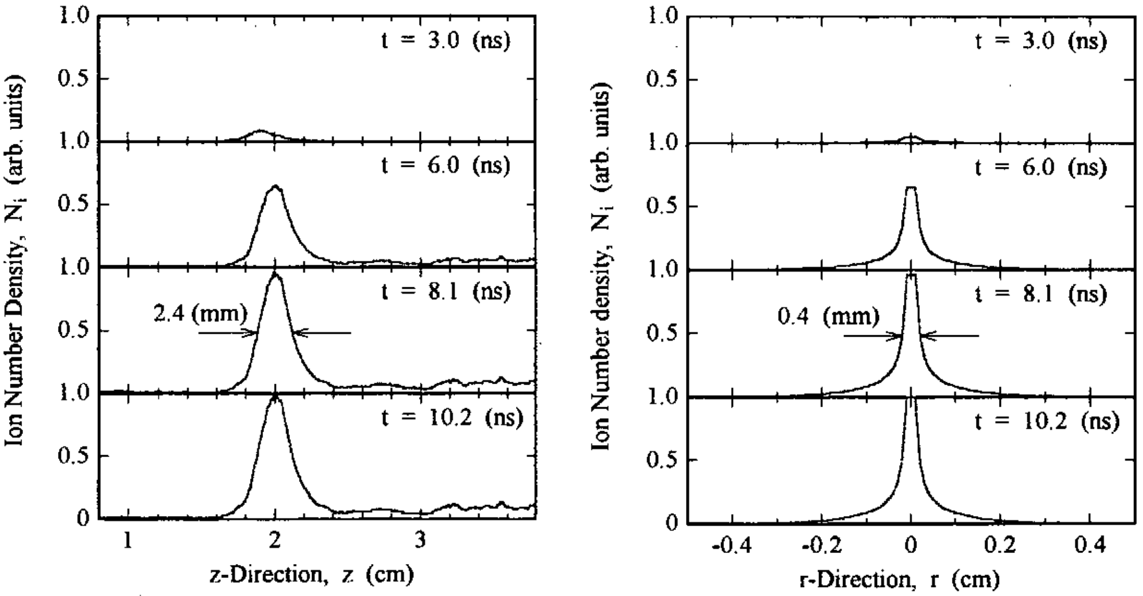

Fig. 8 Simulation results of ion-number density distribution along z-axis at various timing.

Fig. 9 Simulation results of ion-number density distribution in r direction at z = 2.0 mm.

Figure 8 shows the typical particle distribution along the z-axis, associated with Fig. 7. The point of z = 0 corresponds to the geometric focus point. The initial thermal energy is 20 eV. At t = 8.1 ns, the proton beam is focused within 2.4 mm (FWHM) in the z direction. The best focus point takes place at z = 2.0 mm, being in good agreement with the experimental data of z = 2.5 mm.

Figure 9 shows the particle distribution in the r direction, at z = 2.0 mm corresponded to the best focusing point in Fig. 8. This profiles have been estimated from the trajectories of protons in r-z plane, since the code does not calculate the component in the θ direction. At t = 8.1 ns, we have achieved tight focusing of the proton beam: it is focused within 0.4 mm (FWHM) in the r direction. From the comparison of Figs. 8 and 9, we find that the LIB is focused in a cylindrical area, which is consistent with the experimental results.

Table 1 shows the comparison of the experiment and simulations on the focusing area. As mentioned above, the simulation results of the diameter have been estimated from the trajectories of protons in the r-z plane. Furthermore, the simulation result does not include defocusing effects due to divergence as well as deviation in the r direction. Therefore, the above simulation results seem to be considerably smaller than the experimental data. The simulation results of the axial length of the focusing also show better focusing than experiment.

Table 1 Comparison of experiment and simulation.

Results	**Initial Energy (eV)**	**Diode Voltage (kV)**	**Diode Current (kA)**	**Focusing size (mm)**		
				z-Deviation	**Length**	**Diameter**
Experiment	----	935	165	2.5	4.5	6.0
Simulations	0	948	162	1.6	3.0	0.4
	10	938	164	1.8	2.5	0.4
	20	939	164	2.0	2.4	0.4
	100	937	164	2.0	2.2	0.4

Figure 10 shows the comparison of the particle distribution along the z-axis with the initial thermal energy (100 eV) and the smaller one (0 eV) as a parameter. The distribution with the higher energy is moved 0.4 mm downstream from the lower energy. There are little change in the upstream, whereas a significant change in the downstream. It can be considered that the particles in the downstream have moved the upstream region.

The local divergence, however, could not be expressed by the above models. To evaluate the local divergence, we have to consider the nonuniformity of the anode plasma as well as the plasma expansion into the acceleration gap.

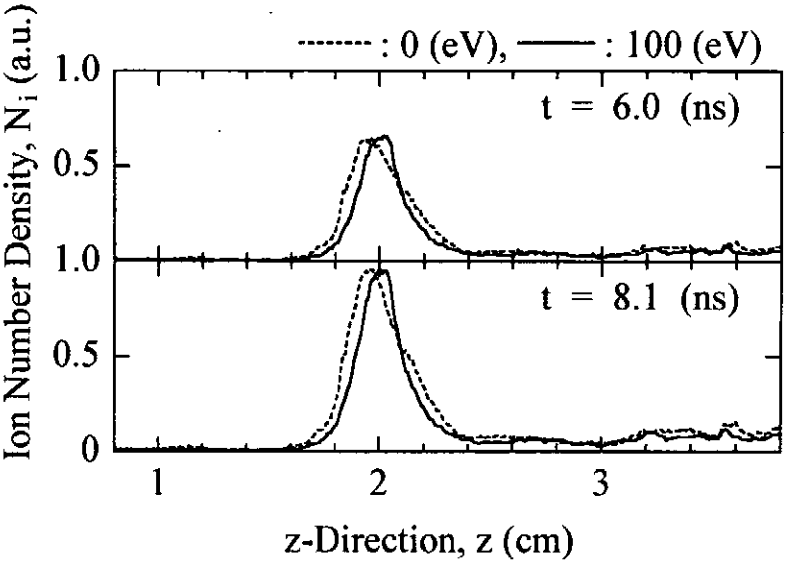

Fig. 10 Comparison of ion-number density distribution between the initial energy of 0 (eV) and of 100 (eV).

References

[1] K. Yatsui *et al.* : *Proc. 11th Int'l Conf. on Plasma Phys. and Controlled Nucl. Fusion Res. Kyoto, Japan* IAEA-CN-47/B-III-9 (1986).

[2] W. Jiang *et al.* : *Jpn. J. Appl. Phys.* 32 (1993) L752.

[3] W. Jiang *et al.* : *Laser Part. Beams* 138 (1995) 343.

[4] W. Jiang *et al.* : *Phys. Plasmas* 2 (1995) 325.

[5] A. Tokuchi *et al.* : *Proc. 2nd Int'l Symp. on Inertial Confinement Fusion Res. by High-Power Particle Beams,* ed. by K. Yatsui (Nagaoka University of Technology), (1986) 430.

[6] K. Imanari *et al.*: *Laser Part. Beams* (submitted for publication) (1995).

Effects of Impurities on Operation of Grid-Controlled Vacuum Arc Ion Source

Jun Hasegawa, Hirotaka Nakai, Hironori Iwasaki,
Mitsuo Nakajima and Kazuhiko Horioka

Department of Energy Sciences, Tokyo Institute of Technology,
Nagatsuta 4259, Midori-ku, Yokohama, Japan

Abstract

This paper presents results of our study on the effects of impurities on a grid-controlled vacuum arc ion source. To investigate the presence of the impurities in the vacuum arc copper plasmas, we have performed mass spectroscopy of the ion beams. We have found that the vacuum arc plasmas contain carbon ions and protons as impurities. We have also discovered the correlation between flux variations of the impurities and modulations of the ion beam waveforms.

1. Introduction

The goal of this study is to develop sources for high-current ion injectors. Requirements for such ion sources include the following: high brightness, high reproducibility, and high repetition rate. As a candidate of the ion sources that satisfy these requirements, we developed a vacuum arc ion source.

The vacuum arc plasma usually has strong spatial and temporal flux variations, which distort the optics of conventional extraction gaps. Therefore, the ion beams extracted by conventional extractors have large beam noise and poor reproducibility. Humphries *et al.* originally proposed and developed a gird-controlled extractor, which can control the ion beam current and reduce the beam noise[1]. The principle of this extractor is as follows. This extractor uses a negatively biased grid as the extraction anode, which repels source plasma electrons and confines them in a plasma expansion chamber. Ions separated from the electrons enter the extraction gap and form a virtual anode by their space charge. The virtual anode suppresses the flux variations and stabilizes the ion beam extraction. Because the ion beams are extracted in a space-charge-limited mode, the current density equals to the space-charge-limited value(Child-Langmuir current density).

We used the grid-controlled extractor for our vacuum arc ion source and tested its basic operations in the previous experiments[2]. From the previous results, we confirmed that the grid-controlled extractor is very effective to extract stable ion beams from time-varying vacuum arc plasmas. However, we also found that there are several problems to be solved. One of the major problems is that the waveforms of the ion beams often become very noisy and lose their reproducibility although the grid control is active. In such a situation, the current density increases beyond the Child-Langmuir value. This implies that the source plasma contains lighter ions than copper ions (a copper cathode was used in our experiments). To confirm it experimentally, we have performed mass spectroscopy of the copper ion beams. In this paper, we report the results of the mass spectroscopy and discuss the effects of impurities on the reproducibility of the ion beams extracted from the grid-controlled vacuum arc ion source.

2. Experimental Setup

A schematic drawing of the vacuum arc ion source is shown in Fig. 1. The arc discharge is driven by a pulse forming network (PFN) which has an impedance of 5Ω and a pulse length of 100μs. The arc current is typically 200A, which is determined by the charging voltage of the PFN. We use copper as cathode material to produce copper plasmas. The cathode is surrounded by an alumina insulator. The extraction gap width is typically set to 2cm. In the present experiments, the extraction gap is operated in two different ways: pulse extraction and dc extraction. In case of pulse extraction, the extraction voltage is powered by a Blumlein type PFN, which has an output impedance of 12Ω and a pulse length of 30μs. The extraction voltage is applied with a matching resister in parallel, which assures almost rectangular

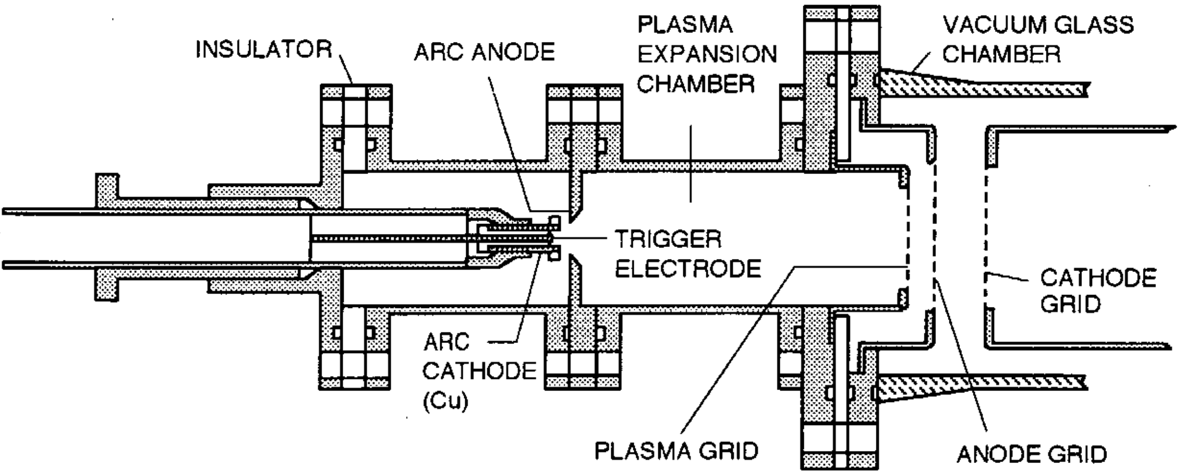

Fig. 1 Schematic drawing of vacuum arc ion source

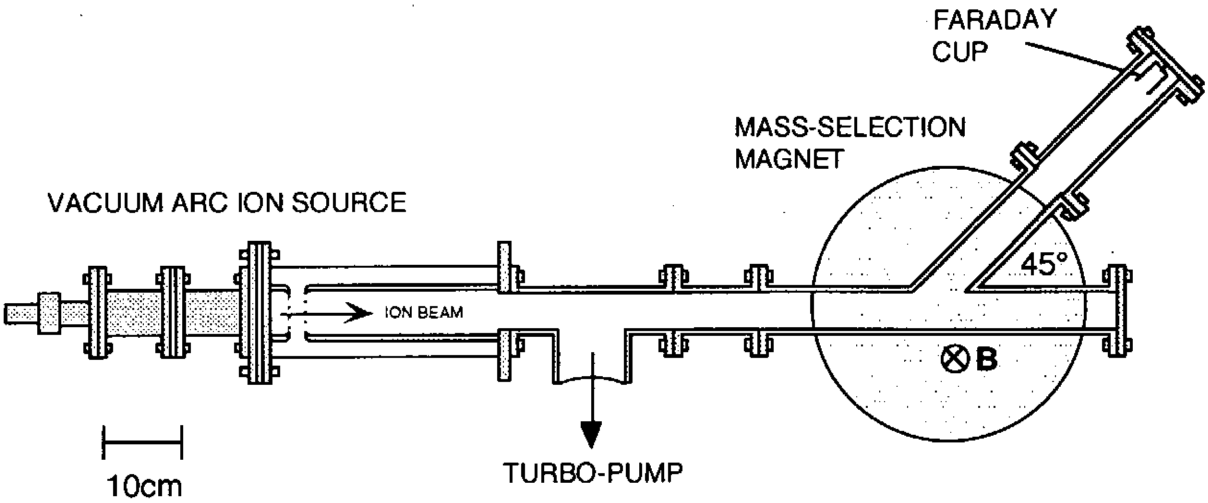

Fig. 2 Experimental apparatus for mass spectroscopy

10kV-acceleration pulse[2]. In case of dc extraction, the source is electrostatically maintained at high voltage during the operation. Because the source plasma is supplied for about 100μs, the pulse length of the extracted ion beam is also about 100μs. More detailed structures of the ion source are described in Ref. 2.

The experimental apparatus for the mass spectroscopy is shown in Fig. 2. The vacuum arc source is connected to a mass-selection magnet that can produce a maximum magnetic field of 0.5T. A Faraday cup installed downstream detects the ion beams bent by 45 degrees by the magnet. A turbo-molecular pump maintains the base pressure of the vacuum chamber at 10^{-5} Torr.

3. Results and Discussions

The result of mass spectroscopy is shown in Fig. 3. In this measurement, ion beams were extracted by the pulse-extraction voltage(10kV, 30μs). Each dot in the figure expresses the average ion beam current of each shot. Figure 2 reveals that the extracted ion beams contain carbon ions and protons in addition to copper ions. Therefore, the source plasma clearly contains carbon ions and protons as impurities. Because the amount of the carbon ions is comparable to that of copper ions, the carbon ions enhance the Child-Langmuir value of the extraction gap.

Figure 4 shows waveforms of ion beams extracted by dc-extraction voltage(6kV) and then selected by the magnet. The upper traces is a C^+ beams and lower trace is a Cu^+ beam. These two waveforms are measured separately. The point is that flux of the C^+ beam fluctuates strongly and has no reproducibility. This strong variations can be attributed to the flux

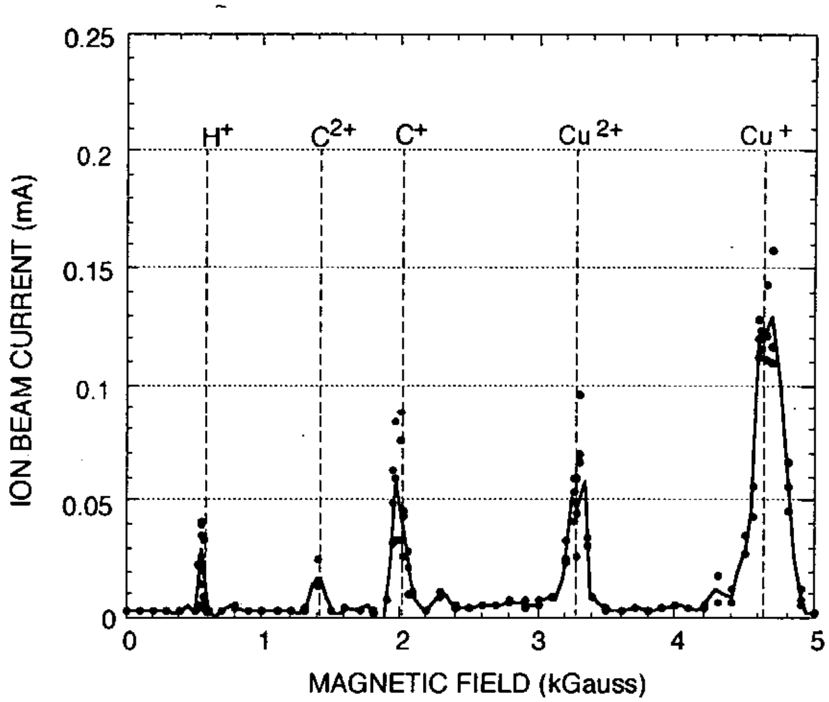

Fig. 3 Charge-to-mass distribution of vacuum arc ion beams. Cu cathode, Extraction voltage10kV

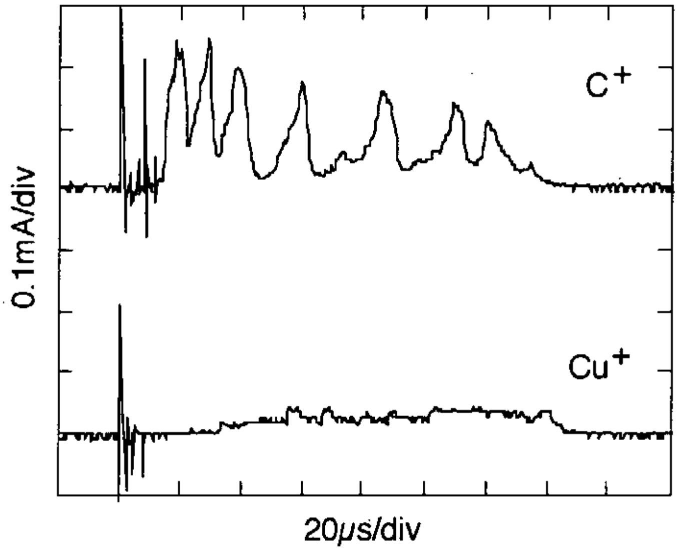

Fig. 4 Waveforms of C^+ beam and Cu^+ beam extracted over 100μs. Upper trace is C^+ and lower trace is Cu^+.

variations of the carbon ions in the vacuum arc source plasmas. From these results, it is reasonable to consider that these strong flux variations of the impurities(mainly carbon) cause the beam noises and degrade the reproducibility of the waveforms.

We consider that sources of these impurities are hydrocarbonic compounds that are attached to the arc cathode surface because the impurities consist of carbon and hydrogen.

These hydrocarbons may originate from the vacuum pump oils in the residual gas. A cause of the strong flux variations of the impurities may be unstable behaviors of the cathode spots. To confirm it, we must do similar experiments in a higher vacuum.

4. Concluding remarks

We have explored the effects of impurities on the operation of the grid-controlled vacuum arc ion source. From the mass spectroscopy measurements, we found that the vacuum arc plasmas contain large amount of carbon ions as impurities. Moreover, the flux of the carbon ions in the vacuum arc plasma has strong variations, which affects the space-charge-limit value of the extraction gap. Consequently, these strong flux variations of the impurities lead to the beam noises and degrade the reproducibility of the ion beams. To investigate this process more precisely and reveal the sources of the impurities, we need to perform more detailed experiments.

References

[1] S. Humphries, Jr. et al., "Grid-controlled extraction of pulsed ion beams," J. Appl. Phys., vol 59, no. 6, p1790, (1986)

[2] J. Hasegawa, M. Nakajima and K. Horioka, "Space Charge Effects on the Characteristics of Grid-Controlled Vacuum Arc Ion Sources," NIFS-PROC-23, p35, (1995)

AIR BREAKDOWN INDUCED BY A HIGH-POWER SHORT-PULSE MICROWAVE

T. Wakisaka, M. Yatsuzuka and S. Nobuhara
Department of Electrical Engineering, Himeji Institute of Technology,
Himeji, Hyogo 671-22

1. Introduction

High power microwaves of its power levels in excess of 1 GW have been generated using intense relativistic electron beams with accelerating voltage of the order of a MV and current in excess of kA. [1, 2) At Himeji Institute of Technology the high-power microwave with the peak power of 20 MW, frequency of 12 GHz and pulse duration of 14 ns has been produced by a virtual cathode oscillator (vircator). [3, 4) These high power microwaves offer new applications in a variety of fields such as particle accelerations, impulse radar, laser pumping, power beaming and environmental cleanup. Research on laser-triggered lightning has received considerable attention in the recent years. [5) One problem in laser-triggered lightning experiments is strong attenuation of laser energy by rains, clouds, and laser-produced plasma. If microwave-triggered lightning is possible instead of laser, microwaves propagate with a small loss in thunderclouds compared with lasers and also are able to radiate much extensive region of targets. In this paper we report on the fundamental experiment of air breakdown induced by a high-power short-pulse microwave.

2. Generation of High-Power Microwave

2.1 Virtual cathode oscillator

The high-power, short pulsed microwave is generated with a axially extracted vircator at Himeji Institute of Technology. Figure 1 shows a schematic of experimental setup of vircator diode for microwave generation. The electron beam diode consists of an annular cathode of diameter of 3 cm and 1 mm in thickness and a stainless mesh anode (mesh wire diameter: 0.25 - 0.37 mm and transparency: 62.8 - 68.4 %). The A-K gap spacing is typically 3.5 mm. The electron beam current was measured with a Rogowski coil, and the diode voltage was measured with a resistive divider. The emitted microwaves were extracted axially with a circular waveguide with a diameter of 4.5 cm and were radiated through a conical horn at the end of circular waveguide. The microwave signals were picked up by a probe located on the wall of circular waveguide and also by an open–end rectangular waveguide antenna at the position of 1 m from the conical horn. The signal from the probe or antenna was detected by a crystal diode for power measurement. The microwave frequency was determined from the propagation time of microwave in a 105–m rectangular waveguide dispersive line.

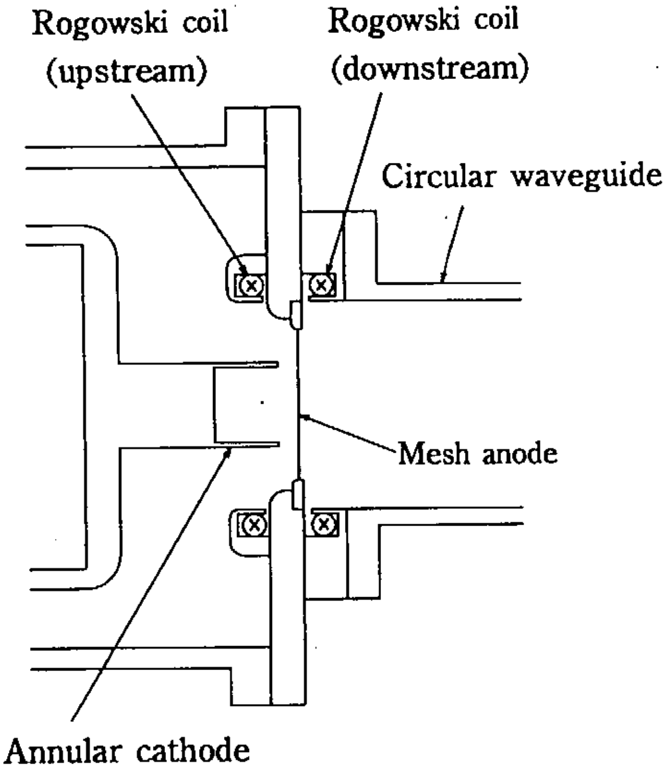

Fig. 1. Schematic of vircator diode.

2.2 *Microwave generation*

Figure 2 shows the typical time evolution of diode voltage, electron beam current and microwave emission from the top. As seen in Fig. 2, the peak power of microwave is 20 MW and the pulse duration (Full Width at the Half Maximum: FWHM) is 14 ns. Although not shown here, the radiation frequency was found to be 12 GHz. Figure 3 shows the microwave power as a function of shot number in repeated operation for various wire diameters of anode mesh, where △ , ○ , □ , and × indicate the wire diameter of 0.22, 0.25, 0.29, and 0.37 mm, respectively. The transparency of each anode mesh was almost constant in Fig. 3. With the smaller wire diameter of mesh, the higher microwave power is generated, but the number of operation with microwave emission decreases. Microwave emissions cease to appear after a few repeated operations because the anode mesh was broken by the strongly pinched electron beam.[4] The anode mesh of wire diameter of 0.22 mm was used at the present experiments on the microwave-induced air breakdown.

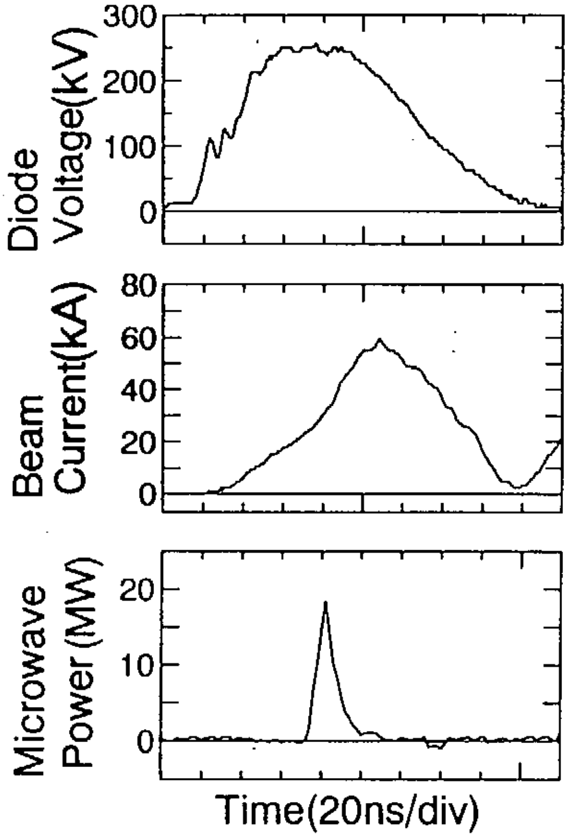

Fig. 2. The time evolution of diode voltage, electron beam current and microwave emission from the top.

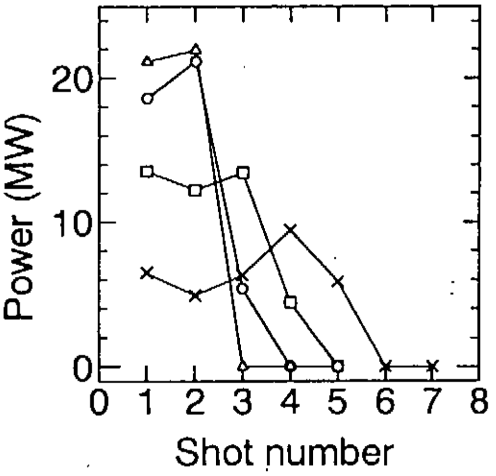

Fig. 3. Microwave power in the repeated operations, where △, ○, □, and × indicate the wire diameter of 0.22, 0.25, 0.29, and 0.37 mm, respectively.

3. Apparatus and Procedures for Microwave-Induced Air Breakdown

Figure 4 shows a schematic of experimental set up for microwave-induced air breakdown. The conical horn with a dielectric lens mounted at the horn aperture is used as a transmitting antenna. High-power microwaves through the dielectric lens are focused on a discharge electrode gap in the center of a stainless steel vacuum chamber with a diameter of 31 cm and length of 32 cm. The discharge electrode consists of a pair of needle (a diameter of 7 mm and a tip angle of 19.3°) and plane (diameter of 6 cm) electrodes. The gap spacing between the needle and plane electrodes was 1.5 cm which is less than the wavelength of microwave. Then, the microwave power density should be uniform in the gap spacing between the electrodes. The acrylic window and microwave absorber (Eccosorb CV) at the opposite side of the transmitting antenna allow incident microwaves to transmit in the vacuum chamber without reflection. Thunderclouds usually occur at the height of 3 - 10 km at which air pressure is estimated to be 200 - 500 Torr. Then, the experiment presented here was done under the air pressure range from 100 Torr to atomospheric pressure. Lights of corona discharge and breakdown were observed with a polaroid camera at a side window of vacuum chamber.

At first, a DC voltage was applied to the discharge electrode without microwave irradiation. The DC voltage increased gradually till an onset of corona discharge, obtaining the corona onset voltage. By further increasing the DC voltage exceed the corona onset voltage, the gap-breakdown voltage was measured. Secondly, the microwave irradiates to the electrode gap space being applied a DC voltage less than the breakdown voltage.

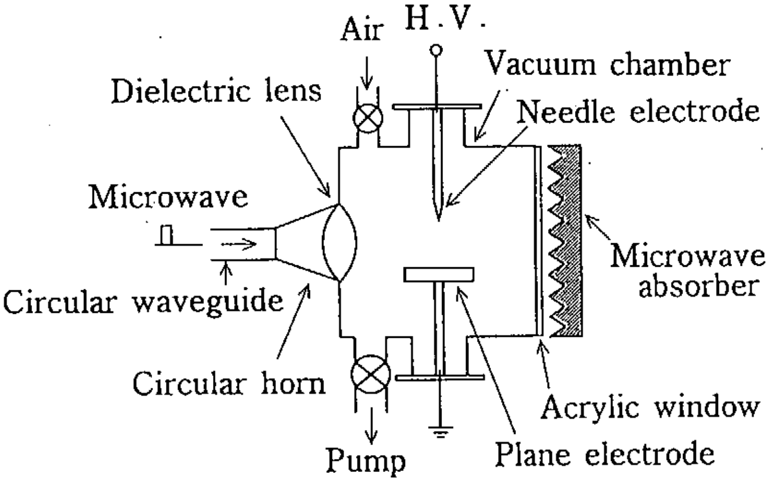

Fig. 4. The experimental arrangement for microwave-induced air breakdown.

4. Results and Discussion

4.1 Negative polarity [6)]

Figure 5 shows the DC voltage applied to the electrodes vs. air pressure for the negative polarity which means the needle electrode is negative voltage, where ■ stands for the corona onset voltage V_C, ● the DC breakdown voltage V_B, and ○ the minimum voltage of microwave-induced breakdown V_M. The hatched region indicates the DC applied voltage between the electrodes at which the microwave can induce the breakdown. As seen in Fig. 5, the microwave-induced breakdown is observed at the pressure range from 100 to 760 Torr, and at the pressure range less than 150 Torr, the microwave induces the breakdown at the DC voltage less than the corona onset voltage. In the pressure range above

200 Torr, the existence of corona discharges is necessary for microwave–induced breakdown. Figure 6 shows the photographs of (a) the corona discharge before microwave irradiation and (b) the breakdown induced by microwave irradiation at the pressure of 200 Torr, where the black and white of photographs were inversed using a computer.

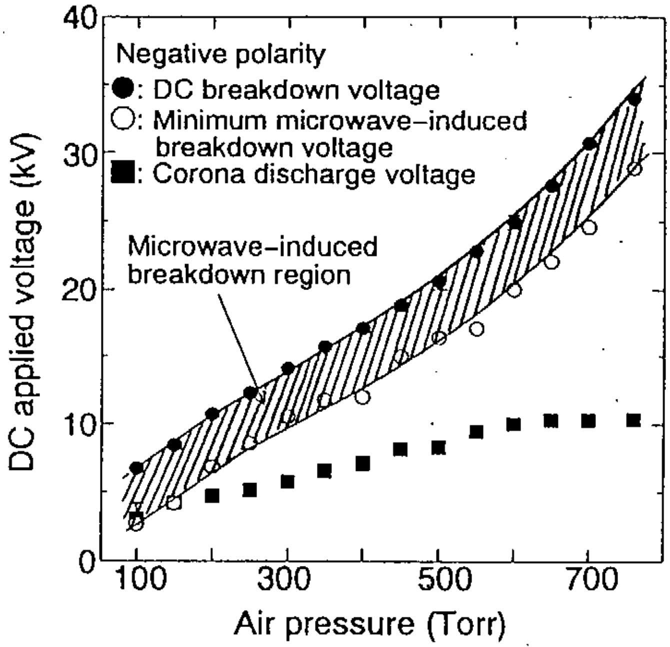

Fig. 5. Microwave–induced breakdown for the negative polarity.

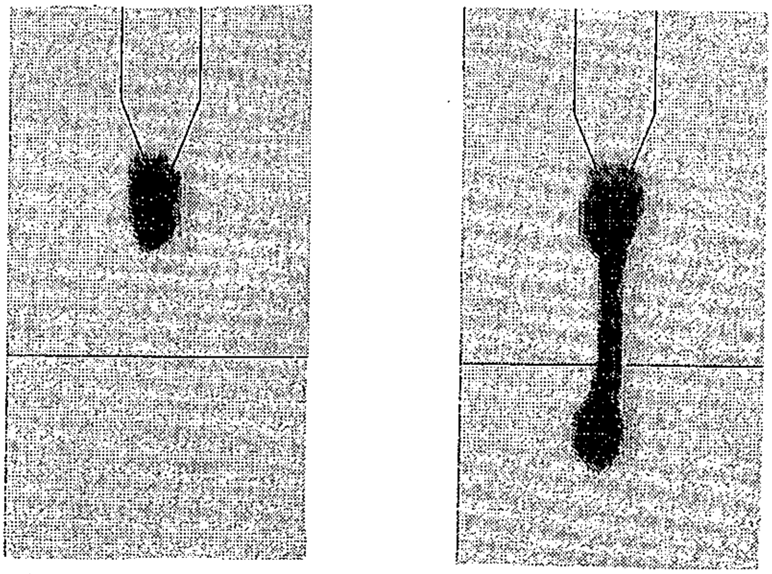

(a)

(b)

Fig. 6. Photographs of (a) the corona discharge before microwave irradiation and (b) the breakdown, induced by microwave irradiation at the air pressure of 200 Torr, where the black and white of pictures were inversed using a computer.

4.2 Positive polarity

Figure 7 shows the DC voltage applied to the electrodes vs. air pressure for the positive polarity, where ■, ●, and ○ indicate V_C, V_B, and V_M, respectively. The microwave-induced breakdown appears in the pressure region less than 300 Torr. In the pressure less than 150 Torr, the microwave induces the breakdown without corona discharges. Figure 8 (a) and (b) show the inversed photographs of the corona discharge before microwave irradiation and the breakdown path after the microwave irradiation at the pressure of 150 Torr, respectively. Figure 8 (c) and (d) show the photographs of the corona discharges before and after microwave irradiation at the pressure of 450 Torr, respectively. As seen in Fig. 8 (d), the microwave irradiation results in a weak extensive luminescence near the plane electrode surface, but no discharge path between the electrodes.

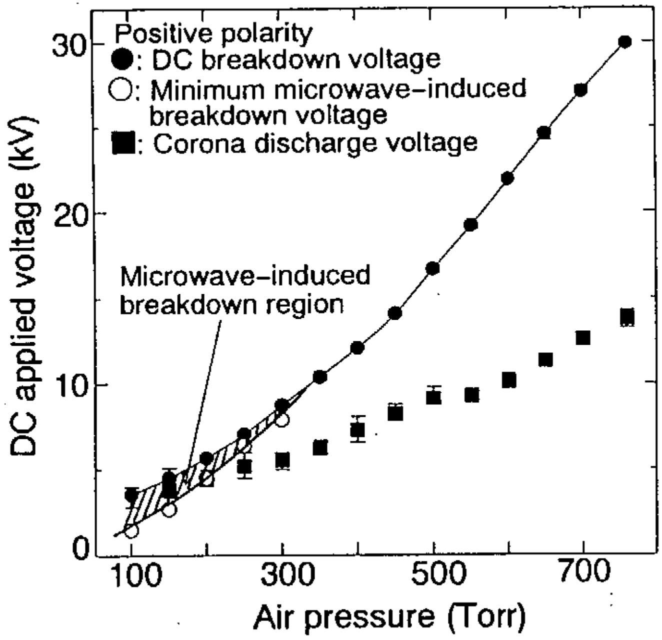

Fig. 7. Microwave-induced breakdown for the positive polarity.

The ratio of the minimum microwave-induced breakdown voltage V_M in Figs. 5 and 7 to the DC breakdown voltage V_B is plotted as a function of air pressure in Fig. 9, where ○ is for the negative polarity and ● is for the positive polarity. As seen in Fig. 9, the microwave-induced breakdowns occur at the air pressure range less than 300 Torr and V_M/V_B reduces with decreasing air pressure in both polarities. Figure 9 also shows that the high-power microwave can easily induce breakdown for the negative polarity than for the positive polarity. At the pressure larger than 300 Torr, no microwave-induced breakdown appear for the positive polarity. These results are ascribed to the existence of many electrons, generated by corona discharges, in the gap space at the negative polarity. Because negative corona discharges release a large number of electrons in the gap space, but positive coronas drive little electrons.

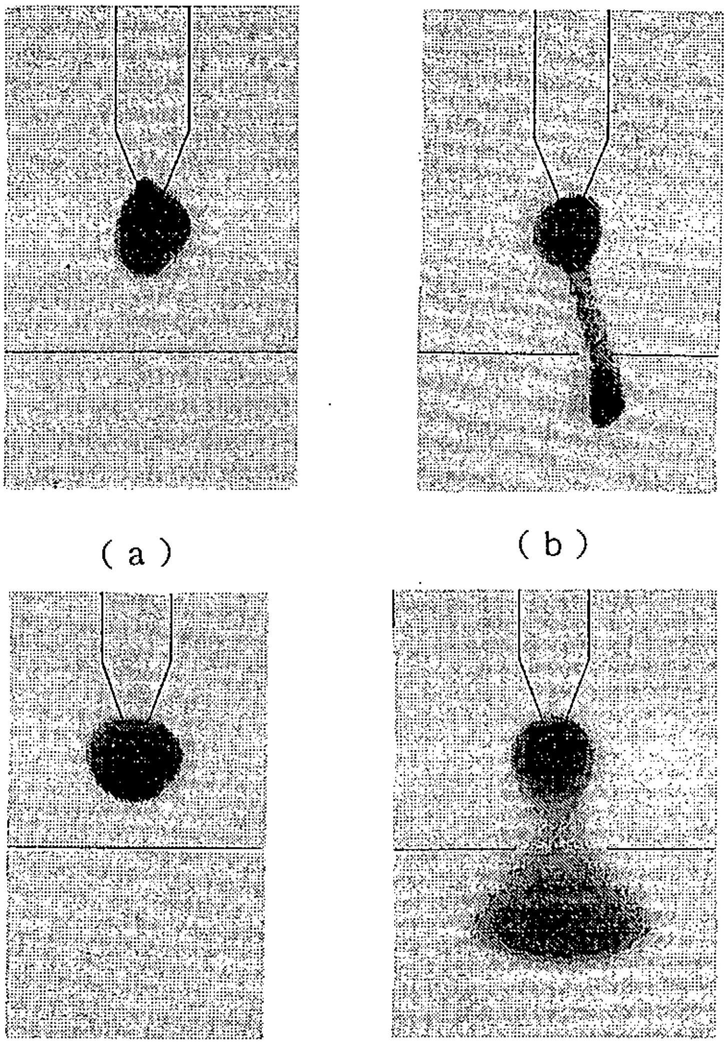

(a) (b)

(c) (d)

Fig. 8. Photographs of (a) the corona discharge before microwave irradiation and (b) the breakdown path after microwave irradiation the pressure of 150 Torr, respectively. Photographs of the corona discharges (c) before and (d) after microwave irradiation at the pressure of 450 Torr, respectively.

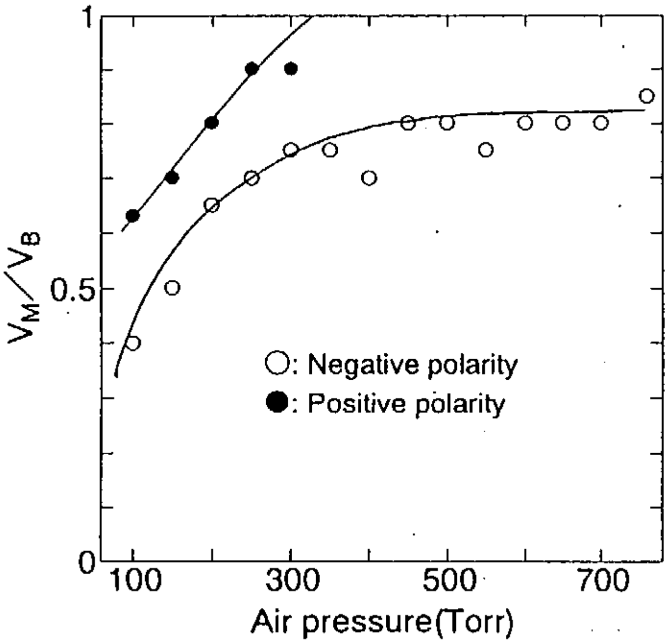

Fig. 9. The ratio of the minimum microwave-induced breakdown voltage V_M in Figs. 5 and 7 to the DC breakdown voltage V_B as a function of air pressure, where ○ is for the negative polarity and ● is for the positive polarity.

5. Conclusion

Air breakdowns induced by a high-power, short-pulse microwave with the peak power of 20 MW, frequency of 12 GHz and pulse duration of 14 ns were studied experimentally with the needle-plane electrode system. The conclusions obtained are as follows:

(1) At the pressure range less than 150 Torr, the microwave-induced breakdown occurs without corona discharge at both polarities.

(2) For the negative polarity, the microwave is able to induce breakdowns at the pressure range from 150 Torr to atmospheric pressure with the existence of corona discharges.

(3) Microwave-induced breakdowns at the negative polarity appear easily than at the positive polarity. At the pressure larger than 300 Torr, no microwave-induced breakdown appear in the positive polarity.

From the studies mentioned above, triggered lightning by a high-power pulsed microwaves might be possible, provide that there are a large number of initial electrons or with further higher-power microwave sources.

References

1. V. L. Granatstein and I. Alexeff: *"High-Power Microwave Sources"*, (Artech House, Boston, 1987).

2. J. Benford and J. Swegle:*"High-Power Microwaves"*, (Artech House, Boston, 1992).

3. M. Yatsuzuka, K. Nagakawa, Y. Hashimoto, O. Ishihara and S. Nobuhara: IEEE Trans. on Plasma Science, 22, 939 (1994).

4. M. Yamabuchi, M. Yatsuzuka and S. Nobuhara: Report of Workshop on Plasma Science, EP-95- (1995) [in Japanese].

5. T. Shindo and S. Sasaki: J. IEE Jpn. 111, 739 (1991) [in Japanese].

6. T. Wakisaka, M. Yatsuzuka and S. Nobuhara: J. IEE Jpn. (in press)[in Japanese].

Dielectric Surface Flashover with UV and Plasma Background

F. Hegeler,*) H. Krompholz, L.L. Hatfield, and M. Kristiansen

Pulsed Power Laboratory
Departments of Electrical Engineering and Physics
Texas Tech University
Lubbock, Texas 79409-3102, USA

Abstract

Surface flashover on insulators under UV irradiation or with a plasma background is investigated with high-speed electrical and optical sensors in order to clarify differences in the breakdown development compared to the pure vacuum case. Results with a plasma background show a more rapid development in the breakdown initiation compared to measurements in vacuum with no plasma. With a magnetic shielding technique using permanent magnets, the duration of an applied voltage pulse can be increased by a factor of 2 to 3 without causing flashover. UV illumination on the electrodes decreases the flashover voltage (for the dc case) or the voltage pulse duration without breakdown (for the pulsed case), whereas UV illumination on the dielectric surface increases the flashover potential.

1. Introduction

Surface flashover across insulators often limits the power density transferable through high voltage systems. The physical mechanisms leading to the breakdown are poorly understood. Therefore, in high voltage operating systems, the distance between high voltage components is designed with a large safety factor which increases weight and dimensions of the system. For space applications, for example, where weight is an important factor, insulator technology needs to be improved.

Our preceding investigation of insulator surface flashover in a pure vacuum environment revealed two distinct phases for the early stage of breakdown: a linearly rising current with a duration of several tens of nanoseconds (I), followed by an exponential current rise (II). Soft x-ray emission started simultaneously with the current and stopped at the transition from linear to exponential current rise [1]. In addition, the above-surface charge carrier amplification processes have been observed with a laser deflection sensor and a streak camera [2]. Laser deflection measurements confirmed a rapid development of a plasma, above the insulator surface, during the early phase of the discharge, with electron number densities in the range of 10^{17} to 10^{18} cm^{-3}. Streak camera measurements verified the formation of an intense visible emission 25 to 50 μm in diameter just above the dielectric surface during the formation of the discharge. The experimental data found from those measurements were consistent with the

---

*) Present affiliation: Department of Electrical Engineering and Computer Science, Kumamoto University, Kumamoto, 860, Japan.

standard model for dielectric surface flashover, i.e., a saturated secondary electron avalanche [3] with electron induced gas desorption [4]. In this simple model the surface breakdown is considered to be initiated by field emitted electrons at the triple point, the area where cathode, dielectric, and vacuum are in close proximity. These electrons are accelerated in the electric field; most of them strike the insulator surface and emit additional electrons. The current density saturates at a point where the surface is charged positively and the secondary electron emission yield is unity. Electrons which strike the insulator surface desorb gas molecules, and the gas drifts away from the insulator with the thermal velocity. The gas drifts above the saturated surface current, is ionized by the more energetic electrons, and the final discharge occurs.

Low Earth Orbit (LEO) plasma and UV irradiation influence the dielectric surface composition, the surface charging, the surface flashover of insulators, and might provide starting electrons for the breakdown process. Therefore, it is essential to study the physical mechanisms involved in the pre-flashover process in this environment in real time (e.g., with nanosecond temporal resolutions) in order to design new insulation techniques. This research simulates the plasma and UV environment of the LEO, and it measures the pre-flashover current, voltage, and x-ray emission. Magnetic shielding techniques are used to significantly improve the performance of the electrically stressed insulator.

2. Experimental Setup

The experimental apparatus has been designed and constructed as a coaxial system with a closely matched impedance. Two modes, a dc-charged mode and a pulse charged mode, are used with this system (see Figure 1). In the dc-charged mode, an RG-19 transmission line, with an impedance of 52 Ω and a one-way transit time of 135 ns, is charged by a 100 kV dc-voltage supply through a high-voltage resistor, R_c, of 500 MΩ. The voltage is manually increased in increments of 0.5 kV until breakdown occurs. In the pulse-charged mode, a transmission line with a one-way transit time of 100 ns is dc-charged to voltages of up to 70 kV. A voltage pulse of 200 ns duration with an amplitude of half the charge voltage is generated by closing the spark gap. This pulse travels through a transmission line with a one-way transit time of 135 ns to the test gap. The voltage wave doubles its amplitude to the original charging voltage at the initially open test gap until flashover occurs. The system is terminated in a shorted transmission line with a one-way transit time of 145 ns.

The test chamber is constructed with a coaxial geometry. The inner conductor consists of copper rods. A copper mesh with 50% optical transmittance is utilized as an outer conductor, which has a diameter of 30 cm and a length of 35 cm. This experiment uses planar dielectric samples which have the advantage of a relatively localized arc channel when breakdown occurs. Measurements have been performed with Lexan and Pyrex as dielectric samples. The surface area of the samples is 75 mm by 50 mm and they are 3 mm and 6 mm thick for Pyrex and Lexan, respectively. All samples are cleaned with deionized water and then treated in an ultrasonic cleaner. Afterwards, they are kept at a pressure of less than 10^{-5} torr for at least 18 hours prior to breakdown testing. Brass or copper semi-spherical electrodes with a radius of 6 mm and an angular cut of 2° (i.e., to ensure good dielectric surface contact at the tip of the electrode) form the test gap on the insulator.

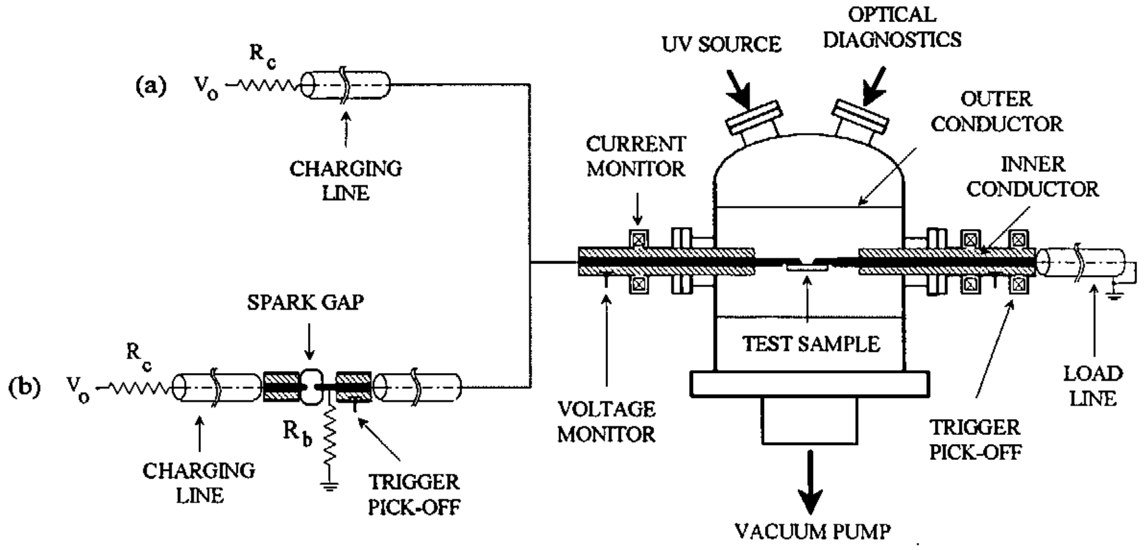

Fig. 1. Experimental apparatus with its coaxial geometry showing both modes of operation: (a) dc-charged mode and (b) pulse-charged mode.

In the experimental setup, fast current probes, capacitive voltage dividers, and an x-ray sensor are used for the investigation of the insulator surface flashover. Current measurements are obtained with a transmission line type current sensor [5]. It has a sensitivity of 0.1 V/A, a risetime of less than one nanosecond, and a two-way transit time of 310 ns during which the sensor output is proportional to the primary current input. The sensor reproduces the primary current with insignificant waveform distortion, i.e., there are negligible limitations of the amplitude transfer function such as high or low frequency cutoffs. A standard capacitive voltage divider with coaxial geometry is used as a voltage probe. Three voltage probes are used with the experimental setup, one each on the source and load side of the test gap for voltage measurements, and one at the spark gap as a trigger pick up. The RC-time constant of the voltage sensors was increased to 2 μs by adding a 910 Ω resistor between the sensor output and the oscilloscope input (e.g., 50 Ω). Soft x-ray emission is measured with an Amperex XP 2020 photomultiplier tube (PMT), operated at 2.4 kV, in conjunction with an NE 102 plastic scintillator. A 10 μm aluminum foil absorbs the visible light emitted by the discharge. The PMT has a propagation delay of 33 ns and a risetime of 3 ns. The sensitivity of the sensor is estimated from the scintillation and photomultiplier efficiencies, the transfer characteristics, and the geometry of the setup. Assuming that the electron energy to x-ray conversion is purely due to Bremsstrahlung in the copper electrode (e.g., anode), an electron current of 80 mA with an electron energy of 20 keV produces a photomultiplier output voltage of about 1V.

Plasma and UV radiation are used to simulate the space environment. An Argon plasma is generated by an electron cyclotron resonance (ECR) plasma source. A 2M137-M14 Magnetron, operating at a frequency of 2.46 GHz and an r-f output power up to 1.2 kW, is used as a microwave source. Four solenoid magnets provide the required magnetic flux density of 0.0875 Tesla for which the electron cyclotron frequency roughly equals the microwave frequency. Argon gas with a pressure of $5 \cdot 10^{-4}$ torr is released into the chamber. Argon plasma with a density of approximately 10^{12} cm^{-3} is produced and drifts through a 1 m long, 10 cm diameter, stainless steel tube into the test chamber. At the test gap, the plasma electron temperature and density are estimated by Langmuir probe measurements and found to be approximately 3 to 5 eV and 10^4 to 10^6 cm^{-3}, depending on the applied microwave power. The Debye length is on the same order as the length of the dielectric sample. Therefore, near the test sample, no "quasineutral" plasma exists, but a collection of charged particles, electrons and ions, are found. The magnetic field from the solenoid magnets is attenuated outside of the ECR plasma source with steel endplates and shorting rods in order to minimize the magnetic flux density in the test chamber. At the test gap, the magnetic field is found to be 1 mT.

An Oriel 150 W dc Xenon arc lamp is used to illuminate the dielectric test sample with UV irradiation. Its spectrum ranges from 190 nm to several micrometers. Indirect photon flux measurements of the solar simulator are performed by radiating a Cu-plate in the vacuum chamber and measuring the photoelectron current with a current meter, Keithley 610C. With a UV irradiation area of $^1/_2$ cm^2, an electron emission current of 300 nA is measured. Assuming a photon emission efficiency of 10% for copper (i.e., for photons with a wavelength between 190 nm and 290 nm) the solar simulator has a photon flux of $4 \cdot 10^{13}$ photons $cm^{-2} s^{-1} nm^{-1}$, which is approximately the same order of magnitude as solar radiation.

For measurements with an external magnetic field, rare earth Neodymium magnets are placed into the dielectric test sample as shown in Figure 2. On the backside of a Lexan sample, two parallel slots are machined across the entire width of the sample. The grooves are 25 mm apart, measured between the centerlines of the slots, and each groove is 4.5 mm wide and 4 mm deep. The 35 NE magnets have the form of a cube with a side length of 4.5 mm. An array of 6 rare earth magnets is mounted with Super Glue in each of the two slots below the cathode or in the middle of the test gap. This arrangement produces a homogeneous magnetic field of approximately 30 mT parallel to the surface and perpendicular to the electric field which is applied between the two electrodes on the test sample. The magnetic flux density in relation to the sample surface is given in Table I. The maximum magnetic field of $B_y = 40$ mT is found inside the insulator at a normal distance of $z = -3$ mm to the surface.

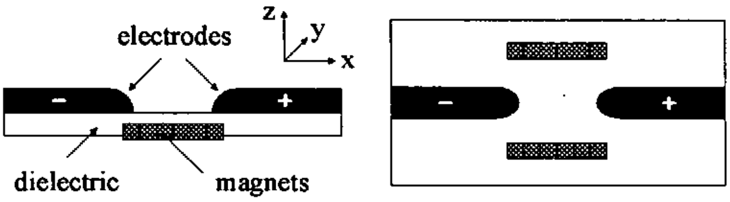

Fig. 2. Dielectric test sample with implanted rare earth magnets: side and top views of the sample.

Table I. The magnetic flux density in relation to the sample surface, measured normal to the surface at the centerline of the test gap.

Distance normal to the surface, z [mm]	-3	0	2	5	7.5	10
Magnetic flux density, B_y [mT]	40	30	26	15	6.5	2

Andrew 84147/LFL4-50A and 84147/LFL2-50A coaxial cables with a bandwidth of several GHz are utilized for signal lines. The output of the sensors is displayed by four Tektronix (TEK) 7104 oscilloscopes which have a bandwidth of 1 GHz. Each scope is equipped with a 7A29 vertical amplifier and a 7B10 or 7B15 time base. The scopes are triggered simultaneously by a 50V pulse with a risetime of less than 1 ns which was generated by a high speed differential comparator, NE521, in conjunction with a 2N2222 transistor which is biased in an avalanche mode. The traces of the TEK scopes are recorded with TEK C1001 or C1002 digitizing cameras, interfaced with a 486/33 MHz PC.

3. Results and Discussion

3.1. Plasma environment

The insulator breakdown on Pyrex and Lexan is measured with and without plasma background for various electrode separations (0.5 to 2 cm), applied voltage amplitudes, and external magnetic fields. The results for Lexan, as a typical example, with an electrode separation of $d_g = 10$ mm are shown below. Surface flashover on Pyrex showed similar results. All plasma cases shown below have a density of approximately 10^6 cm^{-3}. The ECR plasma source was turned on about 10 minutes prior to the first discharge on a virgin dielectric sample to ensure steady state conditions in the test chamber. The experimental setup uses the pulsed charged mode in order to observe the effects with a plasma background. The applied voltage pulse is detected by a voltage probe which is located on the source side of the dielectric sample. The breakdown current is measured on both sides, the source and the load side. The current sensor on the source side observes the low resolution current waveforms which include the displacement current and the current reflection at the open test gap during the early phase of breakdown (see Figure 3a). The high resolution pre-flashover current without reflection is seen on the load side (see Figure 3b). Figure 3 shows the sensor signals for a surface breakdown on Lexan in vacuum (i.e., without plasma or UV). The breakdown delay time, Δt, is 70 ns (i.e., the breakdown delay time, Δt, is defined from the time when 50% of the applied voltage is reached, to the time when 50% of the final current amplitude is reached). The early breakdown current shows a linearly rising current to an amplitude of a few amperes, followed by an exponential current. A linear current rise can be attributed to a constant current density with a linear increase of the channel width due to lateral electron diffusion. The exponential current corresponds to the final Paschen-type breakdown in the desorbed gas. The x-ray emission signal indicates the presence of free electrons, above the surface during the early phase of breakdown, with a mean free-path length on the order of the gap distance. The collisional ionization of the desorbed surface gas drastically reduces the number of highly energetic electrons hitting the anode, and x-ray emission stops.

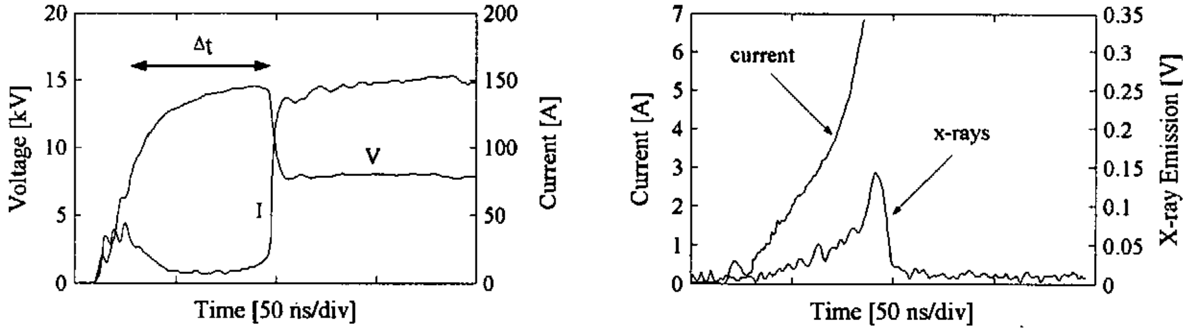

(a) (b)

Fig. 3. Surface flashover in vacuum on Lexan at $d_g = 10$ mm, $V_{applied} = 17$ kV, and Δt = 70 ns: (a) source current and voltage, (b) high resolution load current and x-ray emission.

Figure 4 shows only the high resolution pre-flashover current and the x-ray emission signal for a discharge with and without plasma background and with the effect of an applied magnetic field. The low resolution voltage and current waveforms are similar to the ones shown in Figure 3(a), and therefore, are not given here. The figure captions include the breakdown delay time, Δt, for each case. The early phase of breakdown with a plasma background is given in Figure 4(a). With plasma, x-ray emission increases, and the breakdown current rises faster, and thus, the breakdown is accelerated compared to the pure vacuum case. When the applied voltage pulse arrives at the test gap, all free electrons inside the electrical chamber (i.e., the grounded outer conductor as shown in Figure 1) are collected at the anode electrode at a low impact energy within a few ns. The plasma ions are frozen for the duration of the breakdown process and no additional plasma drifts through the mesh inside of the electrical chamber within 100 ns. It is expected that a slightly negative net charge density is generated on the insulator surface by the impacting plasma, prior to the initiation of breakdown. This effect would account for both the more rapid rise of the initial breakdown current (i.e., a negative charge density on the insulator surface decreases the secondary electron emission yield) and the increase of the x-ray emission (i.e., a larger fraction of the field emitted electrons from the cathode are accelerated over the entire gap). The surface charge density of the insulator will be measured in the future in order to confirm this assumption.

Figure 4(b) and (c) show the results for surface flashovers with plasma and with an external magnetic field. The magnetic insulation effects with an $E\times B$ drift away from the surface are shown in Figure 4(d) for comparison. A positive magnetic field indicates a resulting $E\times B$ drift which points away from the surface, a negative B-field relates to an $E\times B$ drift into the surface. With an external magnetic field of only 30 mT, significant changes in the breakdown development are seen. With an $E\times B$ drift away from the surface, the current shows a strictly linearly rise and the amplitude of the x-ray emission is drastically increased. Furthermore, the breakdown is drastically delayed. The standard deviation of this breakdown delay time is 25%. An $E\times B$ drift into the surface shows a decrease in x-rays. Otherwise, the breakdown development is similar to the case in vacuum. Prior to the applied voltage pulse, the external magnetic field prevents the plasma from reaching the test gap; the plasma instead impacts the sample near the poles of the permanent magnets (see Figure 2). Induced plasma drifts due to possible charge separations are unknown, however, during the early phase of breakdown. An $E\times B$ drift away from the surface "lifts-off" a larger fraction of electrons from the insulator and increases the mean free-path length of electrons. The long linear current rise indicates that either the electron induced gas desorption is reduced or that the ionization of the gas is delayed. An $E\times B$ drift into the surface confines the electrons closer to the surface and reduces the number of highly energetic electrons which produce x-rays. The results of the pulsed breakdown measurements with magnetic fields correspond well with previous dc breakdown measurements in vacuum [1] in which the magnetic field was generated outside of the electrical test chamber.

3.2. UV environment

UV induced surface flashover on Lexan has been investigated predominantly using the dc charged mode. For dc surface flashover, the breakdown time is measured from the time when an early phase breakdown current amplitude of 30 mA is reached, to the time when 50% of the final current amplitude is reached.

A pressure increase in the vacuum chamber of approximately 8% is found when the dielectric sample is irradiated with the entire spectrum of the Xenon arc lamp which ranges from 190 nm to several micrometers. The background pressure of the chamber is 10^{-6} torr. When the UV part of the spectrum is blocked by a low pass filter with a cutoff wavelength of 390 nm, a pressure increase of only 4% is detected. This result indicates that the UV photons with energies higher than of 3 eV are either more efficient in the gas desorption from the dielectric surface or that they are able to desorb additional gas with higher bondage energy.

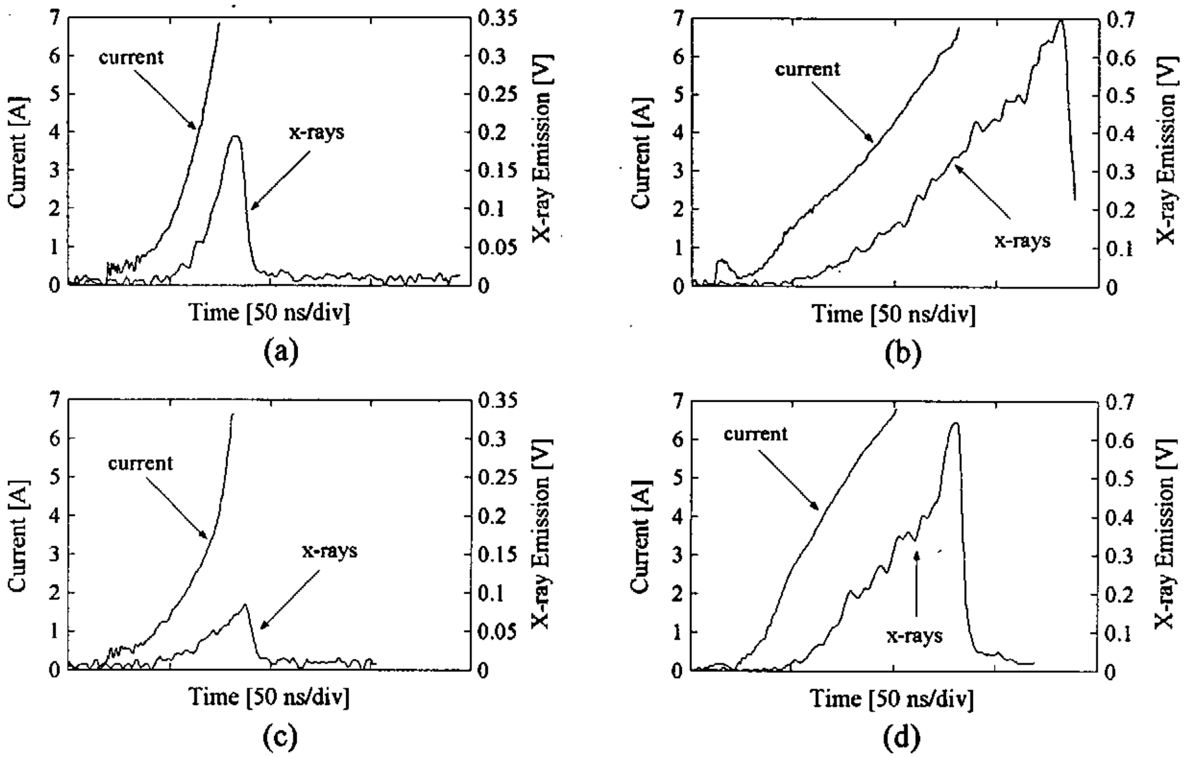

(a)

(b)

(c)

(d)

Fig. 4. Insulator breakdown on Lexan at $d_g = 10$ mm: (a) to (c) with a plasma background; (a) $V_{applied} = 17$ kV, $B_y = 0$, $\Delta t = 60$ ns, (b) $V_{applied} = 18$ kV, $B_y = +30$ mT, $\Delta t = 160$ ns, and (c) $V_{applied} = 16$ kV, $B_y = -30$ mT, $\Delta t = 60$ ns, and (d) without plasma, $V_{applied} = 18$ kV, $B_y = +30$ mT, and $\Delta t = 100$ ns

Since the band gap energy of dielectrics is on the order of 10 eV [6], the dielectric sample was tested for the emission of photoelectrons when illuminated by the solar simulator which has a maximum photon energy of 6 eV. A short current pulse with an amplitude of more than 1 pA is detected from a virgin dielectric sample. Within 1 second from the start of the UV illumination, the current decreases below the measurable threshold (i.e., < 10 fA) of the Keithley current meter. The analog current meter was too slow to detect the initial current amplitude accurately, but these current measurements indicate that electrons are emitted from the dielectric by photons from the solar simulator. These photoemissions from the insulator might be due to surface effects such as irregularities in the molecule bond structure [6].

The UV source was turned on 5 minutes prior to the first discharge and was operated continuously for the duration of a measurement cycle on one test sample (i.e., a discharge occurred every 10 minutes; the maximum number of applied discharges on each sample was 10).

The lowest dc breakdown voltage is found when the sample is irradiated by UV at the triple point. In this case the breakdown develops at an average electric field strength of 1.5 to 2 kV/cm. When the middle of the insulator gap is irradiated with UV (i.e:, the electrodes are not irradiated), the flashover potential is by approximately 10% higher compared to the case without UV. In addition, UV irradiation of the dielectric increases the duration of the linear current rise (phase I), and thus, the breakdown time, by a factor of 2 to 10, dependent on the breakdown voltage. The slower development of the breakdown might relate to the UV induced gas desorption and to the positive surface charge prior to breakdown which decreases the secondary electron emission yield.

The influences of external magnetic fields are investigated on Lexan with an electrode separation of 20 mm. The results of the experiment are shown in Figure 5. Without UV irradiation, a "normal" conditioning of the sample is seen, whereas UV illumination at the triple point only slightly increases the breakdown voltage with each successive discharge. With UV and with an *E*x*B* drift away from the surface, no significant increase in the breakdown voltage amplitude is seen whereas an *E*x*B* drift into the surface increases the breakdown voltage by a factor of 3 compared to the case with $B_y = 0$. The low breakdown voltage for the UV case is due to the increase of the free electron number above the surface. Although a magnetic flux density of 30 mT is sufficient to "lift-off" field emitted electrons from the surface for the pure vacuum case [1, 7], and therefore, prevent a breakdown development at these low electric fields, this magnetic field is not adequate for the UV case. A higher B-field is required due to the initial UV induced positive surface charge. The *E*x*B* drift into the surface confines the electrons closer to the surface and might decrease the number of free electrons by an increase of recombination with the positive charge at the surface. The dynamic process of recombination and UV induced electron emission has not been clarified, however.

UV induced surface flashover for a pulsed applied voltage is shown in Figure 6, where the location of the UV irradiation area on the insulator is varied. As for the dc measurements, UV irradiation on the dielectric increases the breakdown delay time compared to the case without UV. UV illumination at the triple point shows the fastest breakdown development of these three UV irradiation patterns. The longest breakdown delay time is found for the case where the entire test gap is exposed to UV as shown in Figure 6(b). The breakdown development with UV illumination at the anode is only slightly slower compared to the case with UV at the triple point. This is due to the limited number of photoemissions during the pulsed breakdown. The surface flashover is mainly altered due to the UV illumination of the sample prior to the applied voltage pulse. Continuous UV illumination at the cathode or anode emits electrons which might generate a negative surface charge on the dielectric if they strike the surface. UV irradiation on the insulator desorbs gas and produces a positive charge at the surface.

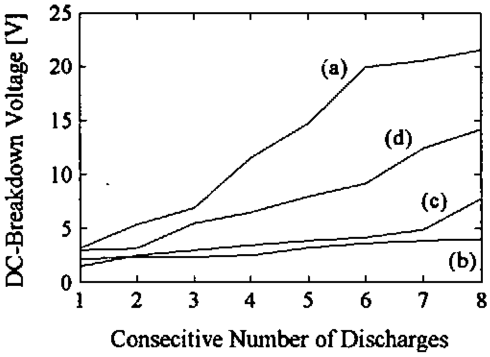

Fig. 5. The effect of external magnetic fields on the dc dielectric flashover voltage amplitude with UV illumination on Lexan at a gap distance of 20 mm: (a) without UV, (b) to (d) with UV. (c) with an ExB drift away from the surface, and (d) with an ExB drift into the surface (30 mT was applied at the cathode region). The standard deviation of the breakdown voltage is within 25%, 5%, 10%, and 20% from its amplitude for the curves (a) to (d), respectively.

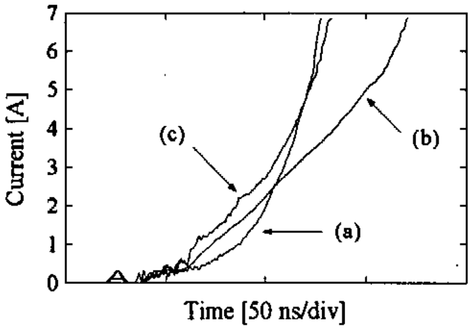

Fig. 6 The early phase current of a typical insulator breakdown on Lexan which is exposed with dc UV irradiation. $V_{applied} = 17$ kV, $d_g = 10$ mm, first discharge on each sample, and the diameter of the UV irradiation is roughly 10 mm on the surface. The center of the UV irradiation is focused at: (a) the triple point ($\Delta t = 90$ ns), (b) in the middle of the gap ($\Delta t = 140$ ns), and (c) at the anode/dielectric interface ($\Delta t = 100$ ns).

4. Conclusion

The presence of plasma or UV radiation changes the behavior of insulator flashover. Plasma impact on the dielectric surface prior to breakdown alters the charge density and a more rapid breakdown development is seen. A low magnetic flux density of only 30 mT is sufficient to drift the plasma away from the insulator gap, and with an $E \times B$ drift away from the surface the breakdown delay time is drastically increased.

As expected, UV illumination at the triple point decreases the dc flashover voltage. This effect might be attributed to the continuous emission of photoelectrons at the cathode. When only the insulator is irradiated by UV (i.e., the electrodes are not irradiated), the breakdown voltage is slightly higher than for the case without UV illumination. Photoelectrons from the insulator do not initiate the breakdown. Gas desorption and a positive surface charge density enhance the breakdown potential in the insulator gap whereas additional electrons emitted from the surrounding metals decrease the applicable electric field.

The current, x-ray emission, and the external magnetic field effects of plasma or UV induced breakdown indicate that the breakdown process is governed by a surface flashover mechanism within the framework of the saturated secondary electron avalanche model with electron induced gas desorption.

Acknowledgment

This work has been supported by BMDO/TNI through DNA/RAST under contract # DNA001-90-C-0110. This paper presents results which have been previously approved for publication.

References

[1] Hegeler, F., Masten, G., Krompholz, H., and Hatfield, L. L., "Current, Luminosity, and X-Ray Emission in the Early Phase of Dielectric Surface Flashover in Vacuum," *IEEE Transactions on Plasma Science*, Vol. 21, No. 2, 1993, pp. 223-227.

[2] Masten, G., Müller, T., Hegeler, F., and Krompholz, H, "Plasma Development in the Early Phase of Vacuum Surface Flashover," *IEEE Transactions on Plasma Science*, Vol. 22, No. 6, 1994, pp. 1034-1042.

[3] Boersch, H., Hamisch, H., and Ehrlich, W., "Oberflächenentladungen über Insulatoren in Vacuum (Surface Flashover on Insulators in Vacuum)," *Z. Angew. Physik*, Vol. 15, No. 6, 1963, pp. 518-525 (in German).

[4] Anderson, R. A. and Brainard J. P., "Mechanism of Pulsed Surface Flashover Involving Electron-Stimulated Desorption," *Journal of Applied Physics*, Vol. 51, No. 3, 1980, pp. 1414-1421.

[5] Krompholz, H., Doggett, J., Schoenbach, K., Gahl, J., Harjes, C., Schaefer, G., and Kristiansen, M., "Nanosecond Current Probe for High-Voltage Experiments," *Rev. Sci. Instrum.*, Vol. 55, No. 1, pp. 127-129, 1984.

[6] *Engineering Dielectrics*, Volume IIA, Electrical Properties of Solid Insulation Materials: Molecular Structure and Electrical Behavior, American Society for Testing and Materials, Philadelphia, 1983.

[7] Bergeron, K. D., "Theory of the Secondary Electron Avalanche at Electrically Stressed Insulator-Vacuum Interfaces," *Journal of Applied Physics*, Vol. 48, No. 7, 1977, pp. 3073-3080.

Characteristics of multichannel gap

S.Takano,Y.Hasegawa,T.Muso and J.Irisawa

Department of Electrical Engineering, Nagaoka University of Technology,
Nagaoka, Niigata 940−21, Japan

Abstract

A overvoltage mode of 24 needle electrodes to a rod electrode of 50cm long has been tested. Voltage raising rates up to 11kV/ns, developed by a non−liniear coaxial cable type of ferrite sharpener, have been applied to the gap. Expected values of multichannel arc were proportional to a parameter of dV/dt·mm. A 100% probability of multichannel arc was attained at 4 [kV/ns·mm].

1.Introduction

Rail−gap switches are widely used in high voltage pulse power systems to minimize the switch inductance and perform a fast switching action. So far, many triggering methodes, such as field distortion triggers (1), ultraviolet radiation source triggers (2), glow discharge triggers (3), corona discharge triggers (4) and KrF eximer laser radiation triggers (5), have been applied to gaps in oder to initiate simultaneous multi arcs.

This paper discribes the performance characteristics of simple overvoltage mode of multichannel arcs without any triggers applied to the gap. A non−linear coaxial cable type of ferrite sharpner (6) has been used to realize high dV/dt pulses of maximum 11kV/ns and maximum voltage of 40kV. The gap is composed of 24 steel needle electrodes separated by 2cm each and a 50cm long brass rod of 1.8cm diameter.

2.Experimental Details

High raising rates of voltage were created by a ferrite sharpener whose main compornent of non−linear coaxial line is shown in Fig.1. A piece of ferrite bead is TDK−HF70BB 2.5×5×0.8mm. The low raising rate of pulse incident to the ferrite sharpener is steepened at the end of the ferrite sharpener which is illustraited in Fig.2. A measuring circuit of ferrite sharpener characteristics is shown in Fig.3. Input pulses incident to the ferrite sharpener were generated by the pulse generator. The bias circuit is to set the starting point on the hysterisis loop of the ferrite. Voltages were measured by Tektronix high voltage probe : P6015A and Hewlett Packard digital oscilloscope : HP54510A.

Typical output voltage waveforms of open ended ferrite shapener are shown in Fig.4. Bias currents were very effective to dV/dt. Output voltage waveforms of terminated end by 52Ω coaxial cable are also shown in Fig.5.

Parameters of this experiments were ① gap length : 1mm～5mm, ② pulse polarity : +,−, ③ dV/dt : −11.42kV/ns～+10.83kV/ns. 100 shots at each experimental conditions were performed, then the data were handled by taking the mean. A number of arc channeles were detected by Sony CCD video camera : CCD−TR650.

3.Experimental Results

(a) Gap voltage behavior

Typical gap voltage traces for possitive needle electrodes are shown in Fig.6. The number of simulataneous arc channels was 4 in upper traces and 5 in lower traces. The applied voltage to the gap was 40kV with raising rate of 10kV/ns. The gap length was 1mm. The mean breakdown voltage was about 25kV which is about eight times higher than the stady state hold−off voltage of the gap. The jitter of the breakdown voltage was rather large and 15kV. Fig.7 shows typical gap voltage traces for negative needle electrode. Experimental conditions were as same as Fig.6 except for the polarity. The breakdown voltages were apparently low compaired to the positive polarity.

(b)Probability distributions of arc channels

Probability distributions of arc channels are shown in Fig.8 for positive needle electrode and negative needle electrode. When the gap length d=1mm, the maximum probability attained to 35% at the number of arc channels 4 for positive polarity. We can't recognize meaningful differencies between shapes of distribution for both positive and negative.

(c) Expected value of multi−channel arc

Fig.9 shows the expected value of multi−channel arc vs. dV/dt ／gap length d.

The expected value of multi−channel arc increased proportional to dV/dt／gap length d. That is to say when the gap length is kept constant, the large dV/dt applied to the gap makes more simultaneous arc channels. Alternatively, when the gap length becomes broad, we have to apply higher dV/dt pulse to the gap to get many simultaneous arc channels.

(d) Realization probability of multi−channel arc

Fig.10 shows the rearranged figure of Fig.9. If we define the multi−arc to be the simultaneous existence of more than two arcs, the criteria of the multi−atc was ∼ 4kV/ns·mm.

4.Conclusion

The multi−arc gaps have been investigated extensively. The high dV/dt pluses up to ∼11kV/ns have been applied to 24 needles−a rod electrode gap. Basic data of gap voltage behaviors, probability distributions of arc channels, expected values of multichannel arc and the realization probability of multi−channel arc have been obtained.

References

1) G.R.Neil and R.S.Post, "Multichannel high−energy railgap switch." Rev. Sci. Instrum., 49(3), 1978

2) R.L.Standstrom, H.Shields and J.I.Levatter, "Performance characteristics of a high−repetition rate, multichannel rail−gap switch." Rev. Sci. Instrum., 58(4), 1987

3) N.Seddon and P.H.Dickinson, "Rail−gap switches triggerd by semiconductor edge discharges." Rev. Sci. Instrum, 58(5), 1987

4) D.B.Cohn, W.H.Long, Jr., E.A.Stappaerts, M.J.Plummer and J.B.West, "Multichannel switch triggered by low−voltage auxiliary discharge." Rev. Sci. Instrum., 53(2), 1982

5) R.S.Taylor and K.E.Leopold, "UV radiation triggered rail−gap switches." Rev. Sci. Instrum., 55(1), 1984

6) F.Kawasaki, S.Takano and J.Irisawa, "Studies of coaxial line containing ferrite beads and its applications." J.I.E.E., 112−A(5), 1992

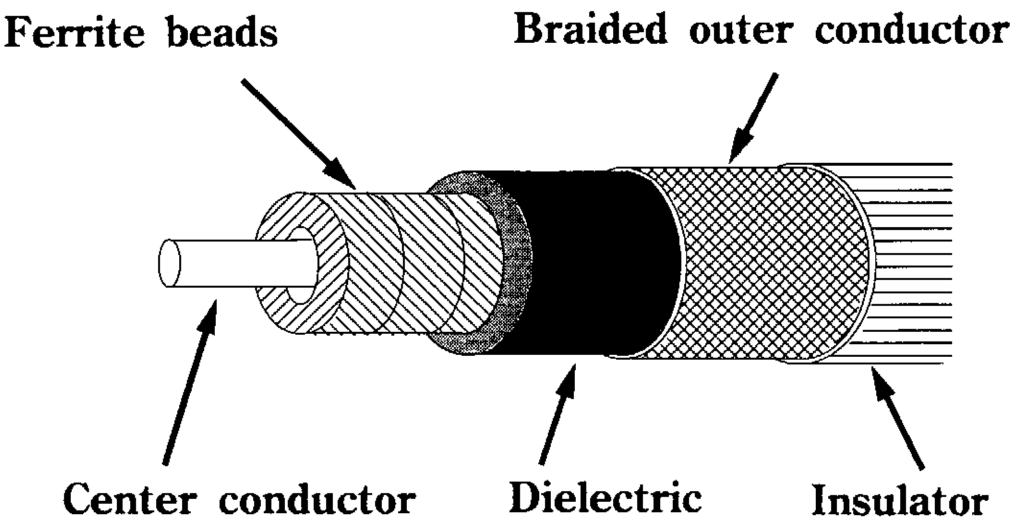

Fig.1 Coaxial line with ferrite beads.

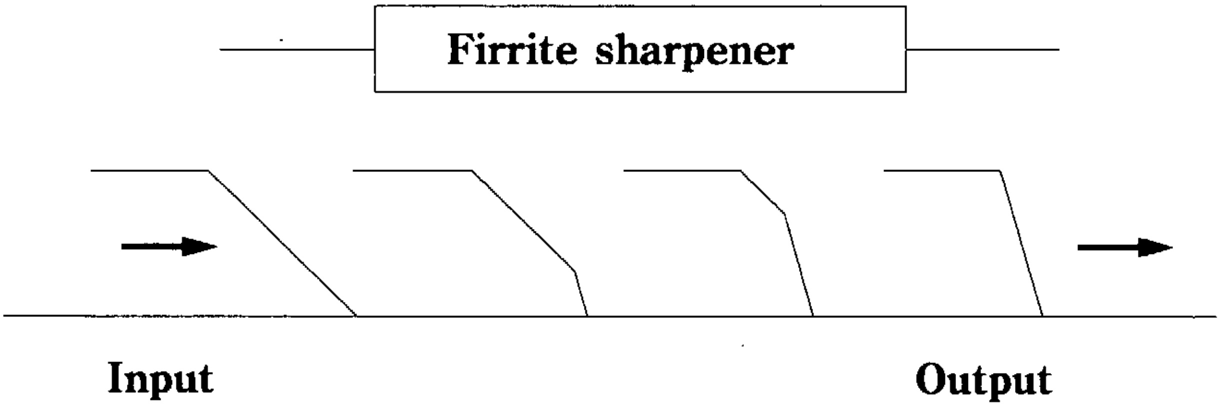

Fig.2 Voltage wave forms traveling a ferrite sharpener.

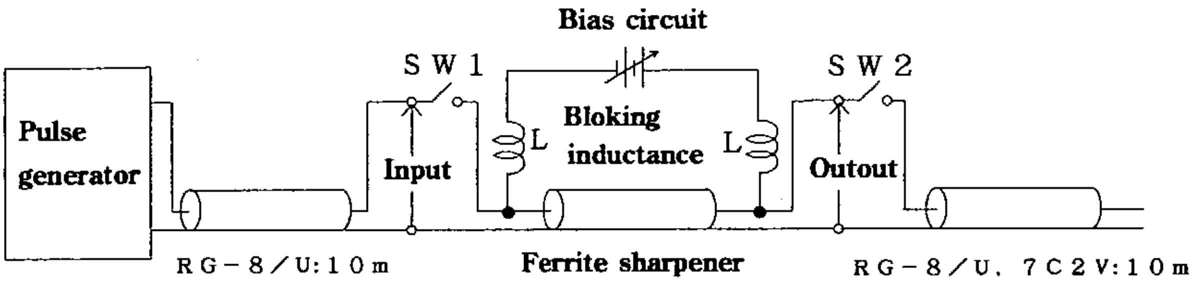

Fig,3 Measuring circuit of characteristics of ferrite sharpener.

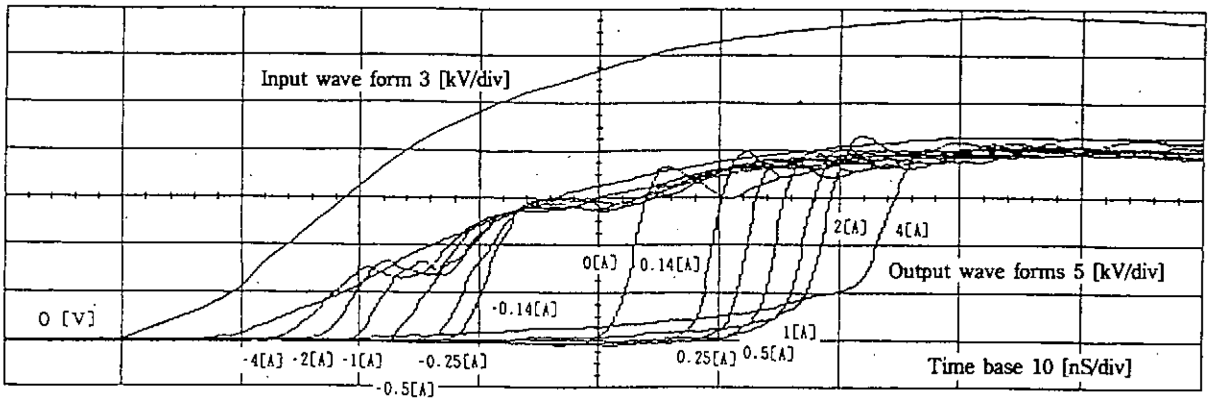

Fig.4 Output voltage of open end.

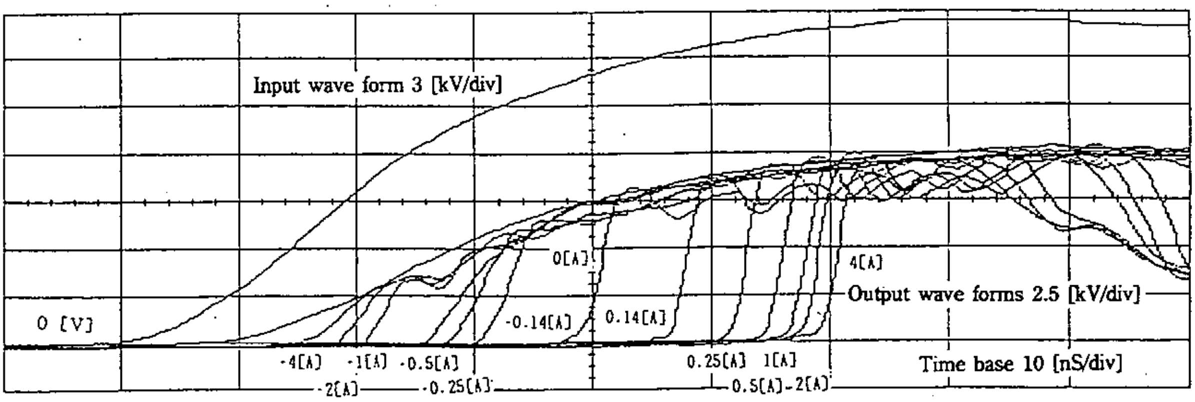

Fig.5 Output voltage of terminated end by 52 Ω coaxial cable.

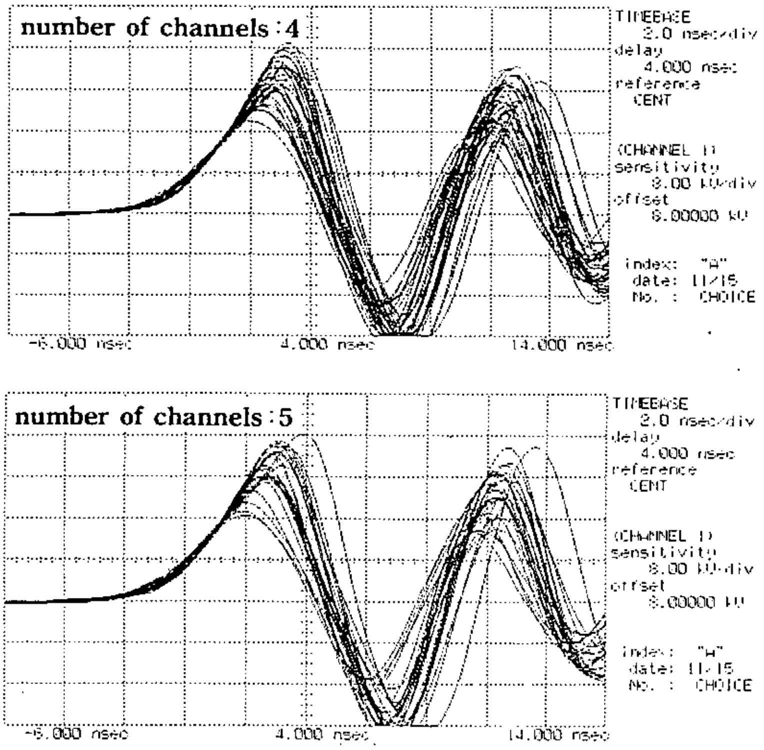

Applide voltage 40(kV),10(kV/ns) Gap length : 1mm

Fig.6 Gap voltage traces(Needle electrode:possitive).

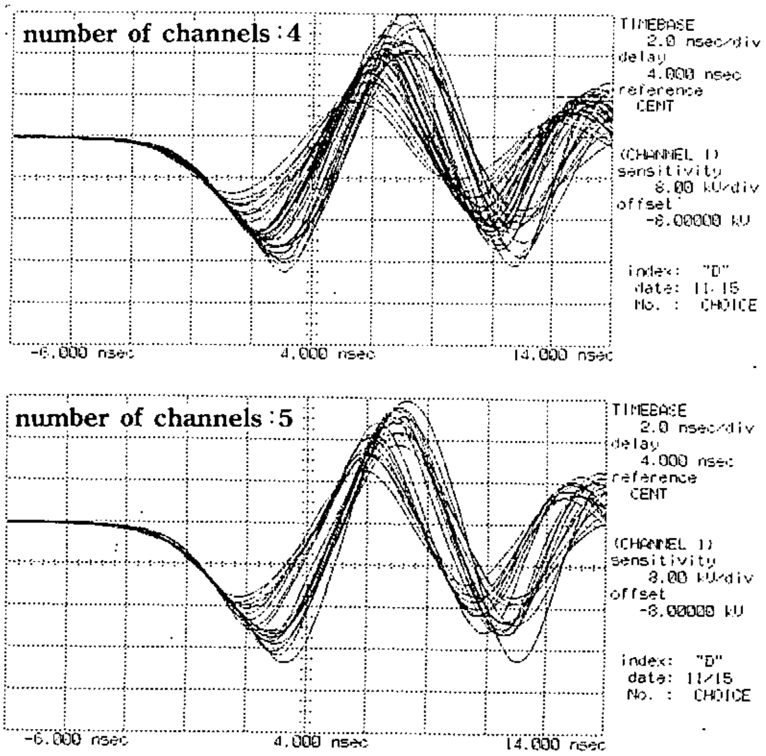

Applide voltage 40(kV),10(kV/ns) Gap length : 1mm

Fig.7 Gap voltage traces(Needle electrode:negatave).

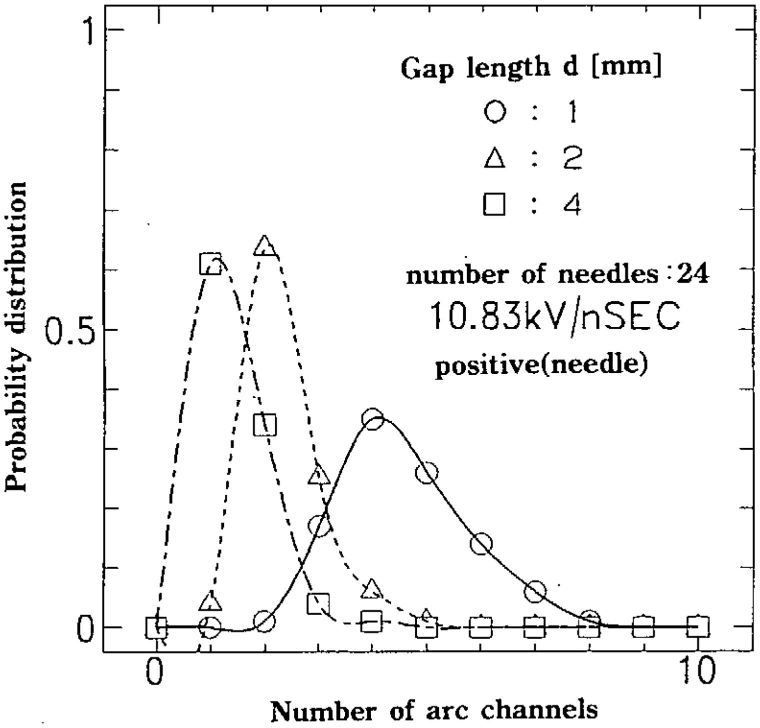

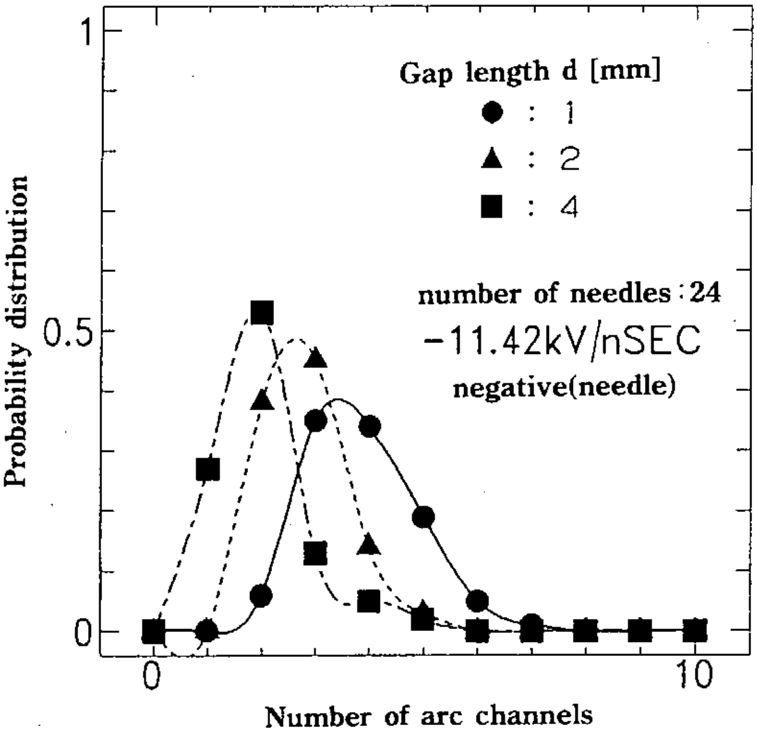

Fig.8 Probability distribution of number of arc channels.

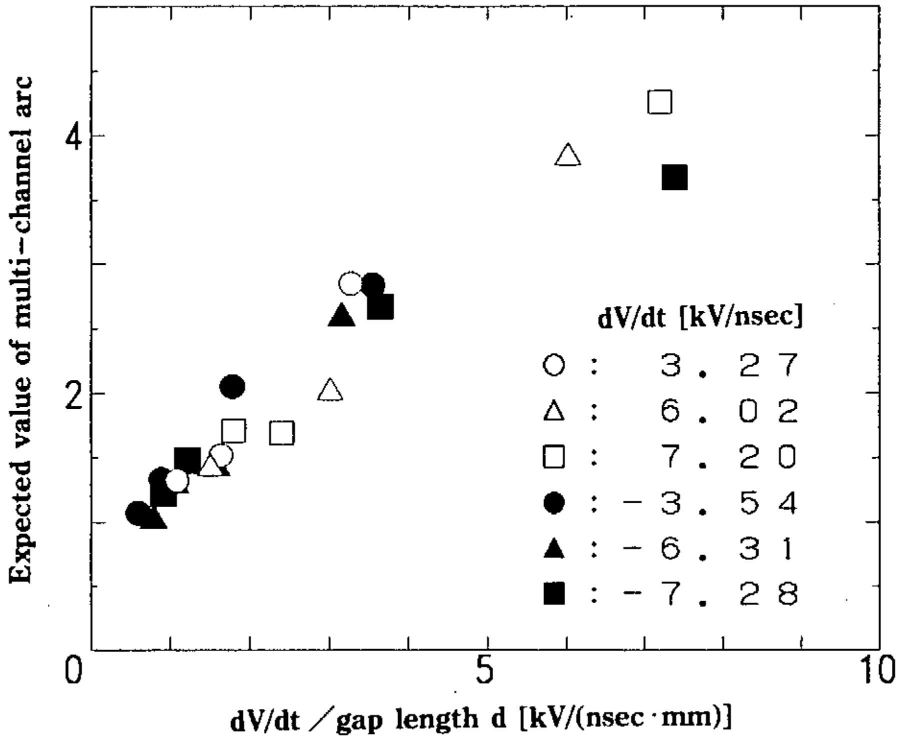

Fig.9 Expected value of multi−channel arc vs. dV/dt ⁄gap length.

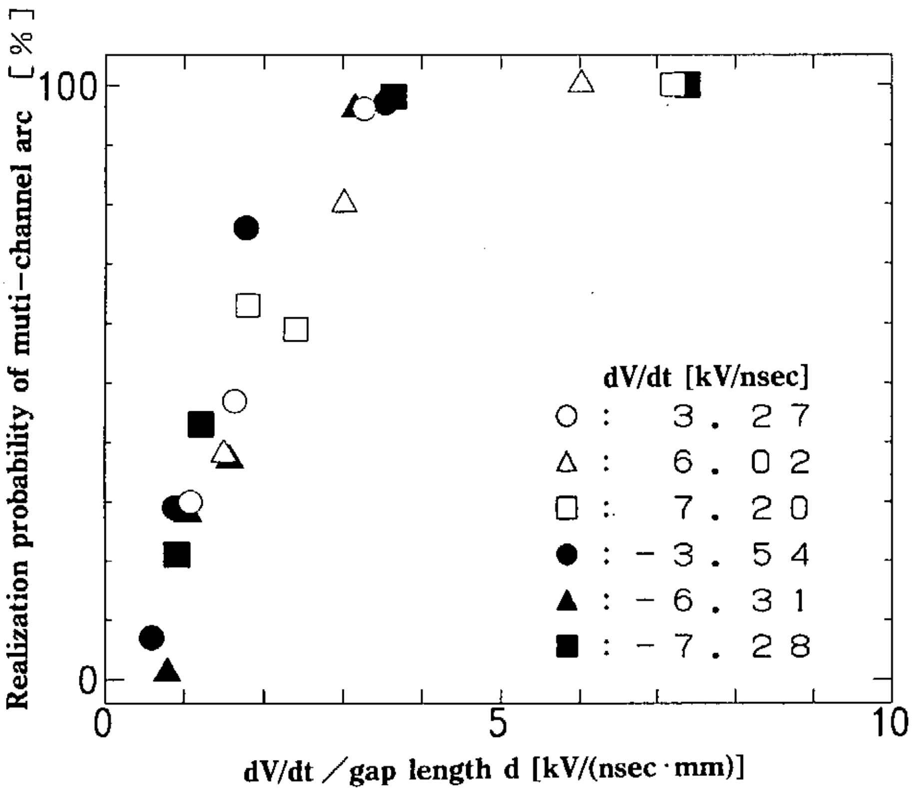

Fig.10 Realization probability of multi−channel arc vs. dV/dt ⁄gap length.

Unstable Behavior of Parallel Fuses as Opening Switches

Naoyuki Shimomura, Masayoshi Nagata,
Department of Electrical and Electronic Engineering
The University of Tokushima

Chris Grabowski,
Department of Electrical and Computer Engineering
The University of New Mexico

Koichi Murayama and Hidenori Akiyama
Department of Electrical Engineering and Computer Science
Kumamoto University

Abstract

Several fuses are often connected in parallel to treat large energies when fuses as an opening switch are used. The waveforms of total current flowing through parallel fuses and of the output voltage could not be distinguished from those in the case of a single fuse, and therefore the currents flowing through each fuse have not been observed in detail. As a result, the actual behaviors of parallel fuses, like an interaction between fuses, are not well known. Here, the experiment using two fuses is carried out to understand the behavior of parallel fuses clearly. The waveforms of current flowing through each fuse are different. Unstable behaviors of parallel fuses are observed, and the condition and probability of appearance of the unstable behavior are discussed. The cause of unstable behavior is that the changing rate of fuse-resistivity on input energy is different in each state of wire. What factor mainly causes the unstable behavior is discussed by numerical analysis. Flaws on the surface of a fuse are a critical factor which triggers the unstable behavior.

1 Introduction

Fuses have often been used as opening switches for pulsed power generators with an inductive energy storage[1]-[7]. The practicality of using several fuses connected in parallel has been demonstrated[6], and in some experiments up to hundreds of fuses have been used[3]. The appearance of the waveforms of total current flowing through parallel fuses and of the output voltage could not be distinguished from those in the case of a single fuse, and therefore the currents flowing through each fuse have not been investigated in detail. As a result, the actual behaviors of parallel fuses, including interactions between the fuses, are not well known.

The purpose of this work is to discuss the behavior of parallel copper fuses in water when used as an opening switch. Only two fuses are considered in order to understand the phenomena clearly. An unstable behavior, in which the difference of currents flowing through each fuse increases, is observed, and plays an important role in the action of the parallel fuses. The cause of the unstable behavior is discussed, and further, what factor mainly causes the unstable behavior is discussed by numerical analysis.

2 Experimental Configuration and Results

Figure 1 shows the equivalent circuit of the small pulsed power generator used in the experiment. The two fuses are connected in parallel in water and are labeled '*a*' and '*b*'. They consist of copper wires with a 0.05 mm diameter, and their length is varied between 5 and 30 cm in the experiment. The capacitor whose nominal voltage is 20 kV is initially charged up to 5 kV. The voltage across the fuses is measured by a resistive voltage divider, and the currents flowing into the two fuses are measured by two Rogowski coils.

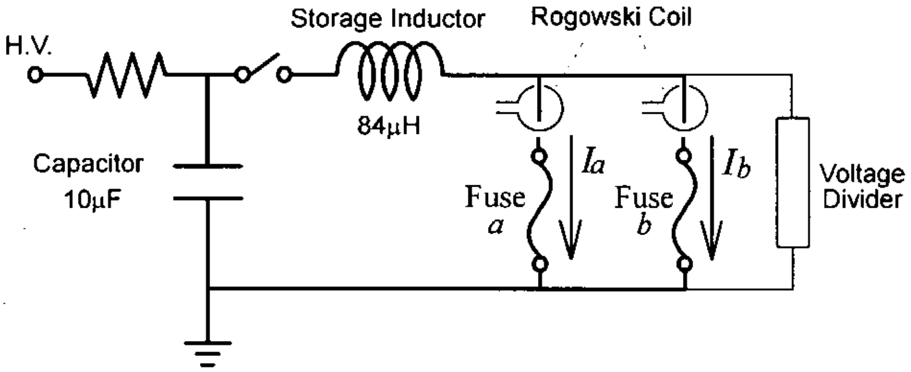

Fig.1 Equivalent circuit of the experimental apparatus.

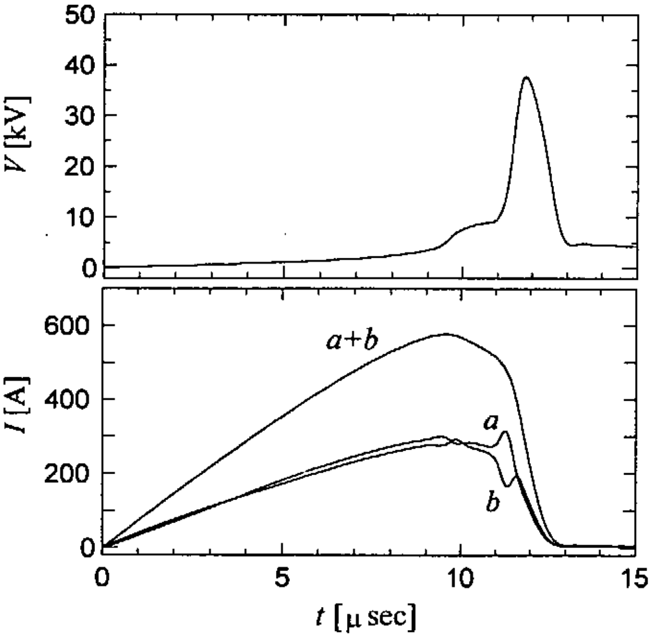

Fig.2 Waveforms of voltage across fuses, currents through fuses.

Figure 2 shows typical waveforms of voltage across fuses, V, and currents through fuses, I. The length of the wires in this case is 20 cm. The labels of a, b and $a+b$ on the current waveforms indicate the currents through fuse a, fuse b, and the sum of currents, respectively. The waveforms of V and I_{a+b} are found to be very similar to the waveforms which were obtained in the case of a single fuse. It has been considered that individual currents flowing through parallel fuses would be identical if the wires have the same dimensions, but the waveform of I_a clearly does not correspond everywhere to the one of I_b; significant differences are observed near 11 μs. Though the waveforms in Fig. 2 are typical, waveforms with fewer unstable regions or more unstable regions are also observed.

3 Distribution of Unstable Behavior

It has been considered previously that the difference between the current waveforms for two parallel fuses having the same dimensions was too small to observe, since the waveform of total current flowing through the parallel fuses is very similar to that of a single fuse. If a difference in the resistances of two fuses develops, more current will then flow through the fuse of lower resistance and more energy will be deposited in that fuse. Since an increase in the deposited energy then yields a larger rate of increase in fuse resistance, the resistance of this fuse then increases until it again equals the resistance of the other fuse. However, the experimental results as demonstrated in Fig. 2 show the considerably larger differences in the waveforms of current and resistance for each parallel fuse than are expected. The reason why explosions of two fuses do not perfectly synchronize with each other is discussed here.

To discuss the unstable behavior of parallel fuses used as an opening switch, a model is considered, as shown in Figure 3. The two parallel fuses, a and b, are represented by variable resistive elements. The currents through fuse a and fuse b and those resistances are labeled $i_a(t)$, $i_b(t)$, $R_a(t)$ and $R_b(t)$, respectively. We now define the quantities $\alpha(t)$ and $\beta(t)$ in the following equations:

$$R_b(t) = \alpha(t) R_a(t), \tag{1}$$

$$\frac{dR_b(t)}{dE} = \beta(t) \cdot \frac{dR_a(t)}{dE} \tag{2}$$

Here, $dR(t)/dE$ means $\Delta R/\Delta E$ at t where E is the energy deposited in the fuse. The unstable conditions are,

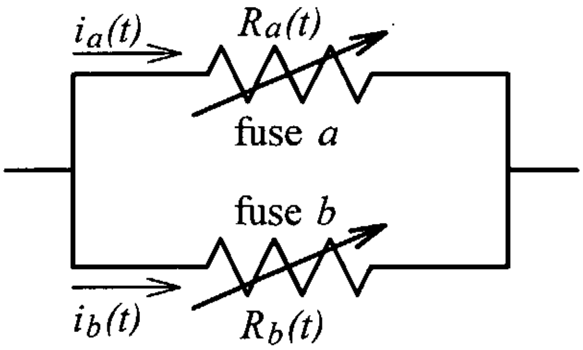

Fig.3 Modeling of two parallel fuses.

$$\alpha(t) > \alpha(t+\Delta t) \quad (\text{at } \alpha(t) < 1) \tag{3}$$

and $$\alpha(t) < \alpha(t+\Delta t) \quad (\text{at } \alpha(t) > 1), \tag{4}$$

since $\alpha(t)$ represents the degree of current-difference between two fuses and $\alpha(t)=1$ implies an equilibrium as described above. The above equations are transformed into the forms:

$$\alpha^2(t) > \beta(t) \quad (\text{at } \alpha(t) < 1) \tag{5}$$

and $$\alpha^2(t) < \beta(t) \quad (\text{at } \alpha(t) > 1). \tag{6}$$

Without knowing the actual change in the currents, the values of $\alpha^2(t)$ and $\beta(t)$ give us the information concerning the stability of the change.

Figure 4 shows an expanded view of the current waveforms of Fig. 2 from 8.5 μs to 12.5 μs and the values of $\alpha^2(t)$ and $\beta(t)$ calculated from eqs. (1) and (2). The unstable regions painted gray in Fig. 4 are determined by the unstable conditions expressed by eqs. (5) and (6).

Now, we can determine whether the fuse-current changes are unstable or not by knowing information about the fuse resistance. The distribution of unstable regions for two parallel fuses *a* and *b* is mapped in Fig. 5, which is obtained from eqs. (5) and (6). Here both fuses are assumed to have the same characteristics, which was obtained in a single-fuse experiment: the diameter and length of wire were 0.05 mm and 18 cm, and the initial capacitor charging voltage was 5 kV. The fuse resistivity is adopted instead of fuse resistance, since the initial dimensions of the parallel wires are the same. The abscissa and ordinate of the figure show the resistivities for the two fuses, accordingly, all of the possible combinations of the resistivities of the fuses during explosion are mapped out on the coordinate plane. The unstable regions are determined by the substitution of ρ and *d*ρ/*dE* into eqs. (5) and (6). The unstable regions are painted in gray, while the remaining regions are stable regions. The

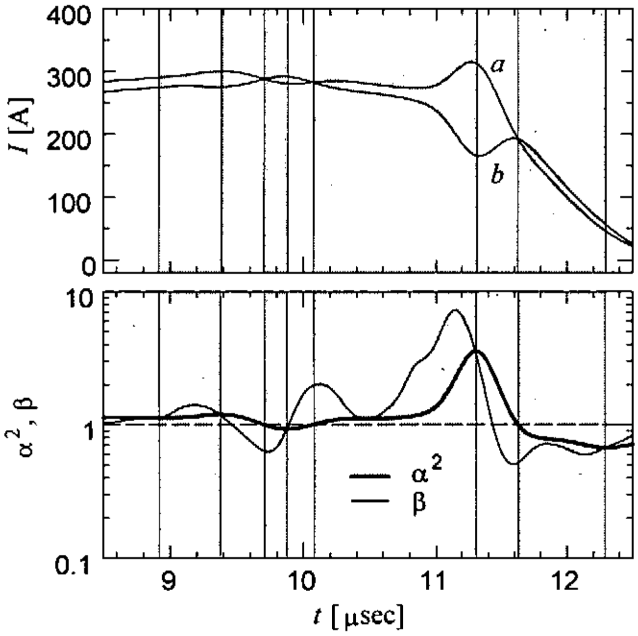

Fig.4 Correspondence between unstable regions on current waveforms, $\alpha^2(t)$ and $\beta(t)$.

behavior of the fuses is expressed on the coordinate plane of Fig. 5 by tracing out the paths of the resistivities of the fuses during melting and explosion. The trace generally travels from the lower-left corner to upper-right corner because the fuse resistivity increases during explosion. If the behaviors of the parallel fuses are totally synchronous during melting and explosion, the two fuses always have same resistivity; consequently, the trace is a straight line with slope of 1 as shown in Fig. 5, and its line could be called the equilibrium line. Note that the unstable regions are distributed symmetrically with respect to the equilibrium line, because the identical parallel fuses here have identical but opposite changes in resistivity. In stable regions, any trace would approach the equilibrium line, while in unstable regions the trace would travel away from the line.

The unstable regions appear where the resistivity is around 0.01, 0.04 and 0.4 mΩcm, which correspond to each of the phases of *dρ/dE*. A rapid increase of *dρ/dE* occurs in several phases of the fuse explosion, at the beginning of the melting phase of the copper wire where ρ is about 0.01 mΩcm and at the beginning of the vaporization phase where ρ is about 0.04 mΩcm [5][7]. The increase of *dρ/dE* near 0.4 mΩcm might be due to further transformation of the melted wire during the vaporization[2]. It is reasonable to assume that the regions just on and very near the equilibrium line where an unstable region is very close to the line are regions of unstable equilibrium, and, conversely, the other regions just on and very near the line are regions of stable equilibrium. As a result, any trace for two parallel fuses on the graph of Fig. 5 is destined to travel from the unstable equilibrium into the unstable region, since the region is so narrow that the equilibrium conditions will not be maintained. Small differences of initial dimensions and configuration between two wires and/or a kind of disturbance in the fuse action might easily make the behavior of the parallel fuses unstable. Since it is very difficult to know the precise details concerning the small differences between two wires or when a disturbance will occur, the behavior of the parallel fuses is not able to be predicted precisely.

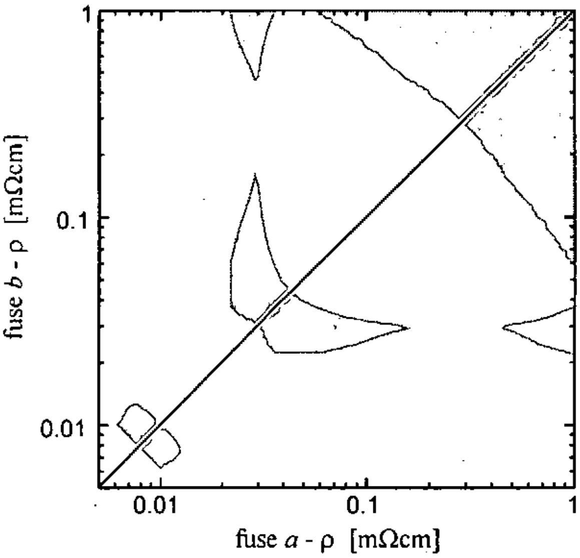

Fig.5 Distribution of unstable regions of parallel fuses, calculated from the resistivity of the single fuse.

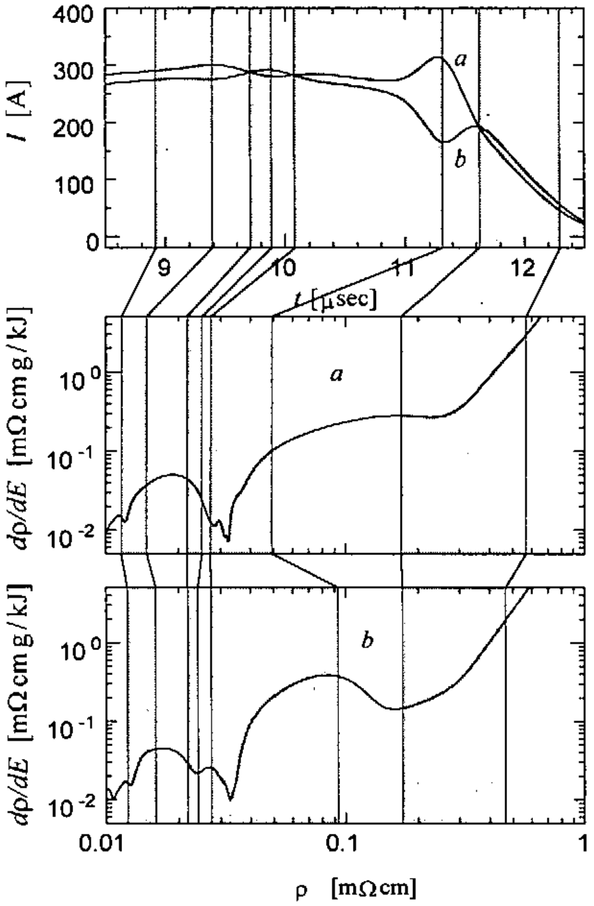

Fig.6 Correspondence between unstable regions on current waveforms and resistivity changes.

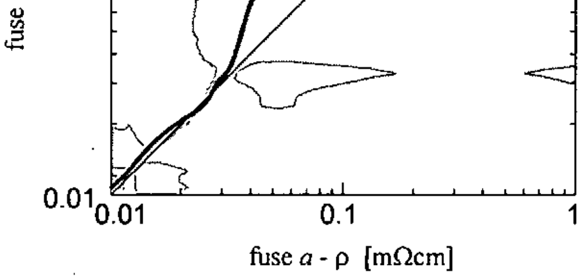

Fig.7 Distribution of unstable regions of real parallel fuses and the trace representing the fuse action.

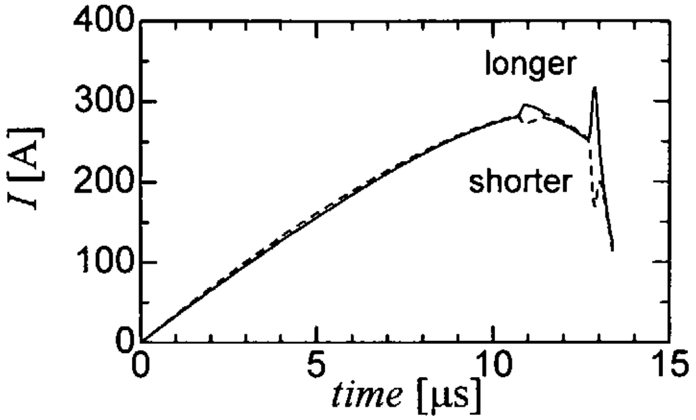

(a) (0.05mm, 20cm), (0.05mm, 19cm)

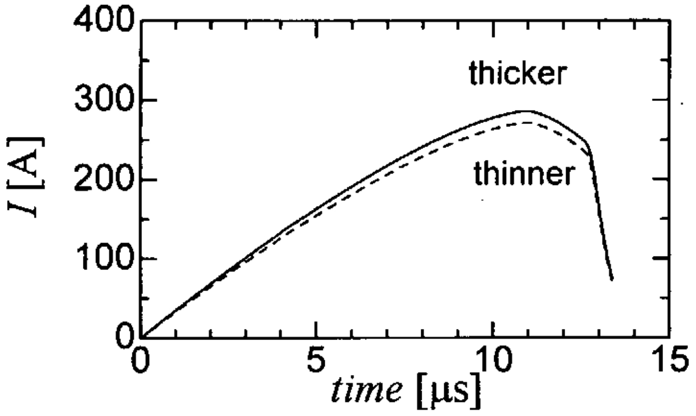

(b) (0.05mm, 20cm), (0.0487mm, 20cm)

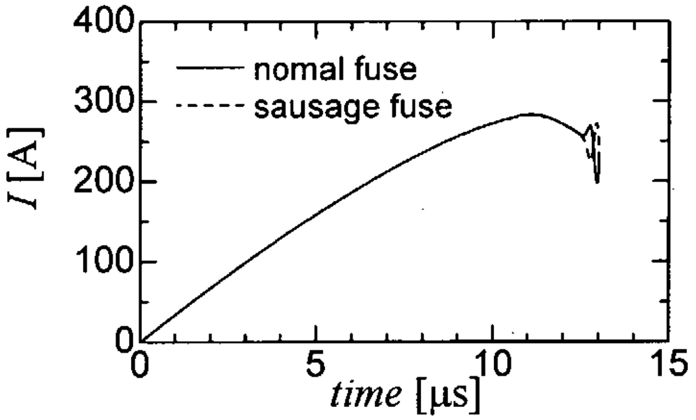

(c) (0.05mm, 20cm), ((0.05mm, 19cm)+(0.0495mm, 1cm))

Fig.8 Current waveforms through parallel fuses obtained by numerical analysis.

A somewhat more detailed view of the unstable behavior, which is obtained from the data of experiments using two parallel fuses, has to be considered. Figure 6 shows the relationship between the current waveforms and resistivity variations for the two fuses. The current waveforms are the same ones that are shown in Fig. 4. The unstable regions are painted gray, too. The correspondence between the appearances of the unstable region and the rapid increases of $d\rho/dE$, described above, is confirmed in practice.

Figure 7 shows the distribution of the unstable regions calculated from the results in Fig. 6. The differences in $d\rho/dE$ for the two fuses are responsible for the asymmetry. The curved line shows a trace of resistivities calculated for the fuses in the experiment, and the trace clearly passes through unstable regions. The curved line moves away from the equilibrium line in the unstable regions and comes close to it in the stable regions. As was mentioned above, any differences in initial dimensions and/or the disturbance in the fuse action can trigger the unstable behavior; then the variation of $d\rho/dE$ becomes unstable.

4 Numerical Analysis

To discuss what factor mainly causes the unstable behavior, numerical analysis is performed. The setup used in numerical analysis is same as the experiment, consequently, two parallel fuses are adopted. One of two parallel fuses is variously changed in dimension.

Figure 8 shows the waveforms of current through parallel fuses. Figure (a) is obtained by the experiment which one of parallel fuses is shorter. Extremely local concentration of current to the shorter fuse are observed at about 13 μs. When a thin fuse is installed to parallel fuses, figure (b) is obtained. Though current through the thicker fuse is more than one through thinner, there is no local concentration, Figure (c) is obtained when the fuses shown in Fig. 9 , which simulates a flaw, are used. The concentration in Fig. (c) is comparatively large in spite of the small difference of dimension between two fuses. Therefore flaws on the surface of a fuse are a critical factor which triggers the unstable behavior.

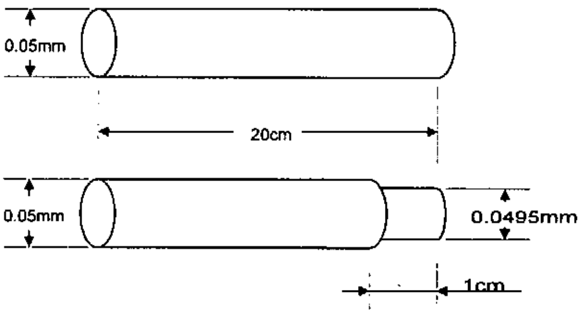

Fig.9 Dimension of the parallel fuses

5 Conclusion

Different waveforms for the currents flowing through each fuse were observed in spite of identical fuse dimensions, and it was confirmed that there were unstable behaviors in the action of the fuses. By defining the equations to express the unstable conditions, a distribution of unstable regions was then able to be mapped onto a graph of fuse-resistivities, thus showing the trend in the behavior of the parallel fuses. This mapping reveals that the variations in the rate of change of the fuse-resistivity, which is a function of input energy are responsible for the unstable regions. Their distribution introduces the probability of the appearance of unstable behaviors; therefore, it is reasonable that any difference of initial dimensions for the two wires and/or any kind of disturbance in the fuse action could immediately trigger an unstable behavior. In particular, flaws on the surface of a fuse are a critical factor which triggers the unstable behavior.

REFERENCES

[1] J.N.DiMarco and L.C.Burkhardt, "Characteristics of a Magnetic Energy Storage System Using Exploding Foils", *J.Appl. Phys.*, vol.41, no.9, pp.3894 -3899, 1970.

[2] L.Vermij, "The Voltage Across a Fuse During the Current Interruption Process", *IEEE Trans.Plasma Sci.*, vol.8, no.4, pp.460-468, 1980.

[3] G.Cooperstein, et al., "Inductive Energy Storage System at NRL", *6th IEEE Conf. on High-Power Particle Beams*, pp843-846, 1986.

[4] A.Guenther, M.Kristiansen and T.Martin, "OPENING SWITCHES", ADVANCES IN PULSED POWER TECHNOLOGY Vol.1 ,PLENUM PRESS, 1987.

[5] Ihor M. Vitkovitsky: "HIGH POWER SWITCHING", Van Nostrand Reinhold Company, 1987.

[6] N.Shimomura, H.Akiyama and S.Maeda, "Compact Pulsed Power Generator by an Inductive Energy Storage System with Two-Staged Opening Switches", *IEEE Trans.Plasma Sci.*, vol.19, no.6, pp.1220-1227, 1991.

[7] V.A.Burtsev, V.N.Litunovskii and V.F.Prokopenko, " Electrical explosion of foils. I and II," *Sov.Phys.Tech.Phys.*, vol.22, no.8, pp.950-961, 1977.

Correlation between plasma behavior and hot spots generation on plasma focus experiments

Takeshi Yanagidaira, Hiroshi Kurita, Toshikazu Yamamoto,
Katsuji Shimoda, Morihiko Sato and Katsumi Hirano
Department of Electronic Engineering, Gunma University
Kiryu, Gunma 376, Japan

Abstract

Correlation between X-ray generation and constriction of pinched column was investigated on plasma focus discharges (45 kV, 0.8 MA) with additional Ar-gas puff into embedded hydrogen using diagnostic tools including a temporal- and spatial resolved soft X-ray imaging system and a Mach-Zehnder interferometer. An interferogram taken immediately after the peak emission from the micropinch (250 μm in radius, ~1 mm in length) showed a gap (4 mm in length) in the plasma column. This can be explained that axial outflow of charged particles from the micropinch plays an important roll. It is shown that the soft X-ray imaging system is useful as a diagnostic tool for temporal resolved 1D observation of rapid changing sources.

1 Introduction

There is an increasing number of applications of pinched plasmas as an intense source of soft X-ray radiation in fields such as X-ray microlithography, X-ray microscopy, and soft X-ray laser excitation. The plasma focus or the gas puff z pinch can provide such soft X-ray sources. These plasmas are strong line and bremsstrahlung emission sources, when the discharges are carried out using high Z admixtures such as argon or neon.

Energy losses due to these radiation can change pressure balance in the pinched column, giving rise to extreme constriction. Dynamics on radiative pinches have been investigated for the most part theoretically.[1,2) The density and the temperature were already evaluated by spectroscopic studies for extremely constricted plasmas generated by vacuum sparks[3) or plasma focus[4,5). However, temporal correlation between the X-ray emission and the constriction of pinch has not been clarified.

In this paper, we intend to confirm the extreme constriction of soft X-ray radiating plasma by simultaneous observations using newly developed time resolved 1D imaging system and an interferometer.

2 Experimental

2.1 Plasma focus device

To generate the soft X-ray, a Mather type plasma focus device with a squirrel cage outer electrode was employed. The inner and the outer diameter of the coaxial electrodes were 50 and 100 mm. The lengths of the outer and the inner electrodes were 230 and 280 mm, respectively. The condenser bank consisted of 28 × 1.56 μF capacitors. The device was operated at the bank voltage of 45 kV and an embedded gas pressure of 6 Torr hydrogen. To obtain intense soft X-ray emission, argon was additionally puffed with a fast acting valve through the inner electrode immediately before each discharge.[6] When the bank is operated at 45 kV, the current in the plasma column was 0.8 MA at its peak approximately.

2.2 Soft X-ray imaging system

To make a temporal- and spatial resolved measurement, a soft X-ray imaging system which consisted of a filtered pinhole camera and a detection system was developed.[7] The schematic diagram of the detection system is shown in Fig. 1. The detector is composed of a soft X-ray sensitive scintillator plate, slits, a bundled fiber optics and photomultiplier tubes. The image of the soft X-ray source is formed on a plastic scintillator plate NE142 with thickness of 0.2 mm through the pinhole of 0.1 mm in diameter. The visible image generated by the soft X-rays is divided into six pieces by the six slits and the bundled six channel optical fibers which are arrayed in perpendicular to the electrode axis. The signal from each channel is spatially integrated in the radial direction. Therefore, the system enables a measurement in a wide region. Each channel of the optical signals is led to the photomultipliers (Hamamatsu Photonics H1161) and recorded in the storage oscilloscope (Hewlett Packard 54542A). The signals and the pinhole image are then processed as mentioned in section 2.4. The advantage of this system is that the 1D X-ray image can be continuously recorded just like by a streak camera but with a high linearity. The temporal and the spatial resolution of the detection system were 5.2 ns and 1.28 mm, respectively.

2.3 Soft X-ray pinhole camera

A soft X-ray pinhole camera with a quantitative image acquisition system was developed for soft X-ray observation with temporal resolution.[8] A pinhole image of the X-ray source is made on the MCP through a pinhole and Be-Ag combination foil filter (25 μm and 1 μm in thickness, respectively). The spectral response of the filters and MCP system is also described in the previous paper.[8] The combination of the filters and the MCP gives a pass band between 1.8 keV and 3.4 keV, which accepts Ar K-lines.

2.4 Processing of the soft X-ray image

Spatial resolution in the detection system described in section 2.2 is limited by the detector channel separation as in the multichannel detection system. To determine the shape and the location of the emitting sources with sufficient accuracy, the X-ray pinhole camera was employed in conjunction. The view fields of the adjacent channels in the detection system were a little overlapped. Therefore, the system is detectable over an area of more than 20 mm×20 mm in the plane including the electrode axis continuously. Although an X-ray emitting hot spot may be recorded in the adjacent channels, spatial resolution of the pinhole camera with the MCP allow to identify the peaks in the waveforms from each photomultiplier and construct a spatially and temporally resolved display similar to the streak photograph as shown in Figs. 3(c), 4(c) and 5(c). This is accomplished by taking product of the line density of the pinhole image by waveforms obtained by the photomultipliers which is weighing averaged over channels in order to correct variation in sensitivity depending on channel arrangement and the source location. Waveform distortions due to the system impulse response were corrected by an inverse filter. Some ripples appeared in the display during this procedure.

2.5 Interferometry

To obtain the electron density of the pinched plasma a Mach-Zehnder interferometer was employed. The light source was a TEA N_2 laser whose light pulse was less than 1 ns in FWHM. The interferogram was registered on a Polaroid 665 film. In order to correlate pinch dynamics with the X-ray emission, the timing of exposure was recorded on the oscilloscope for each discharge.

The alignment of the diagnostic tools is shown in Fig. 2.

3 Results and Discussion

Hot spot generation in this experiment was not reproducible in number or in brightness shot to shot. In this chapter we present three examples typically observed in the experiments. The first example in which several hot spots spread along the electrode axis is shown in Fig. 3(a). A clear correlation is recognized between the pinhole image and peaks in the temporally and spatially resolved X-ray signals from photomultipliers as shown in Fig. 3(b). From them, we can construct a display similar to the streak photograph which indicates relationship between the location of sources and the time of appearance of sources (Fig. 3(c)). It is found that the hot spots appear near the inner electrode face in the earlier phase and are successively generated along the electrode axis. In this shot, the interferogram was taken 10 ns before the first X-ray signal (Fig. 3(d)). It can be seen that the $m = 0$ instability occurs at several parts of the pinched column and result in necking particularly at the point close to the anode. The first X-ray spot lies between the neck and the anode as shown in Fig. 3(a).

In the second example, filamentary soft X-ray sources are observed as shown in Fig. 4(a). The interferogram was taken just before the beginning of the soft X-ray emission (Fig. 4(b)). A pinch column with radius of 0.5~2 mm have been formed. In this case the soft X-ray emission is generated from the whole pinched region at maximum compression (Fig. 4(c)).

The third example, an X-ray radiating column which was somewhat elongated along the electrode axis can be seen as shown in Fig. 5(a). In this case, the interferogram was taken approximately 7 ns after the peak emission (Fig. 5(b),(c)). It is obviously recognized that a lack of the plasma column for about 4 mm. The extreme constriction of pinch can be responsible to X-ray radiation in this shot. However, it is considered that at the moment at which the interferogram is taken, the extremely pinched plasma is already extinguished.

The outflow of charged particles along the pinch axis will result in a decrease in density in the pinch column.[3,9] After processing the pinhole picture shown in Fig. 5(a) by the

Penumbra method[10], we can recognize the X-ray source consisting of two bright cores (250 μm in radius, ~1 mm in length). Characteristic time of the decrease in the line density due to plasma outflow is $\tau \sim h/c_a$, where h is the height of the necking part of the pinch and c_a is the Alfvén speed.[3] For our plasma h and c_a were evaluated to be 4 mm and 3×10^7 cm/s, respectively. Therefore, τ was estimated to be 1.3×10^{-8} s. It may be acceptable to suppose extinction of extremely constricted plasma at the time the interferogram was taken.

There are several parameters which affect the dynamics of the extreme constriction. They include the line density, the temperature, and the pinch current. The Pease-Braginskii current in this experiment is estimated to be 0.8 MA.[11] Therefore, the Pease-Braginskii current was barely reached by the discharge current of 0.8 MA. On the other hand, the axial flow of plasma causes decrease in line density. This energy loss prevent the radiative collapse in this experiment. It is seen that micropinching to a final radius of about 250 μm was achieved in a time scale of less than a few nanoseconds.

References

1) J. W. Shearer: Phys. Fluids **19** (1976) 1426.
2) A. E. Robson: Phys. Fluids **B1** (1989) 1834.
3) K. N. Koshelev and N. R. Pereira: J. Appl. Phys. **69** (1991) R21.
4) J. M. Bayley, G. Decker, W. Kies, M. Mälzig, F. Müller, P. Röwekamp, J. Westheide and Y. V. Sidelnikov: J. Appl. Phys. **69** (1991) 613.
5) P. Röwekamp, G. Decker, W. Kies, F. Schmitz, G. Ziethen, J. M. Bayley, K. N. Koshelev, Yu. V. Sidelnikov, F. B. Rosmej, A. Schulz and D. M. Simanovskii: *Dense Z-Pinches Third International Conference* , eds. M. Haines and A. Knight (AIP press, New York, 1993) p.332.
6) H. Kitaoka, A. Sakurai, T. Yamamoto, K. Shimoda and K. Hirano: J. Phys. Soc. Jpn. **64** (1995) 4191.
7) T. Yanagidaira, H. Kurita and K. Hirano: Jpn. J. Appl. Phys. **34** (1995) 5821.
8) Y. Takahama, J. Du, T. Yanagidaira and K. Hirano: Rev. Sci. Instrum. **65** (1994) 2505.
9) P. S. Antsiferov, K. N. Koshelev, A. E. Kramida and A. M. Panin: J. Phys. D: Appl. Phys. **22** (1989) 1073.
10) D. Ress, R. A. Lerche, R. J. Ellis, S. M. Lane and K. A. Nugent: Rev. Sci. Instrum. **59** (1988) 1694.
11) K. Hirano and H. Kitaoka: J. Phys. Soc. Jpn. **65** (1996) 139.

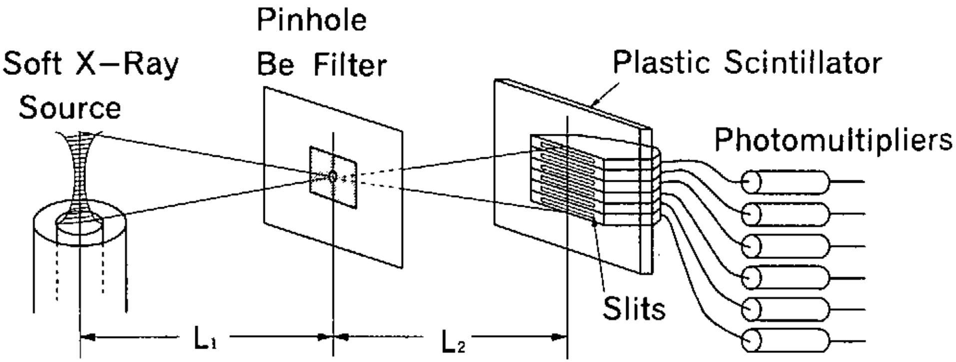

L_1=441 [mm], L_2=147 [mm]
Diameter of Pinhole : d=0.1 [mm]
Thickness of Be Filter : 25 [μm]
Thickness of Plastic Scintillator : t=0.2 [mm]
Slit width : w=0.1 [mm]

Fig. 1. Schematic diagram of detection system.

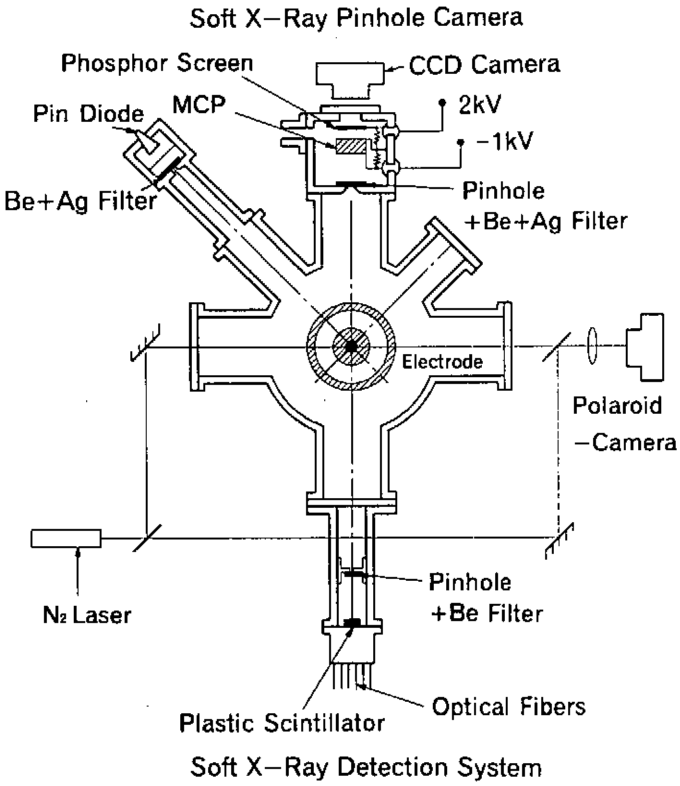

Fig. 2. Alignment of the diagnostic tools.

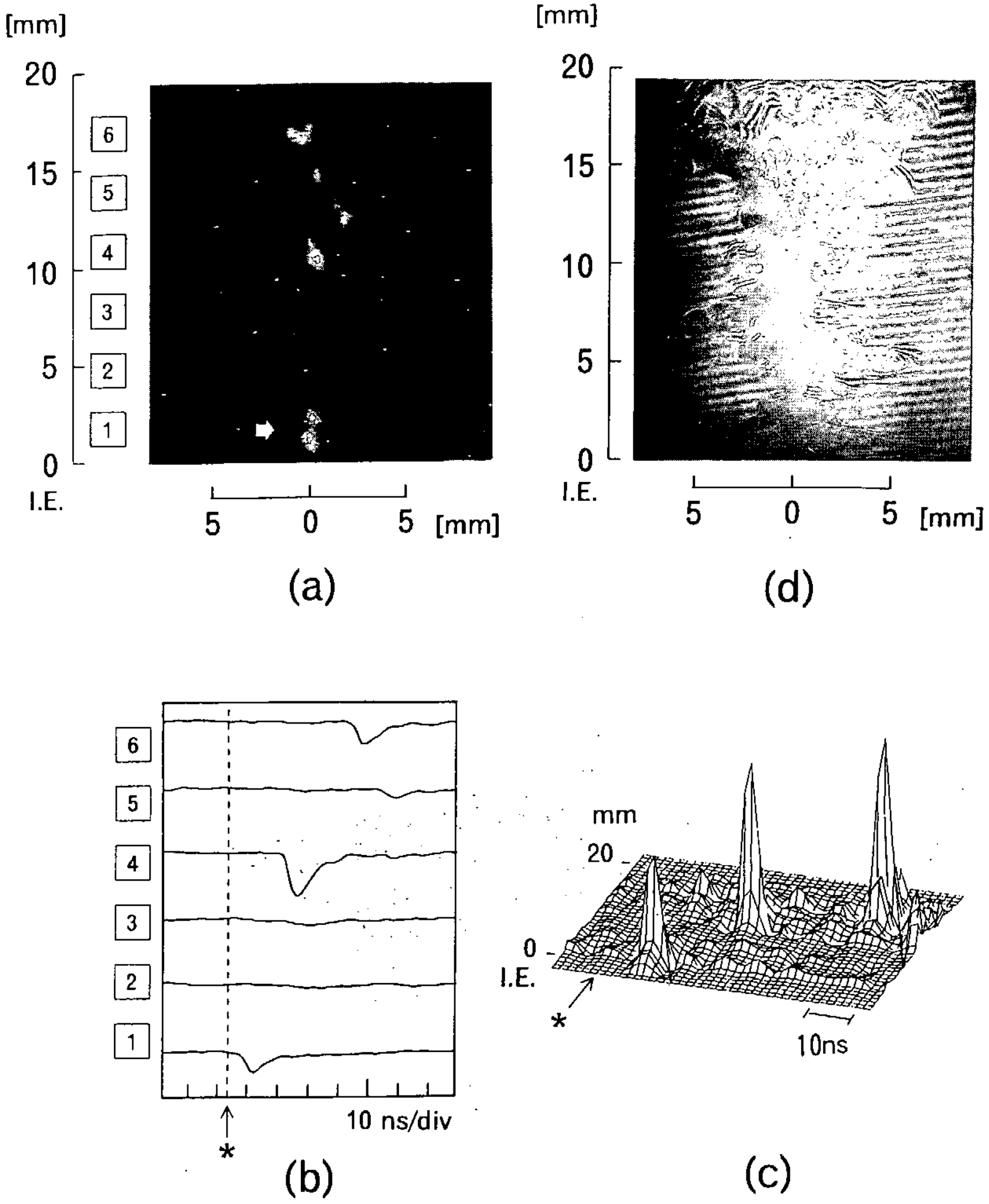

Fig. 3.

(a) Time integrated soft x–ray pinhole picture. several hot spots are observed. The first spot is pointed by an arrow. I.E.: Inner Electrode.

(b) Photomultiplier signals from each channel. The timing for the interferogram is shown by an asterisk '*'.

(c) Time history of x–ray emission.

(d) Interferogram of plasma taken 10 ns before the x–ray emission.

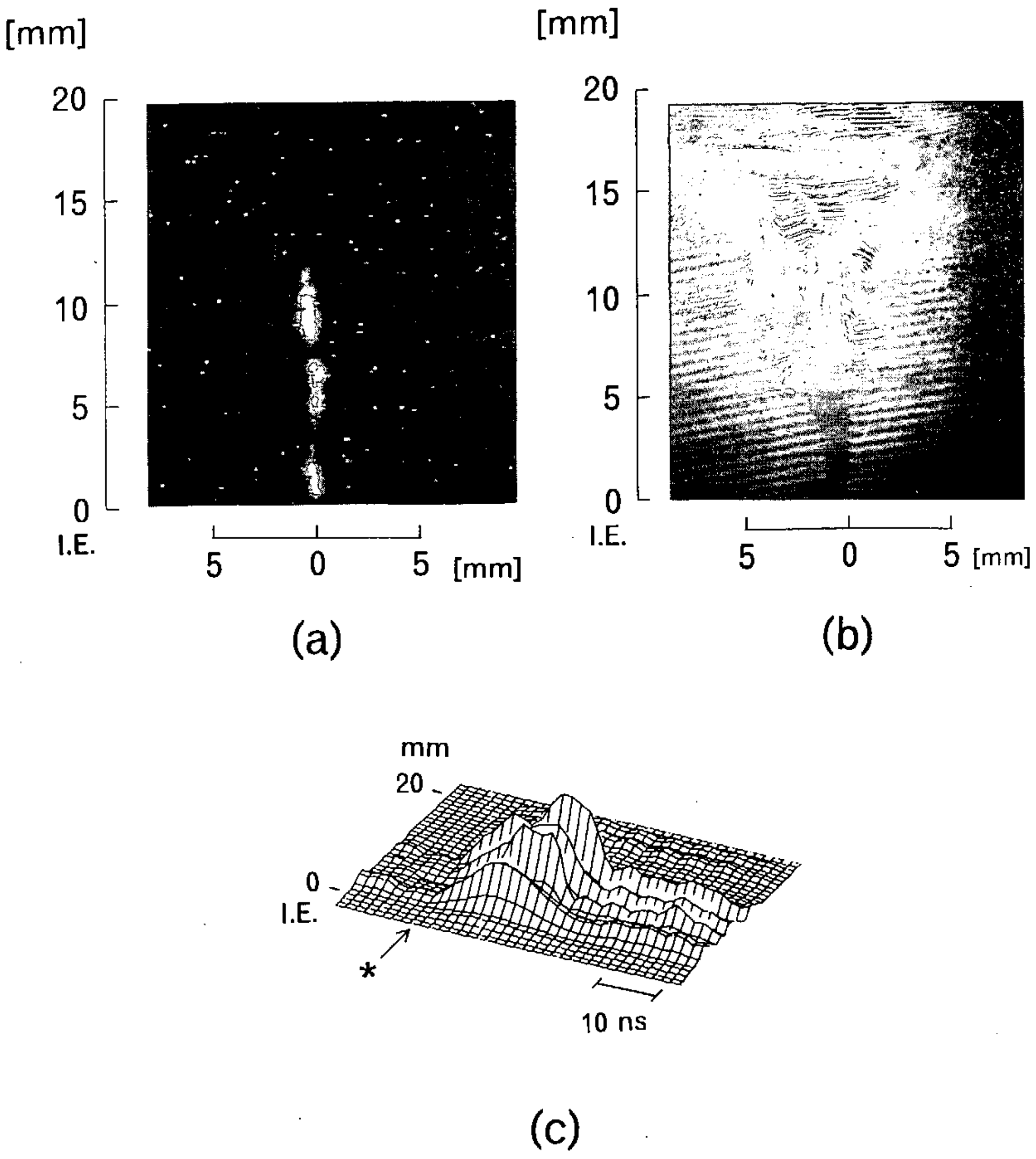

Fig. 4.
(a) Time integrated soft x–ray pinhole picture. Filamentary sources are observed.
(b) Interferogram of plasma taken immediately before the x–ray emission.
(c) Time history of x–ray emission.

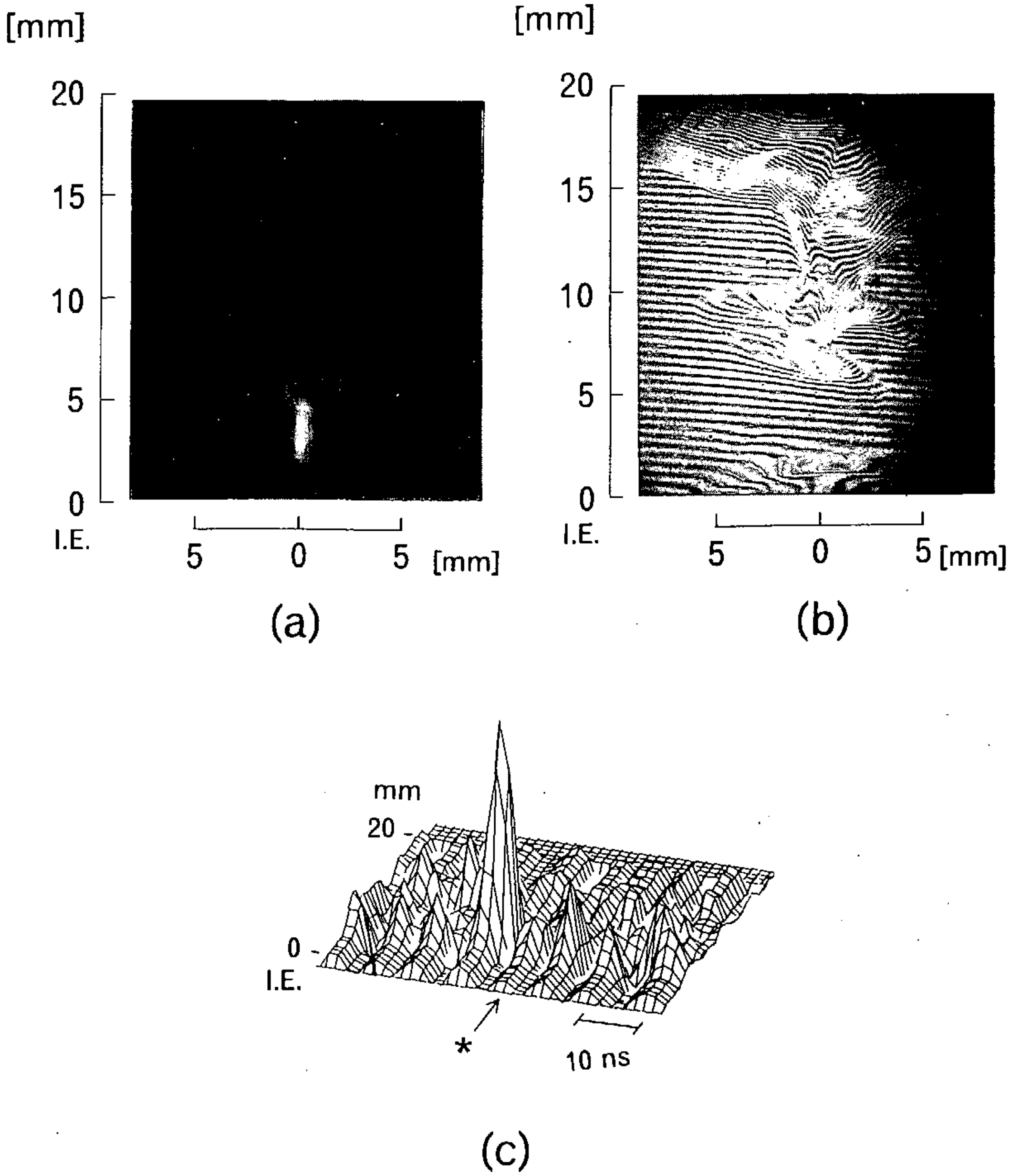

Fig. 5.
(a) Time integrated soft x–ray pinhole picture. The x–ray source consists of two bright cores.
(b) Interferogram of plasma taken 7 ns after the peak emission. There appears a large gap in plasma column.
(c) Time history of x–ray emission.

Spatial distribution of the soft X-ray emission in 150 kJ plasma focus with a high Z gas puff

H. Kitaoka, A. Sakurai, T. Yamamoto, K. Shimoda, M. Sato and K. Hirano
Department of Electronic Engineering, Gunma University
Kiryu, Gunma 376, Japan

Abstract

Intense soft X-rays were generated by a plasma focus device with a fast acting valve for additional Ar gas puff. When the delay time (from opening the valve to the begining the high current discharge for plasma focus) was 6ms, the soft X-ray emitting was filamentary. On the other hand when the delay time was longer than 7ms, the soft X-ray spots were spread.

1. Introduction

Soft X-ray source with high brightness is required for a lot of purpose and as X-ray spectroscopy, high density lithography for the manufacture of electronic devices, X-ray microscopy and X-ray laser pumping. Suitable soft X-ray source can be produced in the high energy density plasma by Z pinch and the plasma focus.

In the pinch plasma experiment, the soft X-ray emission comes from very small regions known as the hot spots or micropinch when high *Z* materials are admixed into hydrogen or deuterium which are normally employed in the Z pinch experiment (1-3) . However, the strong collapse occurs in a narrow region of the percentage of admixed gas.

In the gas-filled mode the soft X-ray images are typically divided into three categories, that is, they are filament, spots and, mixture of spots and filament, in spite of the identical experimental condition. The various features of the soft X-ray radiation are considered to be turning by reproducibility in shot to shot. The strongest soft X-ray emission was obtained in the filament category (4) .

In the previous paper, we compared the intensity of the soft X-ray emissions with the plasma focus device between with and without gas puff (5) . It was clarified that the soft X-ray intensity by the plasma focus device with high *Z* puffing is more than one order higher than that of the gas embeded with additional high *Z* gas.

However, it is found that there is much difference in the soft X-ray intensity and the shape of the source. They depend on the delay time which is from the opening of the fast acting valve to the high current discharge of the plasma focus.

We examine effects of the delay time on the intensity and the shape of the soft X-ray source generated in the plasma.

2. Apparatus

2.1 Plasma focus device

A Mather type plasma focus device with a squirrel cage outer electrode was employed to produce a high energy density plasma. A cross sectional view of the device is described elsewhere [5]. The diameters of coaxial electrodes are 50 and 100mm. The lengths of outer- and inner electrode were 230 and 280mm, respectively. The condenser bank consisted of 28 × 1.56 μF, 80kV capacitors. The device was operated at the bank voltage of 45kV in this experiment.

Argon was puffed with a fast acting valve through the inner electrode immediately before each discharge. The hydrogen base pressure of 8 hPa and the argon plenum pressure of 0.3 MPa were employed.

2.2 Diagnostic Tools

A soft X-ray pinhole camera with a quantitative image acquisition system has been developed for soft X-ray image observation with time resolution. A pinhole image of the X-ray source is made on the MCP through a pinhole and Be-Ag combination foil filter (25 μm and 1 μm in thickness, respectively) which prevent the visible light also emitted from the source. The spectral response of the MCP system is described in a previous paper [6]. The combination of the filters and the MCP gives a pass band between 3.7 and 7 Å, which accepts Ar *K*-lines (~ 4 Å). Using the system we can evaluate a number of photons which pass through the pinhole after taking absorption by the metal foils into account.

The soft X-rays were monitored with an X-ray PIN diode which was coupled with the filter as the pin hole camera. The viewing field of the diode is limited by a collimator to observe only plasma produced by the discharge.

The alignment of the diagnostic tools is shown in Fig. 1.

3. Result and Discussion

We observed the filament source and the spot source in the soft X-ray image. The shape of the soft x-ray source in the plasma can be varied by changing the delay time.

When the delay time was shorter than 6ms in the device, Ar *K*-lines was not observed. When the delay time is 6ms that corresponds to small gas puffing, the soft X-ray emitting was mostly filamentary and sometimes accompanied one or two small spots (Type I).

On the other hand, when the delay time was longer than 7ms, typical several intense examples spots appeared (Type Ⅱ) of the soft X-ray images are compaired in Figs. 2(a) Type Ⅰ and Type Ⅱ . The soft X-ray image of a filament and a spot along the electrode axis is seen in the Type Ⅰ , whereas that of a lot of scattered spots are observed in the Type Ⅱ .

The spatial distributions of intensity in contour plots are shown in Figs. 2(b) Type Ⅰ and Type Ⅱ . A few bright cores are seen along the electrode axis in Fig. 2(b) Type Ⅰ , whereas the bright spots are spread in Fig. 2(b) Type Ⅱ .

The phosphor currents of the pinhole camera, which are the time history of soft X-ray emissions, are shown in Figs. 2(c) Type Ⅰ and Type Ⅱ . Type Ⅰ has a single intense pulse but Type Ⅱ has several pulses, which correspond to each spot 7) . This means that the hot spots are generated successively. The soft X-ray emission in Type Ⅰ is stronger than ~ 1 order that of Type Ⅱ .

The soft X-ray outputs in the axial direction are shown in Figs. 2(d) Type Ⅰ and type Ⅱ . These are calculated by using Figs. 2(b) Type Ⅰ and Type Ⅱ . It is clear that Type Ⅰ is higher intensity and smaller in size than that of the type Ⅱ . In Type Ⅱ , two peaks caused by the scattered spots are recognized.

The locations of the hot spots exist to be the constricted part of the plasma column. In conclusion, it is easy to generate a compact and filamentary soft X-ray source in the plasma focus.

References

1) J. M. Bayley, G. Decker, W. Kies, M. Mälzig, F. Müller, P. Röwekamp, J. Westheide and Y. U. Sildelnikov: J. Appl. Phys. **69**(1991)613.
2) I. V. Volobuev, V. A. Gribkov, D. Denus, N. V. Kalachev, T. A. Kozlova, O. N. Krokhin, S. Sledziński, S. A. Startsev and S. Czekaj: Sov. J. Plasma Phys. **14**(1988)401.
3) R. Lebert, A. Engel, K. Gäbel, D.Rothweiler, E. Förster and W. Neff: *Dense Z-Pinches Third International Conference,* eds. M. Hains and A. Knight (AIP Press, New York, 1993) p.324.
4) K. Hirano and H. Kitaoka: J. Phys. Soc. Jpn. **65**(1996)139.
5) H. Kitaoka, A. Sakurai, T. Yamamoto, K. Shimoda and K. Hirano: J. Phys. Soc. Jpn. **64**(1995)4191.
6) Y. Takahama, J. Du, T. Yanagidaira and K. Hirano: Rev. Sci. Instrum **65**(1994)2505.
7) T. Yanagidaira, H. Kurita and K. Hirano: Jpn. J. Appl. Phys. **34**(1995)5821.

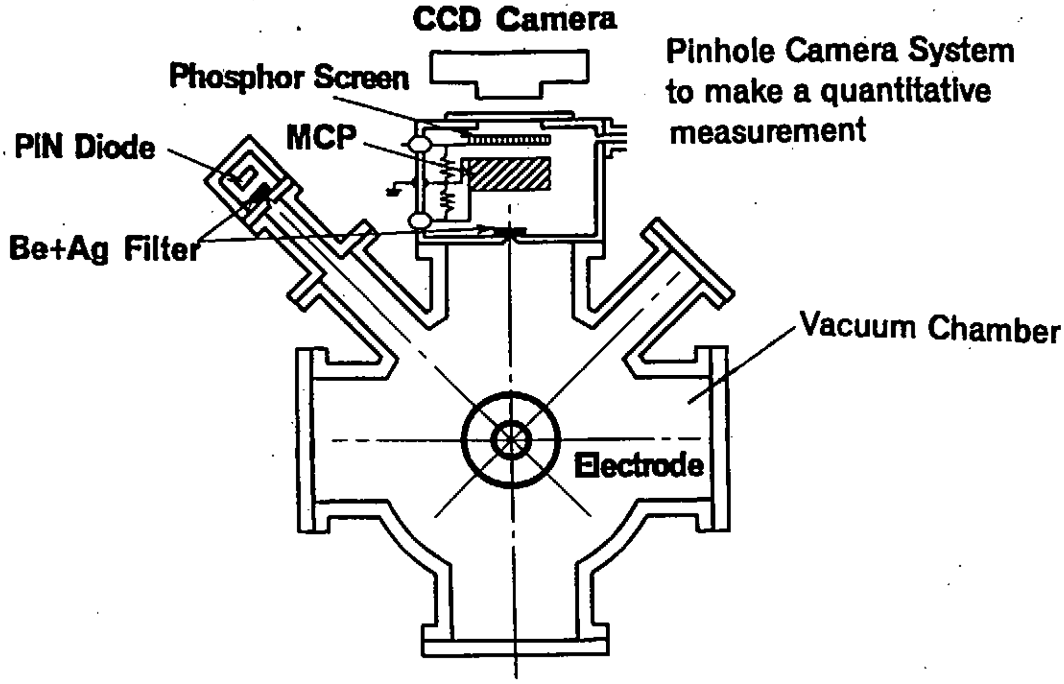

Fig.1. Alignment of diagnostic tools

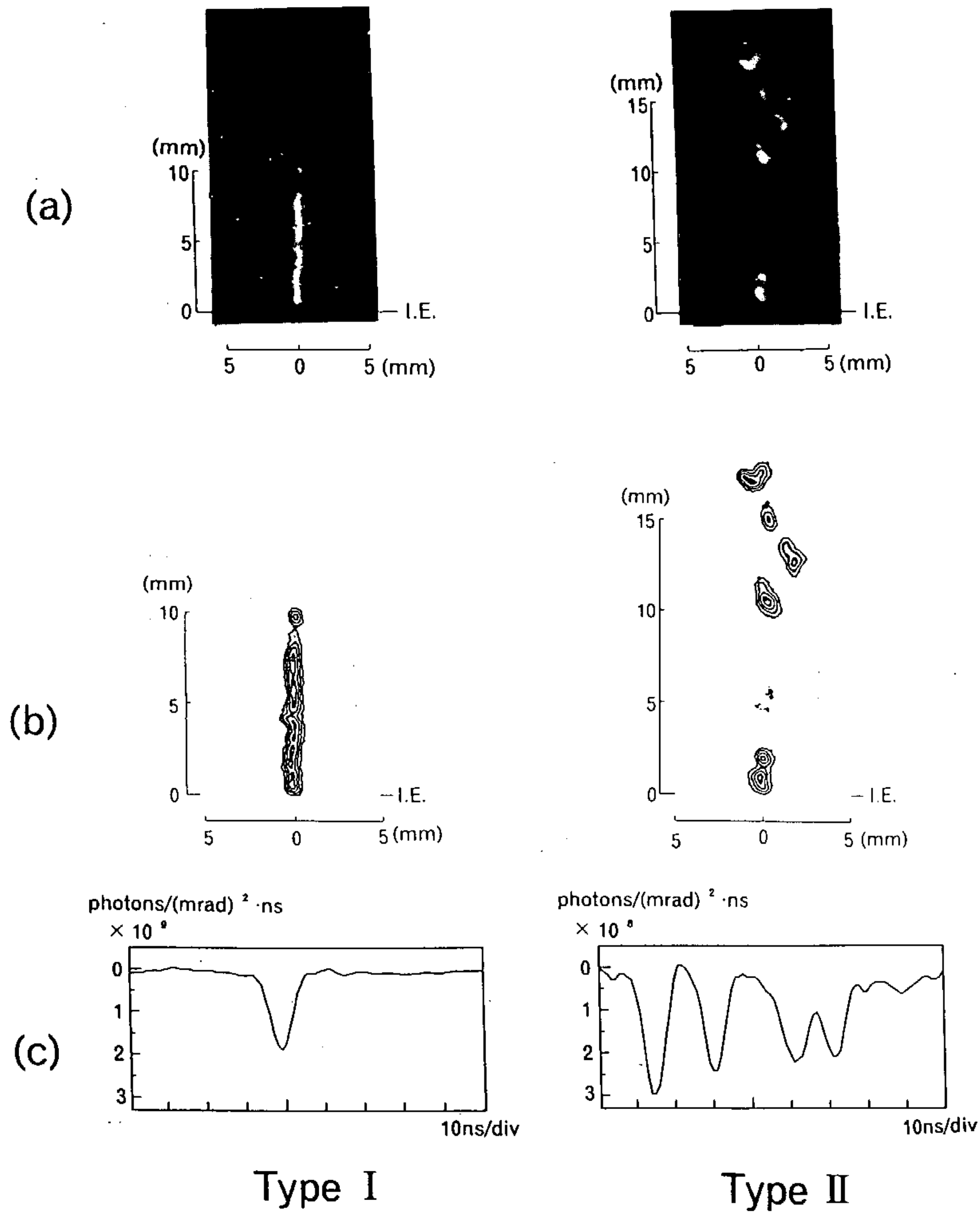

Fig.2. Correlation between the pattern of the soft X-ray emission region and the soft X-ray intensity. (a) ~ (d) in each type are same experimental shot.
In Type I is the filamentary source of the soft X-ray emission. On the other hand Type II is the spread spot source.
(a) Examples of soft X-ray pinhole image. (b) Contour plots of the soft X-ray intensity, lines pairs per 3.0 × 10^8 photons/mm^2·mrad^2·1shot. (c) Time history of the soft X-ray emission. Each peak correspond to filament or spots.

(d)

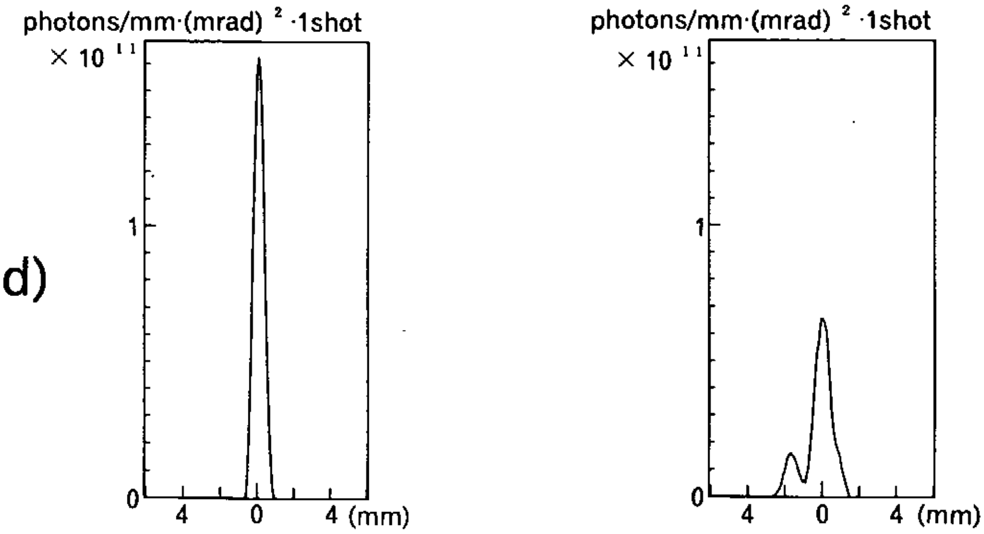

Type I

Type II

(d) Calculated results of the soft X−ray intensity in the direction of the electrode axis. Calculation was made using Fig.2 (b).

Pinch Characteristics and Soft X-ray Radiation of Z-Pinch Plasma Produced by Fine Particle Injection

Daiju Itagaki, Seizo Furuya, Daigo Kaneko, Tatsuya Okuda and Shozo Ishii

Tokyo Institute of Technology

Abstract

A fine particle Z-pinch plasma, which can be an excellent soft X-ray source, has been firstly demonstrated. A method of particle injection using shock wave enabled to produce the Z-pinch plasma from the fine particles. A number of fine particles with the diameter ranging from 1μm to 100μm were injected between electrodes within 30ms. These particles were made, evaporated and ionized by high current of about 300kA to form Z-pinch plasma.

Intense soft X-ray emissions were observed when the number and the size of fine particles were optimized.

1 Introduction

Z-Pinch plasma is expected to be a compact and intense soft X-ray source [1]. In general, the initial state fo Z-pinch plasmas are roughly divided into gases and solids. The metal vapor plasma is produced from solid materials, such as fibers or array of wires.

The gas-puff Z-pinch has an advantage of high repetition rate operation, however, the medium of the plasma is limited. On the other hand, the fiber Z-pinch plasma can be produced from various materials [2]. Usually, frozen deuterium, carbon or metallic fibers are used. The advantage of the fiber Z-pinch is to obtain the high plasma density and wide range of X-ray emission spectrum. This plasma is also studied for X-ray laser application. However, it is difficult to set the fibers with the diameter of about 10 $\sim$ 300μm between the electrodes.

Recently, we have proposed a new method of Z-pinch, in which the fine particles with the diameter ranging from 1μm to 100μm are used as a plasma medium. Fine particles have both characteristics of the solid and gaseous materials. Therefore, this method would combine both advantages of the gas-puff Z-pinch and the fiber Z-pinch [3]. The fine particles must be injected rapidly from a small nozzle to the discharge space. Immediately, these particles are evaporated and ionized by high current pulse. When the plasma pinches, the soft X-ray is radiated.

We performed several basic experiments for fine particle injection. To realize the fast and easy control of the particle injection, we had used the electrostatic acceleration [3]. However, the total mass of injected particles was too small to initiate a discharge.

We concluded that the sufficient amount of the fine particles is necessary to initiate a Z-pinch plasma. In this study, a new injection system has been established utilizing a shock wave effect. A number of particles have been injected. The discharge has initiated between the Z-pinch electrode, of which gap is longer than 5mm. In order to fully evaporate and ionize the injected particles, we used a high energy capacitor discharge. The soft X-ray emission and the number of injected particles are measured simultaneously.

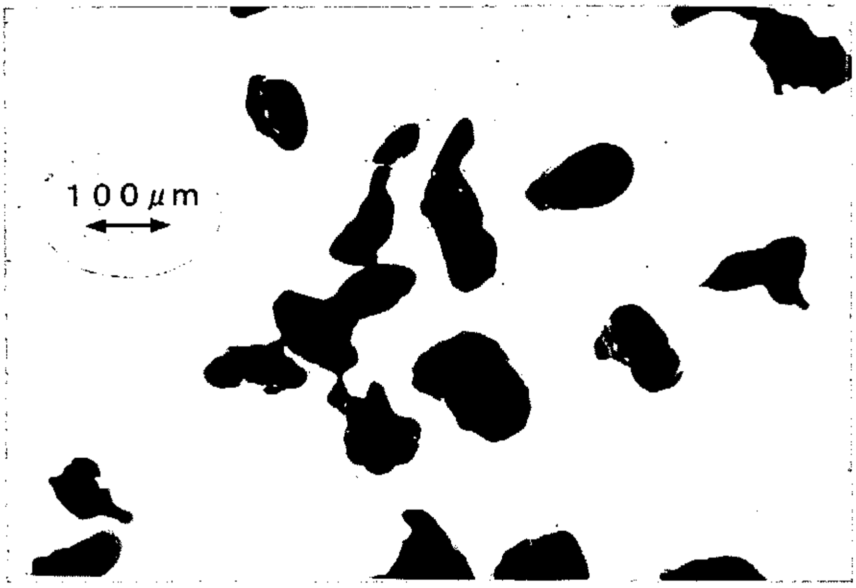

Figure 1 Microscopic photograph of Al fine particles

2 Experimental Setup

Figure 1 shows the Al fine particles observed by a microscope. The black part of the figure shows the Al particles. The average diameter is about 100μm.

Figure 2 shows the schematic diagram of the apparatus. This apparatus is divided into three parts, such as particle injection section, main discharge chamber, and capacitor banks. The plasma was produced in a vacuum chamber evacuated to a pressure of less than 5×10^{-4} Torr.

Figure 3 shows the particle injection section and the main discharge section. Three metallic electrodes named such as (Upper, Middle, Lower), are used. The electrode *M* is connected to the earthed point. The electrode *M* and the *L* act as the particle injection electrodes. The Z-pinch plasma is produced between the *M* and *U* electrodes. The gap length is 5mm. In order to decrease the breakdown voltage, the electrode configuration is determined to enhance the electron emission from the cathode. A graphite needle electrode is used as cathode. Cathode is operated as high voltage side. A brass plane electrode is used as anode. The main bank capacitance is 27μF. The charging voltage is 20kV, therefore, stored energy is 5.4kJ. The peak current and the rise time are about 300kA, about 2.5μs, respectively.

In Figure 3, the fine particles are stored on the electrode *L*. Four copper foils are connected with the electrode *M* for generating shock waves. Another end of the foil almost touches the particles. The electrode *L* is connected with a 5.4μF capacitor bank charged up to 15kV. When the switch fired, discharge occurs between the particles and the copper foils. Then, strong shockwave is produced near the particles. By this shock wave, the particles are blowed up and some parts of them are injected through the hole of the electrode *M* between Z-pinch electrodes. Injected particles are immediately ionized between electrode *U* and *M*.

In this study, four kinds of measurement were performed. Figure 4 shows the measuring system, which consists of four portions. First, the number of the injected particles was measured by means of a laser transmitting method. Injected fine particles are irradiated with 633nm He-Ne laser light. The light transmits through the discharge region and is received by a photodetector. When there are no fine particles, the detector picks up signal constantly. When the fine particles are injected, the detector signal decreases. An interference filter is used to prevent the strong light from main discharge.

In order to observe the dynamics of the plasma, a high speed framing camera (IMACON 792) was used. The framing speed is 10 frames/μs and the exposure time is 20 ns. Time integrated visible spectral emission from the plasma was observed by an optical multichannel anallizer (OMA).

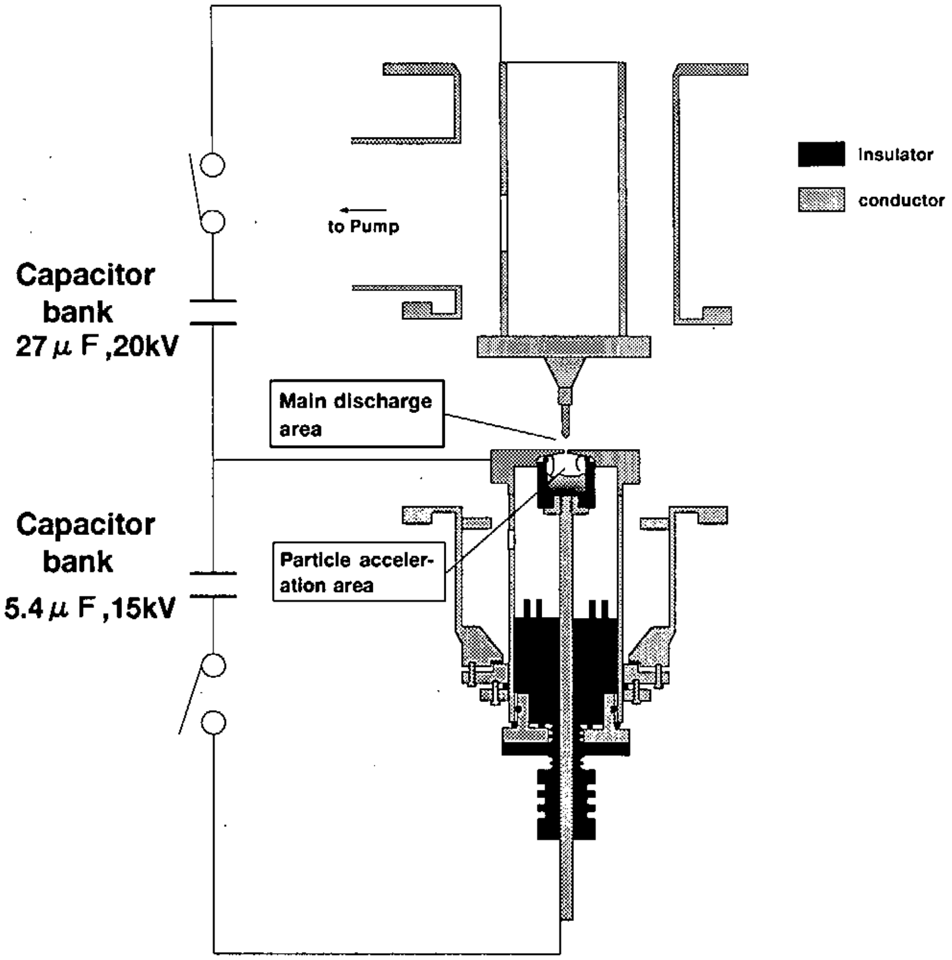

Figure 2 Schematic diagram of the experimental apparatus

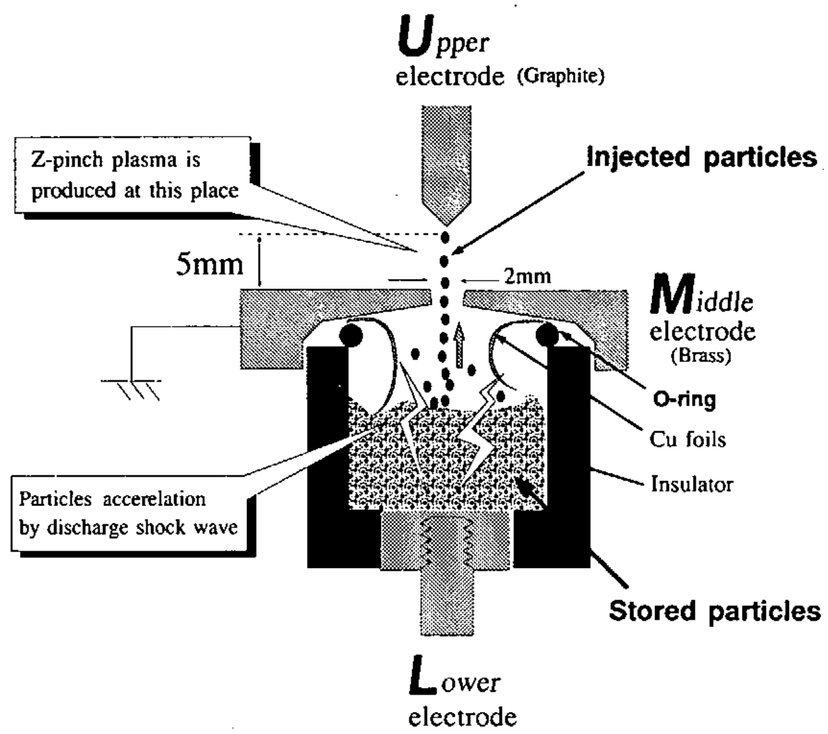

Figure 3 Schematic view of injection and discharge electrodes

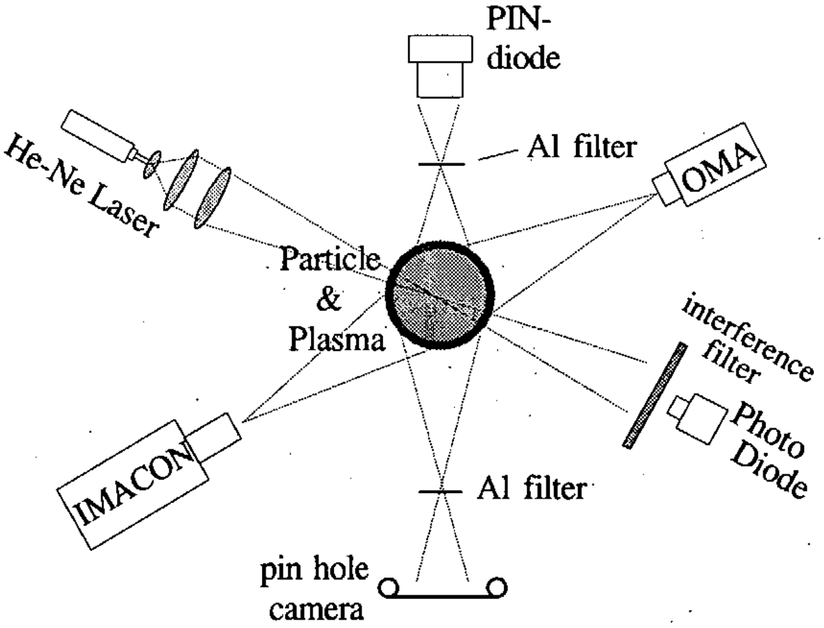

Figure 4 Measuring system

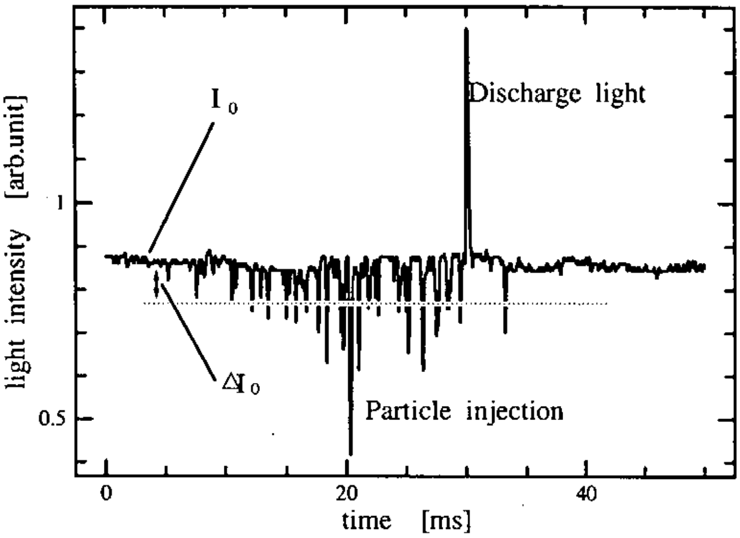

Figure 5 Typical waveform of the transmitting light intensity

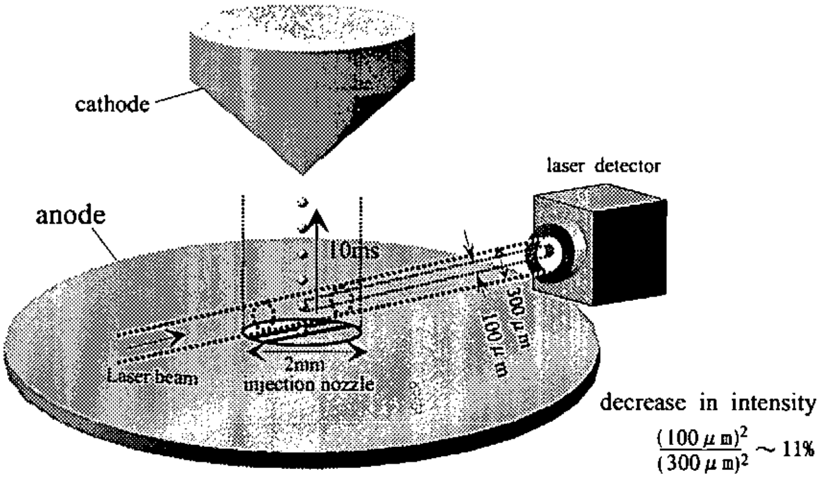

Figure 6 Estimation of the diameter of the laser beam

The soft X-ray emission from the plasma was observed by a PIN diode and also by a pinhole camera with Al filter of 8μm is used. This detector can sense the X-ray spectrum above 0.8keV.

3 Experimental Result

Figure 5 shows the typical waveform of the transmitted light intensity through the injected fine particles. One peak pulse corresponds to one fine particle. About 30 particles are detected until 30ms. Then main discharge is initiated. The particle velocity and the number density can be estimated using this Figure 5.

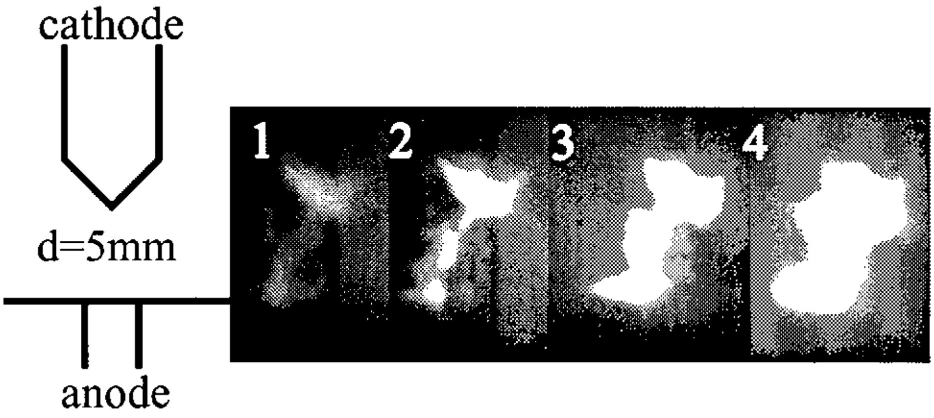

(a) Framing photograph

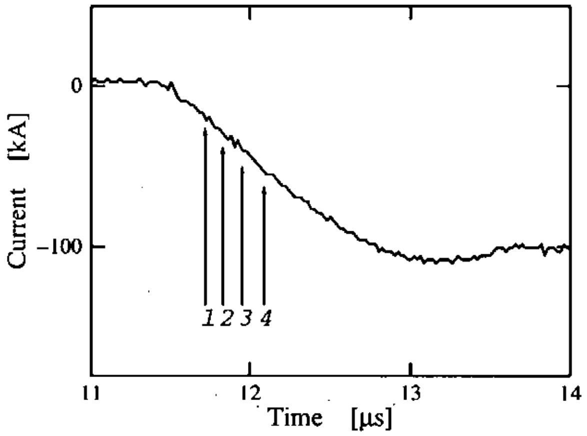

(b) Timing of the frame

Figure 7 Macroscopic behavior of the plasma

The distance between the storage space of the particles and the axis of laser beam is 15mm. Therefore, the mean velocity of the particles is calculated as below.

$$15\text{mm}/30\text{ms} = 0.5[\text{m/s}] \tag{1}$$

The laser system is shown in Figure 6. The diameter of the injection nozzle is 2mm, however, the diameter of laser beam is only about 300μm. Therefore the real number of injected particles is 5 times as many as the number detected by the laser method.

Figure 7(a) shows the sequential motion of the plasma and (b) shows the timing of the framing photographs. Discharge occurs along the several particles in the frames 1-2. About ten particles are seen in the frame 2 around the discharge path. The expanding velocity of the plasma is about 1cm/μs.

Figure 8 shows the visible emission spectrum from the plasma. Al I(atom) and Al III(ion) spectrum are observed when the Al fine particle is used. Cu I, Cu II, Zn I spectra are also observed when the brass anode is used.

Figure 9 shows the time integrated soft X-ray image observed by the pinhole camera. The soft X-ray is emitted from a small region called "hot spot".

Figure 10 shows the relations between the number density of fine particles par unit length and the emission intensity of soft X-ray. When Al particles with the diameter ranging about 100μm are discharged, emission intensity is weak. On the other hand, intense soft X-ray emission is observed when about 50,000 particles of copper with the diameter ranging about 1μm is evaporated and ionized.

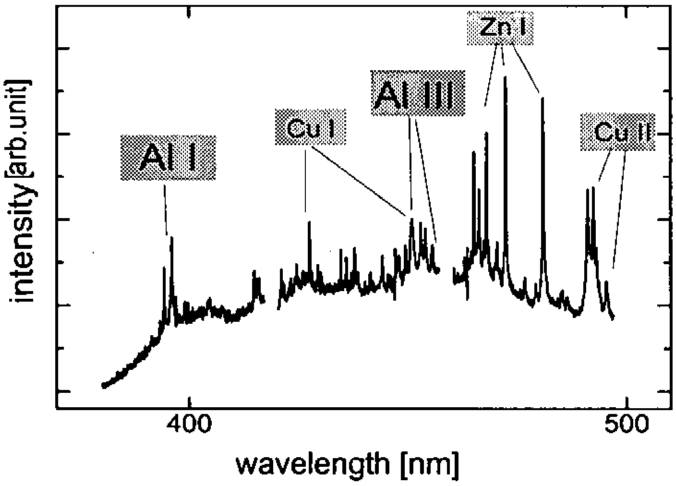

Figure 8 Visible emission spectrum of the plasma

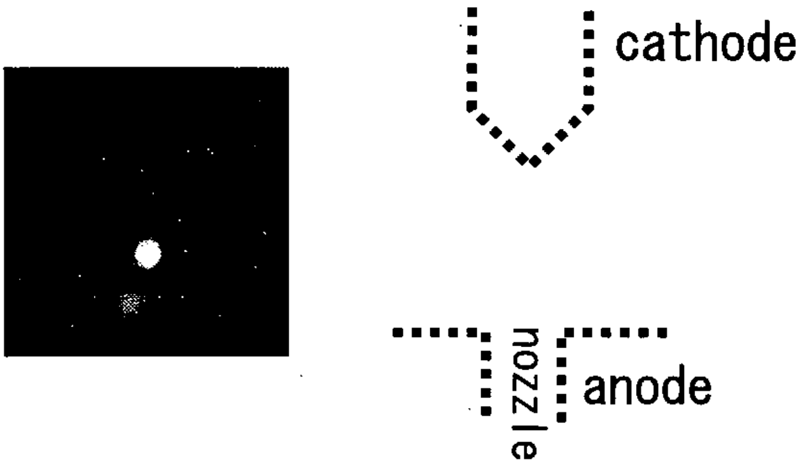

Figure 9 Pinhole photograph

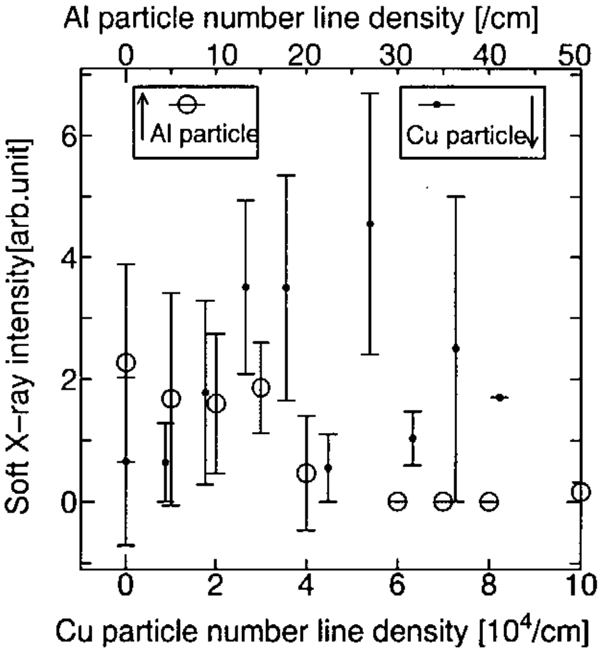

Figure 10 Relation between particle linear number density and the emission intensity of the soft X-ray

4 Discussion

The calculation of the number of particles needed for discharge initiation is important. The particles will be partially evaporated by the prebreakdown current emitted from the cathode. This model was proposed by Biondi et. al. [5]. The minimum number density is about 2×10^{16}atoms/cm^3 when the electrode separation is 5mm and the applied voltage is 20kV. If just one particle of 100μm diameter is fully evaporated, the discharge can be initiated. However, prebreakdown current is too small to fully evaporate such a large particle in several microseconds. Therefore, it seems that the discharge is initiated not only by the injected particles but also by the particles adhering to the electrodes. From the visible spectrum in Figure 8, the evaporation from the fine particle and the electrode material is estimated to be comparable.

As shown in Figure 10, intense soft X-ray emission is observed when the small particles are used. If particles are too big and too many, they can't be fully evaporated in the initial discharge process. In that case, plasma temperature might be low.

Moreover, the emission intensity is weak when the particle density is too low. It might be because that the temperature increase cannot be compensated by radiative energy loss efficiently.

5 Conclusion

A novel method of Z-pinch plasma by using the fine particle injection is established. We developed a particle injection system by means of a shock wave. The particles are injected within about 30ms. The atomic and ionic spectra which correspond to the material of the fine particles were observed. Therefore, we conclude the evaporation and ionization of the fine particles by high current discharge has been established for the first time. Intense soft X-ray emissions are observed when about 50,000 particles with the diameter of 1μm are evaporated and ionized.

References

[1] M.Yokoyama et.al. : Plasma Rikogaku (in Japanese), p195-200, (1988)

[2] W.Kies et.al. : J.Appl.Phys., Vol.70-12, p7261,(1991)

[3] T.Hoshide et.al., NIFS-PROC-18, p107(1994)

[4] Q.P.Ai et.al., NIFS-PROC-23, p176(1995)

[5] D.K.Davies and M.A.Biondi : J.Appl.Phys., Vol.39-7,p2979,(1968)

The soft x-ray radiation from Z-pinch plasma produced by injecting metal vapor; the vapor is produced by a wire explosion

E. Goto, S. Furuya, B. Rahmani, O. Tsuboi and S. Ishii
Department of Electrical and Electronic Engineering, Tokyo Institute of Technology,
O-okayama, Meguro-ku, Tokyo 152, JAPAN

If it is possible to make any kind of elements into plasma, we can obtain a greater number of spectral lines emitted from the plasma. To create a hollow cylindrical metal plasma by Z-pinch, we have proposed a pre-discharge with a small capacitor to make metal wire into vapor to be injected between Z-pinch electrodes. To establish the maximum pinch at the current peak of 300kA in 2.5μs, initial radius and mass per unit length of the cylindrical plasma have been optimized. In Z-pinch experiments, we confirmed that maximum pinch occurred just before the Z-discharge current peak. At the same time, we obtained intense soft x-ray radiation from the plasma.

1. Introduction

Z-pinch plasma can easily create high-energy-density plasma, and is used as a high intensity pulsed soft x-ray source and soft x-ray lasers(1). Since the implosion of hollow cylindrical plasma proposed by Turchi and Baker(2), such as imploding liner(3), wire array(4) and hollow gas puff Z-pinch(5), transfer the energy from a energy storage bank to plasmas efficiently. UV and soft x-ray radiation can be obtained from Z-pinches driven by the even small power supply. The gas puff Z-pinch has the advantage in high repetition rate operation. Since puffing material must be gaseous state such as Hydrogen or noble gases, solid elements are not applicable in gas puff Z-pinch.

To obtain high intensity x-ray radiation from the plasma, K-shell emission from the element with the high atomic number, Z, is a promising way. Now the largest pulsed power supply in the world, Saturn(6), can ionize Cu (Z=29) atom to K-shell state. As the plasma medium is limited to gas, only Ar (Z=18) atom is available. K-shell spectral lines from Ar plasma is restricted. If it is possible to make any kind of elements into plasma, we can obtain a greater number of spectral lines emitted from the plasma. Making metallic elements with the high Z into plasma is necessary for photopumping of soft x-ray lasers, such as Na-Ne scheme(7), Al-Mg scheme(8) and Ne-Fe(9) scheme. In these schemes, metallic materials such as Na, Al, Mg and Fe must be highly ionized.

The wire array Z-pinch is conventional method to produce the imploding plasma. Gazaix has proposed to generate a hollow cylindrical metal plasma using an auxiliary discharge with metallic foil(10). In any case, these types of Z-pinch require complicated handling procedure to set multiple wire arrays or thin metallic foil in the apparatus. As a consequence, high repetition rate operation is impossible.

To overcome these problems in producing metal plasmas, we have proposed a novel Z-pinch scheme named *metal vapor puff Z-pinch*(11). This method uses pre-discharge with a small capacitor to make metal wire into vapor to be injected between Z-pinch electrodes. Another superiority of metal vapor puff Z-pinch is as follows. The metal wire has the high resistance compared to that of the thin metallic foil, it is easy to introduce the energy to the wire with a simple electrical power system. A detailed description about the superiority is presented in Sec.2.2.

In Sec.2.1, a design of initial condition of metal vapor is described. In Sec.3, the experimental setup of metal vapor puff Z-pinch is written. In Sec.4.1, the characteristics of metal vapor puffing, before the main discharge current has been switched on, is presented. In Sec.4.2, metal vapor puff Z-pinch plasma by a wire explosion is described. The results of this report are summarized in Sec.5.

2. Production of hollow cylindrical metal vapor

2.1 Initial parameters of metal vapor

The initial radius and the line mass density must be optimized to establish the highest temperature and the intense soft x-ray radiation(12)-(14). Imploding dynamics of the hollow cylindrical plasma is simply analyzed by a following equation, namely "slug model".

$$m\frac{d^2r(t)}{dt^2}=-\frac{\mu_0 I^2(t)}{2\pi r(t)} \tag{1}$$

Where $I(t)$, m and $r(t)$ are the current, the mass per unit length and the radius of the plasma, respectively. There is a following relationship between m, τ, $I(\tau)$ and the initial radius of the plasma, R_0, where τ is the implosion time.

$$\frac{mR_0^{\,2}}{I^2(\tau)\,\tau^2}=const. \tag{2}$$

The energy transfer efficiency from the power supply to the plasma is maximized, when the maximum pinch is established at the current peak. The maximum current and its rise time are mainly determined by the parameters of the power supply.

In the Z-pinch experiment, we have used a conventional capacitor bank, in which the current rises up to 300kA in 2.5μs. Eq.(1) coupled with the circuit equation is solved numerically by the Runge-Kutta method. When mass is kept to be 1.0mg and R_0 is varied, the calculated imploding profiles are shown in Fig.1(a). The calculation is terminated at the time, in which the plasma radius becomes 10% of R_0. When the initial radius R_0 is 5mm, the maximum pinch is established rather before the current peak. On the other hand, as R_0 is 30mm, the pinch occurred after the peak. When R_0 is 15mm, the pinch is established at the current peak. From the result of calculations, we obtained the optimal value of mR_0^2 as follows:

$$mR_0^{\,2}=22.5\ \text{mg}\cdot\text{mm} \tag{3}$$

To certify the validity of Eq.(3), the calculation is carried out by using three different values of R_0 satisfying Eq.(3). The result is shown in Fig.1(b). In all cases, the pinch occurred at the time of current peak; apparently Eq.(3) is valid.

2.2 Electrical discharge system to make initial metal vapor

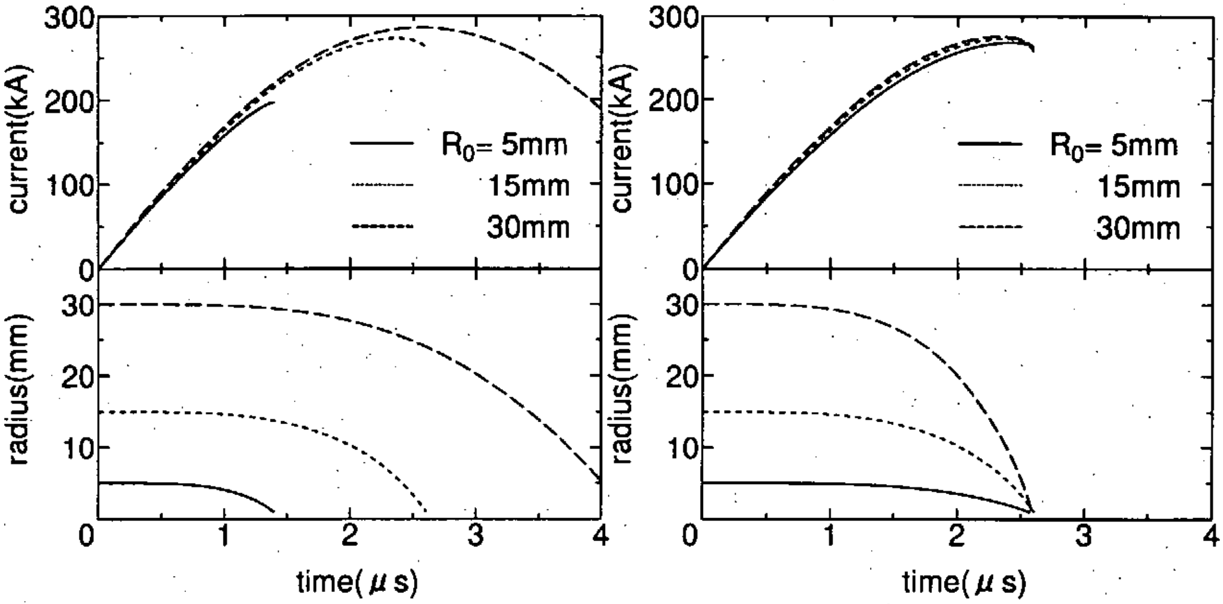

(a) $m = 1.0$mg/cm (b) $mR_0^2 = 22.5$mg·mm

Fig.1 The motion of the hollow cylindrical plasma calculated by slug model

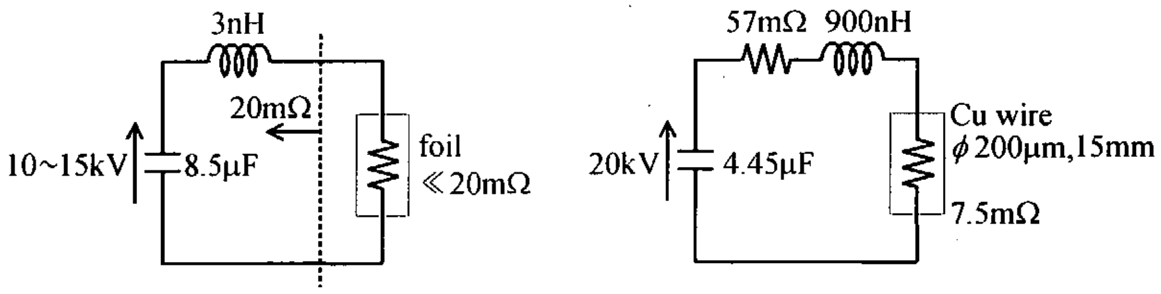

(a) Gazaix's method (b) Our method

Fig.2 The equivalent circuits to produce the hollow cylindrical metal vapor

Since R_0 is chosen to be 20mm in this experiment, $m = 0.6$ mg/cm is required. We have employed an exploding wire discharge excited by a small capacitor bank to obtain the cylindrical metal vapor jet. At first sight the method is seemed to be similar with Gazaix's one$^{(10)}$. However, the characteristics of the driving circuits are quite different. Since thin Al foil has low resistance in Gazaix's method, it is not easy to transfer the electrical energy into the foil completely. Therefore, a low impeadance generator with a dielectric surface discharge switch and a parallel plate transmission line must be used to suppress the resistance of the electrical system. The equivalent circuit in Gazaix's method is shown in Fig.2(a). On the other hand, metal wire has larger resistance which is comparable to that of the circuit on our method, so it is easy to transfer the electrical energy to the wire. Therefore, a conventional electrical system with a triggatron gap switch and coaxial cables (RG-8U) can be used. The equivalent circuit of our method is shown in Fig.2(b). Copper wire with the diameter of 200μm and the length of 15mm are used. The density per unit length of the wire is 2.8mg/cm, then the total mass of the wire is 4.2mg which is suitable for the optimized pinch condition mentioned before.

3. Experimental setup

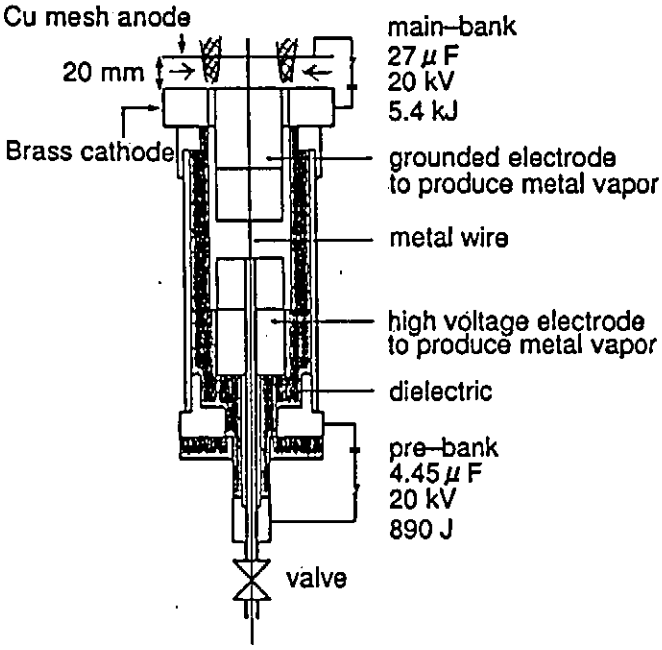

Fig.3 Experimental setup

The experimental setup is shown in Fig.3. An anode is made of copper mesh to eliminate stagnation of injected metal vapor. A grounded brass cathode is designed to produce metal vapor and has nozzles for vapor puffing. The main electrode separation is 20mm. The principle of metal vapor puff Z-pinch is similar to that of gas puff Z-pinch. The cylindrical metal vapor jet is produced by wire explosion powered by a pulsed high current discharge. As soon as the metal vapor reaches the anode, the main Z-discharge is fired. The main discharge is powered by a 27μF capacitor bank, *main-bank*, charged to 20kV. A 4.45μF capacitor bank, *pre-bank*, charged to 20kV also used to produce metal vapor. The stored energy of the main-bank and the pre-bank are 5.4kJ and 890J, respectively. Sixteen nozzle holes of 4mm-diameter are drilled at the cathode on a circle of 20mm radius to form a circular array of nozzles. We used a 200μm-diameter copper wire throughout the experiment. The metal wire must be set between the electrodes located under the main electrodes before each shot, a specially designed wire loading device enable us to set the wire without breaking vacuum. The discharge vessel is evacuated to about 5×10^{-5}torr by an oil-diffusion pump.

Temporal and spatial behavior of puffed metal vapor and Z-pinch plasma are observed by an image converter camera (HADLAND PHOTONICS: Imacon 792). Since the light intensity emitted from the puffed metal vapor was very week, an image intensifier has been added to the camera for observing vapor evolution. On the other hand, neutral density filters are placed in front of the camera lens for the measurement of Z-pinch plasma because of very strong light emitted from the plasma. We also use a glass window removed Si p-i-n photo diode (HAMAMATSU PHOTONICS: S1722-02) and an x-ray pinhole camera to observe temporal and spatial evolution of the soft x-ray radiation from the Z-pinch plasma. Since the photo diode and the x-ray pinhole camera has been operated with an 8μm-thick Al foil which can transmit soft x-ray of photon energy between 0.8 and 1.54keV and above 2keV. The pinhole camera has a 300μm-diameter pinhole and soft x-ray images are recorded on Fuji NEOPAN 400 PRESTO film.

4. Experimental results

4.1 Characteristics of metal vapor puffing

The visible light from the metal vapor was recorded by a photomultiplier (HAMAMATSU PHOTONICS: R1547 with the peak response of wavelength of 530nm and R446 with that of 330nm. An averaged spatial distribution of metal vapor was observed by open-shutter photograph. Temporal evolution of the injected metal vapor was recorded by framing and streak pictures.

Fig.4 is an open-shutter photograph of injected copper vapor. The nozzle is on the right side in the photograph. It is confirmed that the copper vapor is puffed keeping the arrayed profile without radial diffusion. Fig.5 shows the pre-discharge current waveform, the intensity of visible light from the injected copper vapor by the PMT R1547, and framing pictures in which the viewing area is the same as in Fig.4. The pictures were taken for the exposure time of 0.2μs at 1μs intervals. The framing timings are also shown in the figure. The copper vapor begins to exit the nozzle at 5μs after the initiation of the pre-discharge. However, the frame 5 shows the copper vapor just starting to exit the nozzle at 11μs. This disagreement originates from the differences of the sensitivity of the instruments. The copper vapor moves away from the nozzle to the center of view in the frame 6 and reaches on the left of view in the frame 7. The puffed copper vapor velocity is the order of 1cm/μs estimated from the frame 5-7.

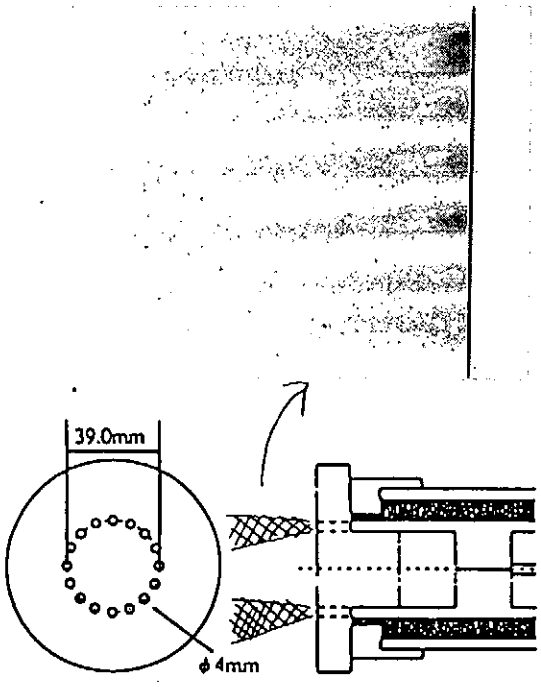

Fig.4 Open-shutter photograph of copper vapor

We took the streak pictures to measure the puffed metal vapor velocity. A slit is located parallel to the puffing direction (z-axis). Fig.6 shows the streak picture, the pre-discharge current waveform and the intensity of visible light from the copper vapor obtained by the

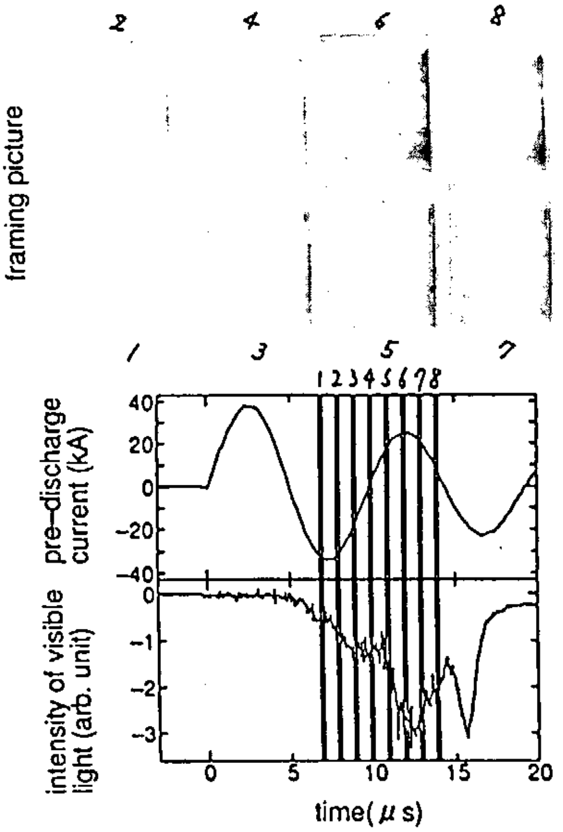

Fig.5 Pre-discharge current waveform, intensity of visible light and framing picture

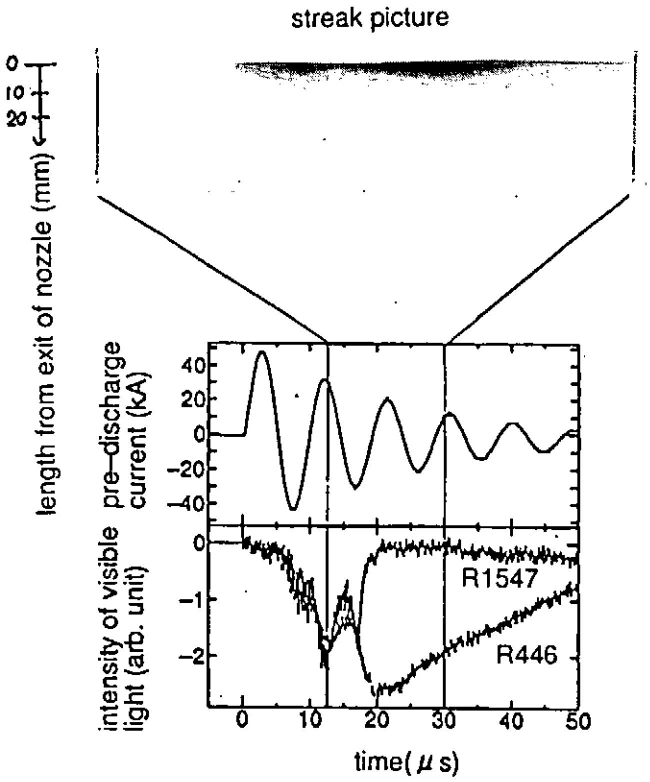

Fig.6 Pre-discharge current waveform, intensity of visible light and streak picture

PMT R1547 and R446. The streak picture has the time scale in horizontal axis and the dimensional scale in vertical axis, then the slope in the picture indicates the puffed velocity of the metal vapor. From the slope in Fig.6, the puffed velocity is obtained as about 1mm/μs.

To estimate the amount of puffed metal vapor(10), the metal vapor is deposited to a slide glass placed 20mm apart from the nozzle electrode. The depositing arrangement for diagnostics is shown in Fig.7. From the thickness of the deposit obtained by ten shots, more than 20% of an initial mass of the copper wire is puffed to the main-discharge spacing. Since the initial radius of 4mm equal to that of the nozzle has become to the deposited radius of 5mm, the radial expansion of the each copper vapor jet is very small.

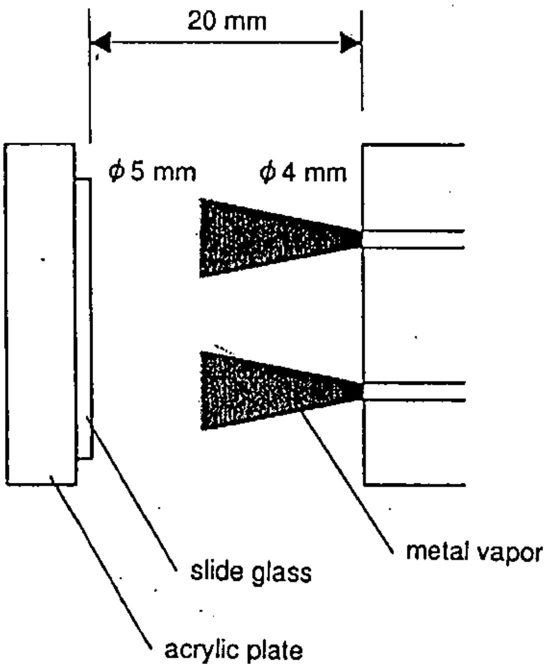

Fig.7 Experimental arrangement to measure an amount of puffed metal vapor

4.2 Metal vapor puff Z-pinch plasma by a wire explosion

The main discharge started at 20, 50 and 100μs after the initiation of the pre-bank discharge. Only in 50μs case, well organized pinch phenomena has been established. The following results are in 50μs cases. Fig.8 shows the streak picture, the main-discharge current waveform and the soft x-ray output signal obtained by Si p-i-n photo diode. A slit is located at the center between Z-pinch electrodes perpendicular to z-axis to observe radial plasma motion. When maximum pinch occurred at 2.5μs after the beginning of the main-discharge current, two spikes in soft x-ray output was observed. At the same time, a dip in the main-discharge current was observed, that corresponded to the increase of the inductance of the plasma column at the maximum pinch. Fig.9 shows the spatial profile of the soft x-ray emission taken by the x-ray pinhole camera. This time-integrated x-ray picture was taken at the same shot as in Fig.8. Since the soft x-ray was emitted from two spots, there would be the relation between the number of spots and spikes in x-ray output.

We also took the framing pictures to observe the two dimensional behavior of the pinched plasma. Fig.10 shows the framing picture, the main-discharge current waveform and the soft x-ray output signal. This shot is different one from those shown in the Fig.8 and 9. The pictures were taken with the exposure time of 40ns at 200ns intervals. The framing timings are also shown in the figure. The plasma evolution is summarized as follows: At first,

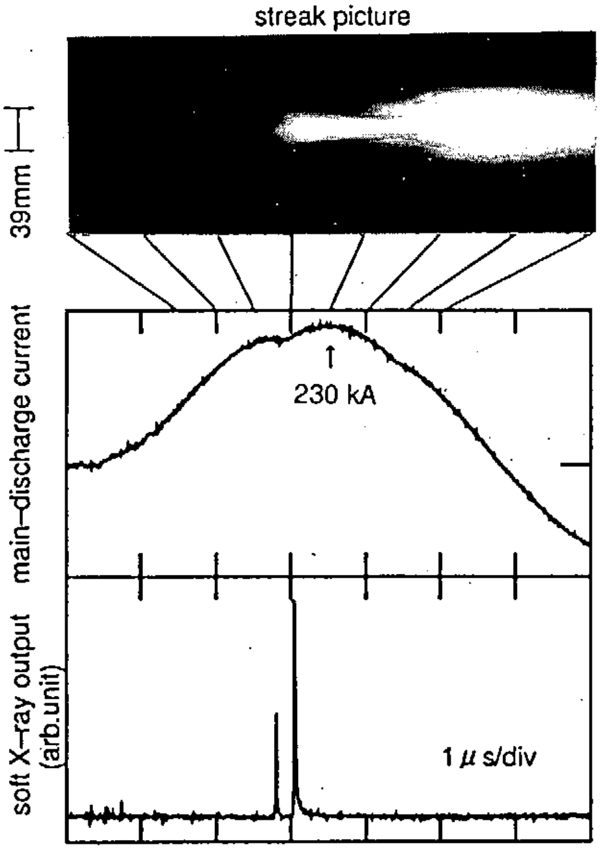

Fig.8 Main-discharge current waveform, soft x-ray output and streak picture

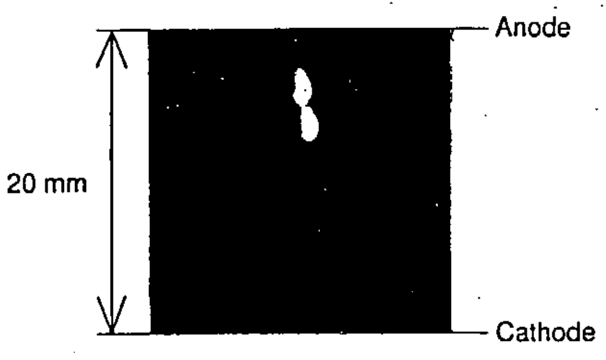

Fig.9 Time-integrated soft x-ray pinhole picture

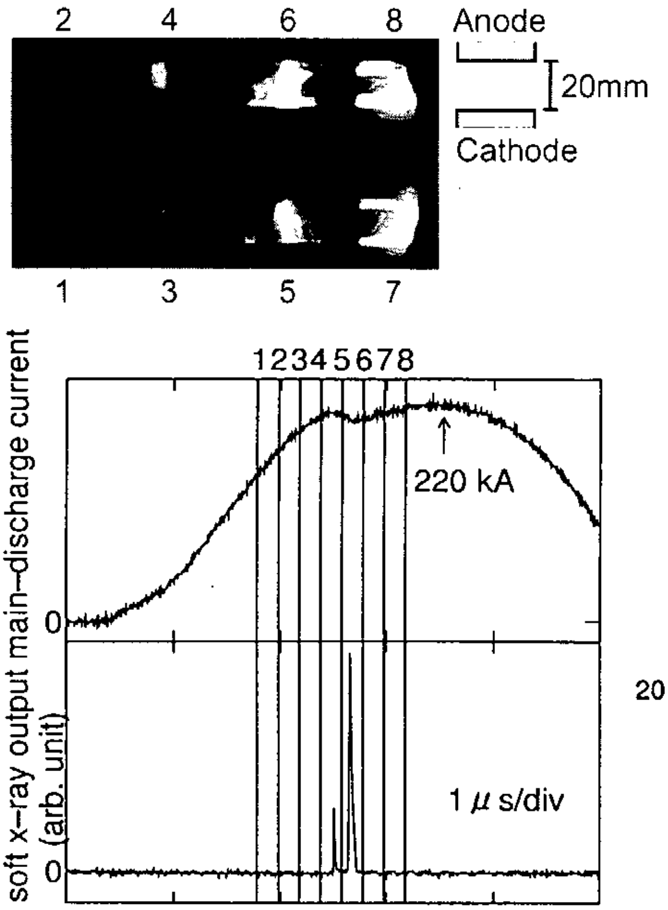

Fig.10 Main-discharge current waveform, soft x-ray output and framing picture

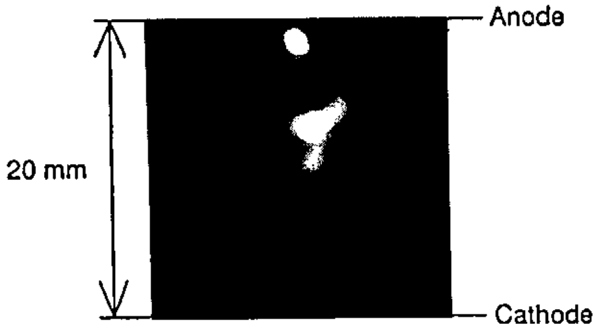

Fig.11 Time-integrated soft x-ray pinhole picture

the vapor near the anode was pinched at the frame 4 and the soft x-ray radiation was observed at the time between the frame 4 and 5. In the second, at the time between the frame 5 and 6, the intense soft x-ray radiation was observed. At the same time, a dip in the main-discharge current was observed; therefore the vapor near the cathode was pinched at the time. Fig.11 shows the time-integrated x-ray picture taken at the same shot that shown in Fig.10. It is apparent that the soft x-ray was emitted from three spots, one near the anode and the rest around the center between the electrodes. The first and second pulses of soft x-ray emission might be radiated from the spot near the anode and the rest, respectively.

5. Conclusion

The high energy density Z-pinch plasma created by injecting hollow cylindrical metal vapor between the electrodes has been examined experimentally. The metal vapor is produced by the wire explosion powered by the pulsed high current pre-discharge. To establish the maximum pinch at the Z-pinch current peak of 300kA in 2.5μs, mR_0^2 is calculated by slug model. Here m is the mass per unit length of metal vapor and R_0 is the initial radius of hollow cylindrical metal vapor. Then we obtained mR_0^2 equals to 22.5mg·mm and examined experimentally. We have measured the characteristics of copper vapor puffing, before the Z-discharge current has been switched on. Taking framing and streak picture by image converter camera, the puffed vapor velocity is obtained as about 1mm/μs. By measuring the thickness of the deposit onto slide glass, more than 20% of the initial mass of the copper wire is puffed to the main-discharge spacing. In the Z-pinch experiment, we confirmed that maximum pinch occurred just before the Z-discharge current peak. At the same time, we could obtain intense soft x-ray radiation from the plasma.

References

(1) N. R. Pereira et al.: J. Appl. Phys. 64 (1988) R1
(2) P. J. Turchi et al.: J. Appl. Phys. 44 (1973) 4936
(3) W. L. Baker et al.: J. Appl. Phys. 49 (1978) 4694
(4) C. Stallings et al.: Appl. Phys. Lett. 29 (1976) 404
(5) J. Shiloh et al.: Phys. Rev. Lett. 40 (1978) 515
(6) R. B. Speilman et al.: IEEE International Conference on Plasma Science 177 (1990) 231
(7) J. L. Porter et al.: Rev. Sci. Instrum. 63 (1992) 5703
(8) N. Qi et al.: Phys. Rev. A, At. Mol. Opt. Phys. 47 (1993) 2253
(9) J. Nilsen : J. Quant. Spectrosc. Radiat. Transf. 46 (1991) 547
(10) M. Gazaix et al.: J. Appl. Phys. 56 (1984) 3209
(11) Y. Hoshina et al.: NIFS-PROC-14 (1993) 89
(12) M. Gersten et al.: Phys. Rev. A 33 (1986) 477
(13) C. Deeney et al.: J. Quant. Spectrosc. Radiat. Transf. 44 (1990) 457
(14) C. Deeney et al.: J. Appl. Phys. 75 (1994) 2781

Gas-Puff Z-Pinch Plasmas driven by Inductive Energy Storage Pulsed Power Generator ASO-II

K.Murayama, S.Katsuki, H.Akiyama
Department of Electrical Engineering and Computer Science
Kumamoto University, Kumamoto 860, Japan

ABSTRACT

A soft x-ray emitted from a gas-puff z-pinch plasmas is expected to be a light source of lithography that produces semiconductors, micromachines and so on. An inductive energy storage pulsed power generator ASO-II, which was developed in our laboratory, has been used as a power source of a gas-puff z-pinch plasmas and is compared with a fast bank with same energy. Also, solid and mesh electrodes are used as a cathode and the behavior of pinched plasmas is observed with an image converter camera. Using ASO-II, the intensity of soft x-ray is increased and the stability of hot spots, that are points of the radiating soft x-ray, is improved.

1. Introduction

The soft x-ray radiated from gas-puff z-pinch plasmas can be used for industrial applications such as x-ray lithography, x-ray microscopes and so on. The intensity of soft x-ray and the spacial stability of hot spots are very important for the industrial applications. To achieve these things, the pulsed power is necessary as a power source of gas-puff z-pinch plasmas. Though capacitive energy storage pulsed power generators have been used, those are large and heavy machines. On the other hand an inductive energy storage pulsed power generator is compact and light-weight.

In this paper, an inductive energy storage pulsed power generator ASO-II, which was developed at Kumamoto university, is used. The intensity of soft x-ray is measured, and also the photographs of pinch plasmas and hot spots are taken by an image converter camera and a pin-hole camera with a thin aluminum respectively. The obtain results are compared with those of a fast bank with the same energy as ASO-II.

2. Experimental Apparatus

A schematic diagram of a gas-puff z-pinch device and the inductive energy storage pulsed power generator ASO-II are shown in Fig.1. The ASO-II has a coaxial configuration and consists of capacitor, triggered spark gap switch, water vessel, and opening switch. The capacitor has a capacitance of 14.9 μF and a maximum storage energy of 27 kJ. The water vessel has 1.5 m diameter and wire fuses as an opening switch can be placed radially in it. The length and number of parallel fuses are able to be varied from 5 cm to 66 cm and from 1 to 24, respectively. The storage inductance of ASO-II is about 0.7 μH.

In the gas-puff z-pinch device, the Ar gas is injected from a ϕ5 mm hole of anode to a cathode through a fast opening valve. As the cathode, a solid electrode made of brass or a mesh electrode made of ϕ60 mm copper tube covered by 1 mm grid stainless mesh is used in this experiment. The separation between two electrodes is 10 mm.

After charging the capacitor, the triggered spark gap switch is turned on. The current flows through the fuses and then the copper wires are vaporized because of joule heating. Since the resistance of the wire fuses increases, the high voltage across fuses is induced and the breakdown of the spark gap occurs. Then the current is transferred to the gas-puff z-pinch section.

In this experiment, a delay time, which is a differential time between the beginnings of the coil current for the fast opening valve and the fuse current, is changed. The charging voltage is 25 kV, and the copper wires are used as an opening switch. In the case of a fast bank, no opening switch is used and the spark gap is closed.

The coil current is measured with a B-dot probe and the source and load currents are measured with Rogowski coils, as shown in Fig.1. The soft x-ray is detected by a pin-photo diode with a Al filter of 3 μm thickness. The behavior of pinch plasmas is observed with an image converter camera. A pin-hole (the diameter of 400 μm) camera with a 3 μm Al filter is used to investigate a spacial stability of hot spots. The pin-hole camera is placed in the discharge chamber shown in Fig.2.

3. Experimental Results and Discussions

Fig.3 shows the relation between the soft x-ray intensity and delay time. The Symbols of ○, ● are the results for a solid electrode and the symbols of □, ■ are the results for a mesh electrode. The empty and solid symbols are for the cases driven by a fast bank and the ASO-II respectively. The 8 copper wire fuses with the diameter of 0.2 mm and the length of 20 cm are used. In the case of a solid electrode, the soft x-ray signals are observed between about 650 μsec and 900 μsec delay time and the intensities of them increase wholly by using ASO-II. When the mesh electrode is used, the soft x-ray signals are observed between about 600 μsec and 1100 μsec delay time, and the intensities increase by using ASO-II.

Figs.4-7 and Figs.8-11 are the results for a solid electrode and a mesh electrode respectively. The numbers on the current waveform correspond with the numbers of the photographs. The exposure time of these photographs is 10 nsec and inter-frame time is 50 nsec.

Fig.4 shows the behavior of plasmas driven by a fast bank in the case of 800 μsec delay time. In these photographs, the injected gas is reflected on the surface of a cathode and the plasma pinches near the cathode. The pulse signal of soft x-ray is detected by a pin-photo diode at the number 6 of photographs. After the soft x-ray emission, the plasma diffuses radially. Fig.5 is in the case of 1000 μsec delay time. These photographs indicate that the influence of the reflected gas is more stronger and plasma is not uniform. The plasma column is very unstable and the soft x-ray signal is not detected. Fig.6 shows the pinch plasma driven by ASO-II in the case of 800 μsec delay time. The injected gas becomes the plasma uniformly, which pinches gradually. The time till the emission of soft x-ray is faster and the plasma column is stable in comparison with Fig.4. The Soft x-ray is emitted at the photograph number 15, and then the plasma diffuses. Fig.7 shows the case driven by ASO-II in 1000 μsec delay time. The plasma is not uniform and the plasma column is very unstable as same as Fig.5. Moreover the soft x-ray is not detected.

Fig.8 shows the pinched plasma driven by a fast bank in the case of 800 μsec delay time. Unlike the cases using a solid electrode, the reflection of the injected gas does not occur and the plasma pinches from the upper position to the lower one gradually. The unstableness of the plasma column is observed from these photographs. Fig.9 is in the case of 1000 μsec delay time. The plasma column is unstable as same as the case using a solid electrode, however the soft x-ray is emitted at the photograph number 14. Fig.10 shows the pinched plasma driven by ASO-II in the case of 800 μsec delay time. Though the behavior of plasmas is not so different, the plasma column is more stable in comparison with Fig.8. Fig.11 shows the case of 1000 μsec delay time. The behavior of plasmas is almost the same as the cases using other mesh electrode, and the soft x-ray is emitted. The plasma column is leaning and warping obviously.

Fig.12 shows the spatial distribution image of hot spots for 10 shots taken by a pin-hole camera with 3 μm Al filter. Figs.11 (a) and (b) show the pin-hole photographs in the cases driven by a fast bank and ASO-II, respectively. A solid electrode is used. Figures of (c) and (d) are the ones in the cases driven by a fast bank and ASO-II, respectively. A mesh electrode is used. The deviation of hot spots from z-axis is decreased by using a mesh electrode and ASO-II.

The soft x-ray emission increases by using ASO-II, and the plasmas pinch more stably and the deviation of hot spots is smaller. Those reasons are considered as follows: current with a faster rise time flows into z-pinch plasmas by using an opening switch, and an inductive energy storage pulsed power generator can supply a high induced voltage with a fast rise time during a short pulse width at an initial phase of the discharge. Therefore more uniform discharges occur in comparison with those by a fast bank. The intensity of the soft x-ray in the case of a mesh electrode is smaller in comparison with the case of a solid electrode. This reason may be related to the density of the injected gas.

4. Conclusion

A gas-puff z-pinch plasmas are driven by an inductive energy storage pulsed power generator ASO-II, and intensity of the soft x-ray, behavior of plasmas and the spacial distribution of hot spots are compared with those by a fast bank. Using ASO-II, intensity of the soft x-ray became larger. Moreover plasmas pinched more stably and the spacial stability of hot spots was improved in both electrodes of mesh and solid. These results are important when the gas-puff z-pinch plasmas are applied as a light source.

REFERENCES

(1) E.W.Becker, et. al. : "Fabrication of microstructures with high aspect ratios and great structural heights by synchrotron radiation lithography, galvanoforming, and plastic moulding (LIGA process)", Microelectronic Engineering 4, pp.35-56 (1986)

(2) Hirodhi Arita, et. al. : "Soft x-ray emissions by high-current vacuum discharges", IEEE Transactions on plasma science, Vol.18, No.4, pp695-698, (1990)

(3) J.S.Pearlman and J.C.Riordan : "X-ray lithography using a pulsed plasma source", J.Vac.Sci.Technol., 19(4), pp1190-1193, (1981)

(4) Janusz Bryzec, et. al. : "Micromachines on the march", IEEE Spectrum May, pp20-31, (1994)

(5) J.Bailey, et. al. : "Evaluation of the gas puff z pinch as an x-ray lithography and microscopy source", Appl. Phys. Lett., 40(1), pp33-35, (1982)

(6) F.J.Wessel, et. al. : "Implosion of an aluminum jet onto a coaxial wire: A zpinch with enhanced stability and energy transfer", Phys. Rev. Lett., Vol.69, pp3181-3184, (1992)

(7) M.Badaye, et. al. : "An improved gas puff design for a z-pinch x-ray source", Rev. Sci. Instrum., Vol.61(5), pp1457-1459, (1990)

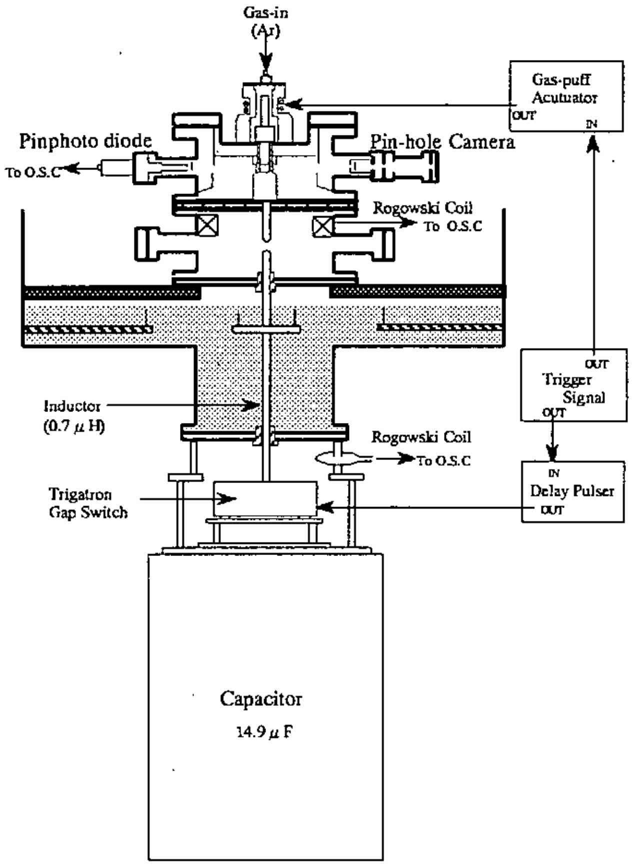

Fig.1 Experimental setup

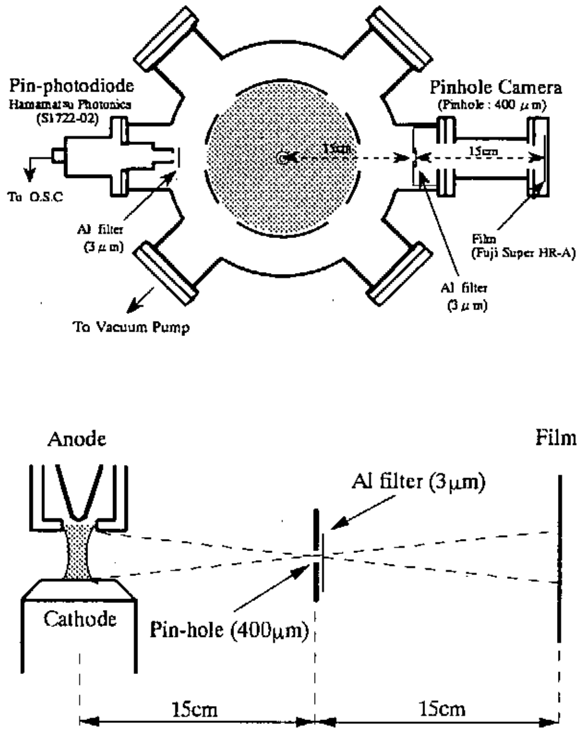

Fig.2 Arrangement of pin photo diode and pin-hole camera

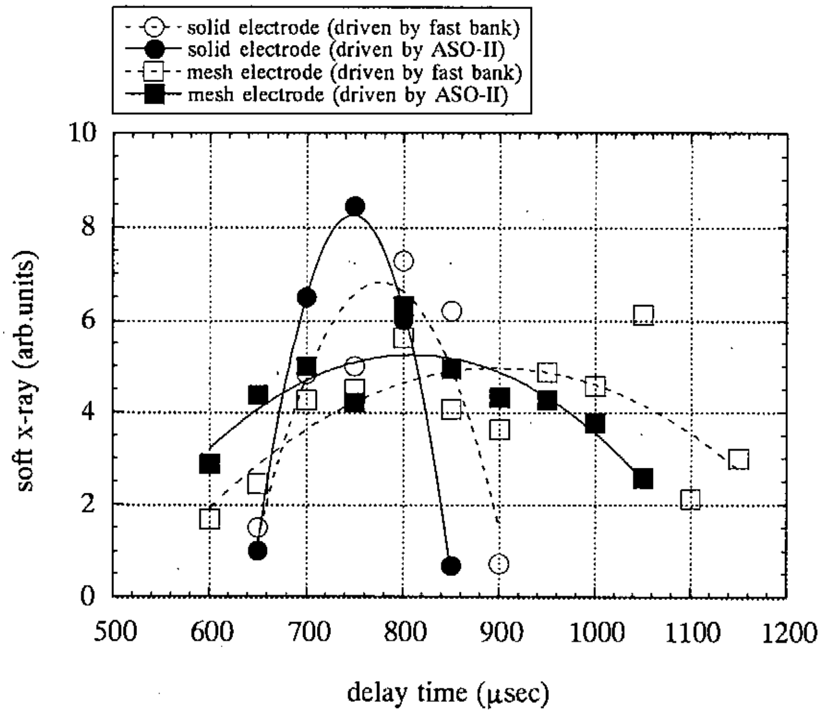

Fig.3 Relation between the intensity of soft x-ray and delay time

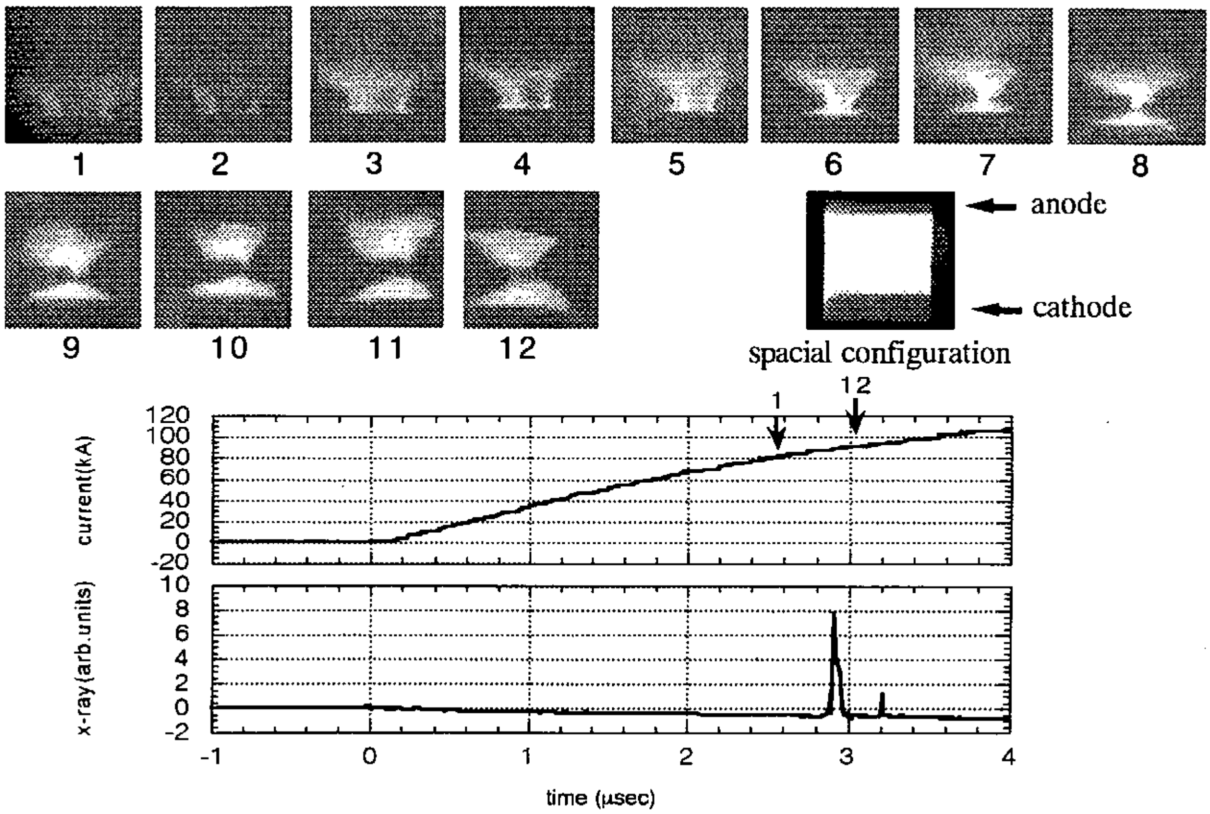

Fig.4 Framing photograph of z-pinch plasma and waveforms of current and soft x-ray (driven by a fast bank, solid electrode, delay time 800μsec)

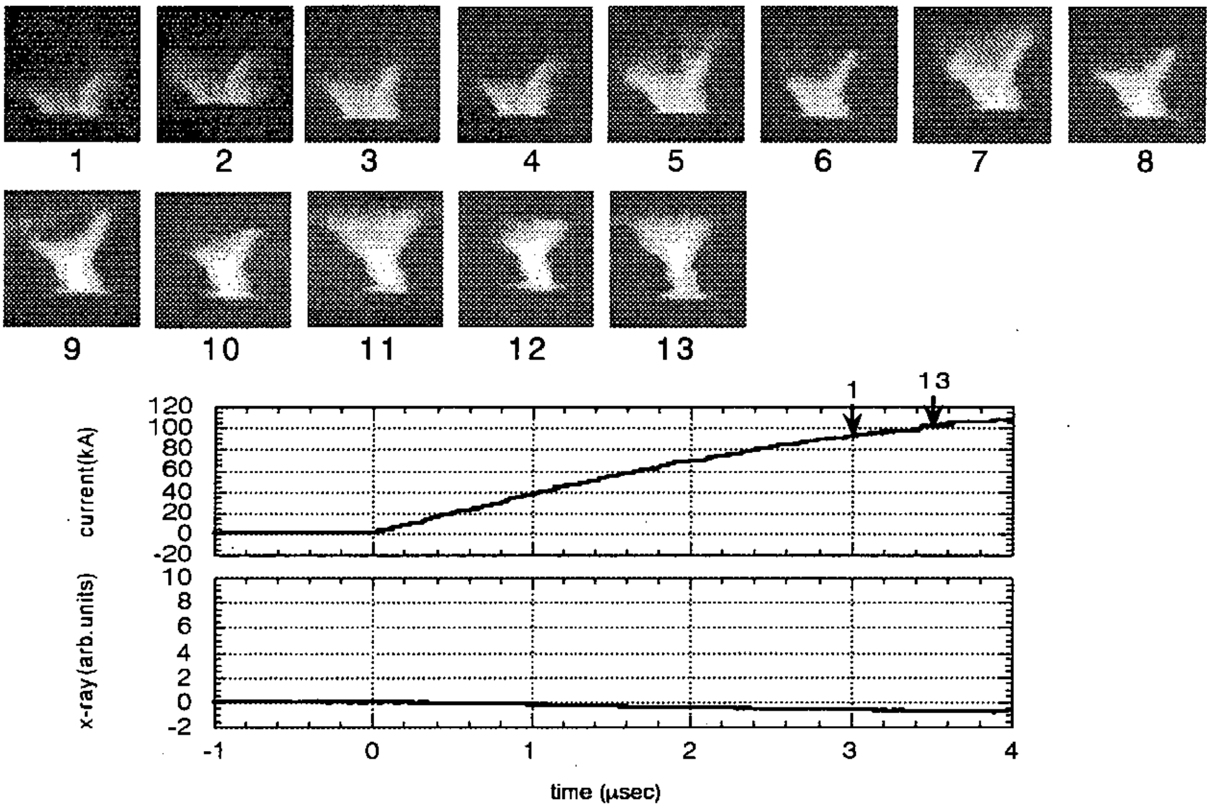

Fig.5 Framing photograph of z-pinch plasma and waveforms of current and soft x-ray (driven by a fast bank, solid electrode, delay time 1000μsec)

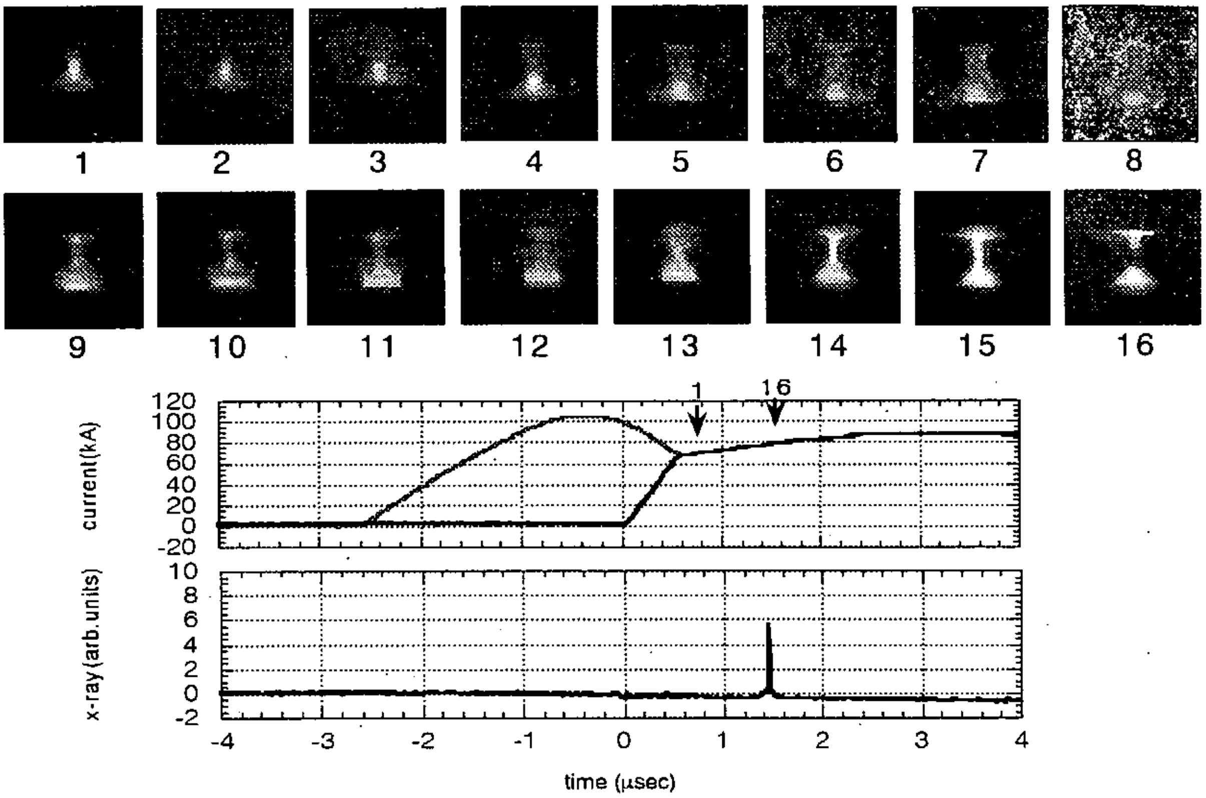

Fig.6 Framing photograph of z-pinch plasma and waveforms of current and soft x-ray (driven by ASO-II, solid electrode, delay time 800μsec)

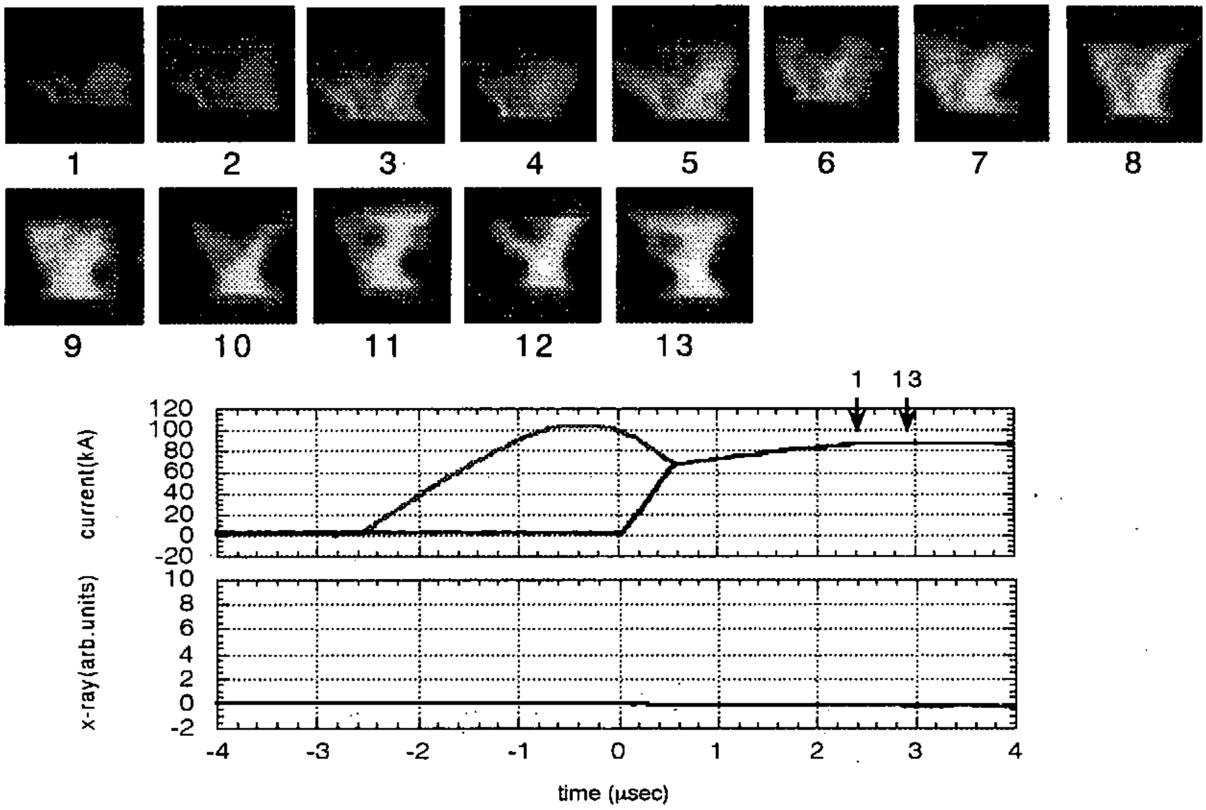

Fig.7 Framing photograph of z-pinch plasma and waveforms of current and soft x-ray (driven by ASO-II, solid electrode, delay time 1000μsec)

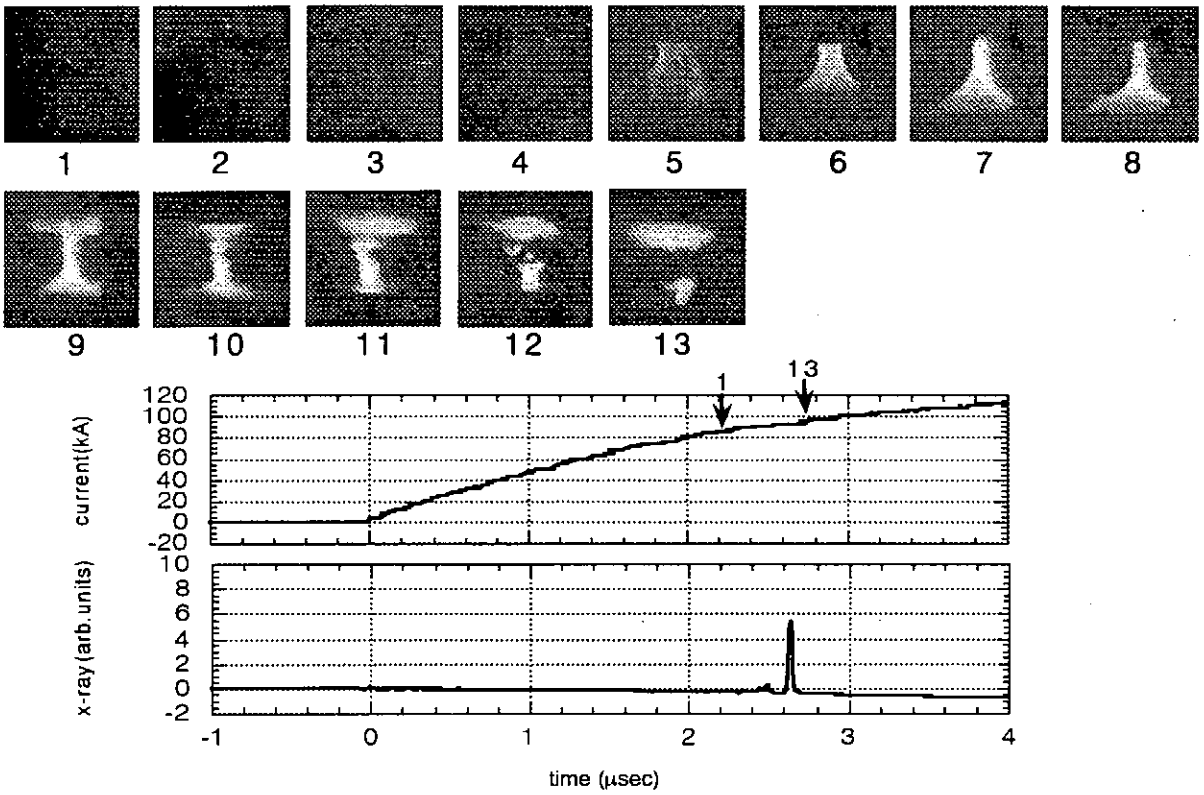

Fig.8 Framing photograph of z-pinch plasma and waveforms of current and soft x-ray (driven by a fast bank, mesh electrode, delay time 800μsec)

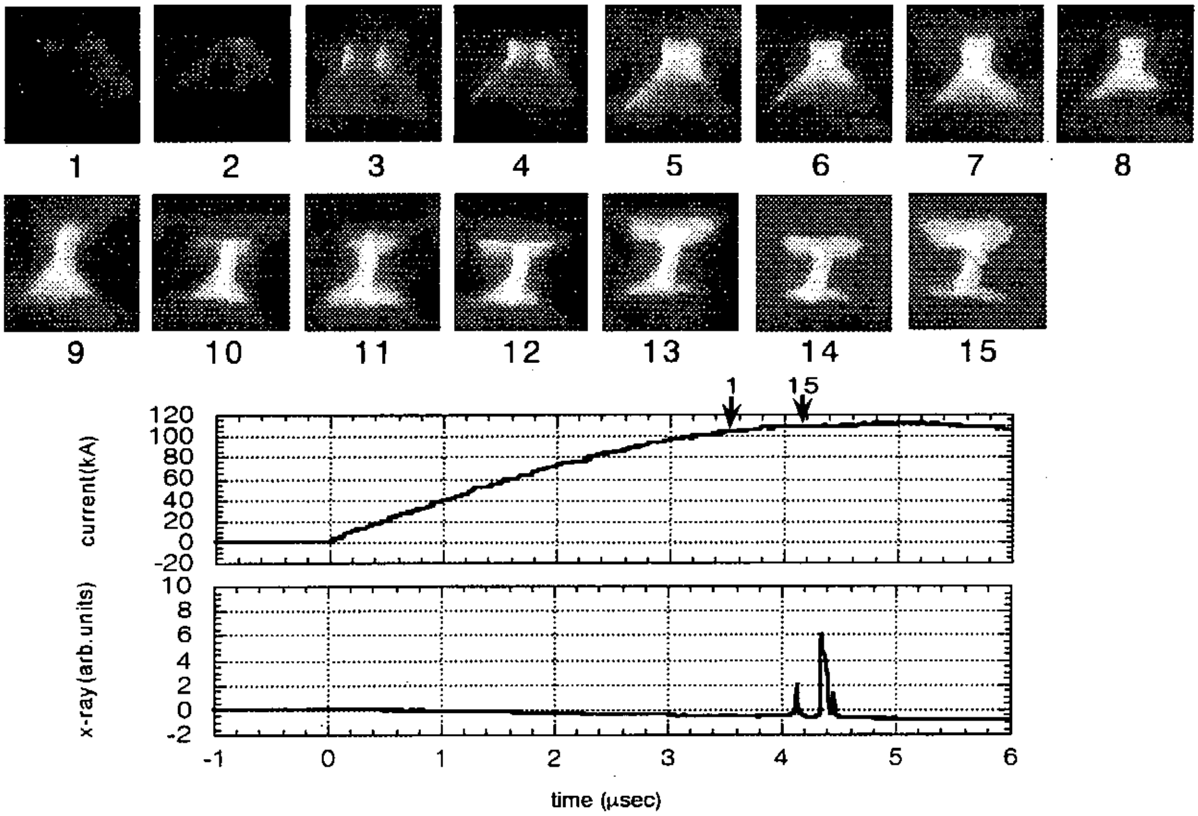

Fig.9 Framing photograph of z-pinch plasma and waveforms of current and soft x-ray (driven by a fast bank, mesh electrode, delay time 1000μsec)

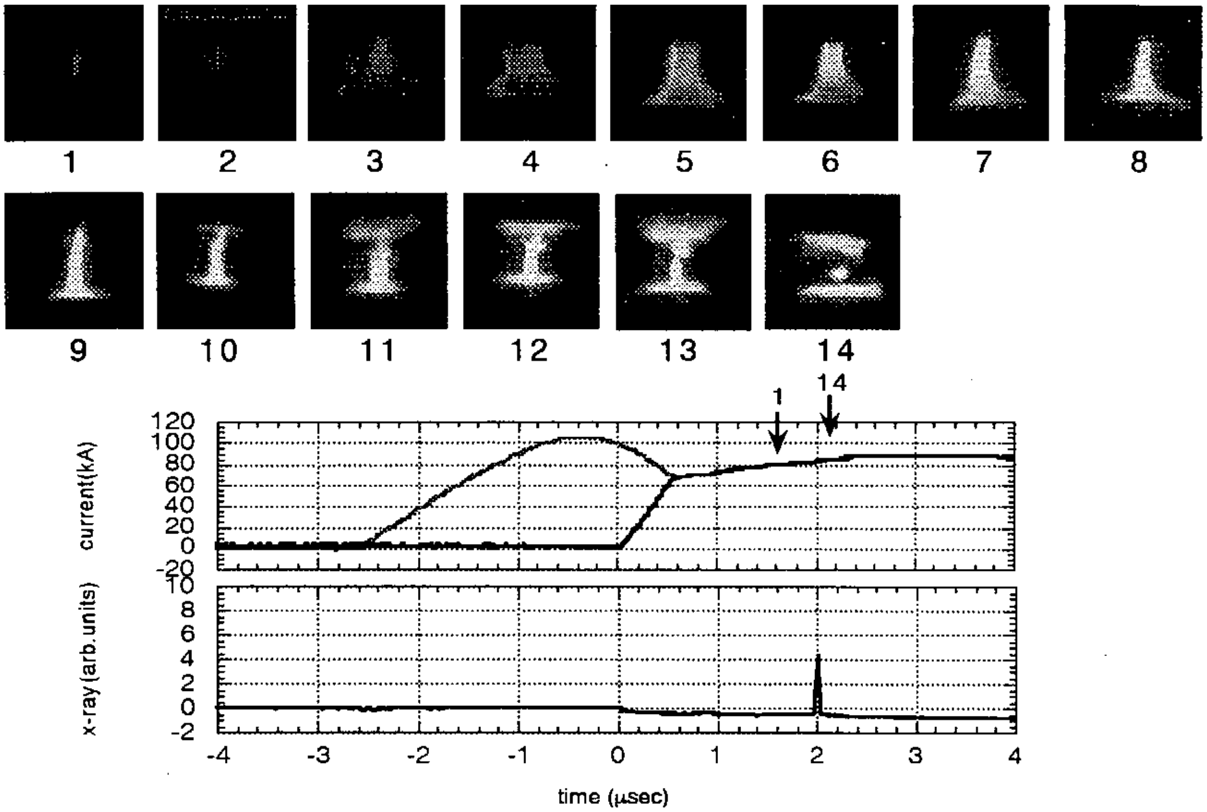

Fig.10 Framing photograph of z-pinch plasma and waveforms of current and soft x-ray (driven by ASO-II, mesh electrode, delay time 800μsec)

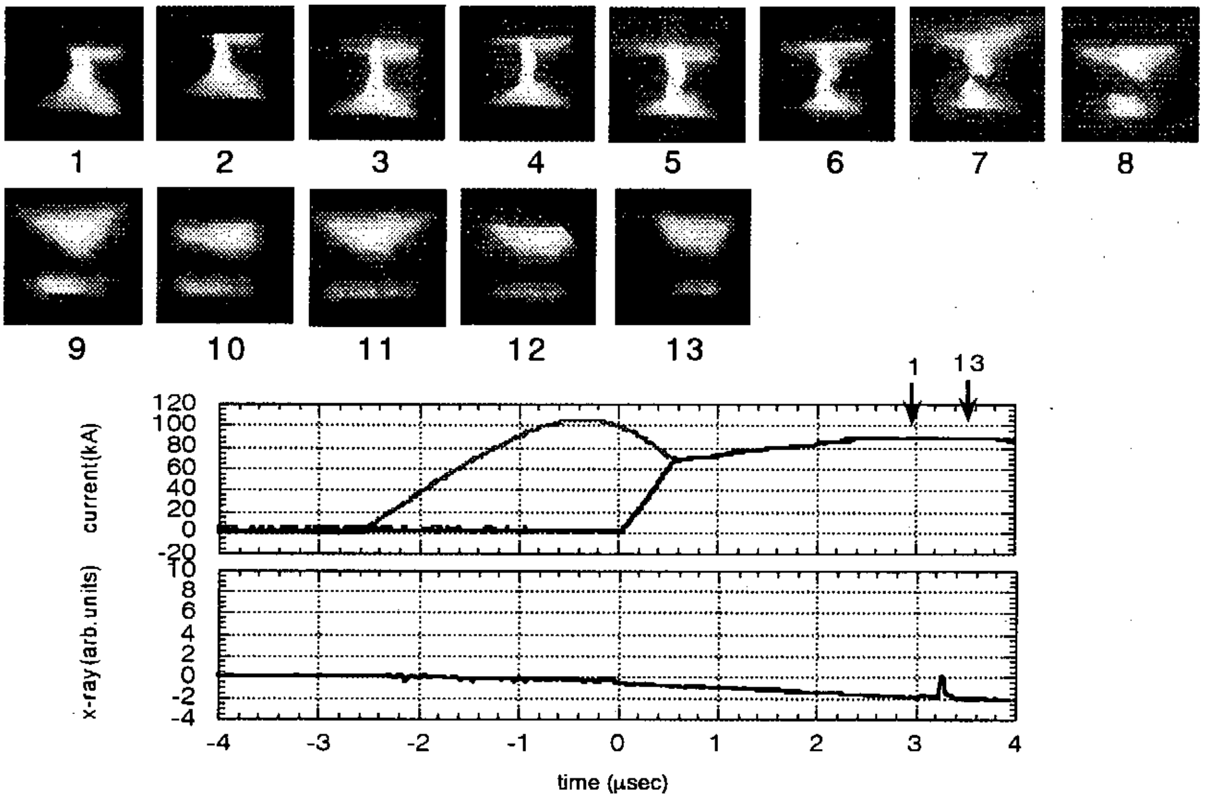

Fig.11 Framing photograph of z-pinch plasma and waveforms of current and soft x-ray (driven by a fast bank, mesh electrode, delay time 1000μsec)

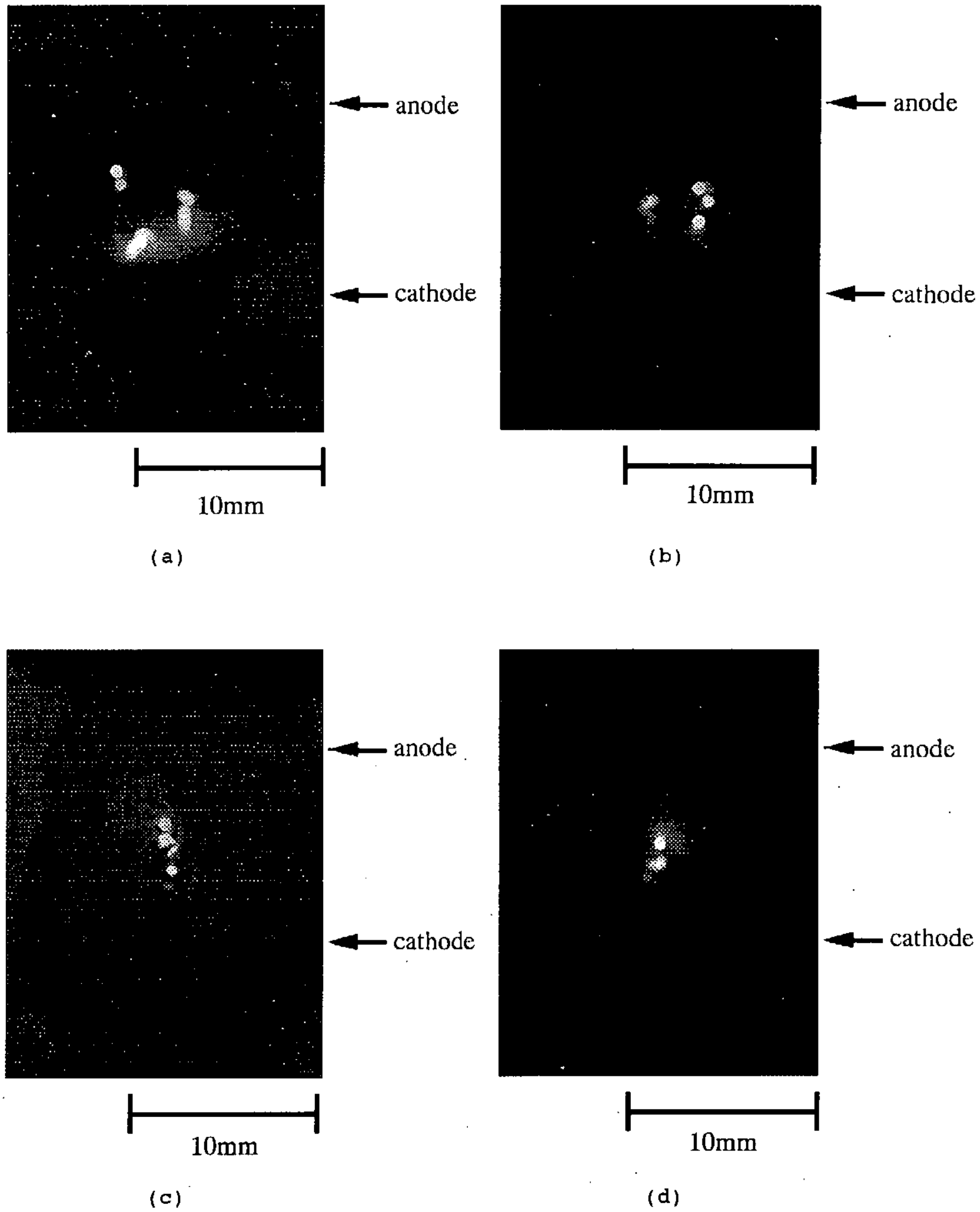

Fig.12 Pin-hole photographs (delay time 800μsec, 10shots):
(a) solid electrode, driven by a fast bank
(b) solid electrode, driven by ASO-II
(c) mesh electrode, driven by a fast bank
(d) mesh electrode, driven by ASO-II

Soft X-ray Lithography by a Gas-Puff Pinch

Toshikazu Yamamoto, Jian Du, Tetsuya Ohata,
Katsuji Shimoda, Morihiko Sato and Katsumi Hirano
Department of Electronic Engineering
Gunma University

Abstract

Soft X-ray emission generated by a plasma focus with an additional Ar gas puff is examined to exposure the photoresist, PMMA for the microlithography. The etched depth of the photoresist is measured with an atomic force microscope at the various mask widths and the modulation transfer function is obtained as a figure of merit for the spatial resolution. The upper limit of the spatial frequency, 320 lp/mm is obtained. This corresponds to the spatial resolution of 1.6μm.

1 Introduction

Intense sources of soft X-rays have received considerable interest in the field such as industrial microlithograpy [1,2] and microscopy.[3-6] By use of soft X-rays, it is expected to easily obtain a higher resolution in these applications. Synclotron orbital radiation (SOR),[7] pulsed plasmas including the Z-pinch plasma and laser produced plasmas have been studied by a number of authors as the soft X-ray sources. SOR has extremely high brightness, and is suitable for a mass production of the semiconductor devices. However, the SOR is expensive and not easily accessible to many researchers.

Since Z-pinch plasma generates pulsed soft X-rays of nanosecond duration, and so it is considered that the Z-pinch is useful for the soft X-ray microscope for live and moving specimens without blurring. However, it is not well known that a suffcient dose of the soft X-ray is possible in a single shot. In order to obtain the appropriate exposure for microlithography, multiple discharges of the Z-pinch device may be required. On the other hand, the photoresist for the soft X-ray is hardly obtained. Therefore, we inevitably employ photoresist which is prepared for the exposure with the electron beam. Several authors have estimated the sensitivity of photoresist for the soft X-rays.[2]

In this paper, we intend to discuss feasibility of the photoresist, that is developed for the electron beam exposure, using the soft X-ray source.

2 Apparatus

In this experiment, a Mather-type plasma focus device with a squirrel cage outer electrode was employed to generate soft X-rays. The diameters of the inner and the outer electrodes were 50 and 100 mm. The lengths of the electrodes were 280 and 230 mm, respectively. The condenser bank consisted of 28 × 1.56 μF, 80 kV capacitors. The device was operated at the bank voltage of 45 kV and an embedded gas pressure of 6 Torr H_2. To obtain intense soft X-ray emission, additional argon was puffed with a fast-acting valve through the inner electrode immediately before each discharge. When the bank was operated at 45 kV, the current in the plasma column was approximately 0.8 MA at its peak.

A soft X-ray pinhole camera[8)] with a quantitative image acquisition system was used for soft X-ray image observation with time resolution. A pinhole image of the X-ray source is made on the MCP through a pinhole and Be + Ag foil filters (25 μm and 1μm in thickness, respectively) which prevent the visible light also emitted from the source. The spectral response of the MCP system is described in a previous paper.[9)] The combination of the filters and the MCP gives a pass band between 3.7 and 7 Å, which accepts Ar K-lines. The schematic diagram of soft X-ray exposure system is shown in Fig. 1. A positive type PMMA (polymethylmethacrylate) photoresist (OEBR-1000, Tokyo Ohka) was employed. The photoresist was spin-coated on silicon wafer and prebaked at 170 °C for 20 minutes. The photoresist was placed at a distance of 24 cm from the electrode axis. A Be foil, 25μm in thickness, was used as a X-ray extraction window.

Nets of 19 μm meshes and 6 μm in thickness (G1000HS, Oken) which are made of Cu were placed as a mask in contact in front of the photoresist. To obtain a wedge-shaped photomask, 2 nets were put with an inclined angle of 10°.

The soft X-rays were monitored with an X-ray PIN diode which was coupled with a set of filters (25 μm Be and 1 μm Ag). The viewing field of the diode was limited only to the plasma produced by the discharge using a collimater.

The feature of the soft X-ray sources which are recorded with the pinhole camera are shown in Fig. 2 a) a single discharge, and b) overlapped by 60 discharges. The average intensity of the soft X-ray at the photoresist by a single shot is $\sim 2.6 \times 10^2$ mJ/cm^2. A number of discharges give a stable source in that feature (~15 mm in length and ~1 mm in diameter). It is possible to exposure the photoresist by the required dose to control the number of the discharge.

3 Experimental results

The soft X-ray source in this experiment has a large ratio of the source length to the diameter, and so there is a longer penumbra of the mask in the parallel direction to the electrode axis than that of the parpendicular direction. Therefore, we discuss only the performance in the parpendicular direction for the spatial resolution. A mask image observed with an atomic force microscope (AFM, Nanoscope II, Digital Instrument) is shown in Fig. 3. The picture was taken after development of 14 min. at 25°C. The depth made by etching was also measured with the AFM in Fig. 3. Examples of the cross sectional view along the lines of A-A', B-B' and C-C' are shown in Fig. 4.

The modulation transfer function, MTF is defined as

$$MTF = \frac{I_{\max} - I_{\min}}{I_{\max} + I_{\min}} \tag{1}$$

where $I_{\max}$ and $I_{\min}$ are the maximum and the minimum depth of the cross section as shown in Fig. 4. The MTF is commonly used as the figure of merit for describing the spatial resolution of optical systems.[10)] The MTF which is calculated using the etched depths along the dotted line described in Fig. 3 is shown in Fig. 5. If we assume that the 60 % of the MTF is the upper limit of the spatial frequency, we obtain 320 lp/mm, approximately. This corresponds to the spatial resolution of 1.6 μm.

The spatial frequency can be improved more than one order higher by arrangement of the soft X-ray source, mask and photoresist.

References

1) J. S. Pearlman, J. C. Riordan and A. C. Kolb: Radiat. Phys. Chem. **25** (1985) 709.
2) I. Okada, Y. Saitoh, S. Itabashi and H. Yoshihara: J. Vac. Sci. Technol. **B4** (1986) 243.
3) R. Feder, J. S. Pearlman, J. C. Riordan and J. L. Costa: J. Microscopy **135** (1984) 347.
4) R. Feder, V. Banton, D. Sayre, J. Costa, M. Baldini and B. Kim: Science **227** (1985) 63.
5) I. N. Weinberg and A. Fisher: Appl. Phys. Lett. **47** (1985) 1116.
6) I. N. Weinberg and A. Fisher: Nucl. Instrum. Methods **A242** (1986) 535.
7) M. Howells, J. Kirz, D. Sayre and G. Schmahl: Physics Today (1985) 22.
8) Y. Takahama, J. Du, T. Yanagidaira and K. Hirano: Rev. Sci. Instrum. **65** (1994) 2505.
9) W. Parkes, R. Gott and K. A. Pounda: IEEE Trans. Nucl. Sci. **NS-17** (1970) 360.
10) S. G. Glendinning and H. Medecki: Rev. Sci. Instrum. **57** (1986) 2184.

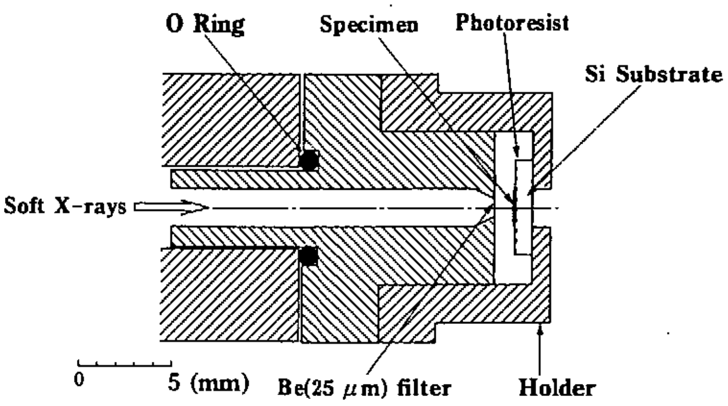

Fig. 1 Schematic diagram of soft x-ray exposure system.

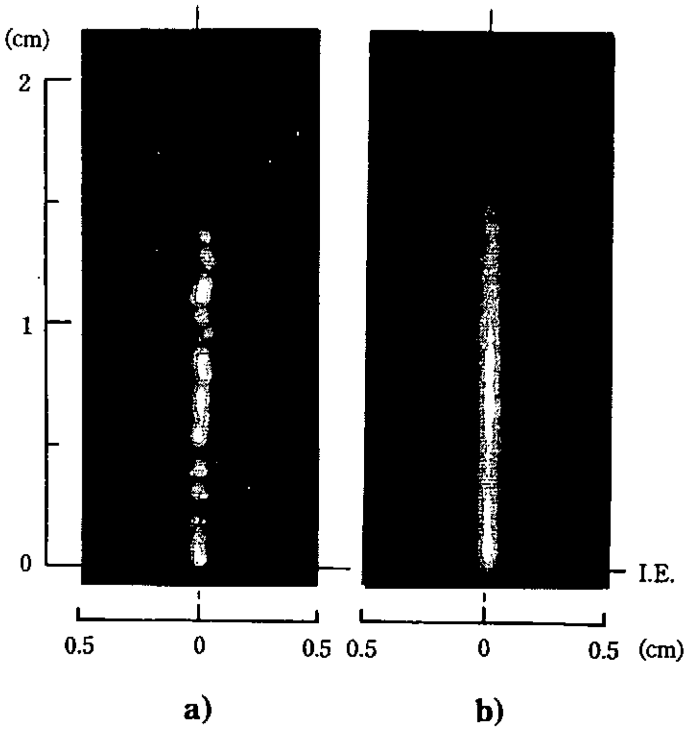

a) b)

Fig. 2 Time integrated soft X-ray pinhole image obtained with single shot a) and 60 shots b).

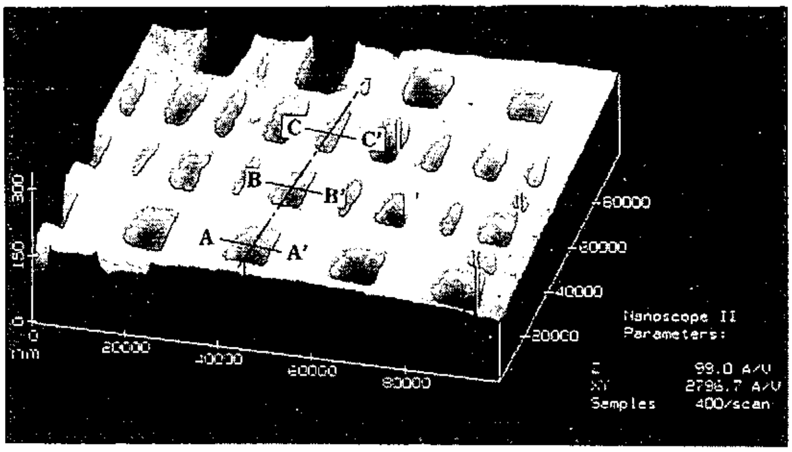

Fig. 3 A mesh image on a photoresist enlarged by an AFM. Lines A–A', B–B', C–C' show the sampling lines for the cross–sectional view of the photoresist.

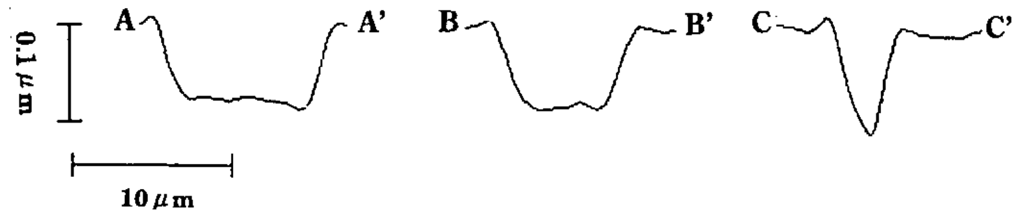

Fig. 4 Cross–sectional view along the lines A–A', B–B', C–C' shown in Fig. 3.

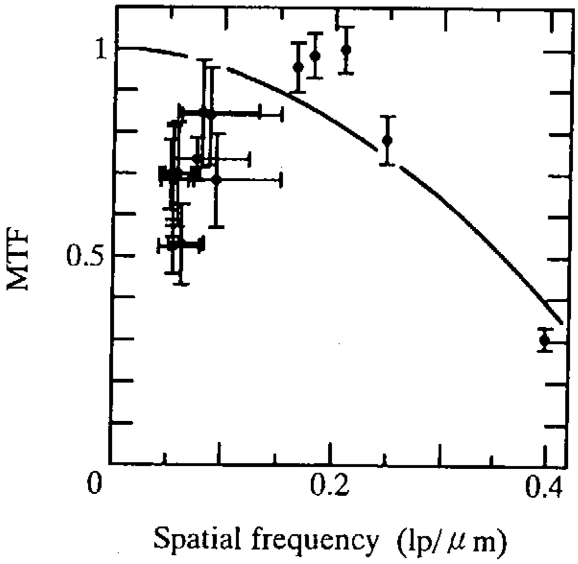

Fig. 5 Modulation transfer function, MTF, for the soft X–ray exposure system measured by the contrast of the mesh image shown in Fig. 3.

Soft X-ray Emission from Capillary Z-discharges Driven by Fast Pulse Power Generator

Tomonao HOSOKAI, Mitsuo NAKAJIMA, Takayuki AOKI,
Kazuhiko HORIOKA and Masao OGAWA
Department of Energy Sciences, Tokyo Institute of Technology,
Nagatuta 4259, Midori-ku Yokohama 226 Japan

Abstract

The plasma dynamics of capillary Z-discharges have been studied for wavelength shortening of the discharge pumped soft X-ray laser. The capillary load filled with argon of 370Pa was directly driven by the current above 100kA with the rise time of a few tens nsec using fast pulse power generator LIMAY-I (13kJ,3Ω-50ns). The possibility of lasing in shorter wavelength region by fast capillary discharges depends on whether we can avoid unstable implosion of the column to get denser and hotter plasma condition. In order to investigate the dynamics of capillary Z-discharges, soft X-ray emission from the column was measured. Obtained spectrums suggest that the plasma column implodes stably without MHD instabilities. The experimental observation was consistent with the results of 1D-MHD simulation and satisfied the lasing condition of Ne-like Ar. These results indicate that the fast capillary Z-discharges have a potentiality of lasing in shorter wavelength region.

1. Introduction

At the present X-ray laser research, only a huge high powered optical laser can produce lasing plasma. The typical conversion efficiency from the output of the driver to the 'laser-driven X-ray laser' is generally 10^{-6} to 10^{-7}. So, the final out-put energy of soft X-ray region is order of μJ at best. On the contrary, discharge plasmas driven by fast pulse power generator are directly inputted electrically stored bank energy, so it must be energy rich, efficient and low cost X-ray sources. The capability of soft X-ray generation more than tens of kJ looks very attractive. If a compact, low cost, and energy rich laser working in soft X-ray region is developed, its applications would become revolutionary important not only in basic scientific fields but also in industrial fields.

For the lasing plasma in soft X-ray region, both high temperature more than 100eV and high electron density more than 10^{19}cm^{-3} are generally needed. Furthermore, the plasma must be stable, uniform and liner to obtain good optical property. The production of such a plasma column is a challenging problem, because the column must be compressed dynamically without MHD instabilities. Recently, it was reported that fast Z-discharge through argon of about 100Pa in capillary of 4mm diameter and 120mm length could produce lasing of soft X-ray (Ne-like Ar 46.9nm), and achieved a gain-length product of 7.2 [1,2]. Extending this technique to the operational range of shorter wavelength is of the major concern of our present study. Here we discuss the possibility of the lasing in soft X-ray region by fast capillary discharges.

2. Experimental Setup

The typical setup of the experiment is shown in figure 1. The capillary load is coaxially set inside a Z-stack insulator of pulse forming line (PFL), which is filled with pure water to prevent from break-down along the capillary outer surface. This structure is so similar to that of a coaxial cable, here capillary load is nearly regarded as a part of PFL, that it has only small effective inductance and helps fast current rise.

Experiments were conducted using polyacetal capillaries of 3mm diameter with length of 100mm which was filled with argon gas. The initial gas pressure was varied from 100Pa to a few hundreds Pa using a differential pumping system. The background pressure of detector chamber keeps about 4×10^{-4}torr. The drive current is monitored by a Rogowski coil inside the Z-stack insulator of PFL.

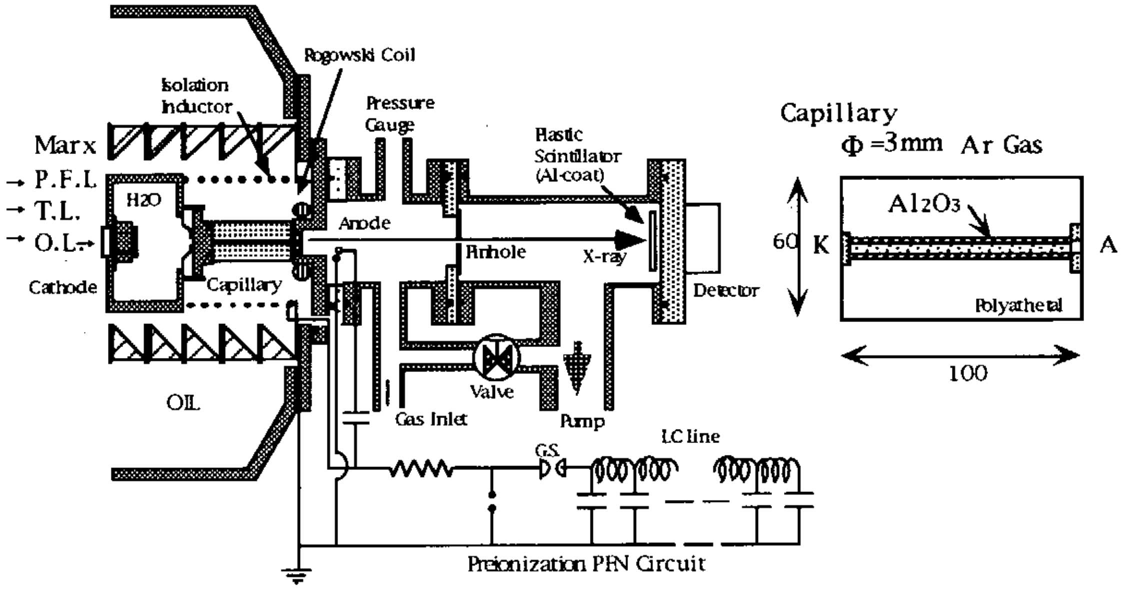

Fig.1 Schematic Diagram of Experimental Set-up for Capillary Z-discharge.

In the experiments, the care was taken to make well-defined discharge condition. Then the plasma was directly driven by fast pulse power generator LIMAY-I (13kJ, 3Ω-50nsec), which consists of Marx generator and PFL. The drive current above 200kA with the rise time less than a few tens nsec was easily available. Undefined factors such as spark plasma column in the gap switch and the effect of wall ablation materials were eliminated from the discharge process. To suppress the effect of wall ablation, the inner surface of the capillary was laminated with an alumina tube. To make well controlled pre-ionized Ar gas, a rectangular current pulse of about 15-20A and duration of several tens μsec generated by pulse forming network (PFN). It was applied just before the main power pulse, where the pre-ionization circuit is isolated from PFL by an inductor.

3. Detectors for the X-Ray measurement

The X-ray emitted from the plasma column is observed through a pinhole from axial direction as shown in Fig.1. We can get spectrums of the soft X-ray under about 300eV region by filtered scintillation detectors and filtered XRD diodes[3] which have different sensitivity for wavelength of soft X-ray.

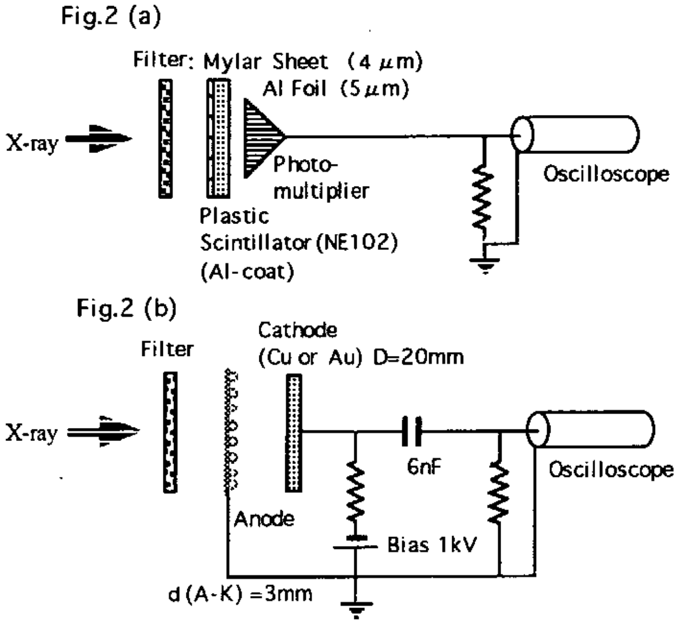

Fig.2 Schematic diagram of the X-ray detectors
(a) Filtered Scintillation Detector
(b) Filtered XRD Detector

A schematic diagram of the X-ray detectors is shown in figure 2. The filtered scintillation detector (as shown in Fig.2(a)) consists of an absorption filter and an aluminum coated plastic scintillator (NE102A) with photo-multiplier. The coated aluminum cut off almost all visible light components. A mylar sheet of 4 μm thickness or an aluminum foil of 5μm thickness is set in front of the scintillator. The sensitivity of the detector depends on material of the filter. The plastic scintillator is relatively insensitive for the photon energy below about 100eV. In case of the mylar filter which has carbon-K edge, the detector is sensitive from about 100 to 300eV. In case of the aluminum filter, it is sensitive nearly 100eV due to aluminum-L edge.

The filtered XRDs are consist of a metal photo cathode of effective diameter of 20mm, wire mesh anode and absorption filter (as shown in Fig.2(b)), which has coaxial geometry to detect fast pulse. The cathode views the soft X-ray source through the filter and the wire mesh anode. Incident photons cause emission of electrons from the cathode surface, and emitted electrons are accelerated across the cathode-anode gap. So the emitted X-ray can be detected as photoelectron current. The wavelength sensitivity of the detector is determined by combination of the absorption filter and cathode material which have different quantum efficiency. We chose a 4 μm-mylar as the filter because it has carbon-K edge below about 300eV. Copper or gold is chosen as the cathode metal from their quantum efficiency profiles [4]. Then the mylar-filtered XRD with copper cathode is sensitive below about 40eV, and with gold cathode is below about 100eV respectively.

4. 1D-MHD Simulation

We have carried out numerical simulations on the plasma dynamics of the capillary Z-discharge using 1D-MHD code MULTI-Z [5,6], which can simulate the dynamics of the current sheet and shock waves self-consistently including the effect of radiation process and the skin effect. The initial condition of the simulation is as follows; The argon gas has uniform temperature of 0.1eV and density of 6.09×10^{-6} g/cc (corresponding to the argon gas pressure of 370Pa) respectively in the capillary. In this simulation, we gave the experimentally obtained discharge current as the input parameter.

5. Results

5.1 Experimental Results

Figure 3 shows the typical wave forms of the end-view X-ray signals and the load current (P=370Pa). From beginning of discharge to about 30nsec, X-ray bellow about 40eV were dominant in the emission. From 30nsec to 40nsec, that of about 40-100eV were dominant, and from 40nsec to 70nsec, that of about 100-300eV were dominant. As mentioned above, the emission was gradually sifted from soft region below 40eV to relatively hard region of 300eV with time. It shows electron temperature rises slowly until 30nsec, after 30nsec it rises rapidly to 300eV.

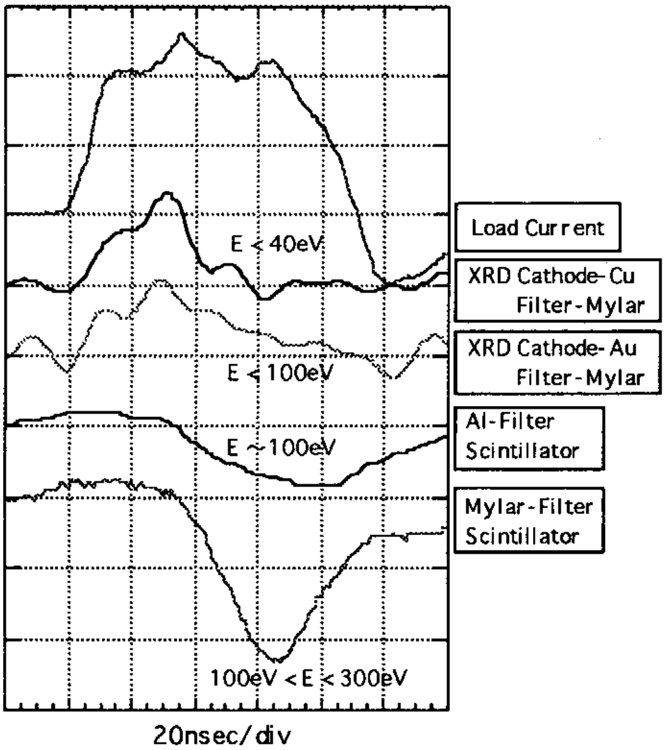

Fig.3 Typical Waveforms of X-ray Detectors and Load Current (50kA/div, 20nsec/div)

5.2 Typical Results of 1D-MHD Simulation

Figure 4 shows the typical flow diagram of the implosion process (P=370Pa). The column implodes at about 25nsec from the current rise and reflect on the Z-axis. Figure 5 shows the typical time-space distribution of electron density and electron temperature. It suggests that the plasma is heated and compressed to electron density of ne-10^{20}cm^{-3} and electron temperature of Te-100eV at about the maximum compression time of about 25nsec. After the maximum compression, the column explode with electron heating. Then the temperature reaches nearly 200eV at 50nsec.

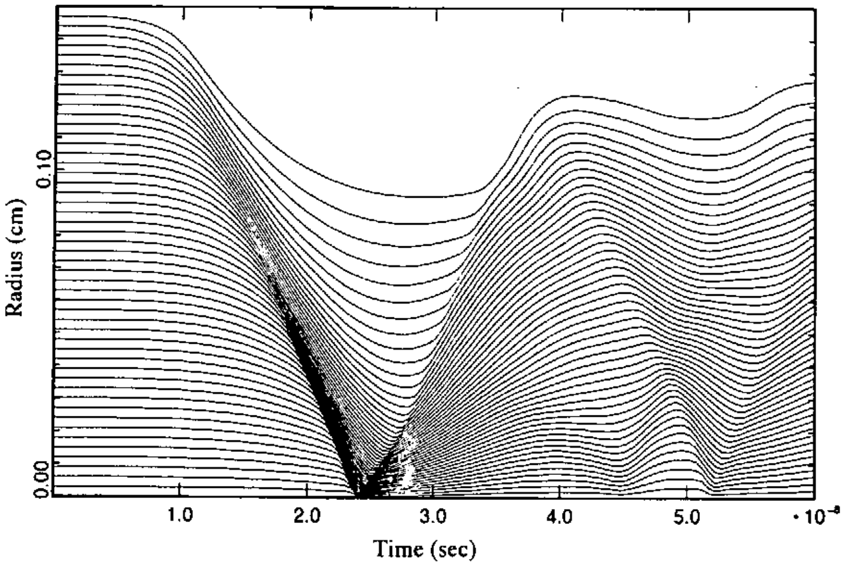

Fig.4 Flow Diagram of Z-discharge Experimentally Observed Wave form (Fig.3) was Used as Drive Current (D=3mm, P=370Pa (Ar))

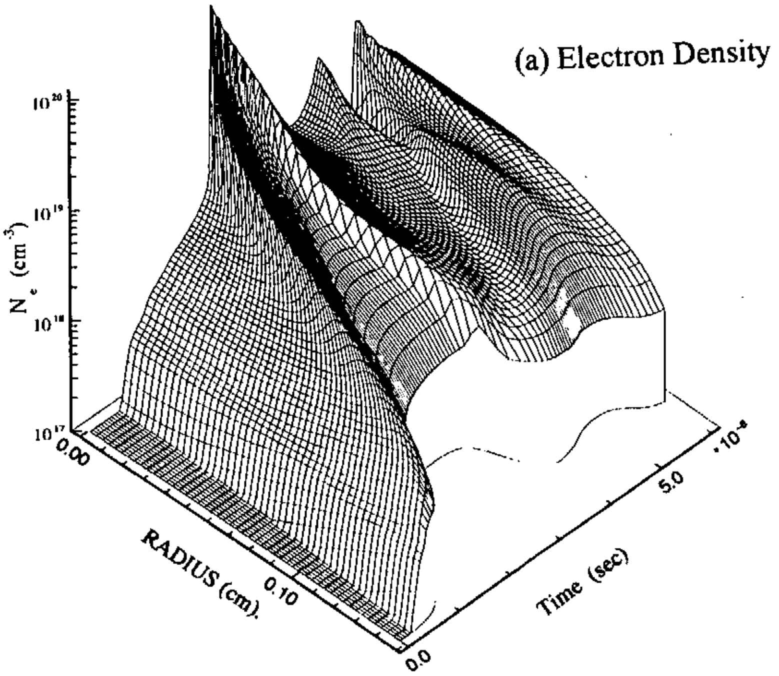

(a) Electron Density

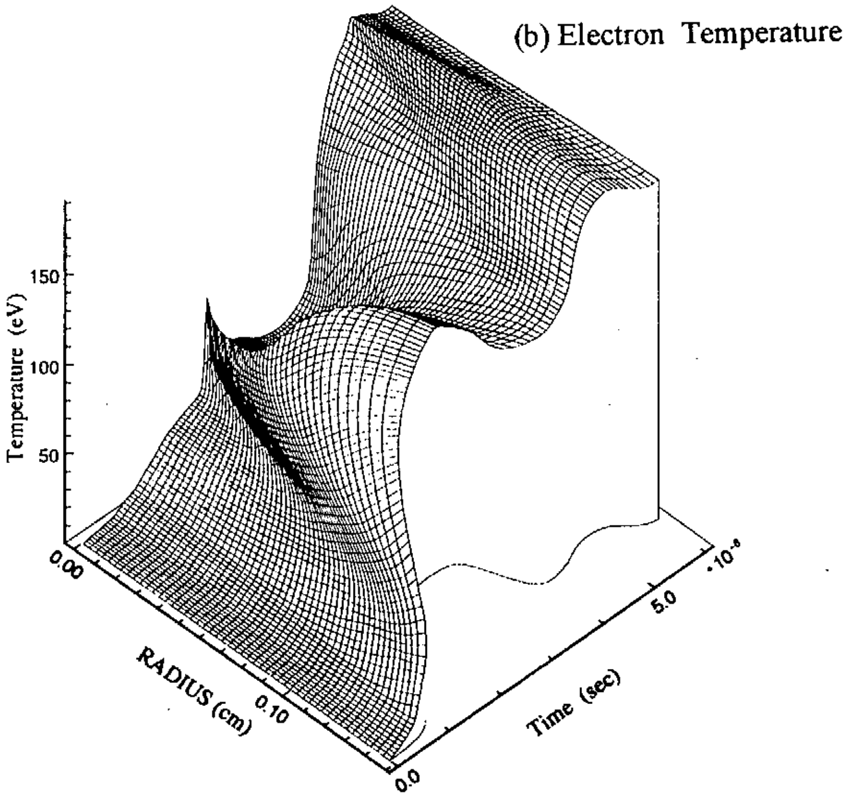

(b) Electron Temperature

Fig.5 Time-Space Distribution of Electron Density and Temperature
(D=3mm, P=370Pa (Ar))

6. Discussion

For proper operation of collisionally excited X-ray laser, it is predicted that the following plasma parameters must be attained at the compression phase [7,8].

For Ar (Ne-like Ar: wavelength 400-700 Å)
ne: (0.5-2) × 10^{19}cm^{-3}, Te: 60-90eV
For Kr (Ne-like Kr: wavelength 170-300 Å)
ne: (2-5) × 10^{20}cm^{-3}, Te: 500-700eV
For Xe (Ni-like Xe: wavelength 91-95 Å)
ne: (2-5) × 10^{20}cm^{-3}, Te: 300-600eV

We must produce a straight and uniform plasma satisfied with above conditions by the fast capillary Z-discharges to succeed in lasing in shorter X-ray region. The possibility depends on whether we can stably implode the column to get such a plasma condition with sufficient uniformity. From the experimental point of view, the critical issue is the stable compression of the plasma column. As shown in Fig.3, the temporal variation of X-ray emission was gradually shifted to hard spectrum region. The spectrums suggested that the plasma column implodes stably within 30nsec and it explodes with electron heating after the implosion. If the column implode unstably with some MHD instabilities, the hard X-ray should be observed early stage in the discharge evolution.

The obtained numerical results of imploding process (in Fig.4) can explain fairly well the experimental plasma behavior. These results suggests the stable one-dimensional implosion of the plasma column. We can cite several factors which may contribute the stable implosion. The fast rising drive current may contribute to the plasma detaching from the inner wall and reduce wall-plasma interaction effects, or improvement of initial uniformity of the load plasma by pre-ionization may suppress growth of MHD instabilities in the compression phase. We have to investigate such a stabilizing mechanisms in detail. As shown in Fig.5 the value of electron density and temperature of argon plasma satisfied enough the lasing conditions at the maximum compression time. So it seems to promise the lasing with Ne-like Ar and also in more harder X-ray region.

We can drive the capillary load by current more than 200kA(peak) with rising time less than a few tens nsec using LIMAY-I. For Krypton or Xenon as the load plasma source, if we can stably compress the column and achieve the dense and hot plasma conditions with sufficient uniformity using capillary Z-discharges, provably we can expect the coherent X-ray radiation in shorter wavelength region.

7. Conclusions

We have driven capillary Z-discharge by fast pulse power generator LIMAY-I, and observed the X-ray spectrums with scintillation detector and XRD diodes. The dynamics of the Z-discharge plasma column were numerically simulated using 1D MHD code. The dynamics obtained experimentally from the spectrums was well explained by the calculated 1D-model, which indicate the column compressed stably by fast capillary Z-discharges. The numerical simulation shows that the plasma satisfy the lasing conditions at the maximum compression time. If we can attain stable implosion with larger current, it seems to succeed in producing the coherent radiation in shorter soft X-ray region.

8. Reference

[1].J.J.Rocca et al., Phys.Rev.Lett.**73**,2192 (1994)
[2].Physics Today, **10**,19 (1994)
[3].J.Raus and V.Piffl, Czech.J.Phys.,**B38**,1222 (1988)
[4].R.H.Day, P.Lee, E.B.Saloman, D.J.Nagel, J.Appl.Phys., **52**,6965 (1981)
[5].R.Ramis, R.Schmalz and J.Meyer-Ter-Vehn, Comput.Phys.Commun.,**49**,475 (1988)
[6].T.Aoki and J.Meyer-Ter-Vehn, Phys.Plasmas., **1**(6),1962 (1994)
[7].A.V.Vinogradov and V.N.Shlyaptsev, Sov.J.Quantum.Electron., **10**(6),754 (1980)
[8].A.V.Vinogradov and V.N.Shlyaptsev, Sov.J.Quantum.Electron., **13**(3),303 (1983)

Early Phenomena of Capillary Discharges in Different Ambient Pressures

T. Sueda, S. Katsuki, H. Akiyama
Department of Electrical Engineering and Computer Science, Kumamoto University,
Kurokami 2-39-1, Kumamoto 860, JAPAN

Abstract

An 80 kJ electrothermal gun facility was assembled at Kumamoto University in order to investigate the dependence of capillary discharges on ambient pressure. The observation of capillary discharges using an image converter camera shows that early phenomena of the discharges vary with ambient pressure. At a pressure of one atmosphere , discharges begin to occur near the radial center of the capillary. On the other hand, at a lower pressure of about 1 Pa, discharges occur near the insulator surface of the capillary. Plasma parameters, such as electron density and electron temperature, and the species of the plasma and neutral gas, are measured by spectroscopic techniques. The electron density at low pressure is more than 10^{17} cm^{-3} at a current of only about 1 kA because of severe wall ablation by the surface discharge. At high pressure, the electron density is quite low for electron currents less than 2 kA. For currents greater than 2 kA, the electron density is over 10^{18} cm^{-3} at both pressures. The temperature estimated from a Boltzmann plot is in the range of 0.6 eV to 0.7 eV at low pressure.

1. Introduction

Electrothermal guns have been developed in order to simulate micro-meteoroid and space debris impacts, and to produce extremely high pressure and temperature for the development of materials [1] [2]. It has been reported that the geometry and design of the capillary have a strong influence on the performance of electrothermal guns [1] [3] [4]. Experiments on electrothermal guns have been conducted at various ambient pressures in the chamber according to their particular application. The 80 kJ electrothermal gun facility at Kumamoto University was assembled in order to investigate the phenomena of capillary discharges and to determine plasma parameters for different ambient pressures.

In this paper, the early phenomena of capillary discharges for different ambient pressures in the chamber are observed by using an image converter camera. Also, plasma parameters, such as electron density and electron temperature, and the species of the capillary plasmas are measured by spectroscopic techniques at different ambient pressures. Then, the relation between the behavior of capillary discharges and the electron density and temperature of the capillary plasmas, for changing ambient pressure, is discussed.

2. Experimental apparatus and procedures

Figures 1 and 2 show the experimental setups for observing radiation from the capillary discharges and for estimating plasma parameters, respectively. The power supply consists of a capacitor bank with a maximum stored energy of 80 kJ and a capacitance of 64 μF, a coil with an inductance of 3.5 μH and a triggered spark gap switch (TGS). Although the electrothermal gun usually consists of electrodes (copper), a capillary (polyethylene) and a barrel (steel), the barrel is removed from the electrothermal gun during these experiments in order to observe the behavior of capillary discharges. The inner diameter and the length of the capillary with a cylindrical configuration are 4 mm or 2 mm, and 30 mm, respectively. A thin copper wire with a diameter of 0.04 mm is placed in the capillary, and is connected to both ends of the capillary.

The discharge current through the electrothermal gun is measured by a Rogowski coil (RC), and the voltage across the capillary plasma is measured by a voltage divider (VD) with a 1/240 voltage ratio. All signals are recorded with digital oscilloscopes (OSC), and then are analyzed by a computer. The image converter camera (Hadland Photonics Limited, IMACON 790) is used to observe the behavior of the capillary discharges. The framing speed, the exposure time, and the inter frame time are 2×10^6 frames/sec, 100 nsec/frame, and 500 nsec, respectively. The delay generator is used to control the time between the triggers of the spark gap switch and the image converter camera .

The time dependence of the radiation from capillary plasmas is measured by using a monochromator (Mininuteman Laboratories, Model 302-VM) with 1200 grooves/mm. The light from capillary plasmas enters the monochromator, with an entrance slit of 300 μm, through a quartz optical fiber with a diameter of 1 mm. A photomultiplier tube (Hamamatsu Photonics Co., R955) is used to detect the light. Either of two wavelengths, 486.1 nm (H_β line) or 324.7 nm (C_u line), is selected. The electron density and temperature in the early phase are estimated by using a Czerny-Turner 320 mm optical multichannel analyzer (Atago Bussan Co., Multiviewer Macs320). The slit width is 25 μm. The light spectrum amplified by an image intensifier is measured by a photodiode array with 1024 channels. The maximum wavelength window of this system is 40 nm, which limits the maximum electron density estimated from the line shape.

3. Stark broadening of H_α line [5] and Relative intensities of neutral copper lines [6]

Stark broadening results from the interaction of the radiator atom with the electric field produced by charged particles near the location of the radiator, and depends on the density of the charged particles. The electron density N_e is equal to the ion density N_i for singly charged ions. Based on the theory of Stark broadening [7], which takes into account quasistatic ions and impact-electron-broadening effects, the expression for the electron density in terms of the linewidth of hydrogen lines is

$$N_e = 8.02\times10^{12}\left(\frac{\Delta\lambda_{1/2}}{\alpha_{1/2}}\right)^{3/2}, \tag{1}$$

where $\Delta\lambda_{1/2}$ is the linewidth (FWHM) in angstroms. The reduced wavelength $\alpha_{1/2}$ is a function of the electron density and temperature, i.e., $\alpha_{1/2} = \alpha_{1/2}(N_e, T)$, and is tabulated in Table III. a. of Ref. 7 for the H_α line. The electron density versus the FWHM of the H_α line, calculated from equation (1) and Ref. 7, is shown in Fig. 3. In a few cases where the deduced density was below 10^{17} cm^{-3}, ion-dynamical corrections to the $\alpha_{1/2}$ values of H_α were included, using data taken from Ref. 7. The electron density was in the range 10^{16} - 10^{19} cm^{-3}, which corresponds to 5 - 300 Å in Stark broadening width (FWHM) in this experiment. Doppler broadening, therefore, was neglected [8] .

The electron temperature generally is estimated by the relative emission intensities of spectral lines. The relative intensities of the spectral lines are used in the following equation

$$\ln\left(\frac{I\lambda}{Ag_u}\right) = C - \frac{E_u}{kT}, \tag{2}$$

where I, λ, A, g_u, E_u, k and T are the relative intensity, wavelength, the transition probability, the statistical weight of the upper level, the energy of the upper level, Boltzmann's constant and temperature. The transition probabilities, the statistical weights and the energy of the upper levels of the copper lines are shown in Ref. 9. A plot of the logarithmic term versus E_u yields a straight line whose slope is equal to -1/kT. The electron temperature is the reciprocal of the slope. The electron density is estimated by using the transitions from three copper lines (510.55, 515.32, 521.82 nm).

4. Results and Discussion

A. Capillary discharges in the early phase

Figures 4 and 5 show typical waveforms of the discharge current and the voltage across the capillary, as well as photographs of capillary discharges observed by the image converter camera, for ambient pressures of 0.1 MPa and 1.3 Pa, respectively. The dotted and solid lines are the waveforms of voltage and current, respectively.

In the high pressure case (0.1 MPa), the voltage waveform across the capillary shows a steep pulse at about 0.8 μsec, caused by the rapid increase in resistance of the thin copper wire placed in the capillary due to melting and vaporization . That is, by the operation of an opening switch. Then, the voltage becomes a constant value of about 8 kV during a dwell time that lasts until about 2.8 μsec, which corresponds to the formation time of a discharge at high pressure. The constant voltage corresponds to the residual voltage of the 64 μF capacitor. After 3 μsec, the voltage becomes a different constant value of about 1 kV, and is independent of the discharge current, as known from the AWA theory [10] [11]. According to the photographs in Fig. 4, the early capillary discharge in the high pressure case occurs near the center of the capillary as an arc discharge and gradually expands, not uniformly.

In the low pressure case (1.3 Pa), after the pulsed voltage is produced by the melting and vaporization of the wire, the voltage across the capillary increases until about 6 μsec, and then becomes constant, although Fig. 5 shows data only for times less than 5 μsec. According to the photographs in Fig. 5, the early capillary discharge occurs at or near the surface of the capillary and develops uniformly. These phenomena are very different from those in the high pressure case. The behavior of discharges in the beginning of capillary discharges therefore changes from surface discharges to arc discharges with decreasing ambient pressure.

B. Spectroscopic measurements

Figures 6 and 7 show typical waveforms of the discharge current and voltage across the capillary, and PMT signals for the (a) C_u line (324.7 nm) and (b) H_β line (486.1 nm) measured by the monochromator for ambient pressures of 0.1 MPa and 13 Pa, respectively. In the case of high pressure, the C_u line is observed and the H_β line is not observed at about 1 μsec when the wire is vaporized. Luminosity of the first photograph in Fig. 4 mainly comes from a copper line. After an arc discharge at about 3 μsec, both the C_u and H_β lines are observed, since wall ablation occurs on the surface of the capillary. In the case of low pressure, the signals from the C_u and H_β lines show almost the same waveform.

The electron density of capillary plasmas in the early phase is estimated from Stark broadening of the H_α line. Typical waveforms of the discharge current and the voltage across the capillary, and of the H_α line (656.28 nm) observed in the direction of axis of the capillary, are shown in Figs. 8 and 9 for 0.1 MPa and 1.3 Pa, respectively. Arrows in Figs. 8 and 9 show the times when the H_α line is observed. The time window is 500 nsec. A nitrogen line also appears near 645 nm at one atmosphere. The dependence of the electron density of the capillary plasma on the discharge current is shown in Fig. 10 for ambient pressures of 0.1 MPa and 13 Pa. Although the electron temperature is assumed to be 1 eV, the calculation of electron density shows only a small dependence on the temperature. In the case of high pressure, the electron density of capillary plasmas at less than 2 kA is quite low, less than 10^{15} cm^{-3}. When the current is more than 2 kA, the density is over 10^{18} cm^{-3}.

In the case of high pressure, the early capillary discharge occurs near the center of the capillary as an arc discharge and gradually expands. Therefore, wall ablation is small at less than 2 kA. On the other hand, in the case of low pressure, the density already becomes more than 10^{17} cm^{-3} at a current of only about 1 kA, since severe wall ablation occurs on the surface of the capillary.

The electron temperature of capillary plasmas in the early phase is estimated by the relative intensities of C_u lines. Because the observation of several C_u lines is difficult, the data is obtained only in the case of low pressure, as shown in Fig. 11. The Boltzmann plots are also shown at the current of 7.5 kA. Some deviations from linearity indicate a small difference from LTE condition and/or self-absorption. The temperature estimated by the Boltzmann plot is roughly 0.6 eV to 0.7 eV.

5. Conclusion

The early phenomena of capillary discharges are observed, and plasma parameters are measured for different ambient pressures. The behavior of discharges at the beginning of capillary discharges varies from surface discharges to arc discharges with increasing ambient pressure. The surface discharge at low pressure occurs immediately after the wire vaporizes, and the arc discharge at high pressure occurs after a dwell time.

The electron density at low pressure is more than 10^{17} cm^{-3} at a current of only about 1 kA because of severe wall ablation by surface discharges. In the case of high pressure, the electron density is quite low at less than 2 kA. At both pressures, the electron density is over 10^{18} cm^{-3} when the current is more than 2 kA. At low pressures, the temperature estimated from a Boltzmann plot is in the range of 0.6 eV to 0.7 eV. In the future, we plan to investigate the temperature of capillary plasmas in more detail.

The authors would like to thank Prof. M. Hagler for useful comments.

Reference

[1] M. Rott, "The LRT/TUM Small Caliber Electrothermal Accelerator", IEEE Trans. on Magnetics, Vol. 29, No. 1, pp. 597-602 (1993)

[2] M. Shahinpoor, J. R. Asay et al., "Use of a Two-Stage Light-Gas Gun as an Injector for Electromagnetic Railguns", IEEE Trans. on Magnetics, Vol. 25, No. 1, pp. 514-518 (1989)

[3] David A. Benson, Steven N. Kempka, "Studies of Confined High-Pressure Discharges in an Electrothermal Capillary", IEEE Trans. on Magnetics, Vol. 29, No. 1, pp. 544-549 (1993)

[4] M. Rott, "Design Optimizations of a Small Caliber Electrothermal Accelerator", IEEE Trans. on Magnetics, Vol. 31, No. 1, pp. 441-446 (1995)

[5] J. Ashkenazy, R. Kipper, and M. Caner, "Spectroscopic measurements of electron density of capillary plasma based on Stark broadening of hydrogen lines", Physical Rev. A, Vol. 43, No. 10, pp. 5568-5574 (1991)

[6] O. E. Hankins, M. A. Bourham, J. Earnhart, and J. G. Gilligan, "Visible Light Emission Measurements From A Dense Electrothermal Launcher Plasma", IEEE Trans. on Magnetics, Vol. 29, No. 1, pp. 1158-1161 (1993)

[7] H. R. Griem, "Spectral Line Broadening by Plasma", Academic, New York (1974)

[8] Dipak H. Oza, Ronald L. Greene, and Daniel E. Kelleher, "Collisonal broadening of the Balmer-α transition of H and He^+ in plasmas", Physical Rev. A, Vol. 37, No. 2, pp. 531-536 (1988)

[9] W. L. Wiese and G. A. Martin, "Wavelengths and Transition Probabilities for Atoms and Atomic Ions Part II Transition Probabilities ", NSRDS-NBS 68, Institute for Basic Standards, NBS Washington, D. C. (1980)

[10] William B. Maier, Abraham Kadish et al., "Comparison of the AWA Lumped-Circuit Model of Electrical Discharges with Empirical Data", IEEE Trans. on Plasma Science, Vol. 18, No. 6, pp. 1033-1037 (1990)

[11] R. T. Robiscoe, Abraham Kadish et al., "Overdamped Arc Discharge Data and an AWA Model", IEEE Trans. on Plasma Science, Vol. 19, No. 3, pp. 529-534 (1991)

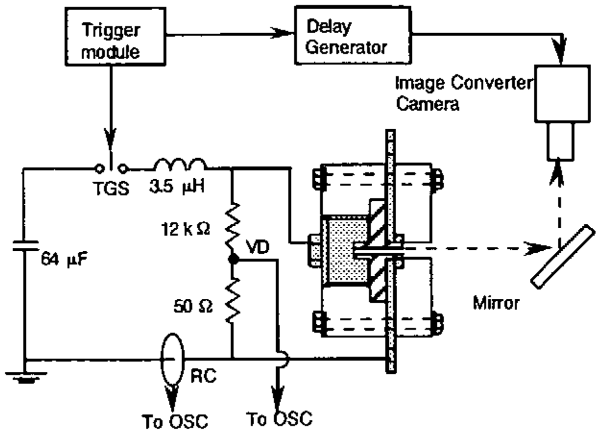

Fig. 1 Experimental apparatus for observing the capillary discharges.

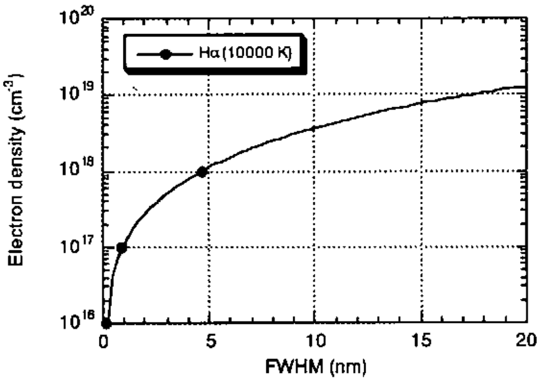

Fig. 3 Electron density calculated from the FWHM for the H_α line.

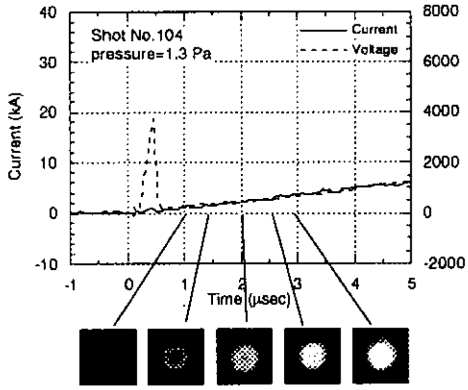

Fig. 5 Waveforms of the discharge current and voltage across the capillary, photographs of early capillary discharges observed by the image converter camera for ambient pressures of 1.3 Pa.

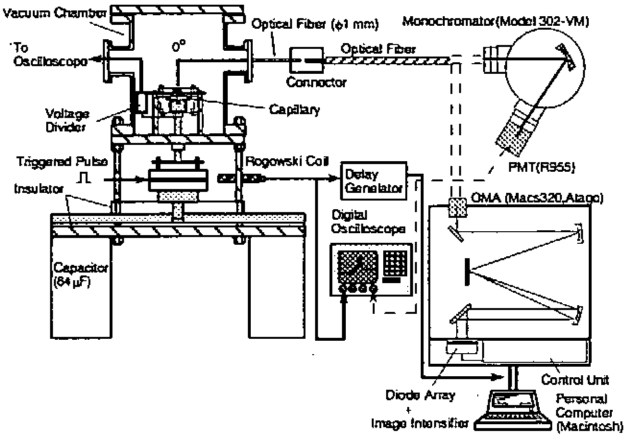

Fig. 2 Experimental apparatus for spectroscopic measurements.

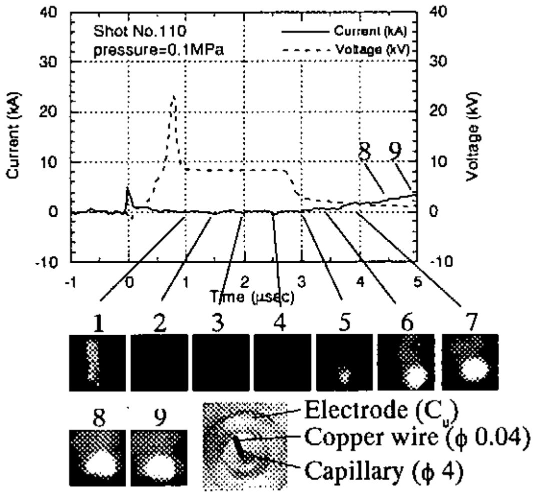

Fig. 4 Waveforms of the discharge current and voltage across the capillary, photographs of early capillary discharges observed by the image converter camera for ambient pressures of 0.1 MPa.

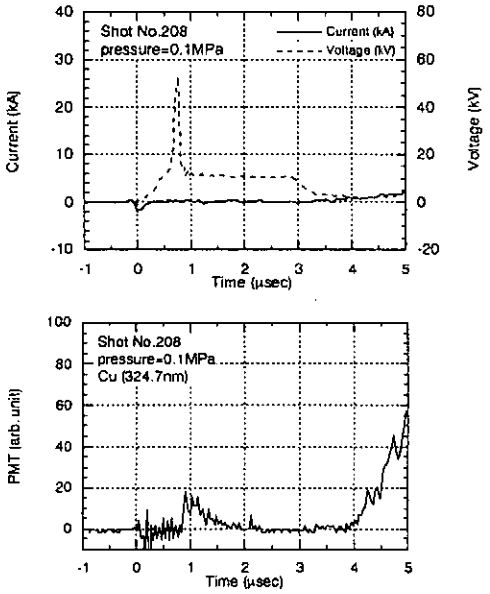

(a) C_u line

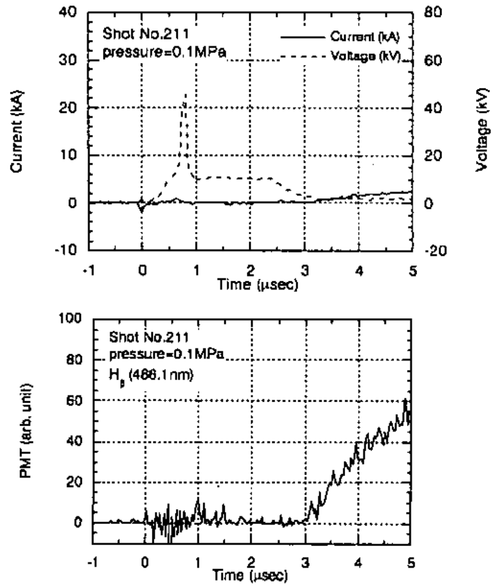

(b) H_β line

Fig. 6 Waveforms of the discharge current and voltage across the capillary, PMT signal for (a) the C_u line and (b) the H_β line measured by using the monochromator for an ambient pressure of 0.1 MPa.

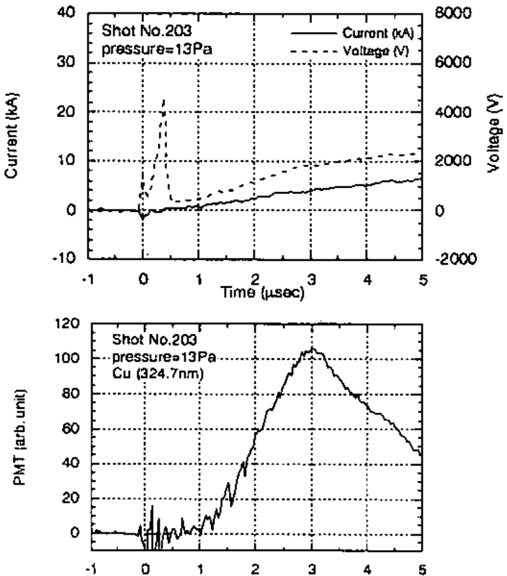

(a) C_u line

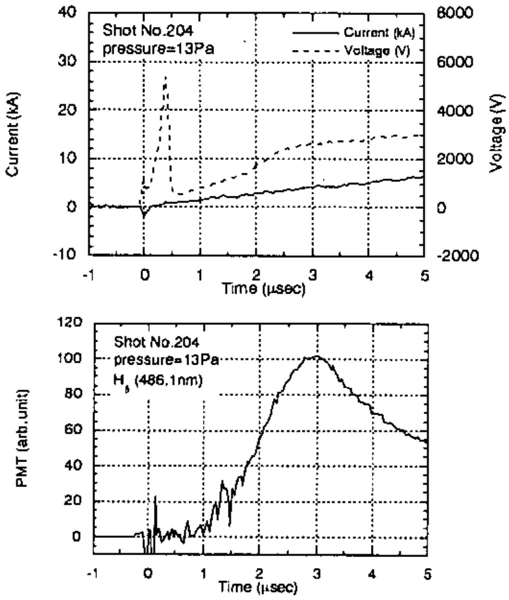

(b) H_β line

Fig. 7 Waveforms of the discharge current and voltage across the capillary, PMT signal for (a) the C_u line and (b) the H_β line measured by using the monochromator for an ambient pressure of 13 Pa.

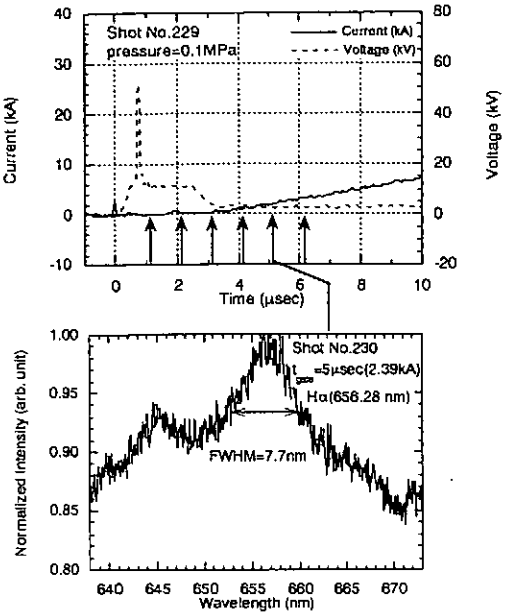

Fig. 8 Waveforms of the discharge current and voltage across the capillary, one of H_α lines observed at 0° on axis of the capillary for ambient pressure of 0.1 MPa.

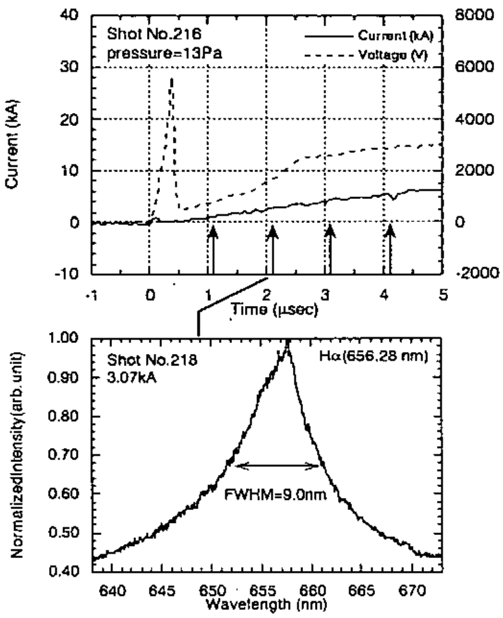

Fig. 9 Waveforms of the discharge current and voltage across the capillary, one of the H_α lines observed at 0° on axis of the capillary for ambient pressure of 13 Pa.

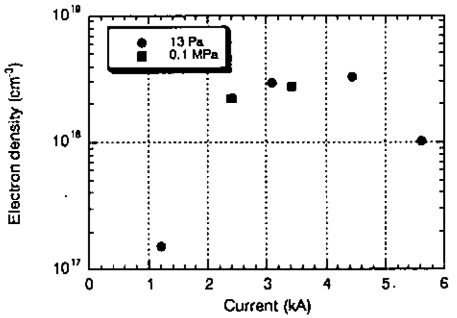

Fig. 10 Electron density of capillary plasmas versus the current for an ambient pressure of 0.1 MPa and 13 Pa.

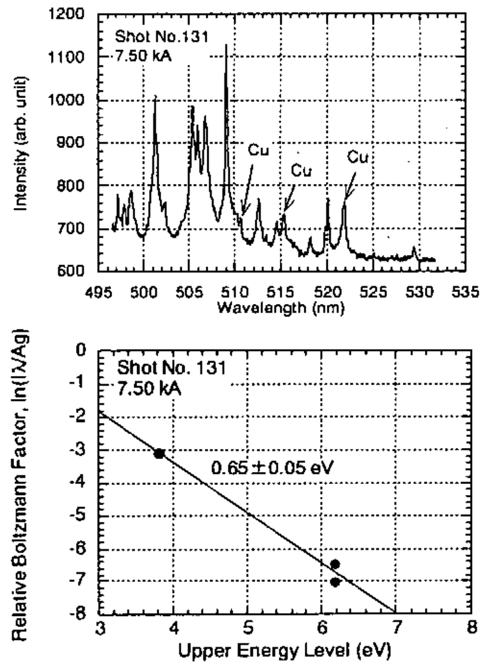

Fig. 11 C_u lines and the Boltzmann plots at 7.5 kA for an ambient pressure of 13 Pa.

Publication List of NIFS-PROC Series

NIFS-PROC-1	*U.S.-Japan on Comparison of Theoretical and Experimental Transport in Toroidal Systems Oct. 23-27, 1989* , Mar. 1990
NIFS-PROC-2	*Structures in Confined Plasmas –Proceedings of Workshop of US-Japan Joint Institute for Fusion Theory Program–* ; Mar. 1990
NIFS-PROC-3	*Proceedings of the First International Toki Conference on Plasma Physics and Controlled Nuclear Fusion –Next Generation Experiments in Helical Systems– Dec. 4-7, 1989* Mar. 1990
NIFS-PROC-4	*Plasma Spectroscopy and Atomic Processes –Proceedings of the Workshop at Data & Planning Center in NIFS–*; Sep. 1990
NIFS-PROC-5	*Symposium on Development of Intensed Pulsed Particle Beams and Its Applications February 20 1990*; Oct. 1990
NIFS-PROC-6	*Proceedings of the Second International TOKI Conference on Plasma Physics and Controlled Nuclear Fusion , Nonlinear Phenomena in Fusion Plasmas -Theory and Computer Simulation-;* Apr. 1991
NIFS-PROC-7	*Proceedings of Workshop on Emissions from Heavy Current Carrying High Density Plasma and Diagnostics;* May 1991
NIFS-PROC-8	*Symposium on Development and Applications of Intense Pulsed Particle Beams, December 6 - 7, 1990*; June 1991
NIFS-PROC-9	*X-ray Radiation from Hot Dense Plasmas and Atomic Processes*; Oct. 1991
NIFS-PROC-10	*U.S.-Japan Workshop on "RF Heating and Current Drive in Confinement Systems Tokamaks" Nov. 18-21, 1991*, Jan. 1992
NIFS-PROC-11	*Plasma-Based and Novel Accelerators (Proceedings of Workshop on Plasma-Based and Novel Accelerators) Nagoya, Japan, Dec. 1991*; May 1992
NIFS-PROC-12	*Proceedings of Japan-U.S. Workshop P-196 on High Heat Flux Components and Plasma Surface Interactions for Next Devices*; Mar. 1993
NIFS-PROC-13	『NIFS シンポジウム 「核燃焼プラズマの研究を考える－現状と今後の取り組み方」 1992年7月15日、核融合科学研究所』

	1993年 7月 *NIFS Symposium* *"Toward the Research of Fusion Burning Plasmas -Present Status and Future strategy-", 1992 July 15, National Institute for Fusion Science;* July 1993 (in Japanese)
NIFS-PROC-14	*Physics and Application of High Density Z-pinches,* July 1993
NIFS-PROC-15	岡本正雄、講義「プラズマ物理の基礎」 平成5年度　総合大学院大学 1994年　2月 *M. Okamoto,* *"Lecture Note on the Bases of Plasma Pysics"* *Graduate University for Advanced Studies* Feb. 1994 (in Japanese)
NIFS-PROC-16	代表者　河合良信 平成5年度　核融合科学研究所共同研究 研究会報告書 「プラズマ中のカオス現象」 *"Interdisciplinary Graduate School of Engineering Sciences"* *Report of the meeting on Chaotic Phenomena in Plasma* Apr. 1994 (in Japanese)
NIFS-PROC-17	平成5年度NIFSシンオジウム報告書 「核融合炉開発研究のアセスメント」 平成5年11月29日-30日　於　核融合科学研究所 *"Assessment of Fusion Reactor Development"* *Proceedings of NIFS Symposium held on November 29-30, 1993 at National Insitute for Fusion Science"* Apr. 1994 (in Japanese)
NIFS-PROC-18	*"Physics of High Energy Density Plasmas Produced by Pulsed Power"* June 1994
NIFS-PROC-19	K. Morita, N. Noda (Ed.), *"Proceedings of 2nd International Workshop on Tritium Effects in Plasma Facing Components at Nagoya University, Symposion Hall, May 19-20, 1994",* Aug. 1994
NIFS-PROC-20	研究代表者　阿部　勝憲　（東北大学・工学部） 所内世話人　野田信明 平成6年度　核融合科学研究所共同研究［研究会］ 「金属系高熱流束材料の開発と評価」成果報告書 K. Abe and N. Noda (Eds.), *"Research and Development of Metallic Materials for Plasma Facing and High Heat Flux Components"* Nov. 1994 (in Japanese)

NIFS-PROC-21
世話人：森田　健治（名大工学部）、金子　敏明（岡山理科大学理学部）
「境界プラズマと炉壁との相互作用に関する基礎過程の研究」
研究会報告
K. Morita (Nagoya Univ.), T. Kaneko (Okayama Univ. Science)(Eds.)
NIFS Joint Meeting "Plasma-Divertor Interactions" and
"Fundamentals of Boundary Plasma-Wall Interactions"
January 6-7, 1995 National Institute for Fusion Science
Mar. 1995 (in Japanese)

NIFS-PROC-22
代表者　河合　良信
プラズマ中のカオス現象
Y. Kawai,
Report of the Meeting on Chaotic Phenomena in Plasma, 1994
Apr. 1995 (in Japanese)

NIFS-PROC-23
K. Yatsui (Ed.),
New Applications of Pulsed, High-Energy Density Plasmas;
June 1995

NIFS-PROC-24
T. Kuroda and M. Sasao (Eds.),
Proceedings of the Symposium on Negative Ion Sources and Their
Applications, NIFS, Dec. 26-27, 1994 , Aug. 1995

NIFS-PROC-25
岡本正雄
新古典輸送概論（講義録）
M. Okamoto,
An Introduction to the Neoclassical Transport Theory
(Lecture note), Nov. 1995 (in Japanese)

NIFS-PROC-26
Shozo Ishii (Ed.),
Physics, Diagnostics, and Application of Pulsed High Energy
Density Plasma as an Extreme State; May 1996